



**HAL**  
open science

# Design of metal silicide nanoparticles in molten salts : electrocatalytic and magnetic properties

Yang Song

► **To cite this version:**

Yang Song. Design of metal silicide nanoparticles in molten salts: electrocatalytic and magnetic properties. Catalysis. Sorbonne Université, 2021. English. NNT : 2021SORUS498 . tel-04292995

**HAL Id: tel-04292995**

**<https://theses.hal.science/tel-04292995>**

Submitted on 18 Nov 2023

**HAL** is a multi-disciplinary open access archive for the deposit and dissemination of scientific research documents, whether they are published or not. The documents may come from teaching and research institutions in France or abroad, or from public or private research centers.

L'archive ouverte pluridisciplinaire **HAL**, est destinée au dépôt et à la diffusion de documents scientifiques de niveau recherche, publiés ou non, émanant des établissements d'enseignement et de recherche français ou étrangers, des laboratoires publics ou privés.



# Sorbonne Université

Ecole doctorale de Physique et Chimie des Matériaux (ED 397)

*Laboratoire de Chimie de la Matière Condensée de Paris*

## **Design of metal silicide nanoparticles in molten salts: electrocatalytic and magnetic properties**

Par Yang SONG

Thèse de doctorat de Physique et Chimie des Matériaux

Dirigée par David Portehault

Présentée et soutenue publiquement le 17 novembre 2021

Devant un jury composé de :

Mme. Drisko Glenna	Chargée de recherche CNRS, ICMCB Bordeaux	Rapporteuse
M. Habrioux Aurélien	Maître de conférence Université de Poitiers, IC2MP	Rapporteur
M. Petit Christophe	Professeur Sorbonne Université, MONARIS	Examinateur
M. Portehault David	Directeur de Recherche CNRS, LCMCP Paris	Directeur de thèse



Except where otherwise noted, this work is licensed under  
<http://creativecommons.org/licenses/by-nc-nd/3.0/>



*To my parents*



# Acknowledgement

I would like to thank firstly the jury members, Dr. Glenna Drisko, Dr. Aurélien Habrioux and Pf. Christophe Petit, for serving as my jury members, and also for your brilliant comments and suggestions in the thesis reports.

I would like to express my special appreciation and thanks to my supervisor Dr. David Portehault for accepting my application for this subject, for encouraging a lot my research and for helping me to grow as a research scientist.

I want to thank Pf. Corinne Chanéac who recommended me to my supervisor, so that we could have the first discussion which is the very starting point of the whole story.

I want to thank a former group member Dr. Ram Kumar, for his pioneering work in metal silicide nanoparticle synthesis.

Many thanks to all the Nanobreakfast members Fernando, Guillaume, Edouard, Anissa, Ram, Alexandre, Francisco, my officemates Amandine, Daniel, Kim, Isabel and PhD students of my promotion. I really appreciate all the discussions we had and the moments we shared together.

And I want to thank all the LCMCP permanents who gave me important training and scientific helps.

I had an amazing time during the three years I worked at LCMCP. I want to thank the lab direction and secretariat for helping me on all the administrative stuff and making everything smooth and joyful in the lab. I want to thank all the LCMCP members I met. You made these three years unforgettable in my life.

I want to thank the funders giving the important financial supports for this PhD subject: China Scholarship Council and Sorbonne Université.

Special thanks to Binghua, Madeleine, Runhe, Kankan, for helping me to integrate into the lab when I arrived, and for your tremendous supports during my whole PhD study.

I would like to thank IFCEN alumni, my friends Chih-Ying, Hao, Yuchen, Dingan, Jinlin, Shuaitao, and my roommates for six years in college, Danmeng, Qingyun, Wencheng. Thank you for your supports during my study.

At the end, special thanks to my family and Zimin. Words cannot express how grateful I am. Thank you for supporting me for everything.



# Summary

<b>General introduction</b> .....	<b>9</b>
<b>Chapter I. Introduction</b> .....	<b>11</b>
I.1 Hydrogen production by water splitting .....	11
I.2 Electrocatalysis of water oxidation in alkaline medium .....	13
I.3 Transition metal silicide nanomaterials .....	16
I.4 Today's challenges towards transition metal silicide nanomaterials.....	19
I.5 Summary and strategy of this work.....	24
References .....	26
<b>Chapter II. Synthesis and electrocatalytic properties of Fe-doped Ni<sub>2</sub>Si nanoparticles ....</b>	<b>43</b>
II.1 Introduction .....	43
II.2 Experimental methods.....	45
II.3 Results and Discussion .....	48
II.3.1 Synthesis and characterization.....	48
II.3.2 Electrocatalytic properties.....	54
II.3.3 <i>Post mortem</i> studies.....	59
II.4 Conclusion.....	64
References .....	66
<b>Chapter III. Ferromagnetic and electrocatalytically active CoSi nanoparticles .....</b>	<b>73</b>
III.1 Introduction .....	73
III.2 Experimental methods.....	74
III.3 Results and discussion.....	76
III.3.1 Characterization of CoSi nanoparticles.....	76
III.3.2 Magnetic properties.....	82
III.3.3 Electrocatalytic properties and <i>post mortem</i> studies.....	84
III.4 Conclusion.....	88
References .....	89
<b>Chapter IV. Synthesis of Na<sub>4</sub>Si<sub>4</sub> .....</b>	<b>95</b>
IV.1 Zintl phase Na <sub>4</sub> Si <sub>4</sub> .....	95
IV.2 Experimental methods.....	98
IV.3 Results and discussion.....	99
IV.3.1 Optimal synthesis of Na <sub>4</sub> Si <sub>4</sub> .....	99
IV.3.2 Impact of the Si source.....	102

IV.3.3	Impact of the reaction time.....	103
IV.3.4	Impact of the argon flow rate.....	104
IV.4	Simple approach to silicon clathrates.....	106
IV.5	Conclusion.....	109
	References.....	110
<b>Chapter V. Synthesis and electrocatalytic properties of a ternary nickel silicophosphide</b>		<b>113</b>
V.1	Introduction.....	113
V.2	Experimental methods.....	115
V.3	Results and discussion.....	117
V.3.1	Synthesis and characterization.....	117
V.3.2	Electrocatalysis of water splitting.....	123
V.3.3	<i>Post mortem</i> study.....	126
V.4	Conclusion.....	129
	References.....	130
<b>General conclusion</b> .....		<b>137</b>
<b>Appendix</b> .....		<b>141</b>

# General introduction

Transition metal silicides are a family of intermetallic compounds delivering various properties including heterogeneous catalysis and magnetism. Recently, dihydrogen production by water splitting received tremendous attention because of the energy transition. Some transition metal silicides have been demonstrated electrocatalytically active for electrolysis of alkaline water. On the other hand, transition metal monosilicides have shown a surface related defect-induced ferromagnetism. Further tuning of the properties of these materials can be achieved by nanostructuring. However, the synthesis approaches towards nanostructures of transition metal silicides remain few, because the formation of their relatively high energy bonds requires high temperature, which cannot be afforded by traditional colloidal synthesis.

Hence, this thesis is dedicated to the design of transition silicide nanoparticles, as well as to the study of their electrocatalytic properties of water splitting in alkaline medium and to their magnetic properties. This thesis includes five chapters:

In the first chapter, we present a brief state-of-the-art concerning the understanding of reaction pathways for electrocatalytic electrolysis of alkaline water, we then highlight state-of-the-art electrocatalysts. Then, the properties of transition metal silicides are presented. Traditional synthesis methods and recently developed approaches towards these phases are reviewed. Finally, two molten salts synthesis strategies using nanoparticles as precursors are proposed.

The second chapter is the proof-of-concept of our first synthesis strategy by insertion of metal species into silicon nanoparticles in molten salts. The obtained nanoparticles of iron silicide, nickel silicide and iron-doped nickel silicides are assessed as electrocatalysts for water oxidation. *Post mortem* studies are conducted to elucidate the origin of the outstanding activity and stability of iron-doped nickel silicides.

The third chapter presents cobalt monosilicide nanoparticles synthesized through the same method as above. Core-shell and homogeneous CoSi nanoparticles can be respectively achieved upon different reaction temperatures. Then, these nanoparticles are measured in OER electrocatalysis and *post mortem* analysis are carried out. Besides, these CoSi nanoparticles show peculiar interface-related ferromagnetic properties, discussed based on magnetic measurements.

The fourth chapter focuses on an important silicon precursor, sodium silicide  $\text{Na}_4\text{Si}_4$ , for our second synthesis strategy. A reproducible and straightforward approach to high purity  $\text{Na}_4\text{Si}_4$  is detailed. The impact of the silicon source, the argon flow rate and the reaction time on synthesis outcome are discussed. The selective thermal decomposition of  $\text{Na}_4\text{Si}_4$  towards type I and type II sodium silicon clathrates is then studied to assess the efficiency as precursor of  $\text{Na}_4\text{Si}_4$  prepared in this work.

The fifth chapter presents our second synthesis strategy. P-doped  $\text{Ni}_2\text{Si}$  and original ternary nickel silicophosphide nanoparticles are obtained by reacting P-doped nickel nanoparticles and  $\text{Na}_4\text{Si}_4$  in molten salts. The electrocatalytic properties in overall alkaline water splitting of the ternary silicophosphide nanoparticles are discussed in respect to those of the binary nickel silicide. Preliminary *post mortem* results further reveal the different behaviors of ternary and binary phases in electrocatalysis.

# Chapter I. Introduction

## I.1 Hydrogen production by water splitting

Facing the climate change challenge, 191 countries ratified the Paris Agreement commit to reduce their greenhouse gas emission and reach climate neutrality by 2050.<sup>1</sup> Under this agreement, high carbon emission energies will be gradually replaced by renewable energies, *e.g.* hydropower, biomass, and geothermal energy. However, the uneven geographic distribution and intermittent production of renewable energies requires an energy carrier to realize a redistribution of energy, which acts as a “buffer” to improve the availability and resilience of renewable energy.<sup>2,3</sup>

Hydrogen (H<sub>2</sub>) produced by water electrolysis is a promising energy carrier for transient renewable energies by offering three main advantages. Firstly, the energy density of hydrogen attains 118 MJ kg<sup>-1</sup>, which is almost three times that of other fossil fuels (44 MJ kg<sup>-1</sup> for gasoline).<sup>4</sup> Moreover, combustion of hydrogen yields only water without emission of CO<sub>2</sub> or other greenhouse gas, in good conformity with the decarbonization principle. Thirdly, the hydrogen production reaction by water electrolysis is zero-carbon-emission on its own. Hence, water electrolysis powered by renewable energy turns to be an auspicious solution to store the surplus electricity, which focuses intense efforts nowadays.<sup>3,5</sup>

The characteristics of typical cells for water electrolysis are listed in **Table I-1**.<sup>6</sup> The alkaline water electrolysis (AWE) is the most applied commercial technology. AWE is extendedly used since the early 1900s thanks to its accessibility and economics. Even though, AWE has some drawbacks: imperfect gas separation, low operating pressure and limited current density. These bottlenecks hindered the development of water electrolysis.<sup>5,7,8</sup> Currently appearing solid-state electrolytes used in solid oxide electrolysis and membrane electrode assemblies could overcome many of the drawbacks of AWE.<sup>6</sup> A ceramic oxide electrolyte is used in a solid oxide electrolyzer, while a polymeric membrane is used in a membrane electrode assembly. The latter can be achieved either in acidic or alkaline media by using proton exchange membranes (PEM)<sup>9</sup> or anion exchange membranes (AEM)<sup>10,11</sup>, respectively. Current solid oxide electrolyzers work at temperature up to 1000 °C, where the kinetics and thermodynamics of chemical reactions are

enhanced. Nevertheless, failures of structure mechanical integrity arise due to the high operation temperature.<sup>6</sup>

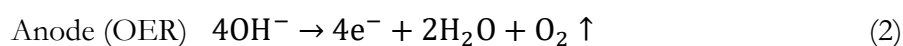
**Table I-1** Characteristics of typical water electrolysis cell (published in 2017).<sup>6</sup>

	Low Temperature Electrolysis			High Temperature Electrolysis		
	Alkaline (OH <sup>-</sup> ) electrolysis	Proton Exchange (H <sup>+</sup> ) electrolysis	Oxygen ion(O <sup>2-</sup> ) electrolysis			
	Liquid	Polymer Electrolyte Membrane	Solid Oxide Electrolysis (SOE)			
	Conventional	Solid alkaline	H <sup>+</sup> -PEM	H <sup>+</sup> -SOE	O <sup>2-</sup> -SOE	Co-electrolysis
Operation principles						
Charge carrier	OH <sup>-</sup>	OH <sup>-</sup>	H <sup>+</sup>	H <sup>+</sup>	O <sup>2-</sup>	O <sup>2-</sup>
Temperature	20-80°C	20-200°C	20-200°C	500-1000°C	500-1000°C	750-900°C
Electrolyte	liquid	solid (polymeric)	solid (polymeric)	solid (ceramic)	solid (ceramic)	solid (ceramic)
Anodic Reaction (OER)	$4\text{OH}^- \rightarrow 2\text{H}_2\text{O} + \text{O}_2 + 4\text{e}^-$	$4\text{OH}^- \rightarrow 2\text{H}_2\text{O} + \text{O}_2 + 4\text{e}^-$	$2\text{H}_2\text{O} \rightarrow 4\text{H}^+ + \text{O}_2 + 4\text{e}^-$	$2\text{H}_2\text{O} \rightarrow 4\text{H}^+ + 4\text{e}^- + \text{O}_2$	$\text{O}^{2-} \rightarrow \frac{1}{2}\text{O}_2 + 2\text{e}^-$	$\text{O}^{2-} \rightarrow \frac{1}{2}\text{O}_2 + 2\text{e}^-$
Anodes	Ni > Co > Fe (oxides) Perovskites: Ba <sub>0.5</sub> Sr <sub>0.5</sub> Co <sub>0.8</sub> Fe <sub>0.2</sub> O <sub>3-δ</sub> , LaCoO <sub>3</sub>	Ni-based	IrO <sub>2</sub> , RuO <sub>2</sub> , Ir <sub>x</sub> Ru <sub>1-x</sub> O <sub>2</sub> Supports: TiO <sub>2</sub> , ITO, TiC	Perovskites with protonic-electronic conductivity	La <sub>2</sub> Sr <sub>1-x</sub> MnO <sub>3</sub> + Y-Stabilized ZrO <sub>2</sub> (LSM-YSZ)	La <sub>2</sub> Sr <sub>1-x</sub> MnO <sub>3</sub> + Y-Stabilized ZrO <sub>2</sub> (LSM-YSZ)
Cathodic Reaction (HER)	$2\text{H}_2\text{O} + 4\text{e}^- \rightarrow 4\text{OH}^- + 2\text{H}_2$	$2\text{H}_2\text{O} + 4\text{e}^- \rightarrow 4\text{OH}^- + 2\text{H}_2$	$4\text{H}^+ + 4\text{e}^- \rightarrow 2\text{H}_2$	$4\text{H}^+ + 4\text{e}^- \rightarrow 2\text{H}_2$	$\text{H}_2\text{O} + 2\text{e}^- \rightarrow \text{H}_2 + \text{O}^{2-}$	$\text{H}_2\text{O} + 2\text{e}^- \rightarrow \text{H}_2 + \text{O}^{2-}$ $\text{CO}_2 + 2\text{e}^- \rightarrow \text{CO} + \text{O}^{2-}$
Cathodes	Ni alloys	Ni, Ni-Fe, NiFe <sub>2</sub> O <sub>4</sub>	Pt/C MoS <sub>2</sub>	Ni-cermets	Ni-YSZ Subst. LaCrO <sub>3</sub>	Ni-YSZ perovskites
Efficiency	59-70%		65-82%	up to 100%	up to 100%	-
Applicability	commercial	laboratory scale	near-term commercialization	laboratory scale	demonstration	laboratory scale
Advantages	low capital cost, relatively stable, mature technology	combination of alkaline and H <sup>+</sup> -PEM electrolysis	compact design, fast response/start-up, high-purity H <sub>2</sub>	enhanced kinetics, thermodynamics: lower energy demands, low capital cost		+ direct production of syngas
Disadvantages	corrosive electrolyte, gas permeation, slow dynamics	low OH <sup>-</sup> conductivity in polymeric membranes	high cost polymeric membranes; acidic: noble metals	mechanically unstable electrodes (cracking), safety issues: improper sealing		
Challenges	improve durability/reliability; and Oxygen Evolution	improve electrolyte	Reduce noble-metal utilization	microstructural changes in the electrodes: delamination, blocking of TPBs, passivation		C deposition, microstructural change electrodes

As for membrane electrode assemblies, polymeric membranes not only replace the corrosive alkaline liquid electrolyte of conventional alkaline electrolysis to improve the system safety, but also fulfill the role of gas separators to enable H<sub>2</sub>/O<sub>2</sub> separation. Thanks to this compact structure, a varying operation pressure is feasible. Moreover, the system response time is largely reduced. The improved response rate can better adapt to the transient renewable energy production.<sup>4,12</sup> Amongst the two types of membrane electrode assemblies, proton exchange membranes is more developed than anion exchange membranes, because H<sup>+</sup> conductor membranes are relatively easier to achieve. However, the acidic regime provided by Nafion proton exchange membranes (equivalent pH ~2) limits the range of suitable electrode catalysts to noble metals.<sup>13</sup> This is the main limitation of proton exchange membranes. In anion exchange membranes, water electrolysis occurs in alkaline medium, so that non-noble catalysts could be used. Thus, anion exchange membranes combining the advantages of AWE and proton exchange membranes shows great potential as upgraded technology in water electrolysis.<sup>13</sup> Hence, researches on low-cost electrocatalysts for alkaline water electrolysis are widely conducted.<sup>14-16</sup>

## I.2 Electrocatalysis of water oxidation in alkaline medium

The two half-cell reactions (1) and (2) of water electrolysis — hydrogen evolution reaction (HER) on the cathode and oxygen evolution reaction (OER) on the anode, are hampered by kinetic factors, thus high overpotentials must be imposed to enable water splitting. In order to make water electrolysis a cost-competitive hydrogen production technology, electrocatalysts are required to lower the consumption of electricity.<sup>17</sup> Among the two electrode reactions, OER involving a four-electron transfer exhibits a higher overall activation energy than HER transferring only two electrons. Therefore, electrocatalysts for OER are of great importance for efficient water electrolysis.



Understanding the alkaline OER mechanism is an essential task attracting extensive attention for designing advanced catalysts. Different methods have been developed to elucidate the rate determining step of OER. Song *et al.* employed the *operando* X-ray absorption spectroscopy to monitor the evolution of chemical species.<sup>18</sup> Hao *et al.* designed a series of experiments using reactive probes to scavenge different oxygen intermediates appearing during the OER to study their individual effects.<sup>19</sup> Besides, density functional theory (DFT) calculations of Gibbs free energies can give an insight in the thermodynamics of intermediate reaction steps.<sup>20</sup>

Nonmetal materials are rarely active in OER electrocatalysis.<sup>21</sup> Generally, OER elementary steps are considered occurring on high-valence metal sites. Two OER mechanisms have been proposed for different types of catalysts (**Figure I-1**), *i.e.* lattice oxygen mechanisms (LOM), for which the O-O bonding involves reversible formation of oxygen vacancy, and adsorption evolution mechanisms (AEM) involving three main adsorbed intermediates \*OH, \*O, and \*OOH.<sup>22</sup> As AEM seems to apply to more catalysts, it will be discussed in the following.

In the four-step adsorption evolution mechanisms, the electrocatalytic efficiency is intrinsically determined by the binding energies of these species on the catalyst surface, which should be neither too strong nor too weak to favor the adsorption/desorption process. For example, if \*O binds strongly onto the catalyst, the formation of M-OOH would be limited. Contrarily, when the M-O bond is too weak, the transformation from M-OH to M-O is unfavorable.<sup>23</sup> To achieve an appropriate binding strength, other elements (metals and/or non-

metals) can be introduced for modulation.<sup>24–26</sup> For instance, many bimetallic OER electrocatalysts achieve very low overpotential, thanks to the synergistic effect of two metals.<sup>27–30</sup> As regard to the exact mechanism, people have not reached a consensus yet. In the case of NiFe-based catalysts, the oxygen evolving site has been considered as either Ni or Fe in the literature.<sup>31–34</sup> One view considered that the outstanding activity of NiFe-based materials originated from the Fe assisted catalysis on Ni sites.<sup>31,32</sup> Li *et al.* concluded that Fe<sup>3+</sup> is a strong Lewis acid, which promotes the oxidation of its neighbor Ni<sup>3+</sup>, and that the resulting high valence Ni<sup>4+</sup> is responsible for the high catalytic activity.<sup>31</sup> On the other hand, other studies suggested that Fe is the active site.<sup>33,34</sup>

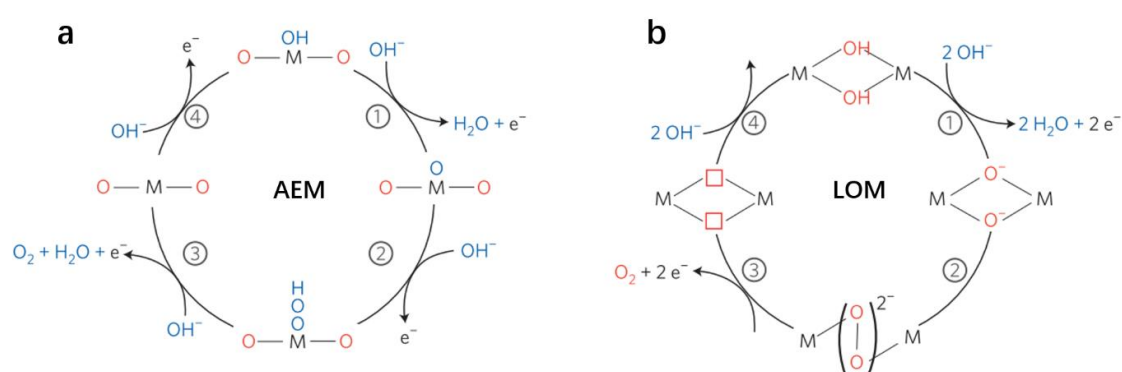


**Figure I-1** Alkaline OER electrocatalysis: (a) adsorption evolution mechanisms (AEM) and (b) lattice oxygen mechanisms (LOM).<sup>22</sup> M denotes the surface active metal sites.

Noble metals are used as electrocatalysts for OER thanks to their high stability in corrosive environment, even in acidic medium.<sup>4</sup> However, the expensive raw materials of these catalysts limits enlargement of the production scale. Considering the high demand of cost-efficient water electrolysis, many researches have been done on earth-abundant electrocatalysts for OER.<sup>17,35</sup> In 2014, Trotochaud *et al.* revealed for the first time the essential role of the incorporated-Fe in Ni (oxy)hydroxide for efficient OER electrocatalysis.<sup>28</sup> Many studies have been conducted on NiFe-based materials afterward. The latter are now among the most active electrocatalysts for OER in alkaline media, delivering high electrocatalytic activities with only earth-abundant elements.<sup>14,36</sup>

While many studies have reported the OER electrocatalysis efficiency of NiFe layered (oxy)hydroxides,<sup>37</sup> their layered structure exhibits moderate electrical conductivity because of intercalated water or anions,<sup>37,38</sup> together with a low surface density of active sites and a tendency towards aggregation, thus leading to fast degradation.<sup>14,37,38</sup> Therefore, designing composite electrodes with an electrically conductive support is required.<sup>16,39,40</sup> Within the most-used support materials for oxidic NiFe-based electrocatalysts, there are mainly carbon-based materials, such as

graphene, reduced graphene oxide (rGO) and carbon nanotubes.<sup>14,36</sup> However, according to the Pourbaix diagram of carbon,<sup>41</sup> the carbon support is thermodynamically unstable under the anodic conditions of water electrolysis in alkaline medium. The possible failure of carbon supports could be detrimental to the stability of the electrode. Joo *et al.* have investigated the deactivation of IrO<sub>2</sub> catalysts supported by carbon black. On one hand, even if the carbon corrosion is slow in the typical OER conditions, dissolution of a small amount of carbon could cause the electrical isolation of IrO<sub>2</sub>, thus resulting in a physical deactivation. On the other hand, the oxidates of carbon (CO and/or CO<sub>2</sub>) could poison the IrO<sub>2</sub> surface to chemically deactivate the catalysts.<sup>42</sup> Therefore, other solutions to the conductivity problem have been proposed.

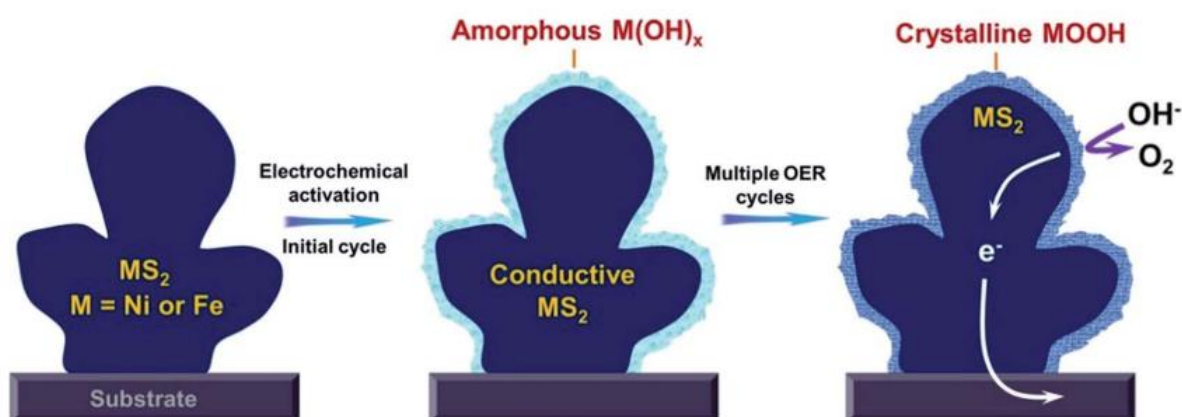


**Figure I-2** *In situ* electrochemical formation of core-shell NiFe disulfide - oxyhydroxide for alkaline OER electrocatalysis<sup>43</sup>

Alloying of Ni and Fe with p-block elements can improve their oxidation resistance and keep the electrical conductivity of the metals. Non-oxidic NiFe-p-block element compounds such as borides<sup>44,45</sup>, phosphides<sup>46</sup>, nitrides<sup>47</sup>, sulfides<sup>43,48</sup>, and selenides<sup>49</sup> were investigated as pre-catalysts for OER through *in situ* complete or partial oxidation during OER. Among them, those undergoing only partial oxidation have emerged as potential solutions to the electrical conductivity limitation. Indeed, under OER conditions a thin surface layer of crystalline<sup>43,50</sup> or amorphous<sup>44</sup> metal (oxy)hydroxide/oxide was formed. These species are highly active for the OER electrocatalysis.<sup>43,44</sup> Meanwhile, the *in situ* generated layer enable charge percolation through the particle cores, which resist oxidation and maintain a conductive nature (**Figure I-2**).<sup>43,44</sup> These *in situ* formed core-shell composite electrocatalysts exhibit excellent activity and stability on OER electrocatalysis.<sup>43,44</sup>

Although NiFe silicides have never been studied as OER electrocatalysts, one can anticipate that if their oxidation during OER is only superficial, they will deliver high electrocatalytic activity,

thanks to their metal-like conductivity ( $\sim 10 \mu\Omega \text{ cm}$  for nickel silicides),<sup>51,52</sup> combined with a very low-cost and low environmental impact due to the natural abundance of the constitutive elements in the Earth's crust. Reaching this goal requires the development of NiFe silicides exhibiting a high surface-to-volume ratio for enhanced electrocatalytic properties.

### I.3 Transition metal silicide nanomaterials

Transition metal silicides are a class of intermetallic compounds, which combine at least one transition metal element and silicon. The difference of electronegativities of constituents in such intermetallics is greater than in alloys. According to the Hume-Rothery rule, the formation of long-range ordered compound is favorable in this case.<sup>53</sup> Metal silicide intermetallics exhibit a metallocovalent character because of the hybridization of Si p- and metal d-orbitals,<sup>54</sup> which results in a reinforced stability *versus* oxidation and leads to a higher hardness at room temperature than their metal components. Most transition metal silicides exhibit a low metal-like resistivity.<sup>55,56</sup>

Research on transition metal silicides started at the beginning of the last century. Bulk metal silicides were produced by reacting the constituent elements at high temperature, but this method usually led to a large concentration of impurities.<sup>57</sup> Aside from powder metallurgy, diffusion couple methods, such as decomposition of silane gas on a metal substrate,<sup>58</sup> co-sputtering of metal and silicon, and the reaction between deposited metal and Si substrate,<sup>59</sup> were also widely used to obtain silicide thin films. Metal silicides exhibit good thermal stability and corrosion resistance because of the formation of a  $\text{SiO}_2$  protective layer.<sup>60</sup> Owing to these characteristics, transition metal silicides were used as heating elements for electrical furnaces and as protective coatings for jet engines made of Mo or W.<sup>57,60</sup>

In the late 1970s, along with the development of Si technology, several transition metal silicide thin films have been investigated in Si integrated circuits as electrical contact materials for microelectronics and as interconnect materials in complementary metal oxide semiconductors (CMOS), thanks to their good resistance against oxidation, thermal stability and high electrical conductivity.<sup>60</sup> Murarka has listed the resistivities of some transition metal silicide thin films prepared by different methods (**Table I-2**).<sup>57</sup> Most of these silicide thin films exhibit a low resistivity of *ca.*  $10^{-5} \Omega \text{ cm}$ , which can be considered conductive, while the resistivities of certain silicides like  $\text{FeSi}_2$  and  $\text{CrSi}_2$  (*ca.*  $10^{-4} \Omega \text{ cm}$  to  $1 \Omega \text{ cm}$ ) behave closer to semiconductors with narrow bandgap.

Thermoelectric materials can convert temperature gradient to electrical voltage, which can be used for sustainable energy production. Optimal thermoelectric materials exhibit high Seebeck coefficient  $S$ , high electrical conductivity  $\sigma$ , and low thermal conductivity  $\kappa$ , *i.e.*, a large figure of merit:  $\zeta T = S^2 \sigma T / \kappa$ . In this domain, lots of progresses in materials design have been made in the last decades.<sup>67-69</sup> However, efficient thermoelectric materials usually contain low abundance elements, such as Te, Bi and Ag, *etc.*<sup>69</sup> In contrast, transition metal silicides achieving high Seebeck coefficient and consisting of metals and silicon with high crustal abundance, are attractive because of the cost of raw materials.<sup>67</sup> The most promising silicides FeSi<sub>2</sub>, CrSi<sub>2</sub>, Mg<sub>2</sub>Si and MnSi<sub>x</sub> exhibit a decent figure of merit compared to some benchmarks such as lead telluride.<sup>67</sup> On the other hand, nanostructuring has been demonstrated an effective pathway to enhance the thermoelectric properties of materials by selective decrease of  $\kappa$ ,<sup>67</sup> which encourages the development of synthesis methods towards metal silicide nanoparticles.

**Table I-2** Reported values of silicide thin film resistivities.<sup>57</sup> The tabulated values of each column are from Robins,<sup>61</sup> Padnos,<sup>62</sup> Neshpor & Samsonov,<sup>63</sup> Keiffer & Benesovsky,<sup>64</sup> Wehrmann,<sup>65</sup> and Murarka,<sup>66</sup> respectively.

Room temperature resistivity ( $\mu\Omega\text{-cm}$ )						
Silicide	Robins	Padnos	Neshpor & Samsonov	Keiffer & Benesovsky	Wehrmann	Murarka
TiSi <sub>2</sub>	16.7	16.7–123	16.9	18	16.7	13–16, 25
ZrSi <sub>2</sub>	106.2	106–161	75.8	75	106.2	35–40
HfSi <sub>2</sub>	—	62	—	—	—	45–50, 60–70
VSi <sub>2</sub>	13.3	9.5–13.3	66.5	13.3	13.3	50–55
NbSi <sub>2</sub>	—	6.3–24.5	50.4	50.4	6.3	50
TaSi <sub>2</sub>	38.0	8.5–38.0	46.1	46	38.0	35–45, 50–55
CrSi <sub>2</sub>	142.0	7–6670	914	142.0	> 250	~ 600
MoSi <sub>2</sub>	21.8	21.5	21.6	21.5	21.8	~ 90, ~ 100
WSi <sub>2</sub> <sup>a</sup>	38.2	33–55	12.5	12.5	38.2	~ 70
FeSi <sub>2</sub>	—	350	10 <sup>3</sup> –10 <sup>6</sup>	—	—	> 1000
CoSi <sub>2</sub>	—	64.8	68	—	—	18–20, 25
NiSi <sub>2</sub>	—	—	118	—	—	50, 50–60
Pd <sub>2</sub> Si	—	—	—	—	—	30–35
PtSi	—	—	—	—	—	28–35

The magnetic properties of transition metal silicides have also been investigated.<sup>61,70–74</sup> While many ternary transition metal silicides are ferromagnetic,<sup>75–77</sup> the majority of binary transition metal silicides are diamagnetic or paramagnetic, even for those containing ferromagnetic metals Fe, Ni and Co. In these cases, only the metal-rich silicides (*e.g.* Co<sub>3</sub>Si, Fe<sub>3</sub>Si) show ferromagnetic properties.<sup>71,78</sup> Their counterpart Si-rich silicides or monosilicides are not ferromagnetic. For instance, FeSi is paramagnetic. NiSi and CoSi are diamagnetic.<sup>72,79,80</sup> However, many nanowires of binary disilicides or monosilicides exhibit magnetic order.<sup>81–83</sup> This peculiar magnetism of nano-objects was attributed to unpaired spins produced by crystal defects, undercoordinated

metal atoms and dangling bonds at the interface and/or grain boundaries of silicides,<sup>71</sup> which could be tuned by the size and morphology of materials. Therefore, one can expect that the synthesis of nanoscaled transition metal silicides is of great interest towards higher magnetic moment silicides.

Furthermore, in the last century, the superconductivity of some binary and ternary metal silicides was revealed.<sup>84,85</sup> Among those whose critical temperature for superconducting transition is above 2 K, one can cite V<sub>3</sub>Si (17 K), WSi<sub>10.7</sub> (2.84 K), ThSi<sub>2</sub> (3.16 K), Sc<sub>5</sub>Ir<sub>4</sub>Si<sub>10</sub> (8.4 K), LaRu<sub>3</sub>Si<sub>2</sub> (7.3 K), and ThIrSi (6.5 K), *etc.*<sup>85,86</sup> Moreover, reinforcement materials in metal-matrix nanocomposites are another potential application of nanoscaled metal silicides. For example, Ti<sub>5</sub>Si<sub>3</sub> has showed an excellent wetting behavior with Al in the preparation of Al-Ti<sub>5</sub>Si<sub>3</sub> nanocomposite.<sup>87</sup>

Recently, transition metal silicides have been reported as efficient catalysts for diverse reactions. Ryabchuk *et al.* reported a reversible hydrogenation/dehydrogenation of N-heterocycles promoted by nickel silicide@SiO<sub>2</sub>, which could be auspicious for hydrogen storage.<sup>88</sup> Hausmann *et al.* found that FeSi supported on Ni foam is capable to achieve selective oxygenation of 5-hydroxymethylfurfural.<sup>89</sup> Besides, transition metal silicides also deliver enhanced catalytic activity on hydrodesulfurization,<sup>90,91</sup> CO methanation,<sup>92</sup> the Rochow process,<sup>93</sup> hydrodechlorination,<sup>94</sup> hydrodeoxygenation,<sup>95</sup> oxidation of H<sub>2</sub> and CO,<sup>96-98</sup> and formation of carbon nanotube,<sup>99</sup> *etc.*<sup>55</sup>

Aside from heterogeneous catalytic reactions, transition metal silicide nanoparticles have been also studied as emerging photoelectrocatalysts and electrocatalysts for both electrode reactions of water splitting.<sup>55</sup> TiO<sub>2</sub>/TiSi<sub>2</sub> heterostructures were demonstrated as high-efficiency photoelectrocatalyst for water splitting.<sup>100</sup> McEnaney *et al.* found that Ni<sub>2</sub>Si and Pd<sub>2</sub>Si nanoparticles were active for HER catalysis.<sup>101</sup> More recently, our group showed that NiSi and Ni<sub>2</sub>Si nanocrystals are active on OER electrocatalysis.<sup>102</sup> Hausmann *et al.* found that FeSi supported by nickel foam delivers high electrocatalytic activity for OER.<sup>89</sup>

Although (electro)catalysis highlighted the interest of nanoscaled metal silicides, they have been mostly developed as thin films or nanowires with moderate specific surface areas, which are not optimized for heterogeneous (electro)catalysis. Thus, novel synthesis methods must be developed to achieve high surface area nanomaterials. State-of-the-art synthesis methods are scrutinized below.

## I.4 Today's challenges towards transition metal silicide nanomaterials

As mentioned above, technologies such as powder metallurgy or arc-melting were widely adopted for metal silicides synthesis in the early years. These methods can achieve a large range of thermodynamically stable metal silicides by varying the reaction equilibrium temperature and the metal-to-silicon ratio according to phase diagrams. On one hand, they allow producing homogeneous products in a highly reproducible way. The intrinsic properties of silicides have been evaluated by using these bulk single-phase silicides. On the other hand, these methods also restrict the range of accessible products. Metastable phases cannot be isolated at the high temperature involved, and the resulting products are usually large grains. With the attractiveness of various properties tuned by sample size, morphology and composition, many other synthesis methods have been developed.<sup>55</sup>

Chen and Liang reviewed the reported methods towards transition metal silicides.<sup>55</sup> These methods use either dual-source precursors (**Table I-3**) or single-source precursors (**Table I-4**). Self-propagating high temperature synthesis relies the combustion between metal and silicon upon ignition, which is enabled by the exothermicity of this chemical reaction. The reaction occurs only in a few second, which consumes few energy, compared to traditional powder metallurgy.<sup>103-115</sup> By using additives such as  $\text{KNO}_3$  to trigger outgassing during the reaction, porous material can be produced.<sup>116</sup> However, poor control on product purity is the main drawback of this method.

High energy ball milling can enable the solid-state reaction of elemental metal and silicon.<sup>55</sup> This method produces materials of fine grains with a low cost and simple process.<sup>117-121</sup> To further downscale the resulting product to the nanoscale,  $\text{ZrSi}_2$  nanoparticles were prepared by adding  $\text{CaCl}_2$  as diluent.<sup>121</sup> Grain refinement can be achieved by extending the milling time to dozens of hours.<sup>118,119</sup> Cooling intervals for the equipment could be required, because the mill's motor could easily wear due to the heating of components.<sup>121</sup> This results in a modest efficiency of ball milling synthesis.

Solid-state metathesis reactions use highly reactive alkali or alkaline earth silicides to reduce transition metal halides or oxides and to form transition metal silicides. In many cases, the reaction is complete within few seconds without external heating or by a simple initiation, *e.g.* gas flam.<sup>122-125</sup> During the process, the byproducts alkali and alkaline earth halides were generated as molten fluxes that slightly dilute the reaction medium, which can be easily removed after reaction. Such a dilution can moderate the reaction for a better control of grain size. However, the temperatures during processing can generally reach the melting point of the produced silicides

because of the large exothermic energy of reactions,<sup>55</sup> so that this method only yields bulk materials.

**Table I-3** Synthesis methods using dual-source precursor towards metal silicides reviewed by Chen and Liang.<sup>55</sup> Nanoparticles (including supported nanoparticles) are underscored in the table.

Dual-source precursor methods	General precursors	General morphologies	Achieved phases and references
Arc melting	Metal + silicon	Bulk materials	FeSi, <sup>103</sup> CoSi, <sup>104</sup> Cu <sub>3</sub> Si, <sup>108</sup> Y <sub>5</sub> Si <sub>3</sub> , <sup>109</sup> Mn <sub>11</sub> Si <sub>19</sub> , <sup>110</sup> Co <sub>2</sub> FeSi, <sup>111</sup> LaFe <sub>11.6</sub> Si <sub>1.4</sub> , <sup>111</sup> (Ru <sub>1-x</sub> Co <sub>x</sub> ) <sub>2</sub> FeSi, <sup>112</sup> ScRuSi, <sup>113</sup> NbOsSi, <sup>114</sup> TaOsSi, <sup>114</sup> LaScSi, <sup>115</sup> LaCu <sub>0.67</sub> Si <sub>1.33</sub> , <sup>105</sup> LaCoSi, <sup>106</sup> , LnNiSi (Ln=La–Nd) <sup>107</sup>
Self-propagating high temperature synthesis	Metal + silicon	Porous materials	MoSi <sub>2</sub> , <sup>126</sup> Ti <sub>5</sub> Si <sub>3</sub> , <sup>126</sup> ZrSi <sub>2</sub> , <sup>126</sup> Ta <sub>5</sub> Si <sub>3</sub> , <sup>127</sup> V <sub>5</sub> Si <sub>3</sub> , <sup>127</sup> Nb <sub>5</sub> Si <sub>3</sub> , <sup>127</sup> TiSi <sub>2</sub> , <sup>128</sup> Mg <sub>2</sub> Si, <sup>129</sup> NiSi, <sup>130</sup> Ni <sub>2</sub> Si, <sup>130</sup> FeSi <sub>2</sub> , <sup>116</sup> , Cu <sub>3</sub> Si <sup>131</sup>
Ball milling	Metal + silicon	Micromaterials	Ni–Si, <sup>132</sup> Fe–Si, <sup>117</sup> Mo– Si, <sup>118,119</sup> Cr–Si, <sup>120</sup> Ti– Si, <sup>120</sup> ZrSi <sub>2</sub> <sup>121</sup>
Solid-state metathesis reactions	Metal halide or oxide + alkali metal silicide	Bulk materials	MoSi <sub>2</sub> , <sup>122,123</sup> WSi <sub>2</sub> , <sup>122</sup> TaSi <sub>2</sub> , <sup>122,123</sup> NbSi <sub>2</sub> , <sup>122,123</sup> VSi <sub>2</sub> <sup>123</sup>
Microwave assisted synthesis	Metal + silicon	Bulk materials, nanowires, nanoparticles, supported nanoparticles	Li <sub>21</sub> Si <sub>5</sub> , <sup>133</sup> <u>Mg<sub>2</sub>Si</u> , <sup>134</sup> CoSi, <sup>135</sup> CoSi <sub>2</sub> , <sup>135,136</sup> Mo <sub>5</sub> Si <sub>3</sub> , <sup>137</sup> Pd <sub>2</sub> Si, <sup>138</sup> WSi <sub>2</sub> , <sup>136</sup> TiSi <sub>2</sub> , <sup>136</sup> MoSi <sub>2</sub> , <sup>136</sup> <u>CoSi<sub>x</sub>/CNTs</u> <sup>139,140</sup>
Chemical vapor deposition	Simultaneous metal and silicon deposition	Thin films, nanorods, nanonet,	Co–Si, <sup>141</sup> Ti–Si <sup>142–144</sup>
	Metal sources with silicon substrates	Metal halide or metal + Si substrate	Nanowires TiSi <sub>2</sub> , <sup>145</sup> CrSi <sub>2</sub> , <sup>146</sup> Fe <sub>5</sub> Si <sub>3</sub> , <sup>147</sup> V <sub>5</sub> Si <sub>3</sub> , <sup>148</sup> CoSi, <sup>82</sup> Co <sub>2</sub> Si, <sup>149</sup> Co <sub>n</sub> Si, <sup>150</sup> Ti <sub>5</sub> Si <sub>3</sub> , <sup>151</sup> MnSi, <sup>152</sup> Ni <sub>2</sub> Si, <sup>153</sup> WSi <sub>2</sub> , <sup>154</sup> Ta <sub>5</sub> Si <sub>3</sub> , <sup>155</sup> Fe <sub>1-x</sub> Co <sub>x</sub> Si <sup>156</sup>

Dual-source precursor methods	General precursors	General morphologies	Achieved phases and references
Silicon sources with metal substrates	SiH <sub>4</sub> or organic Si (SiCl <sub>4</sub> , (CH <sub>3</sub> ) <sub>2</sub> SiCl <sub>2</sub> , <i>etc.</i> ) + metal substrate or metal oxide nanoparticles	Nanowires, thin films, nanoparticles	Ni <sub>2</sub> Si, <sup>157,158</sup> Ni <sub>3</sub> Si <sub>2</sub> , <sup>157</sup> NiSi, <sup>157-159</sup> <u>Ni-Si@SiO<sub>2</sub></u> , <sup>92</sup> <u>FeSi<sub>n</sub>@SiO<sub>2</sub></u> , <sup>160,161</sup> <u>Ni<sub>1-x</sub>Co<sub>x</sub>Si<sub>2</sub></u> , <sup>91</sup> <u>Ni<sub>1-x</sub>Fe<sub>x</sub>Si<sub>2</sub></u> , <sup>90</sup>
Solution synthesis	Various	Nanoparticles	<u>Fe<sub>3</sub>Si</u> , <sup>162</sup> <u>Pd<sub>2</sub>Si</u> , <sup>101</sup> <u>Cu<sub>3</sub>Si</u> , <sup>101</sup> <u>Ni<sub>2</sub>Si</u> , <sup>101</sup> <u>Ni<sub>x</sub>Si-C<sub>8</sub>H<sub>17</sub></u> , <sup>163</sup>
Molten salt synthesis	Metal chloride or oxide + SiO <sub>2</sub> or alkali metal silicide	Nanoparticles, nanotubes	<u>MoSi<sub>2</sub></u> , <sup>164</sup> Mn <sub>5</sub> Si <sub>3</sub> , <sup>165</sup> <u>Ti<sub>5</sub>Si<sub>3</sub></u> , <sup>87</sup>

Microwave-assisted synthesis is a well-known method providing large heating rate, which can favor the nucleation over the growth of grains, and thus decrease the particle size. Mg<sub>2</sub>Si nanoparticles have been achieved by microwave irradiation of elemental Mg and Si.<sup>134</sup> Besides, Pd<sub>2</sub>Si nanowires have been grown by microwave plasma enhanced chemical vapor deposition,<sup>138</sup> which shows the flexibility of microwaves for coupling with other synthesis methods. However, for solid-state reactions, the use of microwaves is not optimal for reactants that are poor microwave absorbers. In this case, susceptors such as SiC and carbon must be used. Based on this feature, Zhang *et al.* prepared carbon nanotubes (CNTs)-supported CoSi<sub>x</sub> nanoparticles.<sup>139,140</sup>

Different from the previous solid-state reactions, chemical vapor deposition methods involve gas-solid or gas-gas reactions, and produce typically nanowires, which are compatible with the microelectronic processing.<sup>82</sup> The gas-gas reaction by simultaneous deposition of metal- and Si-containing vapors is yet challenging because of the difficulty of independent control over the pressures of two vapors.<sup>141-144</sup> As for the two other sub-methods (**Table I-3**), the reaction between the metal halide vapor and the Si substrate has been extensively studied for producing various transition metal silicide (M = Cr, Fe, V, Co, Ti, Mn, Ni, W, Ta, *etc.*) nanowires.<sup>82,146-156</sup> The substrates are generally held at *ca.* 900 °C.<sup>55</sup> By controlling the vapor pressure of the halides, the stoichiometry of the resulting product can be tuned.<sup>55</sup> When using Si-containing vapors, volatile SiH<sub>4</sub>, SiCl<sub>4</sub>, and some organic Si species are usually involved. In this case, silicification can not only occur on metallic substrates to form nanowires,<sup>157-159</sup> but also occurs in metal oxide particles to yield supported or unsupported transition metal silicide nanoparticles.<sup>90-92,160,161</sup>

Despite the processing simplicity delivered by solid-state reactions and the large range of achieved phases, liquid phase syntheses under mild conditions are more adaptive for nanomaterials design, especially because the reactions can occur in a diluted medium.

$\text{Ni}_x\text{Si}-\text{C}_8\text{H}_{17}$  colloids of 2 nm have been obtained in tetrahydrofuran (THF) at 55-65 °C.<sup>163</sup> However, better crystallinity requires higher reaction temperature. Solution synthesis of transition metal silicide nanoparticles is thus based on relatively high boiling point organic solvents.  $\text{Fe}_3\text{Si}$  nanoparticles have been produced by using *o*-1,2-dichlorobenzene as solvent at 220-250 °C.<sup>162</sup> McEnaney *et al.* reported a colloidal synthesis achieving  $\text{Ni}_2\text{Si}$ ,  $\text{Pd}_2\text{Si}$  and  $\text{Cu}_3\text{Si}$  nanoparticles at 375 °C in a mixture of trioctylamine and squalane.<sup>101</sup> Even if they were mentioned as high temperature solution synthesis, it can be noticed that the reaction temperature in liquid medium is few hundred degrees lower than solid-state or gas-solid reactions. Conventional organic solvents can only be operated below 400 °C,<sup>166</sup> which is still limiting the exploration of metal silicide nanomaterials. Indeed, ordering the Si-Si bonds might require higher energy, so that most metal silicides obtained in solution synthesis are only metal-rich phases.

With the purpose of extending the range of transition metal silicide nanoparticles, enlarged medium temperature range is needed compared to usual solvents. Molten salt synthesis is a likely choice, where reactions take place in an inorganic solvent. A typical molten salt synthesis allows operating at temperatures ranging from 100-1000 °C.<sup>166,167</sup> Molten salts provide a diluted reaction medium in which reagents are diluted or dissolved, combined with high temperatures, which can trigger extensive nucleation, increase the reactant mobility and enhance the reaction rate. Unlike organic solvents, the nanoparticles produced in molten salts are organic ligand-free at the benefit of catalytic active site exposure. Previously, molten NaF-assisted synthesis was conducted to produce  $\text{MoSi}_2$  nanoparticles at 1000-1200 °C.<sup>164</sup>  $\text{Ti}_5\text{Si}_3$  nanoparticles have been prepared in the LiCl-KCl eutectic at 700 °C.<sup>87</sup> Apart from the works presented in **Table I-3**, Kumar *et al.* recently explored a reaction between metal salts and  $\text{Na}_4\text{Si}_4$  in LiI-KI molten medium to achieve  $\text{Ni}_2\text{Si}$  and  $\text{NiSi}$  nanocrystals respectively at 300 and 500 °C.<sup>102</sup> In these cases, high temperature phases were achieved as nanoparticles, which makes molten salt synthesis a promising nanoparticle designing pathway to reach a large versatility of transition metal silicide phases.<sup>166,168</sup> However, there are still some limitations of molten salt synthesis, such as the poor control over morphology of nanoparticles because the organic surface stabilizing agents cannot be used, as well as the necessary purification step for removing inorganic salts. These points will be addressed in this thesis.

Apart from dual-source precursor methods, single-source precursor synthesis using a precursor containing both metal and silicon has been also studied (**Table I-4**). With volatile molecules containing metal-silicon bonds *e.g.*  $\text{M}(\text{SiH}_3)_x(\text{CO})_y$  ( $\text{M} = \text{Co}, \text{Fe}, \text{Mn}, \text{Re}$ ) and  $\text{M}(\text{SiCl}_3)_x(\text{CO})_y$  ( $\text{M} = \text{Co}, \text{Fe}, \text{and Mn}$ ), metal organic chemical vapor deposition has been conducted. Metal silicide thin films, nanowires and supported nanoparticles have been

successfully prepared.<sup>169–176</sup> Since the metal-to-silicon ratio is fixed by the precursors, this method allows easier and precise control over the stoichiometry. But this feature also restricts the accessible silicide phases because of the availability of suitable volatile precursors.<sup>55</sup> Another approach by pyrolysis of metal-containing polysilanes, which are usually in the solid state, enable tuning the metal-silicon ratio through the preparation of precursors. This method only yields supported nanoparticles or nanoparticles embedded in a matrix.<sup>175,177–179</sup>

**Table I-4** Synthesis methods using single-source precursor towards metal silicides reviewed by Chen and Liang.<sup>55</sup> Nanoparticles (including supported nanoparticles) are underscored in the table.

Single-source precursor methods	General precursors	General morphologies	Achieved phases and references
Metal organic chemical vapor deposition	$M(\text{SiH}_3)_x(\text{CO})_y$ ( $M = \text{Co, Fe, Mn, Re}$ ), $M(\text{SiCl}_3)_x(\text{CO})_y$ ( $M = \text{Co, Fe, Mn}$ )	Thin films, nanowires, supported nanoparticles	<u><math>\text{CoSi@SiO}_2</math></u> <sup>169,170</sup> $M_3\text{Si}_3 + M\text{Si}_{1.25}$ ( $M = \text{Mn, Re}$ ), <sup>171</sup> $\text{FeSi}_2$ , <sup>171</sup> $\text{FeSi}$ , <sup>172</sup> $\text{Fe}_{1-x}\text{Co}_x\text{Si}$ , <sup>172,173</sup> $\text{MnSi}_{1.8}$ , <sup>174</sup> <u><math>\text{FeSi@SiO}_2</math></u> , <sup>175</sup> <u><math>\text{MnSi@SiO}_2</math></u> <sup>176</sup>
Pyrolysis of metal-containing polysilane	ferrocene–polydimethylsilane, poly(ferrocenylsilane), nickel-containing polycarbosilanes, polydimethylsilane-Ni(acac) <sub>2</sub> , aminopyridinato palladium complex	Supported nanoparticles	<u><math>\text{Fe}_3\text{Si@SiO}_2</math></u> , <sup>175</sup> <u><math>\text{Fe}_3\text{Si@SiC/C}</math></u> , <sup>177</sup> <u>Ni-Si@ceramics</u> , <sup>178</sup> <u><math>\text{Pd}_2\text{Si@SiCN}</math></u> <sup>179</sup>

Nanostructuring of transition metal silicides could bring enhancements on many physical properties (*e.g.*, thermoelectricity, magnetism, mechanical strength, *etc.*) and (electro)catalytic activity. However, despite the large versatility of silicide phases achieved as bulk materials or as 2D nanowires, the occurrences of transition metal silicide nanoparticles remain few. Moreover, many of them are supported nanoparticles. For instance, cobalt silicides have been only reported as supported nanoparticles.<sup>139,169,170,180–182</sup> Since the interaction between nanoparticles and the support could change the exposed facets and surface electronic states of nanoparticles,<sup>183</sup> the chemical and physical properties could be significantly changed for freestanding nanoparticles. Amongst the synthesis approaches reported to date, freestanding nanoparticles of a small portion of transition metal silicide phases have been achieved through microwave-assisted synthesis,<sup>134</sup> chemical vapor deposition on metal oxide nanoparticles,<sup>90,91</sup> solution synthesis,<sup>101,162,163</sup> and molten

salt synthesis.<sup>87,164</sup> Widening the range of transition metal silicide freestanding nanoparticles is not only an intriguing topic in fundamental research, but also an opportunity to develop promising materials with high cost-efficiency for the industry because of the crustal abundance of silicon. The methods for their synthesis are thus the essential scientific bottleneck.

## I.5 Summary and strategy of this work

Hydrogen produced by water electrolysis is an auspicious solution to the transient production of renewable energy. In order to lower the electricity consumption of electrolysis, electrocatalysts are required for kinetically slow electrode reactions of water electrolysis, especially for OER. High valence NiFe-based materials are the benchmarks of precious metal-free OER electrocatalysts to date. Because NiFe oxide/hydroxide/LDH electrocatalysts usually suffer from low electrical conductivity and self-agglomeration, hybrid electrocatalysts with an additional conductive material such as graphene, reduced graphene oxide, or carbon nanotubes are required. Nevertheless, considering the potential instability of carbon-based supports under OER conditions, other electrocatalysts have been designed to overcome the conductivity problem. NiFe-p-block-element intermetallic compounds such as NiFe sulfides, borides, phosphides, *etc.*, exhibit high electrical conductivity. Nanoparticles of these phases have been demonstrated highly active on OER electrocatalysis, owing to their complete or partial oxidation during OER. Those only partially oxidized at the surface form stable core-shell nanocomposite electrocatalysts, with an intermetallic conductive core and a highly electrocatalytically active oxidized shell. Due to the rare occurrence of metal silicide nanoparticles, NiFe silicide nanoparticles only containing earth-abundant elements, have never been evaluated as OER electrocatalysts. Attracted by the diverse properties of metal silicides and their nanomaterials, the present work is dedicated to the design of metal silicide nanoparticles.

Aiming at metal silicide freestanding nanoparticles, several essential factors for synthesis have been considered, including reaction medium, precursors of silicon and metal, *etc.* As for reaction media, molten salt synthesis has been adopted in this work, where liquid-mediated reactions can be triggered at higher temperature than in organic solvents. These liquid media enable reactions at lower temperature than in the solid state by enhancing the mobility of reactants. They also provide diluted media to produce small particles because of the favorable nucleation over growth. Moreover, the insulating organic surface ligands of nanoparticles, which could be detrimental for the electrocatalysis, can be avoided by this synthesis method.

One of the challenges for nanomaterials design in molten salts is the poor control over product morphology. In some cases, it could be overcome by topochemical methods, *i.e.*, using nanoparticles as precursors, so that they could also act as nanotemplates.<sup>168</sup> Furthermore, nanoparticle reagents also present higher reactivity.<sup>184</sup> Hence, silicon nanoparticles and metal nanoparticles are chosen as precursors (**Figure I-3**). As for insertion species, metal halides are used for the reaction with silicon nanoparticles in this work, because the redox reaction between metal halide and elemental silicon is known feasible.<sup>144–151</sup> For the other pathway using metal nanoparticles, the choice of silicon sources is more delicate, this precursor should be (1) dispersible/soluble in molten salts, (2) reactive in the temperature range of molten salts, (3) without strong Si-O bonds, and (4) non-volatile at the reaction temperature. Few silicon sources respond all the requests. The Zintl phase sodium silicide  $\text{Na}_4\text{Si}_4$  is used in this work as silicon species for silicification of metal nanoparticles. Both approaches in **Figure I-3** will be discussed in the following section.

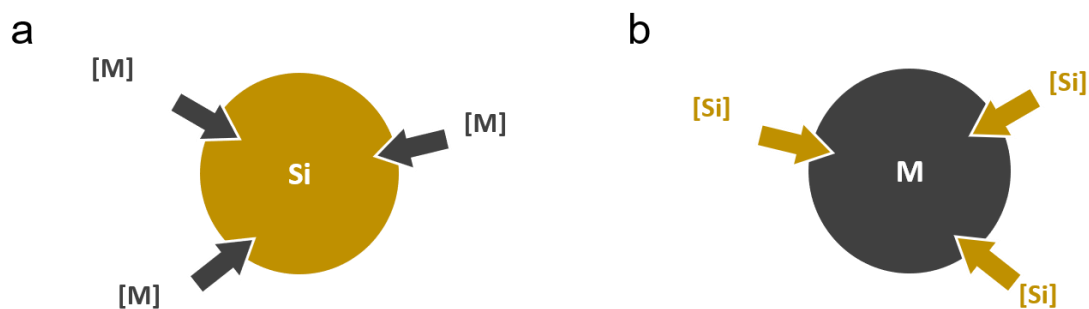


**Figure I-3** Reaction schema (a) insertion of metal species into Si nanoparticles, (b) insertion of Si species into metal nanoparticles.

## References

- (1) FCH 2 JU. Hydrogen paves the way for decarbonising the European economy <https://www.fch.europa.eu/news/hydrogen-paves-way-decarbonising-european-economy>.
- (2) Yu, H.; Shao, Z.; Hou, M.; Yi, B.; Duan, F.; Yang, Y. Hydrogen Production by Water Electrolysis: Progress and Suggestions. *Chinese J. Eng. Sci.* **2021**, *23* (2), 146.
- (3) Brauns, J.; Turek, T. Alkaline Water Electrolysis Powered by Renewable Energy: A Review. *Processes* **2020**, *8* (2), 248.
- (4) Vincent, I.; Bessarabov, D. Low Cost Hydrogen Production by Anion Exchange Membrane Electrolysis: A Review. *Renew. Sustain. Energy Rev.* **2018**, *81*, 1690–1704.
- (5) Ursúa, A.; Gandía, L. M.; Sanchis, P. Hydrogen Production from Water Electrolysis: Current Status and Future Trends. *Proc. IEEE* **2012**, *100* (2), 410–426.
- (6) Sapountzi, F. M.; Gracia, J. M.; Weststrate, C. J. Kee, J.; Fredriksson, H. O. A.; Niemantsverdriet, J. W. Hans. Electrocatalysts for the Generation of Hydrogen, Oxygen and Synthesis Gas. *Prog. Energy Combust. Sci.* **2017**, *58*, 1–35.
- (7) Rashid, M. M.; Mesfer, M. K. Al; Naseem, H.; Danish, M. Hydrogen Production by Water Electrolysis: A Review of Alkaline Water Electrolysis, PEM Water Electrolysis and High Temperature Water Electrolysis. *Int. J. Eng. Adv. Technol.* **2015**, *4* (3), 2249–8958.
- (8) Kreuter, W.; Hofmann, H. Electrolysis: The Important Energy Transformer in a World of Sustainable Energy. *Int. J. Hydrogen Energy* **1998**, *23* (8), 661–666.
- (9) Shiva Kumar, S.; Himabindu, V. Hydrogen Production by PEM Water Electrolysis – A Review. *Mater. Sci. Energy Technol.* **2019**, *2* (3), 442–454.
- (10) Enapter. Device for the Production On-Demand of Hydrogen by Electrolysis of Aqueous Solutions from Dry Cathode. US9340882B2, 2016.
- (11) Enapter. AEM Electrolyser | Scalable Hydrogen Generator | Enapter. 2021, <https://www.enapter.com/electrolyser>.
- (12) Habrioux, A.; Morais, C.; Napporn, T. W.; Kokoh, B. Recent Trends in Hydrogen and Oxygen Electrocatalysis for Anion Exchange Membrane Technologies. *Curr. Opin. Electrochem.* **2020**, *21* (2), 146–159.
- (13) Carmo, M.; Fritz, D. L.; Mergel, J.; Stolten, D. A Comprehensive Review on PEM Water Electrolysis. *Int. J. Hydrogen Energy* **2013**, *38* (12), 4901–4934.

- (14) Zhao, J.; Zhang, J. J.; Li, Z. Y.; Bu, X. H. Recent Progress on NiFe-Based Electrocatalysts for the Oxygen Evolution Reaction. *Small* **2020**, *16* (51), 1–23.
- (15) Suen, N. T.; Hung, S. F.; Quan, Q.; Zhang, N.; Xu, Y. J.; Chen, H. M. Electrocatalysis for the Oxygen Evolution Reaction: Recent Development and Future Perspectives. *Chem. Soc. Rev.* **2017**, *46* (2), 337–365.
- (16) Feng, C.; Faheem, M. B.; Fu, J.; Xiao, Y.; Li, C.; Li, Y. Fe-Based Electrocatalysts for Oxygen Evolution Reaction: Progress and Perspectives. *ACS Catal.* **2020**, *10* (7), 4019–4047.
- (17) Jamesh, M. I.; Sun, X. Recent Progress on Earth Abundant Electrocatalysts for Oxygen Evolution Reaction (OER) in Alkaline Medium to Achieve Efficient Water Splitting – A Review. *J. Power Sources* **2018**, *400*, 31–68.
- (18) Song, F.; Busch, M. M.; Lassalle-Kaiser, B.; Hsu, C. S.; Petkucheva, E.; Bensimon, M.; Chen, H. M.; Corminboeuf, C.; Hu, X. An Unconventional Iron Nickel Catalyst for the Oxygen Evolution Reaction. *ACS Cent. Sci.* **2019**, *5* (3), 558–568.
- (19) Hao, Y.; Li, Y.; Wu, J.; Meng, L.; Wang, J.; Jia, C.; Liu, T.; Yang, X.; Liu, Z. P.; Gong, M. Recognition of Surface Oxygen Intermediates on NiFe Oxyhydroxide Oxygen-Evolving Catalysts by Homogeneous Oxidation Reactivity. *J. Am. Chem. Soc.* **2021**, *143* (3), 1493–1502.
- (20) Hu, C.; Zhang, L.; Gong, J. Recent Progress Made in the Mechanism Comprehension and Design of Electrocatalysts for Alkaline Water Splitting. *Energy Environ. Sci.* **2019**, *12* (9), 2620–2645.
- (21) Zhao, Y.; Nakamura, R.; Kamiya, K.; Nakanishi, S.; Hashimoto, K. Nitrogen-Doped Carbon Nanomaterials as Non-Metal Electrocatalysts for Water Oxidation. *Nat. Commun.* **2013**, *4*, 2–8.
- (22) Song, J.; Wei, C.; Huang, Z. F.; Liu, C.; Zeng, L.; Wang, X.; Xu, Z. J. A Review on Fundamentals for Designing Oxygen Evolution Electrocatalysts. *Chem. Soc. Rev.* **2020**, *49* (7), 2196–2214.
- (23) Rossmeisl, J.; Logadottir, A.; Nørskov, J. K. Electrolysis of Water on (Oxidized) Metal Surfaces. *Chem. Phys.* **2005**, *319* (1–3), 178–184.
- (24) Zhang, B.; Zheng, X.; Voznyy, O.; Comin, R.; Bajdich, M.; García-Melchor, M.; Han, L.; Xu, J.; Liu, M.; Zheng, L.; De Arquer, F. P. G.; Dinh, C. T.; Fan, F.; Yuan, M.; Yassitepe, E.; Chen, N.; Regier, T.; Liu, P.; Li, Y.; De Luna, P.; Janmohamed, A.; Xin, H. L.; Yang, H.; Vojvodic,

A.; Sargent, E. H. Homogeneously Dispersed Multimetal Oxygen-Evolving Catalysts. *Science*. **2016**, *352* (6283), 333–337.

(25) Hao, J.; Yang, W.; Peng, Z.; Zhang, C.; Huang, Z.; Shi, W. A Nitrogen Doping Method for CoS<sub>2</sub> Electrocatalysts with Enhanced Water Oxidation Performance. *ACS Catal.* **2017**, *7* (6), 4214–4220.

(26) Morales-Guio, C. G.; Liardet, L.; Hu, X. Oxidatively Electrodeposited Thin-Film Transition Metal (Oxy)Hydroxides as Oxygen Evolution Catalysts. *J. Am. Chem. Soc.* **2016**, *138* (28), 8946–8957.

(27) Burke, M. S.; Kast, M. G.; Trotochaud, L.; Smith, A. M.; Boettcher, S. W. Cobalt-Iron (Oxy)Hydroxide Oxygen Evolution Electrocatalysts: The Role of Structure and Composition on Activity, Stability, and Mechanism. *J. Am. Chem. Soc.* **2015**, *137* (10), 3638–3648.

(28) Trotochaud, L.; Young, S. L.; Ranney, J. K.; Boettcher, S. W. Nickel-Iron Oxyhydroxide Oxygen-Evolution Electrocatalysts: The Role of Intentional and Incidental Iron Incorporation. *J. Am. Chem. Soc.* **2014**, *136* (18), 6744–6753.

(29) Zhao, Z.; Wu, H.; He, H.; Xu, X.; Jin, Y. A High-Performance Binary Ni-Co Hydroxide-Based Water Oxidation Electrode with Three-Dimensional Coaxial Nanotube Array Structure. *Adv. Funct. Mater.* **2014**, *24* (29), 4698–4705.

(30) Song, F.; Hu, X. Ultrathin Cobalt-Manganese Layered Double Hydroxide Is an Efficient Oxygen Evolution Catalyst. *J. Am. Chem. Soc.* **2014**, *136* (47), 16481–16484.

(31) Li, N.; Bediako, D. K.; Hadt, R. G.; Hayes, D.; Kempa, T. J.; Von Cube, F.; Bell, D. C.; Chen, L. X.; Nocera, D. G. Influence of Iron Doping on Tetravalent Nickel Content in Catalytic Oxygen Evolving Films. *Proc. Natl. Acad. Sci. U. S. A.* **2017**, *114* (7), 1486–1491.

(32) Xiao, H.; Shin, H.; Goddard, W. A. Synergy between Fe and Ni in the Optimal Performance of (Ni,Fe)OOH Catalysts for the Oxygen Evolution Reaction. *Proc. Natl. Acad. Sci. U. S. A.* **2018**, *115* (23), 5872–5877.

(33) Ahn, H. S.; Bard, A. J. Surface Interrogation Scanning Electrochemical Microscopy of Ni<sub>1-x</sub>Fe<sub>x</sub>OOH (0 < x < 0.27) Oxygen Evolving Catalyst: Kinetics of the “Fast” Iron Sites. *J. Am. Chem. Soc.* **2016**, *138* (1), 313–318.

(34) Stevens, M. B.; Trang, C. D. M.; Enman, L. J.; Deng, J.; Boettcher, S. W. Reactive Fe-Sites in Ni/Fe (Oxy)Hydroxide Are Responsible for Exceptional Oxygen Electrocatalysis Activity. *J. Am. Chem. Soc.* **2017**, *139* (33), 11361–11364.

- (35) McCrory, C. C. L.; Jung, S.; Peters, J. C.; Jaramillo, T. F. Benchmarking Heterogeneous Electrocatalysts for the Oxygen Evolution Reaction. *J. Am. Chem. Soc.* **2013**, *135* (45), 16977–16987.
- (36) Mohammed-Ibrahim, J. A Review on NiFe-Based Electrocatalysts for Efficient Alkaline Oxygen Evolution Reaction. *J. Power Sources* **2020**, *448*, 227375.
- (37) Xu, M.; Wei, M. Layered Double Hydroxide-Based Catalysts: Recent Advances in Preparation, Structure, and Applications. *Adv. Funct. Mater.* **2018**, *28* (47), 1–20.
- (38) Wang, Y.; Yan, D.; El Hankari, S.; Zou, Y.; Wang, S. Recent Progress on Layered Double Hydroxides and Their Derivatives for Electrocatalytic Water Splitting. *Adv. Sci.* **2018**, *5* (8), 1800064.
- (39) Ma, W.; Ma, R.; Wang, C.; Liang, J.; Liu, X.; Zhou, K.; Sasaki, T. A Superlattice of Alternately Stacked Ni-Fe Hydroxide Nanosheets and Graphene for Efficient Splitting of Water. *ACS Nano* **2015**, *9* (2), 1977–1984.
- (40) Zhou, D.; Cai, Z.; Lei, X.; Tian, W.; Bi, Y.; Jia, Y.; Han, N.; Gao, T.; Zhang, Q.; Kuang, Y.; Pan, J.; Sun, X.; Duan, X. NiCoFe-Layered Double Hydroxides/N-Doped Graphene Oxide Array Colloid Composite as an Efficient Bifunctional Catalyst for Oxygen Electrocatalytic Reactions. *Adv. Energy Mater.* **2018**, *8* (9), 1701905.
- (41) Chini, M.; Antonsen, R.; Vennesland, Ø.; Arntsen, B.; Mork, J. H. Polarization Behavior of Carbon Fiber as an Anodic Material in Cathodic Protection. In *11DBMC International Conference on Durability of Building Materials and Components*; 2008.
- (42) Joo, T.; Hu, L.; Hong, B. K.; Oh, J. G.; Litster, S. On the Origin of Deactivation of Reversal-Tolerant Fuel Cell Anodes under Voltage Reversal Conditions. *J. Power Sources* **2020**, *472*, 228439.
- (43) Zhou, M.; Weng, Q.; Zhang, X.; Wang, X.; Xue, Y.; Zeng, X.; Bando, Y.; Golberg, D. *In situ* Electrochemical Formation of Core-Shell Nickel-Iron Disulfide and Oxyhydroxide Heterostructured Catalysts for a Stable Oxygen Evolution Reaction and the Associated Mechanisms. *J. Mater. Chem. A* **2017**, *5* (9), 4335–4342.
- (44) Hong, W.; Sun, S.; Kong, Y.; Hu, Y.; Chen, G. Ni<sub>x</sub>Fe<sub>1-x</sub>B Nanoparticle Self-Modified Nanosheets as Efficient Bifunctional Electrocatalysts for Water Splitting: Experiments and Theories. *J. Mater. Chem. A* **2020**, *8* (15), 7360–7367.

- (45) An, L.; Sun, Y.; Zong, Y.; Liu, Q.; Guo, J.; Zhang, X. Nickel Iron Boride Nanosheets on rGO for Active Electrochemical Water Oxidation. *J. Solid State Chem.* **2018**, *265*, 135–139.
- (46) Li, P.; Zeng, H. C. Bimetallic Ni-Fe Phosphide Nanocomposites with a Controlled Architecture and Composition Enabling Highly Efficient Electrochemical Water Oxidation. *J. Mater. Chem. A* **2018**, *6* (5), 2231–2238.
- (47) Fu, G.; Cui, Z.; Chen, Y.; Xu, L.; Tang, Y.; Goodenough, J. B. Hierarchically Mesoporous Nickel-Iron Nitride as a Cost-Efficient and Highly Durable Electrocatalyst for Zn-Air Battery. *Nano Energy* **2017**, *39* (June), 77–85.
- (48) Chen, W.; Wang, H.; Li, Y.; Liu, Y.; Sun, J.; Lee, S.; Lee, J. S.; Cui, Y. *In situ* Electrochemical Oxidation Tuning of Transition Metal Disulfides to Oxides for Enhanced Water Oxidation. *ACS Cent. Sci.* **2015**, *1* (5), 244–251.
- (49) Xu, X.; Song, F.; Hu, X. A Nickel Iron Diselenide-Derived Efficient Oxygen-Evolution Catalyst. *Nat. Commun.* **2016**, *7*, 1–7.
- (50) Li, Y.; Zhang, H.; Jiang, M.; Zhang, Q.; He, P.; Sun, X. 3D Self-Supported Fe-Doped Ni<sub>2</sub>P Nanosheet Arrays as Bifunctional Catalysts for Overall Water Splitting. *Adv. Funct. Mater.* **2017**, *27* (37), 1–8.
- (51) Meyer, B.; Gottlieb, U.; Laborde, O.; Yang, H.; Lasjaunias, J. C.; Sulpice, A.; Madar, R. Intrinsic Properties of NiSi. *J. Alloys Compd.* **1997**, *262–263*, 235–237.
- (52) E. G. Colgan, M. Maenp, M. Finetti, M.-A. N. Electrical Characteristics of Thin Ni<sub>2</sub>Si, NiSi, and NiSi<sub>2</sub> Layers Grown on Silicon. *J. Chem. Inf. Model.* **1982**, *53* (9), 1689–1699.
- (53) J.-P. Gaspard; Ceolin, R. Hume-Rothery Rule in V–VI Compounds. *Solid State Commun.* **1992**, *84* (8), 839–842.
- (54) Bisi, O.; Calandra, C. Transition Metal Silicides: Aspects of the Chemical Bond and Trends in the Electronic Structure. *J. Phys. C Solid State Phys.* **1981**, *14* (35), 5479–5494.
- (55) Chen, X.; Liang, C. Transition Metal Silicides: Fundamentals, Preparation and Catalytic Applications. *Catal. Sci. Technol.* **2019**, *9* (18), 4785–4820.
- (56) Liu, X.; Fechler, N.; Antonietti, M. Salt Melt Synthesis of Ceramics, Semiconductors and Carbon Nanostructures. *Chem. Soc. Rev.* **2013**, *42* (21), 8237–8265.
- (57) Murarka, S. P. Transition Metal Silicides. *Ann. Rev. Mater. Sci.* **1983**, *13*, 117–137.

- (58) Chow, T. P.; Brown, D. M.; Steckl, A. J.; Garfinkel, M. Silane Silicidation of Mo Thin Films. *J. Appl. Phys.* **1980**, *51* (11), 5981–5985.
- (59) Lau, S. S.; Mayer, J. W.; Tu, K. N. Interactions in the Co/Si Thin-Film System. I. Kinetics. *J. Appl. Phys.* **1978**, *49* (7), 4005–4010.
- (60) Reader, A. H.; Van Ommen, A. H.; Weijs, P. J. W.; Wolters, R. A. M.; Oostra, D. J. Transition Metal Silicides in Silicon Technology. *Reports Prog. Phys.* **1993**, *56* (11), 1397–1467.
- (61) Robins, D. A. The Magnetic Susceptibility and Electrical Resistivity of Some Transition Metal Silicides. *Philos. Mag.* **1958**, *3* (28), 313–327.
- (62) Padnos, B. N. Integrated Silicon Device Technology. Volume X. Chemical/Metallurgical Properties of Silicon. 1965.
- (63) Neshpor, V. S.; Samsonov, G. V. Electric, Thermo-Electric and Galvanomagnetic Properties of Transition Metal Silicides. **1960**.
- (64) Kieffer, R.; Benesovsky, F. *Hartstoffe*; Springer-Verlag, 2013.
- (65) Society, E. *High-Temperature Materials and Technology*; Campbell, I. E., Sherwood, E. M., Eds.; Corrosion monograph series; Wiley, 1967.
- (66) Murarka, S. P. Refractory Silicides for Integrated Circuits. *J. Vac. Sci. Technol.* **1980**, *17* (4), 775–792.
- (67) Nozariasbmarz, A.; Agarwal, A.; Coutant, Z. A.; Hall, M. J.; Liu, J.; Liu, R.; Malhotra, A.; Norouzzadeh, P.; Öztürk, M. C.; Ramesh, V. P.; Sargolzaeiaval, Y.; Suarez, F.; Vashae, D. Thermoelectric Silicides: A Review. *Jpn. J. Appl. Phys.* **2017**, *56*, 0–27.
- (68) Ge, Z. H.; Zhao, L. D.; Wu, D.; Liu, X.; Zhang, B. P.; Li, J. F.; He, J. Low-Cost, Abundant Binary Sulfides as Promising Thermoelectric Materials. *Mater. Today* **2016**, *19* (4), 227–239.
- (69) Hasan, M. N.; Wahid, H.; Nayan, N.; Mohamed Ali, M. S. Inorganic Thermoelectric Materials: A Review. *Int. J. Energy Res.* **2020**, *44* (8), 6170–6222.
- (70) Dahal, A.; Gunasekera, J.; Harringer, L.; Singh, D. K.; Singh, D. J. Metallic Nickel Silicides: Experiments and Theory for NiSi and First Principles Calculations for Other Phases. *J. Alloys Compd.* **2016**, *672*, 110–116.
- (71) Goldfarb, I.; Cesura, F.; Dascalu, M. Magnetic Binary Silicide Nanostructures. *Adv. Mater.* **2018**, *30* (41), 1–11.

- (72) Wernick, J. H.; Wertheim, G. K.; Sherwood, R. C. Magnetic Behavior of the Monosilicides of the 3d-Transition Elements. *Mater. Res. Bull.* **1972**, *7* (12), 1431–1441.
- (73) Han, N.; Liu, H.; Zhao, J. Novel Magnetic Monolayers of Transition Metal Silicide. *J. Supercond. Nov. Magn.* **2015**, *28* (6), 1755–1758.
- (74) Williams, H. J.; Wernick, J. H.; Sherwood, R. C.; Wertheim, G. K. Magnetic Properties of the Monosilicides of Some 3d Transition Elements. *J. Appl. Phys.* **1966**, *37* (3), 1256.
- (75) Wu, H.; Kratzer, P.; Scheffler, M. First-Principles Study of Thin Magnetic Transition-Metal Silicide Films on Si(001). *Phys. Rev. B - Condens. Matter Mater. Phys.* **2005**, *72* (14), 1–12.
- (76) Porter, N. A.; Creeth, G. L.; Marrows, C. H. Magnetoresistance in Polycrystalline and Epitaxial Fe<sub>1-x</sub>Co<sub>x</sub>Si Thin Films. *Phys. Rev. B - Condens. Matter Mater. Phys.* **2012**, *86* (6), 1–6.
- (77) Kratzer, P.; Hashemifar, S. J.; Wu, H.; Hortamani, M.; Scheffler, M. Transition-Metal Silicides as Materials for Magnet-Semiconductor Heterostructures. *J. Appl. Phys.* **2007**, *101* (8), 1–5.
- (78) Gomoyunova, M. V.; Grebenyuk, G. S.; Pronin, I. I.; Solov'ev, S. M.; Vilkov, O. Y.; Vyalykh, D. V. Formation and Magnetic Properties of the Silicon-Cobalt Interface. *Phys. Solid State* **2013**, *55* (2), 437–442.
- (79) Petrova, A. E.; Krasnorussky, V. N.; Shikov, A. A.; Yuhasz, W. M.; Lograsso, T. A.; Lashley, J. C.; Stishov, S. M. Elastic, Thermodynamic, and Electronic Properties of MnSi, FeSi, and CoSi. *Phys. Rev. B - Condens. Matter Mater. Phys.* **2010**, *82* (15), 1–6.
- (80) Stishov, S. M.; Petrova, A. E.; Sidorov, V. A.; Krasnorussky, V. N.; Menzel, D. Self-Doping Effects in Cobalt Silicide CoSi: Electrical, Magnetic, Elastic, and Thermodynamic Properties. *Phys. Rev. B - Condens. Matter Mater. Phys.* **2012**, *86* (6), 1–5.
- (81) Lin, J. Y.; Hsu, H. M.; Lu, K. C. Growth of Single-Crystalline Nickel Silicide Nanowires with Excellent Physical Properties. *CrystEngComm* **2015**, *17* (9), 1911–1916.
- (82) Seo, K.; Varadwaj, K. S. K.; Mohanty, P.; Lee, S.; Jo, Y.; Jung, M. H.; Kim, J.; Kim, B. Magnetic Properties of Single-Crystalline CoSi Nanowires. *Nano Lett.* **2007**, *7* (5), 1240–1245.
- (83) Liang, S.; Islam, R.; Smith, D. J.; Bennett, P. A.; O'Brien, J. R.; Taylor, B. Magnetic Iron Silicide Nanowires on Si(110). *Appl. Phys. Lett.* **2006**, *88* (11), 1–3.
- (84) Matthias, B. T.; Hulm, J. K. Superconducting Properties of Cobalt Disilicide. *Phys. Rev.* **1953**, *89* (2), 439–441.

- (85) King, R. B. Topological Aspects of the Chemical Bonding in Superconducting Transition-Metal Borides, Silicides, and Alloys. *Inorg. Chem.* **1990**, *29* (11), 2164–2170.
- (86) Hardy, G. F.; Hulm, J. K. Superconducting Silicides and Germanides. *Phys. Rev.* **1952**, *4* (89), 884.
- (87) Estruga, M.; Girard, S. N.; Ding, Q.; Chen, L.; Li, X.; Jin, S. Facile and Scalable Synthesis of  $\text{Ti}_5\text{Si}_3$  Nanoparticles in Molten Salts for Metal-Matrix Nanocomposites. *Chem. Commun.* **2014**, *50* (12), 1454–1457.
- (88) Ryabchuk, P.; Agapova, A.; Kreyenschulte, C.; Lund, H.; Junge, H.; Junge, K.; Beller, M. Heterogeneous Nickel-Catalysed Reversible, Acceptorless Dehydrogenation of N-Heterocycles for Hydrogen Storage. *Chem. Commun.* **2019**, *55* (34), 4969–4972.
- (89) Hausmann, J. N.; Beltrán - Suito, R.; Mebs, S.; Hlukhyy, V.; Fässler, T. F.; Dau, H.; Driess, M.; Menezes, P. W. Evolving Highly Active Oxidic Iron(III) Phase from Corrosion of Intermetallic Iron Silicide to Master Efficient Electrocatalytic Water Oxidation and Selective Oxygenation of 5-Hydroxymethylfurfural. *Adv. Mater.* **2021**, *33*, 2008823.
- (90) Chen, X.; Wang, J.; Yang, K.; Meng, C.; Williams, C. T.; Liang, C. Structure Investigation and Dibenzothiophene Hydrodesulfurization Properties of Fe-Substituted Ni-Si Intermetallics. *J. Phys. Chem. C* **2015**, *119* (52), 29052–29061.
- (91) Chen, X.; Wang, X.; Xiu, J.; Williams, C. T.; Liang, C. Synthesis and Characterization of Ferromagnetic Nickel-Cobalt Silicide Catalysts with Good Sulfur Tolerance in Hydrodesulfurization of Dibenzothiophene. *J. Phys. Chem. C* **2012**, *116* (47), 24968–24976.
- (92) Chen, X.; Jin, J.; Sha, G.; Li, C.; Zhang, B.; Su, D.; Williams, C. T.; Liang, C. Silicon-Nickel Intermetallic Compounds Supported on Silica as a Highly Efficient Catalyst for CO Methanation. *Catal. Sci. Technol.* **2014**, *4* (1), 53–61.
- (93) Frank, T. C.; Kester, K. B.; Falconer, J. L. Catalytic Formation of Silanes on Copper-Silicon Alloys. *J. Catal.* **1985**, *91* (1), 44–53.
- (94) Acker, J.; Bohmhammel, K. Reactivity of Intermetallic Compounds: A Solid State Approach to Direct Reactions of Silicon. *J. Phys. Chem. B* **2002**, *106* (19), 5105–5117.
- (95) Yang, K.; Chen, X.; Lafaye, G.; Especel, C.; Epron, F.; Liang, C. One-Step Modification of Active Sites and Support in Ni/ $\text{Al}_2\text{O}_3$  Catalyst for Hydrodeoxygenation of Lignin-Derived Diphenyl Ether. *ChemistrySelect* **2018**, *3* (41), 11398–11405.

- (96) Il'chenko, N. I.; Vlasenko, N. V. Kinetics and Mechanism of Oxidation of Hydrogen on Metal-like Nitrides, Borides, and Silicides. *Theor. Exp. Chem.* **1988**, *23* (6), 694–698.
- (97) Vlasenko, N. V.; Ilchenko, N. I. Catalytic Activity of Transition Metal Silicides in Hydrogen Oxidation. **1988**, *36* (1), 189–193.
- (98) Polisski, S.; Goller, B.; Wilson, K.; Kovalev, D.; Zaikowskii, V.; Lapkin, A. *In Situ* Synthesis and Catalytic Activity in CO Oxidation of Metal Nanoparticles Supported on Porous Nanocrystalline Silicon. *J. Catal.* **2010**, *271* (1), 59–66.
- (99) Hang, Q.; Cheng, Q.; Jie, L. Synthesis of Uniform Double-Walled Carbon Nanotubes Using Iron Disilicide as Catalyst. *Nano Lett.* **2007**, *7* (8), 2417–2421.
- (100) Lin, Y.; Zhou, S.; Liu, X.; Sheehan, S.; Wang, D. TiO<sub>2</sub>/TiSi<sub>2</sub> Heterostructures for High-Efficiency Photoelectrochemical H<sub>2</sub>O Splitting. *J. Am. Chem. Soc.* **2009**, *131*, 2772–2773.
- (101) Mccenaney, J. M.; Schaak, R. E. Solution Synthesis of Metal Silicide Nanoparticles. *Inorg. Chem.* **2015**, *54* (3), 707–709.
- (102) Kumar, R.; Bahri, M.; Song, Y.; Gonell, F.; Thomas, C.; Ersen, O.; Sanchez, C.; Laberty-Robert, C.; Portehault, D. Phase Selective Synthesis of Nickel Silicide Nanocrystals in Molten Salts for Electrocatalysis of the Oxygen Evolution Reaction. *Nanoscale* **2020**, *12* (28), 15209–15213.
- (103) Hausmann, J. N.; Beltrán-Suito, R.; Mebs, S.; Hlukhyy, V.; Fässler, T. F.; Dau, H.; Driess, M.; Menezes, P. W. Evolving Highly Active Oxidic Iron(III) Phase from Corrosion of Intermetallic Iron Silicide to Master Efficient Electrocatalytic Water Oxidation and Selective Oxygenation of 5-Hydroxymethylfurfural. *Adv. Mater.* **2021**, *33*, 2008823.
- (104) Kim, S. W.; Mishima, Y.; Choi, D. C. Effect of Process Conditions on the Thermoelectric Properties of CoSi. *Intermetallics* **2002**, *10* (2), 177–184.
- (105) Lu, Y.; Li, J.; Ye, T. N.; Kobayashi, Y.; Sasase, M.; Kitano, M.; Hosono, H. Synthesis of Rare-Earth-Based Metallic Electride Nanoparticles and Their Catalytic Applications to Selective Hydrogenation and Ammonia Synthesis. *ACS Catal.* **2018**, *8* (12), 11054–11058.
- (106) Gong, Y.; Wu, J.; Kitano, M.; Wang, J.; Ye, T. N.; Li, J.; Kobayashi, Y.; Kishida, K.; Abe, H.; Niwa, Y.; Yang, H.; Tada, T.; Hosono, H. Ternary Intermetallic LaCoSi as a Catalyst for N<sub>2</sub> Activation. *Nat. Catal.* **2018**, *1* (3), 178–185.

- (107) Mizoguchi, H.; Park, S. W.; Kishida, K.; Kitano, M.; Kim, J.; Sasase, M.; Honda, T.; Ikeda, K.; Otomo, T.; Hosono, H. Zeolitic Intermetallics: LnNiSi (Ln = La-Nd). *J. Am. Chem. Soc.* **2019**, *141* (8), 3376–3379.
- (108) Pak, A. Y.; Shatrova, K. N.; Aktaev, N. E.; Ivashutenko, A. S. Preparation of Ultrafine Cu<sub>3</sub>Si in High-Current Pulsed Arc Discharge. *Nanotechnologies Russ.* **2016**, *11* (9–10), 548–552.
- (109) Lu, Y.; Li, J.; Tada, T.; Toda, Y.; Ueda, S.; Yokoyama, T.; Kitano, M.; Hosono, H. Water Durable Electride Y<sub>5</sub>Si<sub>3</sub>: Electronic Structure and Catalytic Activity for Ammonia Synthesis. *J. Am. Chem. Soc.* **2016**, *138* (12), 3970–3973.
- (110) Kim, G.; Rim, H. J.; Lee, K. H.; Roh, J. W.; Lee, W. Suppressed Secondary Phase Generation in Thermoelectric Higher Manganese Silicide by Fabrication Process Optimization. *Ceram. Int.* **2019**, *45* (15), 19538–19541.
- (111) Liu, T.; Chen, Y.; Tang, Y.; Xiao, S.; Zhang, E.; Wang, J. Structure and Magnetic Properties of Shortly High Temperature Annealing LaFe<sub>11.6</sub>Si<sub>1.4</sub> Compound. *J. Alloys Compd.* **2009**, *475* (1–2), 672–675.
- (112) Deka, B.; Srinivasan, A. Magnetic and Structural Properties of (Ru<sub>1-x</sub>Co<sub>x</sub>)<sub>2</sub>FeSi Alloys. *Phys. B Condens. Matter* **2015**, *476*, 118–121.
- (113) Hoffmann, R. D.; Rodewald, U. C.; Haverkamp, S.; Benndorf, C.; Eckert, H.; Heying, B.; Pöttgen, R. The High-Temperature Modification of ScRuSi – Structure, <sup>29</sup>Si and <sup>45</sup>Sc Solid State NMR Spectroscopy. *Solid State Sci.* **2017**, *72*, 109–115.
- (114) Benndorf, C.; Heletta, L.; Heymann, G.; Huppertz, H.; Eckert, H.; Pöttgen, R. NbOsSi and TaOsSi – Two New Superconducting Ternary Osmium Silicides. *Solid State Sci.* **2017**, *68*, 32–38.
- (115) Wu, J.; Gong, Y.; Inoshita, T.; Fredrickson, D. C.; Wang, J.; Lu, Y.; Kitano, M.; Hosono, H. Tiered Electron Anions in Multiple Voids of LaScSi and Their Applications to Ammonia Synthesis. *Adv. Mater.* **2017**, *29* (36), 1–7.
- (116) Gras, C.; Zink, N.; Bernard, F.; Gaffet, E. Assisted Self-Sustaining Combustion Reaction in the Fe-Si System: Mechanical and Chemical Activation. *Mater. Sci. Eng. A* **2007**, *456* (1–2), 270–277.
- (117) Abdellaoui, M.; Barradi, T.; Gaffet, E. Mechanism of Mechanical Alloying Phase Formation and Related Magnetic and Mechanical Properties in the FeSi System. *J. Alloys Compd.* **1993**, *198* (1–2), 155–164.

- (118) Yen, B. K.; Aizawa, T.; Kihara, J. Synthesis and Formation Mechanisms of Molybdenum Silicides by Mechanical Alloying. *Mater. Sci. Eng. A* **1996**, *220*, 8–14.
- (119) Heron, A. J.; Schaffer, G. B. Mechanical Alloying of MoSi<sub>2</sub> with Ternary Alloying Elements. Part 1 Experimental. *Mater. Sci. Eng. A* **2003**, *352*, 105–111.
- (120) Stoloff, N. S. An Overview of Powder Processing of Silicides and Their Composites. *Mater. Sci. Eng. A* **1999**, *261* (1–2), 169–180.
- (121) Restrepo, D.; Hick, S. M.; Griebel, C.; Alarcón, J.; Giesler, K.; Chen, Y.; Orlovskaya, N.; Blair, R. G. Size Controlled Mechanochemical Synthesis of ZrSi<sub>2</sub>. *Chem. Commun.* **2013**, *49* (7), 707–709.
- (122) Gillan, E. G.; Kaner, R. B. Synthesis of Refractory Ceramics via Rapid Metathesis Reactions between Solid-State Precursors. *Chem. Mater.* **1996**, *8* (2), 333–343.
- (123) Nartowski, A. M.; Parkin, I. P. Solid State Metathesis Synthesis of Metal Silicides; Reactions of Calcium and Magnesium Silicide with Metal Oxides. **2002**, *21*, 187–191.
- (124) Parkin, I. P. Solid State Metathesis Reaction for Metal Borides, Silicides, Pnictides and Chalcogenides: Ionic or Elemental Pathways. *Chem. Soc. Rev.* **1996**, *25* (3), 199–207.
- (125) Parkin, I. P. Solvent-Free Reactions in the Solid State: Solid State Metathesis. *ChemInform* **2003**, *34* (17), 569–573.
- (126) Sarkisyan, A. R.; Dolukhanyan, S. K.; I. P. Borovinskaya. Self-Propagating High-Temperature Synthesis of Transition Metal Silicides. **1978**, *17*, 424–427.
- (127) Yeh, C. L.; Chen, W. H. An Experimental Investigation on Combustion Synthesis of Transition Metal Silicides V<sub>5</sub>Si<sub>3</sub>, Nb<sub>5</sub>Si<sub>3</sub>, and Ta<sub>5</sub>Si<sub>3</sub>. *J. Alloys Compd.* **2007**, *439* (1–2), 59–66.
- (128) Yeh, C. L.; Chen, W. H.; Hsu, C. C. Formation of Titanium Silicides Ti<sub>5</sub>Si<sub>3</sub> and TiSi<sub>2</sub> by Self-Propagating Combustion Synthesis. *J. Alloys Compd.* **2007**, *432* (1–2), 90–95.
- (129) Godlewska, E.; Mars, K.; Mania, R.; Zimowski, S. Combustion Synthesis of Mg<sub>2</sub>Si. *Intermetallics* **2011**, *19* (12), 1983–1988.
- (130) Deevi, S. C.; Thadhani, N. N. Reaction Synthesis of High-Temperature Silicides. *Mater. Sci. Eng. A* **1995**, *192–193* (PART 2), 604–611.
- (131) Bernard, F.; Souha, H.; Gaffet, E. Enhancement of Self-Sustaining Reaction Cu<sub>3</sub>Si Phase Formation Starting from Mechanically Activated Powders. *Mater. Sci. Eng. A* **2000**, *284* (1–2), 301–306.

- (132) Lee, W. H.; Byun, C. S.; Lee, S. H.; Kim, D. K. Effects of Si and Ni Powder Refining on the Formation Mechanism of Nickel Silicides Induced by Mechanical Alloying. *Metall. Mater. Trans. A Phys. Metall. Mater. Sci.* **2001**, *32* (13), 805–810.
- (133) Zhou, G. T.; Palchik, O.; Nowik, I.; Herber, R.; Koltypin, Y.; Gedanken, A. Microwave-Assisted Selective Preparation and Characterization of  $\text{Li}_{21}\text{Si}_5$  and  $\text{Li}_{17}\text{Sn}_4$ . *J. Solid State Chem.* **2004**, *177* (9), 3014–3020.
- (134) Savary, E.; Gascoin, F.; Marinel, S. Fast Synthesis of Nanocrystalline  $\text{Mg}_2\text{Si}$  by Microwave Heating: A New Route to Nano-Structured Thermoelectric Materials. *Dalt. Trans.* **2010**, *39* (45), 11074–11080.
- (135) Jokisaari, J. R.; Bhaduri, S.; Bhaduri, S. B. Microwave Activated Combustion Synthesis of Bulk Cobalt Silicides. *J. Alloys Compd.* **2005**, *394* (1–2), 160–167.
- (136) Vaidhyanathan, B.; Rao, K. J. Microwave Assisted Synthesis of Technologically Important Transition Metal Silicides. *J. Mater. Res.* **1997**, *12* (12), 3225–3229.
- (137) Jokisaari, J. R.; Bhaduri, S.; Bhaduri, S. B. Processing of Single Phase  $\text{Mo}_5\text{Si}_3$  by Microwave Activated Combustion Synthesis. *Mater. Sci. Eng. A* **2002**, *323* (1–2), 478–483.
- (138) Joshi, R. K.; Yoshimura, M.; Tanaka, K.; Ueda, K.; Kumar, A.; Ramgir, N. Synthesis of Vertically Aligned  $\text{Pd}_2\text{Si}$  Nanowires in Microwave Plasma Enhanced Chemical Vapor Deposition System. *J. Phys. Chem. C* **2008**, *112* (36), 13901–13904.
- (139) Zhang, L.; Chen, X.; Li, C.; Armbrüster, M.; Peng, Z.; Liang, C. Cobalt Silicides Nanoparticles Embedded in N-Doped Carbon as Highly Efficient Catalyst in Selective Hydrogenation of Cinnamaldehyde. *ChemistrySelect* **2018**, *3* (6), 1658–1666.
- (140) Zhang, L.; Chen, X.; Jin, S.; Guan, J.; Williams, C. T.; Peng, Z.; Liang, C. Rapid Microwaves Synthesis of  $\text{CoSi}_x/\text{CNTs}$  as Novel Catalytic Materials for Hydrogenation of Phthalic Anhydride. *J. Solid State Chem.* **2014**, *217*, 105–112.
- (141) West, G. A.; Beeson, K. W. Chemical Vapor Deposition of Cobalt Silicide. **1988**, *131*, 389–394.
- (142) Zhou, S.; Liu, X.; Lin, Y.; Wang, D. Spontaneous Growth of Highly Conductive Two-Dimensional Single-Crystalline  $\text{TiSi}_2$  Nanonets. *Angew. Chemie - Int. Ed.* **2008**, *47* (40), 7681–7684.
- (143) Zhou, S.; Liu, X.; Lin, Y.; Wang, D. Rational Synthesis and Structural Characterizations of Complex  $\text{TiSi}_2$  Nanostructures. *Chem. Mater.* **2009**, *21* (6), 1023–1027.

- (144) Zhou, S.; Xie, J.; Wang, D. Understanding the Growth Mechanism of Titanium Disilicide Nanonets. *ACS Nano* **2011**, *5* (5), 4205–4210.
- (145) Xiang, B.; Wang, Q. X.; Wang, Z.; Zhang, X. Z.; Liu, L. Q.; Xu, J.; Yu, D. P. Synthesis and Field Emission Properties of TiSi<sub>2</sub> Nanowires. *Appl. Phys. Lett.* **2005**, *86* (24), 1–3.
- (146) Ma, J.; Gu, Y.; Shi, L.; Chen, L.; Yang, Z.; Qian, Y. Synthesis and Thermal Stability of Nanocrystalline Chromium Disilicide. *J. Alloys Compd.* **2004**, *376* (1–2), 176–179.
- (147) Varadwaj, K. S. K.; Seo, K.; In, J.; Mohanty, P.; Park, J.; Kim, B. Phase-Controlled Growth of Metastable Fe<sub>3</sub>Si<sub>3</sub> Nanowires by a Vapor Transport Method. *J. Am. Chem. Soc.* **2007**, *129* (27), 8594–8599.
- (148) In, J.; Seo, K.; Lee, S.; Yoon, H.; Park, J.; Lee, G.; Kim, B. Morphology-Tuned Synthesis of Single-Crystalline V<sub>5</sub>Si<sub>3</sub> Nanotubes and Nanowires. *J. Phys. Chem. C* **2009**, *113* (30), 12996–13001.
- (149) Tsai, C. I.; Yeh, P. H.; Wang, C. Y.; Wu, H. W.; Chen, U. S.; Lu, M. Y.; Wu, W. W.; Chen, L. J.; Wang, Z. L. Cobalt Silicide Nanostructures: Synthesis, Electron Transport, and Field Emission Properties. *Cryst. Growth Des.* **2009**, *9* (10), 4514–4518.
- (150) Seo, K.; Lee, S.; Yoon, H.; In, J.; Varadwaj, K. S. K.; Jo, Y.; Jung, M. H.; Kim, J.; Kim, B. Composition-Tuned CoSi Nanowires: Location-Selective Simultaneous Growth along Temperature Gradient. *ACS Nano* **2009**, *3* (5), 1145–1150.
- (151) Yu, L.; Lv, Y.; Zhang, X.; Wang, H. Application of *in situ* Chloride-Generated Route to Ti<sub>5</sub>Si<sub>3</sub> Nanowires from and on Si Substrate. *Mater. Lett.* **2012**, *74*, 46–49.
- (152) Higgins, J. M.; Ding, R.; Degraeve, J. P.; Jin, S. Signature of Helimagnetic Ordering in Single-Crystal MnSi Nanowires. *Nano Lett.* **2010**, *10* (5), 1605–1610.
- (153) Chiu, W. L.; Chiu, C. H.; Chen, J. Y.; Huang, C. W.; Huang, Y. T.; Lu, K. C.; Hsin, C. L.; Yeh, P. H.; Wu, W. W. Single-Crystalline δ-Ni<sub>2</sub>Si Nanowires with Excellent Physical Properties. *Nanoscale Res. Lett.* **2013**, *8* (1), 1–5.
- (154) Banis, M. N.; Meng, X.; Zhang, Y.; Cai, M.; Li, R.; Sun, X. Spatially Sequential Growth of Various WSi<sub>2</sub> Networked Nanostructures and Mechanisms. *J. Phys. Chem. C* **2013**, *117* (37), 19189–19194.
- (155) Banis, M. N.; Zhang, Y.; Xiao, Q.; Cai, M.; Li, R.; Sun, X. Tailoring of Single-Crystalline Complex Ta<sub>5</sub>Si<sub>3</sub> Nanostructures: From Networked Nanowires to Nanosheets. *Cryst. Growth Des.* **2014**, *14* (2), 436–441.

- (156) In, J.; Varadwaj, K. S. K.; Seo, K.; Lee, S.; Jo, Y.; Jung, M. H.; Kim, J.; Kim, B. Single-Crystalline Ferromagnetic  $\text{Fe}_{1-x}\text{Co}_x\text{Si}$  Nanowires. *J. Phys. Chem. C* **2008**, *112* (12), 4748–4752.
- (157) Fan, X.; Zhang, H.; Du, N.; Yang, D. Phase-Controlled Synthesis of Nickel Silicide Nanostructures. *Mater. Res. Bull.* **2012**, *47* (11), 3797–3803.
- (158) Peter, A. P.; Meersschaut, J.; Richard, O.; Moussa, A.; Steenberg, J.; Schaekers, M.; Tökei, Z.; Van Elshocht, S.; Adelman, C. Phase Formation and Morphology of Nickel Silicide Thin Films Synthesized by Catalyzed Chemical Vapor Reaction of Nickel with Silane. *Chem. Mater.* **2015**, *27* (1), 245–254.
- (159) Kim, C. J.; Kang, K.; Woo, Y. S.; Ryu, K. G.; Moon, H.; Kim, J. M.; Zang, D. S.; Jo, M. H. Spontaneous Chemical Vapor Growth of NiSi Nanowires and Their Metallic Properties. *Adv. Mater.* **2007**, *19* (21), 3637–3642.
- (160) Yang, K.; Chen, X.; Wang, L.; Zhang, L.; Jin, S.; Liang, C. SBA-15-Supported Metal Silicides Prepared by Chemical Vapor Deposition as Efficient Catalysts Towards the Semihydrogenation of Phenylacetylene. *ChemCatChem* **2017**, *9* (7), 1337–1342.
- (161) Li, M.; Chen, X.; Guan, J.; Wang, X.; Wang, J.; Williams, C. T.; Liang, C. A Facile and Novel Approach to Magnetic  $\text{Fe}@\text{SiO}_2$  and  $\text{FeSi}_2@\text{SiO}_2$  Nanoparticles. *J. Mater. Chem.* **2012**, *22* (2), 609–616.
- (162) Dahal, N.; Chikan, V. Phase-Controlled Synthesis of Iron Silicide ( $\text{Fe}_3\text{Si}$  and  $\text{FeSi}_2$ ) Nanoparticles in Solution. *Chem. Mater.* **2010**, *22* (9), 2892–2897.
- (163) Baudouin, D.; Szeto, K. C.; Laurent, P.; De Mallmann, A.; Fenet, B.; Veyre, L.; Rodemerck, U.; Copéret, C.; Thieuleux, C. Nickel-Silicide Colloid Prepared under Mild Conditions as a Versatile Ni Precursor for More Efficient  $\text{CO}_2$  Reforming of  $\text{CH}_4$  Catalysts. *J. Am. Chem. Soc.* **2012**, *134* (51), 20624–20627.
- (164) Nersisyan, H. H.; Lee, T. H.; Ri, V.; Lee, J. H.; Suh, H.; Kim, J. G.; Son, H. T.; Kim, Y. H. NaF-Assisted Combustion Synthesis of  $\text{MoSi}_2$  Nanoparticles and Their Densification Behavior. *J. Phys. Chem. Solids* **2017**, *102*, 34–41.
- (165) Yang, Z.; Gu, Y.; Chen, L.; Shi, L.; Ma, J.; Qian, Y. Preparation of  $\text{Mn}_5\text{Si}_3$  Nanocages and Nanotubes by Molten Salt Flux. *Solid State Commun.* **2004**, *130* (5), 347–351.
- (166) Portehault, D.; Delacroix, S.; Gouget, G.; Grosjean, R.; Chan-Chang, T. H. C. Beyond the Compositional Threshold of Nanoparticle-Based Materials. *Acc. Chem. Res.* **2018**, *51* (4), 930–939.

(167) FTsalt - FACT Salt Phase Diagrams  
[http://www.factsage.cn/fact/documentation/FTsalt/FTsalt\\_Figs.htm](http://www.factsage.cn/fact/documentation/FTsalt/FTsalt_Figs.htm).

(168) Gupta, S. K.; Mao, Y. Recent Developments on Molten Salt Synthesis of Inorganic Nanomaterials: A Review. *J. Phys. Chem. C* **2021**.

(169) Liang, C.; Zhao, A.; Zhang, X.; Ma, Z.; Prins, R. CoSi Particles on Silica Support as a Highly Active and Selective Catalyst for Naphthalene Hydrogenation. *Chem. Commun.* **2009**, No. 15, 2047–2049.

(170) Zhao, A.; Zhang, X.; Chen, X.; Guan, J.; Liang, C. Cobalt Silicide Nanoparticles in Mesoporous Silica as Efficient Naphthalene Hydrogenation Catalysts by Chemical Vapor Deposition. *J. Phys. Chem. C* **2010**, *114* (9), 3962–3967.

(171) Aylett, B.; Tannahill, A. Chemical Vapour Deposition of Metal Silicides from Organometallic Compounds with Silicon-Metal Bonds. *Vacuum* **1985**, *35* (10–11), 435–439.

(172) Schmitt, A. L.; Jin, S. Selective Patterned Growth of Silicide Nanowires without the Use of Metal Catalysts. *Chem. Mater.* **2007**, *19* (2), 126–128.

(173) Schmitt, A. L.; Higgins, J. M.; Jin, S. Chemical Synthesis and Magnetotransport of Magnetic Semiconducting Fe<sub>1-x</sub>Co<sub>x</sub>Si Alloy Nanowires. *Nano Lett.* **2008**, *8* (3), 810–815.

(174) Higgins, J. M.; Schmitt, A. L.; Guzei, I. A.; Jin, S. Higher Manganese Silicide Nanowires of Nowotny Chimney Ladder Phase. *J. Am. Chem. Soc.* **2008**, *130* (47), 16086–16094.

(175) Guan, J.; Chen, X.; Yang, K.; Rykov, A.; Wang, J.; Liang, C. Preparation and Size-Dependent Magnetism of Highly Dispersed Iron Silicide Nanoparticles on Silica. *J. Mater. Chem. C* **2014**, *2* (27), 5292–5298.

(176) Guan, J.; Jin, J.; Chen, X.; Zhang, B.; Su, D.; Liang, C. Preparation and Formation Mechanism of Highly Dispersed Manganese Silicide on Silica by MOCVD of Mn(CO)<sub>5</sub>SiCl<sub>3</sub>. *Chem. Vap. Depos.* **2013**, *19* (1–3), 68–73.

(177) Du, V. A.; Sidorenko, A.; Bethge, O.; Paschen, S.; Bertagnolli, E.; Schubert, U. Iron Silicide Nanoparticles in a SiC/C Matrix from Organometallic Polymers: Characterization and Magnetic Properties. *J. Mater. Chem.* **2011**, *21* (33), 12232–12238.

(178) Friebe, L.; Liu, K.; Obermeier, B.; Petrov, S.; Dube, P.; Manners, I. Pyrolysis of Polycarbosilanes with Pendant Nickel Clusters: Synthesis and Characterization of Magnetic Ceramics Containing Nickel and Nickel Silicide Nanoparticles. *Chem. Mater.* **2007**, *19* (10), 2630–2640.

- (179) Zaheer, M.; Motz, G.; Kempe, R. The Generation of Palladium Silicide Nanoalloy Particles in a SiCN Matrix and Their Catalytic Applications. *J. Mater. Chem.* **2011**, *21* (46), 18825–18831.
- (180) Zhang, M.; Yan, Z.; Li, Y.; Jing, J.; Xie, J. Preparation of Cobalt Silicide on Graphene as Pt Electrocatalyst Supports for Highly Efficient and Stable Methanol Oxidation in Acidic Media. *Electrochim. Acta* **2015**, *161*, 48–54.
- (181) Zhang, M.; Pan, D.; Li, Y.; Yan, Z.; Meng, S.; Xie, J. Formation of Cobalt Silicide Nanoparticles on Graphene with a Synergistic Effect and High Stability for Ethanol Oxidation. *RSC Adv.* **2016**, *6* (36), 30293–30300.
- (182) Zhang, L.; Chen, X.; Chen, Y.; Peng, Z.; Liang, C. Acid-Tolerant Intermetallic Cobalt-Nickel Silicides as Noble Metal-like Catalysts for Selective Hydrogenation of Phthalic Anhydride to Phthalide. *Catal. Sci. Technol.* **2019**, *9* (5), 1108–1116.
- (183) Ndolomingo, M. J.; Bingwa, N.; Meijboom, R. Review of Supported Metal Nanoparticles: Synthesis Methodologies, Advantages and Application as Catalysts. *J. Mater. Sci.* **2020**, *55* (15), 6195–6241.
- (184) Buonsanti, R.; Loiudice, A.; Mantella, V. Colloidal Nanocrystals as Precursors and Intermediates in Solid State Reactions for Multinary Oxide Nanomaterials. *Acc. Chem. Res.* **2021**, *54* (4), 754–764.



# Chapter II. Synthesis and electrocatalytic properties of Fe-doped Ni<sub>2</sub>Si nanoparticles

## II.1 Introduction

NiFe oxide/(oxy)hydroxides are among the most active species for OER electrocatalysis in alkaline media, delivering high electrocatalytic activities with only earth-abundant elements.<sup>1,2</sup> However, their moderate electrical conductivity (**Table II-1**), low surface density of active sites and aggregation tendency result in fast degradation of the electrocatalytic properties.<sup>1,3,4</sup> Therefore, designing composite electrodes with an electrically conductive support is usually required.<sup>5-7</sup> Most-used carbon-based supports suffer from corrosion in OER conditions, which is detrimental for performance stability.<sup>8</sup> Non-oxidic compounds of Ni, Fe and p-block elements such as borides,<sup>9,10</sup> phosphides,<sup>11</sup> nitrides,<sup>12</sup> sulfides,<sup>13,14</sup> and selenides<sup>15</sup> are possible pre-catalysts forming NiFe layered (oxy)hydroxides (LDH) by *in situ* oxidation. Among these materials, some undergo only partial oxidation and are potential solutions to the electrical conductivity limitation. By forming a thin surface layer of crystalline<sup>14,16</sup> or amorphous<sup>9</sup> metal (oxy)hydroxide/oxide under OER conditions, these materials enable charge percolation through the particles core that maintains a conductive nature.<sup>9,14</sup> However, the stability of such heterostructures is debatable. The existence and origin of resistance against in-depth corrosion remains to be solved.

**Table II-1** Comparison of the conductivity of reported OER electrocatalysts according to their charge transfer resistances ( $R_{ct}$ ) obtained from electrochemical impedance spectroscopy (EIS).

Catalysts	$R_{ct}$ ( $\Omega$ )	Ref.
NiFeSi-12	17	This work
NiFeSi-50	5	This work
Ni-Fe disulfide	10	14
Ni-Fe hydroxide	17.5	14
(Ni <sub>0.75</sub> Fe <sub>0.25</sub> ) <sub>2</sub> P	5	16
NiFe borate/reduced graphene oxide	38	10
NiFe borate	81	10
NiFe LDH/oxidized graphene/carbon nanotube	100	17

Catalysts	R <sub>ct</sub> (Ω)	Ref.
NiFe LDH	1800	17
NiFe oxide	50	18
NiFe LDH/carbon network	353	19
NiFe LDH	875	19
NiFe LDH	70	20
NiFe <sub>2</sub> O <sub>4</sub> /Ni(OH) <sub>2</sub>	500	21

Nickel iron silicides have never been studied as OER electrocatalysts. One can anticipate that if their oxidation during OER were only superficial, they would deliver high electrocatalytic activity, thanks to their metal-like conductivity ( $\sim 10^{-5}$  Ω cm for nickel silicides),<sup>22,23</sup> combined with a very low cost and low environmental impact due to the natural abundance of the constitutive elements in the Earth's crust. Designing nanostructured architectures where NiFe layered (oxy)hydroxides would be bound to a conductive silicide core, in turn protected versus corrosion, would enhance the surface area of the catalyst material, the electrical conductivity of the whole material, and its stability. These features could be achieved by forming core-shell nanostructures. Therefore, high performance electrocatalysts could be reached by developing NiFe silicide nanocrystals able to form a layered (oxy)hydroxide shell at their surface, with an interface stable versus corrosion.

Besides thin films and nanowires, very few occurrences of nanostructured metal silicides have been reported.<sup>24-27</sup> Among them, McEnaney *et al.* obtained Cu, Pd and Ni silicide nanoparticles through a colloidal synthesis pathway.<sup>28</sup> Kumar *et al.* established recently a molten salt synthesis of nickel silicide nanoparticles from nickel salts and sodium silicide. Despite a low control of morphological features, they revealed significant OER electrocatalytic activity of materials derived from nickel silicides.<sup>29</sup> Nanostructured NiFe silicides are even rarer<sup>30</sup> and have not been studied for OER electrocatalysis, although they have been sparsely assessed for other types of catalysis, like hydrodesulfurization where Si-rich NiFe silicides were derived from silicification of nickel iron oxides.<sup>30</sup>

In the present chapter, we design metal-rich nickel iron silicide nanocrystals by exploiting the high reactivity of silicon nanoparticles as precursors towards nanostructured non-oxides.<sup>31</sup> Using nano-objects as reagents enables size and morphological control in the synthesis of multielement nano-objects when the initial objects are reacted in low temperature organic solvents.<sup>31-35</sup> These procedures rely mostly on metal, oxide, chalcogenide and halide nanoparticles. In this work, we use molten salts as high temperature solvents to trigger the reactivity of covalent silicon nanoparticles and convert them into size-controlled NiFe silicides. The low vapor pressure of molten salts<sup>36,37</sup> offers the opportunity to run liquid-phase reactions at relatively high

temperature and under dynamic vacuum. This feature enables shifting the equilibrium of the reaction between metal salts and silicon nanoparticles and performing for the first time this reaction while eliminating byproducts during the synthesis. The as-obtained Fe-doped Ni<sub>2</sub>Si nanocrystals exhibit high and stable performances in alkaline OER electrocatalysis. We then specifically address the origin of the stability of the electrochemical behavior by scrutinizing the structural and morphological changes occurring during electrocatalysis.

## II.2 Experimental methods

**Reagents.** Lithium iodide (99%, Alfa Aesar), potassium iodide (99%, Sigma-Aldrich), silicon nanoparticles (99%, Nanomakers<sup>®</sup>, France, **Figure II-1**), bulk Si powder (99 %, Sigma-Aldrich), nickel (II) chloride (99%, Alfa Aesar) and iron (II) chloride (99.5%, Alfa Aesar) were stored and manipulated as received in an Ar-filled glovebox (H<sub>2</sub>O < 0.5 ppm, O<sub>2</sub> < 0.5 ppm). Methanol (VWR Normapur grade) was used for washing.

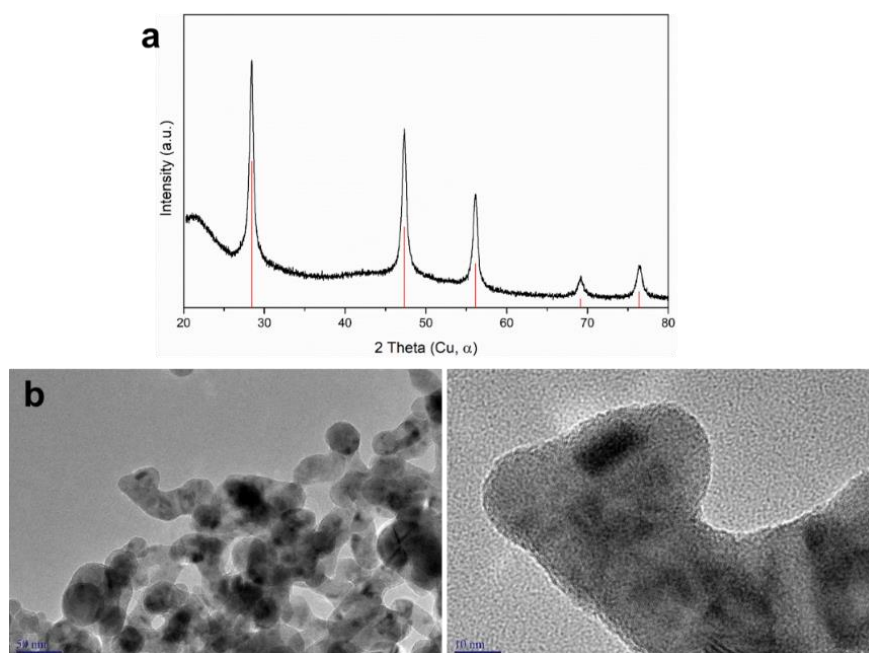


**Figure II-1** (a) Powder XRD pattern of Si nanoparticles used as reagents. Red drop lines indicate a diamond-like structure Si reference. (b) TEM images of Si nanoparticles used as reagents.

**Metal silicide nanoparticles synthesis.** Si nanoparticles, metal chloride NiCl<sub>2</sub>, FeCl<sub>2</sub> or both, 2.9 g LiI (21.7 mmol) and 2.1 g KI (12.7 mmol) were ball-milled during 2 min at 20 Hz (Retsch MM400 ball mill airtight vial of 50 mL, filled with one steel ball of 62.3 g with a diameter of 23 mm) to get a well-mixed fine powder. Precise reactant amounts are listed in the **Table II-2**.

The mixture was loaded in a quartz tube (Ø28×H345 mm) which was then connected to a N<sub>2</sub>-flowed Schlenk line. An intermediate liquid nitrogen trap between the quartz tube and the Schlenk line was set to condensate the volatile byproduct SiI<sub>4</sub>. A vertical furnace from Eraly® was pre-heated to the reaction temperature. Afterward, the quartz tube was evacuated and placed into the furnace. The reaction medium was maintained at the targeted temperature for 6 hours under dynamic vacuum (10<sup>-3</sup> mbar). Then, the hot quartz tube was taken out and cooled down to room temperature. The as-obtained mixture was washed in methanol by seven cycles of centrifugation/redispersion and was later dried in a Schlenk tube under vacuum. The resulting powder was transferred and stored in an Ar-filled glovebox. A typical synthesis yields about 100 mg of powders, which corresponds to a yield of about 90 %.

**Table II-2** Reactant masses, amounts and temperatures for syntheses of Ni, Fe and NiFe silicides. NiFeSi-X where X is the Ni/Fe atomic ratio according to scanning electron microscopy (SEM)-energy dispersive spectroscopy analysis (EDX) corresponding to the o-Ni<sub>2</sub>Si structure.

Samples	Reactant / mg (mmol)			Reaction temperature (°C)
	Si	NiCl <sub>2</sub>	FeCl <sub>2</sub>	
Ni <sub>2</sub> Si	42.1 (1.5)	194.4 (1.5)	/	300
NiFeSi-50	52.5 (1.9)	243.0 (1.9)	47.5 (0.4)	300
NiFeSi-12	42.1 (1.5)	146.0 (1.1)	47.5 (0.4)	300
NiFeSi-3	84.3 (3.0)	194.4 (1.5)	190.1 (1.5)	300
FeSi	63.2 (2.3)	/	190.1 (1.5)	400

**Synthesis under Ar.** 42.1 mg Si nanoparticles (1.5 mmol), 194.4 mg NiCl<sub>2</sub> (1.5 mmol) and 5 g LiI-KI (0.63:0.37 mol.) were ball-milled during 2 min. The same synthesis procedure was followed with the same setup as the synthesis described above, except that the reaction was under Ar flow instead of vacuum. The as-prepared solid was washed in methanol and in deionized water, respectively by six cycles and two cycles of centrifugation/redispersion, and was later dried under vacuum.

**Synthesis from bulk Si powder.** 42.1 mg bulk Si powder (1.5 mmol), 194.4 mg NiCl<sub>2</sub> (1.5 mmol) and 5 g LiI-KI (0.63:0.37 mol.) were ball-milled during 2 min. The synthesis protocol described above was kept. The as-obtained mixture was washed in methanol and in deionized water, respectively by six cycles and two cycles of centrifugation/redispersion, and was later dried under vacuum.

**Synthesis without molten salts.** 42.1 mg Si nanoparticles (1.5 mmol) and 194.4 mg NiCl<sub>2</sub> (1.5 mmol) were ball-milled during 2 min. Later, the same procedure was followed. After thermal

treatment, the resulting powder was directly collected.

**Electrode preparation.** A Pt wire and Ag/AgCl in saturated KCl electrode were respectively used as counter electrode and reference electrode for a typical three-electrode configuration. There are two types of substrates used for the working electrode in this work. A glassy carbon (GC) rotating disk electrode (RDE) with a diameter of 5 mm was used for cyclic voltammetry (CV), linear sweep voltammetry (LSV) and electrochemical impedance spectroscopy (EIS) measurements, and a GC sheet was used for chronopotentiometry (CP) measurements. All catalyst inks were prepared with the same protocol. 3.4 mg of catalyst was sonicated in 480  $\mu\text{L}$  absolute ethanol for 15 min, followed by adding 20  $\mu\text{L}$  of Nafion solution (5 % in alcohols and water, Sigma-Aldrich) for another 10 min of ultrasonication. A given volume of well-dispersed ink was dropped onto the GC sheet or the as-polished RDE substrate to obtain a catalyst loading of  $170 \mu\text{g}_{\text{catalyst}} \cdot \text{cm}^{-2}_{\text{electrode}}$ , and then the substrate was dried for at least 30 min under air. IrO<sub>2</sub> nanoparticles were deposited according to the same protocol.

**Electrolyte purification.**<sup>38</sup> *ca.* 1 g of as-prepared Ni(OH)<sub>2</sub> solid was put into 200 mL as-prepared 0.1M KOH. The suspension was sonicated for 3 min and then rested for at least 6 h. The purified 0.1M KOH supernatant was separated by centrifugation, stored under nitrogen and later used as electrolyte.

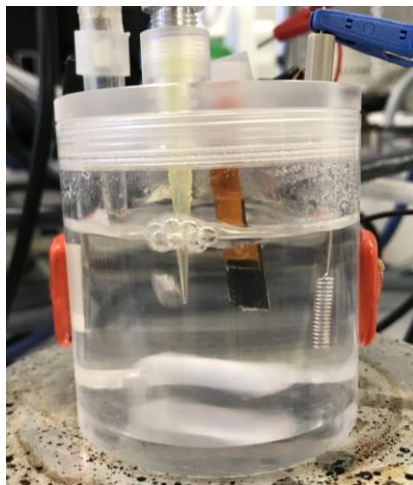


**Figure II-2** The three-electrode configuration used in the custom-made PMMA electrochemical cell.

**Electrochemical measurements.** A custom-made PMMA electrochemical cell was used for all measurements (**Figure II-2**). The electrolyte was bubbled by O<sub>2</sub> for at least 20 min before measurement and during the measurement. The rotating rate of the RDE was set at 1600 rpm for all cyclic voltammetry (CV) measurements. CV and LSV measurements were performed at

scan rate of 20 and 10 mV s<sup>-1</sup>, respectively, from 0 to 1.0 V vs. Ag/AgCl in saturated KCl (equivalent to 1.0-2.0 V vs. RHE). For the chronopotentiometry (CP), the current density was set at 10 mA cm<sup>-2</sup> to monitor the potential evolution. Since a non-rotating GC sheet was used as working electrode substrate, a Teflon-covered stir bar stirred the electrolyte at 350 rpm during the measurements to decrease the limitation on activity due to ion depletion. The electrochemical impedance spectroscopy (EIS) was recorded in a frequency range of 50 000 to 1 Hz with a voltage amplitude of 10 mV.

For all potentials reported in this work, the ohmic drop  $iR$  was compensated, where the resistance is approximately equal to the total impedance measured at a frequency of 50 kHz. The potentials vs. RHE are obtained from conversion of measured potentials based on the equation:  $E_{\text{RHE}} = E_{\text{measured}} + 0.197 + 0.0591 \times \text{pH}$ , where  $\text{pH} = 13$ .

## II.3 Results and Discussion

### II.3.1 Synthesis and characterization

The reactivity between metal chlorides and elemental silicon is appealing to produce metal silicides because of the low cost of these reagents and their abundance. These reactions have been well explored by chemical vapor deposition (CVD) to yield metal silicide nanowires<sup>24,25,27,39-42</sup> usually at *ca.* 900 °C.<sup>25,42</sup> The same reaction has been performed in the solid-state and in molten salts for CrSi<sub>2</sub> at 800 °C.<sup>43,44</sup> This temperature is poorly compatible with the recovery of high surface area nano-objects. To decrease further reaction temperatures, we have used a molten salt medium to ensure liquid-phase reaction, and 40 nm silicon nanoparticles (diamond-like crystal structure, noted *d*-Si) as reagents with enhanced reactivity compared to bulk silicon.

Schematically (**Figure II-3a**), in molten LiI-KI (eutectic molar ratio 0.63:0.37) with a melting point at 286 °C, the metal (II) cations were reduced by Si(0) nanoparticles and further reacted with the Si core by forming metal silicides. In the meantime, Si(0) was oxidized to Si(IV), and combined with iodides from the molten salts to form gaseous SiI<sub>4</sub> (boiling point at 290 °C under atmosphere pressure).<sup>45</sup> The byproduct was collected and analyzed by XRD, and then confirmed to be SiI<sub>4</sub> (**Figure II-4**).

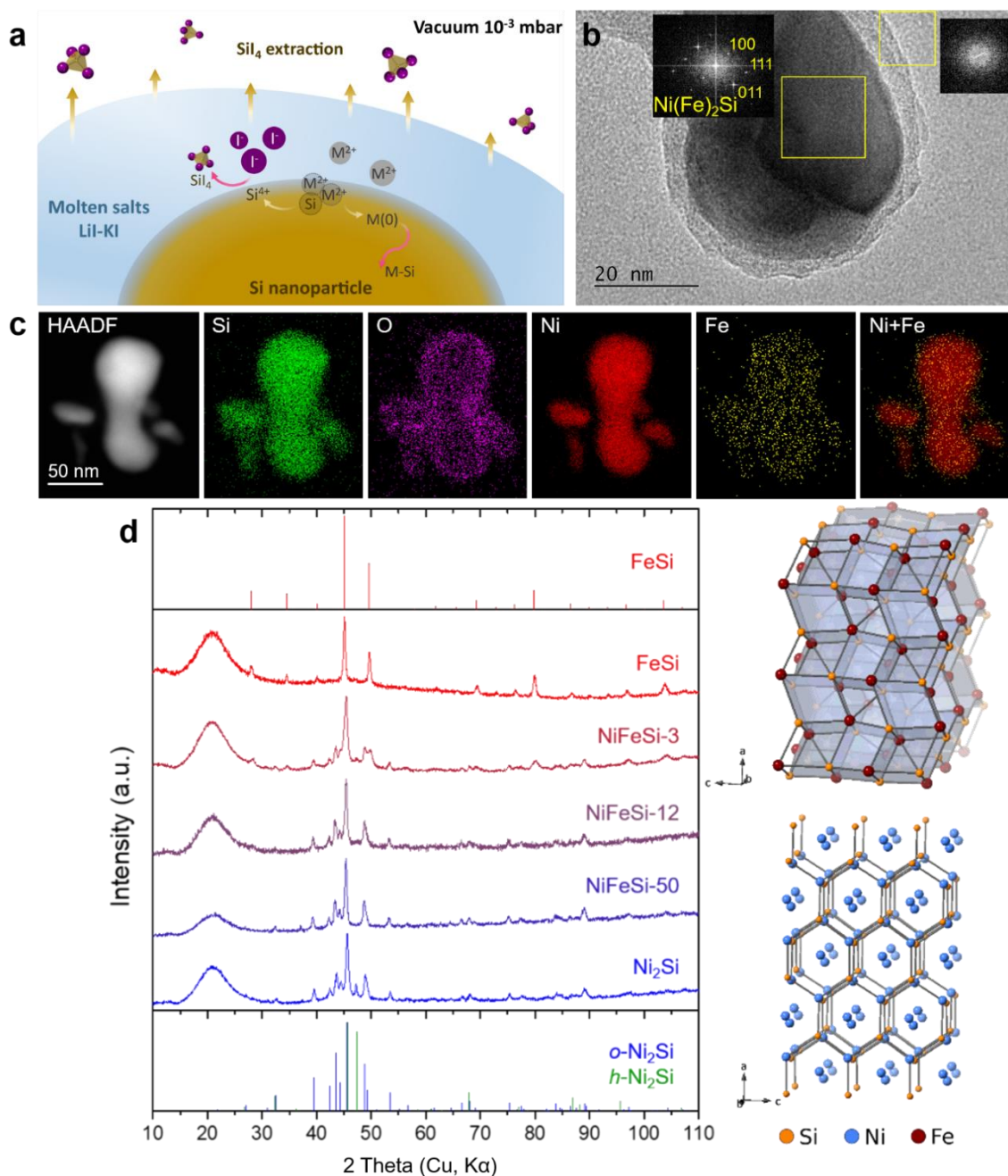


**Figure II-3** (a) Schematic illustration of the reaction between Si nanoparticles and metal salts in molten salts and under vacuum. (b) HRTEM image with corresponding Fast Fourier Transform (FFT, inset) and (c) STEM-EDX chemical mapping of as-prepared NiFeSi-12 sample. The FFT is indexed along the o-Ni<sub>2</sub>Si structure. (d) XRD patterns of the as-prepared samples of Ni, Fe and NiFe silicides. The blue, green and red drop lines denote the references of o-Ni<sub>2</sub>Si, h-Ni<sub>2</sub>Si and FeSi, respectively. The broad bumps between 15-25 ° come from the beam scattering of the protective PMMA plastic dome used for confining the Ar atmosphere around the sample. The o-Ni<sub>2</sub>Si (bottom) and FeSi (top) crystal structures are also displayed on the right.

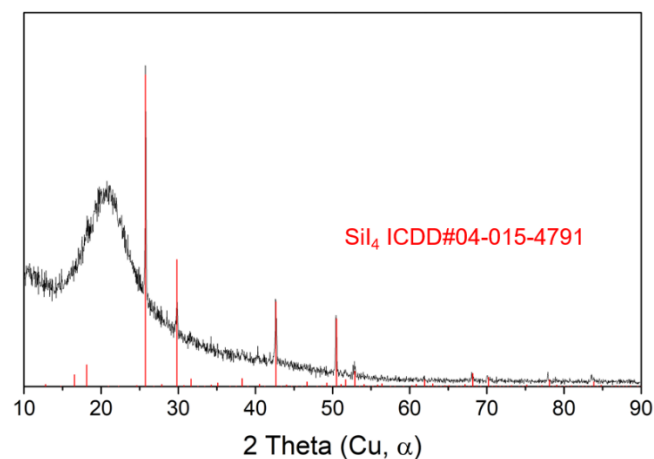


**Figure II-4** Powder XRD pattern of the evaporated and recondensed byproduct of metal silicide synthesis, which can be indexed along the SiI<sub>4</sub> reference (indicated by red lines). The broad bump between 15 and 25 ° comes from the beam scattering of the protective PMMA plastic dome used for confining the Ar atmosphere around the sample.

To ensure sample purification during the synthesis, the reaction was performed at 300–400 °C under dynamic vacuum ( $10^{-3}$  mbar, detailed experimental methods are described in the Experimental methods), which was made possible by the low vapor pressure of LiI-KI in the reaction conditions. At low pressure, silicon tetraiodide is extracted towards a cold trap. The synthesis under dynamic vacuum not only leads to a purified sample, it also ensures total consumption of crystalline silicon nanoparticles (**Figure II-5a**). This demonstrates that evacuating SiI<sub>4</sub> shifts the reaction equilibrium. Ni<sub>2</sub>Si and NiFe silicides (**Figure II-3b-d**) were then obtained at 300 °C, while a higher synthesis temperature of 400 °C was required for FeSi synthesis (**Figure II-3d**). It is consistent with the literature that reports higher formation temperature for FeSi nanowires (1100 °C) than for Ni<sub>2</sub>Si ones (850 °C).<sup>27,41</sup> In all cases, we observe a drastic decrease in the reaction temperature of at least 500 °C. Not only dynamic vacuum, but also the molten salt medium and the silicon nanoparticles play a role in this strong enhancement of reactivity, since bulk silicon reacted in molten salts (**Figure II-5b**) or silicon nanoparticles reacted in the solid state (**Figure II-5c**) yielded large amounts of unreacted silicon species. Therefore, we attribute the large decrease in reaction temperature to the enhanced reactivity of silicon nanoparticles *versus* bulk silicon, to the molten salt liquid medium that fastens reactions, and to equilibrium shift under vacuum.

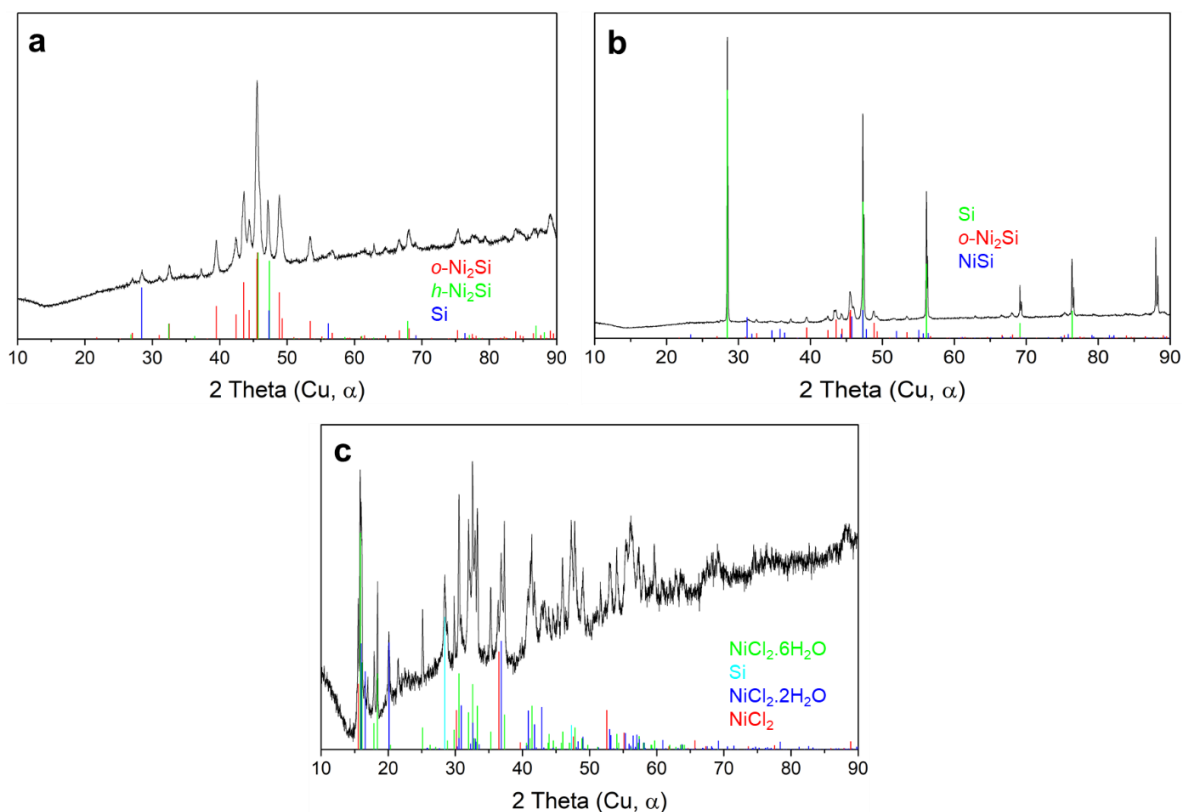


**Figure II-5** Powder XRD pattern: (a) the final product from the reaction between Si nanoparticles and NiCl<sub>2</sub> under 1 atm. argon at 395 °C for 6 h in LiI-KI. Nickel silicides were the major phase, however unreacted Si can be observed, (b) the final product from the reaction between bulk Si powder and NiCl<sub>2</sub> under vacuum at 395 °C for 6 h in LiI-KI. Large amount of Si remains unreacted. Nickel silicides were formed in a minor fraction, (c) the final product from the solid-solid reaction between Si nanoparticles and NiCl<sub>2</sub> under vacuum at 395 °C for 6 h. Unreacted Si and NiCl<sub>2</sub> were found. NiCl<sub>2</sub> appears hydrated because the XRD diagram was acquired in the air.

High resolution transmission electron microscopy (HRTEM, **Figure II-3b**) for the NiFeSi-12 sample (**Figure II-3d**) shows the typical morphology of metal silicide nanocrystals obtained in this work. The nanoparticles with an average diameter of *ca.* 40 nm (**Figure II-6a**) – hence a geometrical surface area of *ca.* 20 m<sup>2</sup> g<sup>-1</sup> – exhibit a crystalline core and an amorphous native oxide layer. The amorphous oxide layer (**Figure II-3b**) most probably arises from exposure to air during sample preparation and storage several days for TEM observations, which highlights the stability of the silicide core under air. All as-obtained silicide samples exhibit similar morphologies (**Figure II-6b-f**), with a particle size that fits the one of the initial Si nanoparticles, thus suggesting a reaction mechanism where the metal atoms diffuse into the silicon particles, whatever the Ni/Fe ratio.

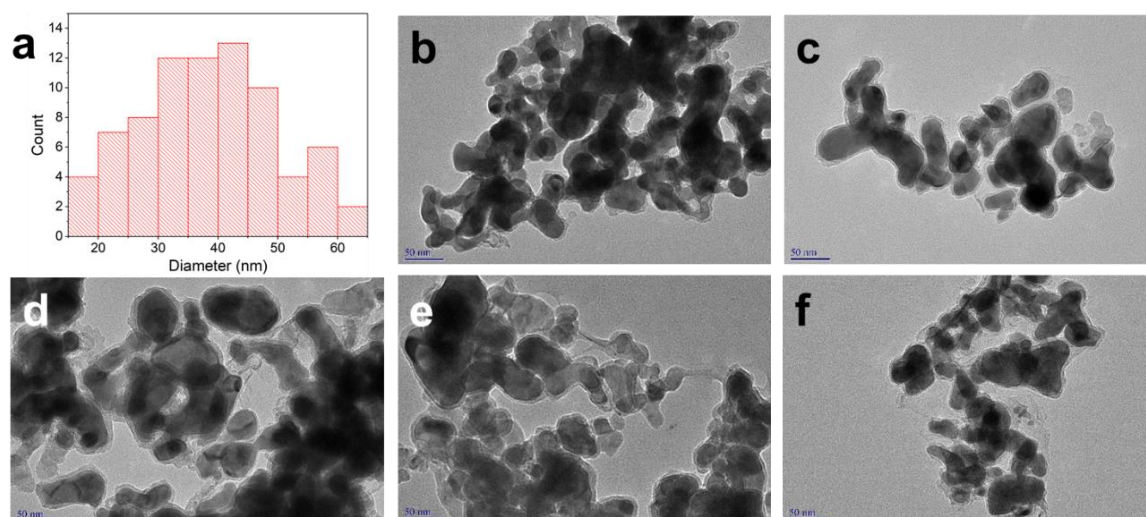


**Figure II-6** (a) Size distribution of NiFeSi-12. TEM images of (b) NiFeSi-50, (c) NiFeSi-12, (d) NiFeSi-3, (e) FeSi and (f) Ni<sub>2</sub>Si.

According to the overlapping of the Ni, Fe and Si scanning transmission electron microscopy (STEM)-EDX maps (**Figure II-3c**), a homogeneous NiFe silicide is formed. STEM-EDX maps (**Figure II-7**) also reveal that the oxide layer is rich in Si, in agreement with the elemental compositions determined by SEM-EDX (**Table II-3**), which indicate an excess of silicon compared to values expected from powder XRD (**Figure II-3d**). In addition, the Ni:Fe ratios of NiFe silicides are lower than the initial reagent ratio, which suggests loss of unreacted iron during washing, in agreement with the high reaction temperature needed to incorporate iron into silicides, as observed for FeSi (**Figure II-3d**).

**Table II-3** Elements atomic ratio of as-prepared Ni, Fe and NiFe silicide samples determined by SEM-EDX.

	Ni <sub>2</sub> Si	NiFeSi-50	NiFeSi-12	NiFeSi-3	FeSi
Ni	1.68	1.96	1.85	0.84	/
Fe	/	0.04	0.15	0.31	0.58
Si	1	1.17	1.74	1	1

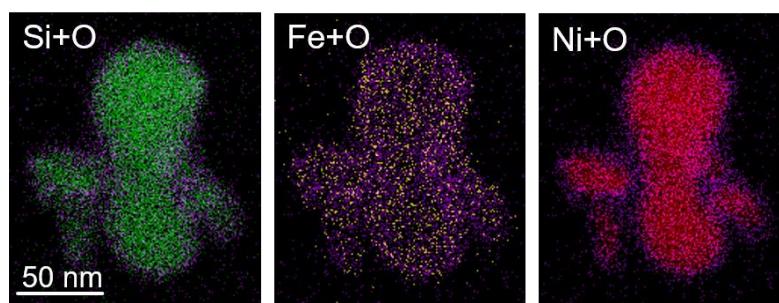


**Figure II-7** STEM-EDX mapping of the as-prepared NiFeSi-12 sample: superposition of oxygen and other elements. Si, Fe, Ni, O distributions are shown in green, yellow, red and purple, respectively.

According to powder XRD patterns (Figure II-3d), no remaining crystalline d-Si could be detected. For NiFeSi-50 and NiFeSi-12 samples, Ni<sub>2</sub>Si is obtained primarily as the orthorhombic phase with a small fraction of the hexagonal polymorph.<sup>46</sup> No iron-based phase is detected, thus confirming that Fe is present as a doping agent in Ni<sub>2</sub>Si. Upon increasing the Fe content above Ni:Fe = 3, a mixture of FeSi and Ni<sub>2</sub>Si crystal structures is formed. For the iron-only sample, FeSi is obtained as a pure crystalline phase.

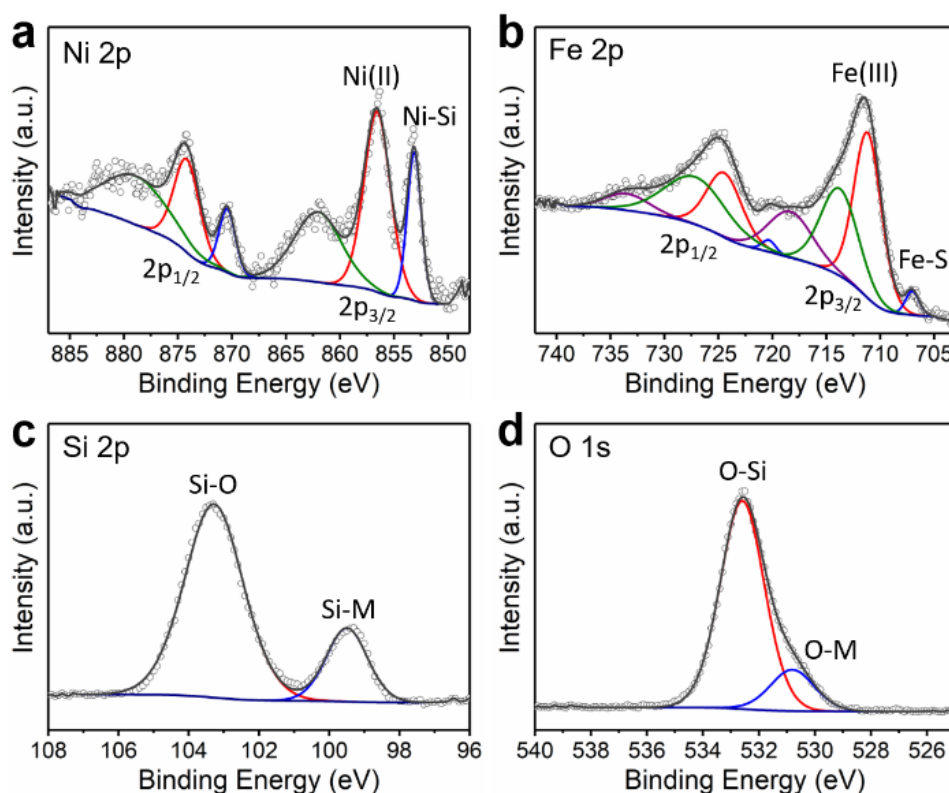


**Figure II-8** XPS of as-prepared NiFeSi-12 sample corresponding to Fe-doped Ni<sub>2</sub>Si: (a) Ni 2p region, (b) Fe 2p region, (c) Si 2p region, (d) O 1s region.

The chemical surface states of the NiFe silicides were analyzed by X-ray photoelectron spectroscopy (XPS) (**Figure II-8**). In the region of Ni 2p<sub>3/2</sub>, the peaks at 856.5 eV and 853.1 eV can be respectively ascribed to the surface oxidic Ni species and Ni-Si.<sup>29,47-49</sup> The latter only slightly shifts to higher binding energy compared to that of Ni, because the electronegativities of Ni ( $\chi_{\text{Ni}} = 1.91$ ) and Si ( $\chi_{\text{Si}} = 1.90$ ) are close.<sup>50</sup> Similarly, the Fe 2p<sub>3/2</sub> spectrum shows two oxidation states of Fe. The peak at 711.2 eV corresponds to surface Fe(III),<sup>51</sup> and the peak at 707.0 eV, which is slightly higher than that of metallic Fe, fits to Fe-Si ( $\chi_{\text{Fe}} = 1.83$ ).<sup>50,52,53</sup> In the Si 2p region, the peak at 103.3 eV can be assigned to silicate or SiO<sub>2</sub>, and the peak at 99.5 eV is characteristic of metal silicides.<sup>54,55</sup> Accordingly, the O 1s spectrum shows a peak at high binding energy 532.6 eV that can be attributed to oxidized silicon,<sup>47</sup> and a peak at 530.8 eV that is ascribed to oxidized metal.<sup>47,51</sup>

### II.3.2 Electrocatalytic properties

We then assessed the electrochemical properties of NiFe silicides. In order to avoid the fortuitous influence of *in situ* Fe deposition on the catalyst activity as well as on the durability in alkaline aqueous electrolytes,<sup>56,57</sup> we adopted a previously reported protocol to remove the Fe impurities in KOH solution by co-precipitation of Ni and Fe.<sup>56</sup> In this work, all electrochemical measurements were performed in iron-free 0.1 M KOH (see Experimental methods for details).

The electrocatalytic activity was investigated on rotating disk electrodes made of hybrid nanocrystals/Nafion films deposited on glassy carbon substrates. Although the electrocatalytic activity would be enhanced by using carbon or Ni foam substrates,<sup>58</sup> this configuration enables direct comparison of activities normalized *versus* the catalyst mass loading and electrode surface. With the as-prepared electrode, cyclic voltammograms (CVs) were recorded at 20 mV s<sup>-1</sup>. For all silicide samples, a reversible anodic wave appearing at lower potential than the water oxidation front is attributed to an oxidation of nickel species.<sup>56</sup> During activation (**Figure II-9**), the water oxidation current increases together with the Ni oxidation/reduction wave area, which indicates that more and more Ni are involved in this reversible redox reaction, so that the amount of high-valence Ni on the surface active for OER electrocatalysis increases. When the CVs reached a steady state, linear sweep voltammetry (LSV) was recorded at 10 mV s<sup>-1</sup> to probe the activated catalysts.

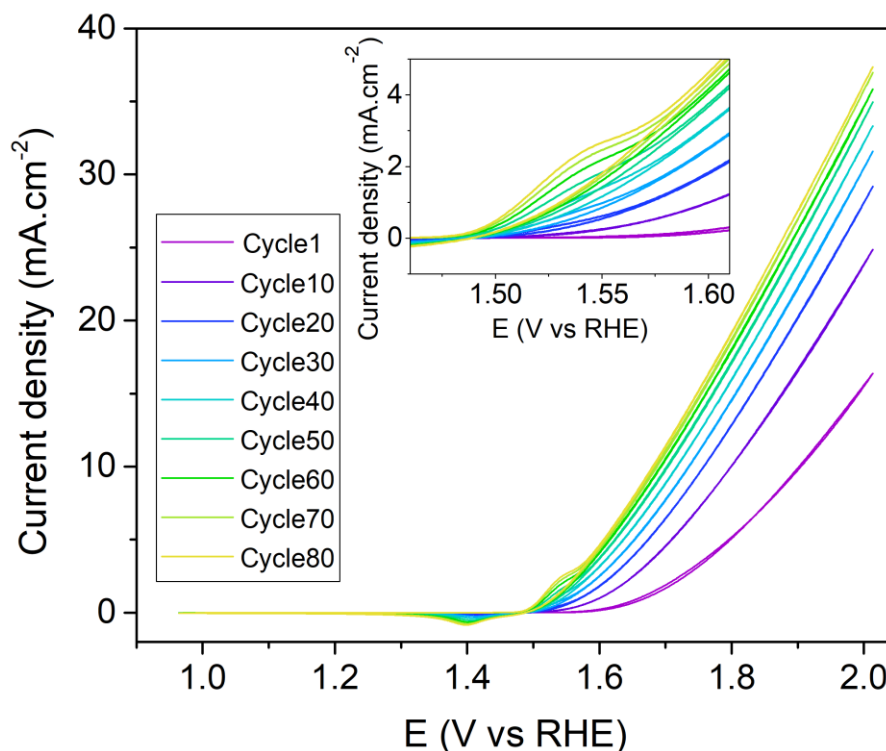


**Figure II-9** CVs showing the electrochemical activation of NiFeSi-12 by continuous potential cycling from 0.96 to 2.01 V vs. RHE at  $20 \text{ mV s}^{-1}$  in  $\text{O}_2$ -saturated 0.1 M KOH.

A comparison between metal silicide nanoparticles and reference commercial  $\text{IrO}_2$  nanoparticles is shown in **Figure II-10a**. The overpotentials at current density of  $10 \text{ mA cm}^{-2}$  in 0.1 M KOH of NiFeSi-50, NiFeSi-12 and NiFeSi-3 are respectively 337, 345 and 393 mV, *versus* 440 mV for commercial  $\text{IrO}_2$ . Hence, NiFe silicides are more active than binary silicides  $\text{Ni}_2\text{Si}$  and  $\text{FeSi}$ , and exhibit activities surpassing commercial  $\text{IrO}_2$ . The overpotentials are also low compared to previously reported NiFe-based catalysts (**Table II-5**) and to other silicides.<sup>29</sup> We observe an increase in the activity with the Ni content of the three NiFe silicide samples. The potential of the Ni oxidation wave increases from *ca.* 1.45 to above 1.5 V/RHE for  $\text{Ni}_2\text{Si}$  and NiFe silicides, respectively, while its area decreases from  $\text{Ni}_2\text{Si}$  to NiFe silicides, suggesting that the amount of oxidized Ni atoms is lower in NiFe silicides than in  $\text{Ni}_2\text{Si}$ . Both trends are in good agreement with previous work.<sup>56</sup>

The activity of NiFe silicide catalysts is confirmed by the Tafel slopes (**Figure II-10b**). NiFeSi-50 shows the lowest Tafel slope of  $63.8 \text{ mV dec}^{-1}$ . NiFeSi-12 and NiFeSi-3 also manifest smaller Tafel slopes than  $\text{IrO}_2$ , with 85.4, 75.3 and  $95.7 \text{ mV dec}^{-1}$ , respectively.

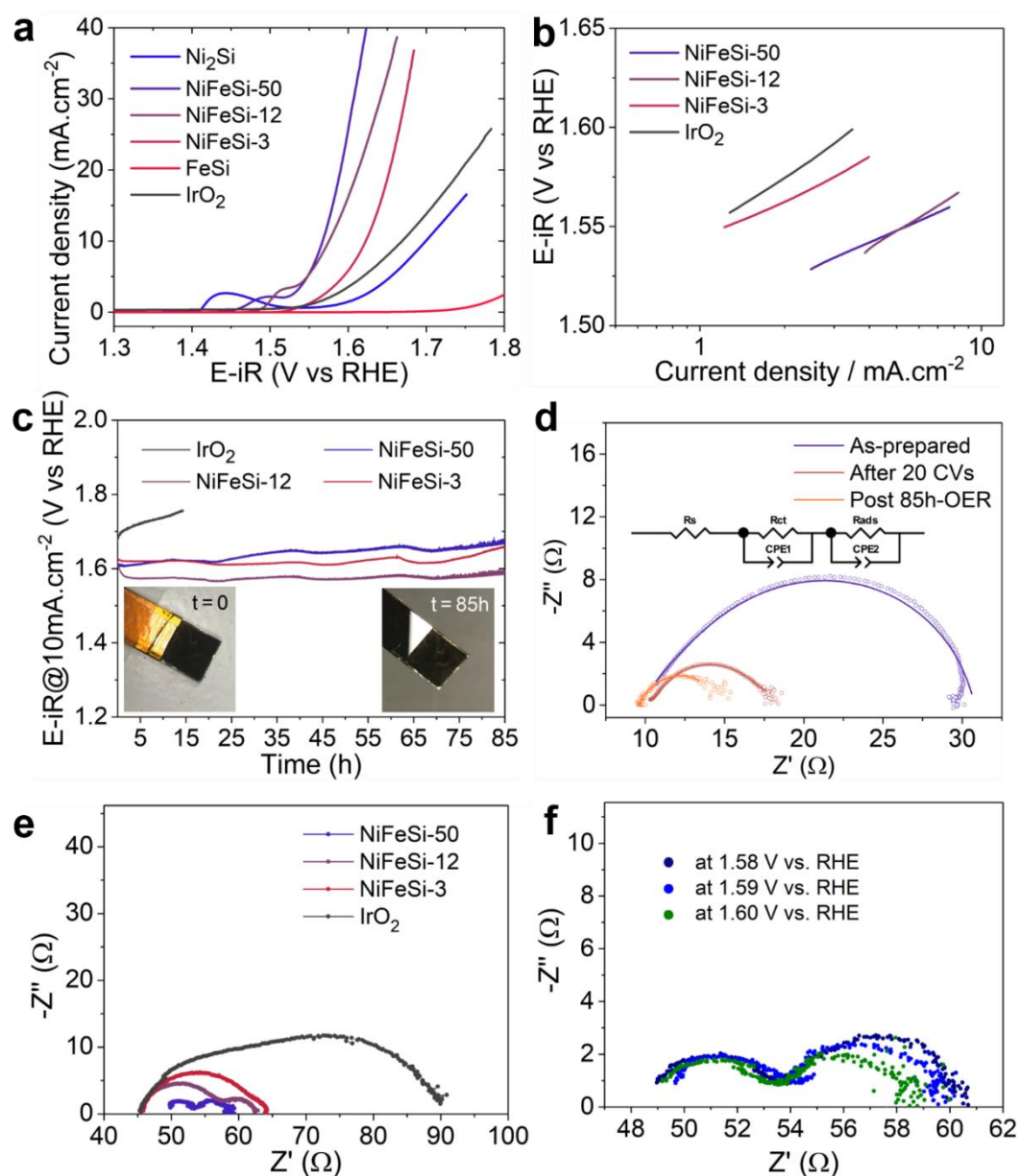


**Figure II-10** OER electrocatalytic properties of metal silicide nanocrystals. (a) LSV curves of the metal silicides nanoparticles and of reference commercial IrO<sub>2</sub> nanoparticles in an aqueous O<sub>2</sub>-saturated 0.1 M KOH electrolyte. (b) Tafel slopes and (c) Chronopotentiometry measurements at 10 mA cm<sup>-2</sup> for NiFe silicides and IrO<sub>2</sub>. Insets show photographs of a NiFeSi-12 working electrode with glassy carbon substrate before and after 85h (the conductive copper foil and insulating cover were removed) of OER. Nyquist plots: (d) recorded under 1.60 V vs. RHE and corresponding fits for NiFeSi-12 at different stages of the electrocatalytic process. The equivalent circuit is shown in the inset. (e) recorded under 1.60 V vs. RHE of metal silicide nanocrystals and reference commercial IrO<sub>2</sub> nanoparticles in O<sub>2</sub>-saturated 0.1 M KOH electrolyte. (f) EIS curves of NiFeSi-50 recorded at different potential from 50 000 to 1 Hz.

To evaluate the durability of the electrocatalytic activity of NiFe silicides, chronopotentiometry (CP) was carried out at 10 mA cm<sup>-2</sup> (**Figure II-10c**) after a pre-activation step by cycling the electrode for 20 times between 1.0 and 2.0 V vs. RHE. The reference IrO<sub>2</sub> used in this work was degraded in the first 15 h with a bias increment of *ca.* 85 mV, while the increments after 85 h for NiFeSi-50, NiFeSi-12 and NiFeSi-3 are *ca.* 55 mV, -35 mV and 25 mV, respectively. The most active NiFeSi-50 in LSV measurements shows the highest increment among three NiFe silicides. This degradation could be related to Fe-leaching during the OER, which would lead to a significant decrease in the Fe content for this sample containing originally the smallest amount of iron.<sup>5</sup> Indeed, Fe-leaching has been identified as the main origin of deactivation for NiFe-based OER electrocatalysts.<sup>56,57</sup> On the opposite, the negative increment for NiFeSi-12 shows self-activation in the first 5 h. The NiFeSi-12 properties after activation demonstrate a great durability in 0.1 M KOH at 10 mA cm<sup>-2</sup> for more than 85 h. The comparison of NiFe silicides with the reported NiFe-based catalysts further confirms this outstanding stability (**Table II-5**). Moreover, NiFeSi-12 exhibits higher activity and stability than previously reported for nickel silicide nanomaterials synthesized in molten salts.<sup>29</sup>

Electrochemical impedance spectroscopy (EIS) was then conducted to assess charge transport in the electrodes and at the electrode-electrolyte interfaces for silicide catalyst at different stages of activation process (**Figure II-10d**). An equivalent circuit with three main components of solution resistance ( $R_s$ ), charge transfer resistance ( $R_{ct}$ ) and mass transfer related to reaction intermediates adsorbed at the electrode surface ( $R_{ads}$ ) was used to fit the experimental curves.<sup>18,59</sup> As shown in **Table II-4**,  $R_{ct}$  decrease during activation, which could relate to the dissolution of the native Si-rich oxide layer. The decrease of  $R_{ads}$  indicates a more efficient adsorption/desorption process on the catalyst surface after activation.

**Table II-4** Comparison of  $R_{ct}$  and  $R_{ads}$  for electrodes (NiFeSi-12) at different stages of electrolysis.

Electrode	As-prepared	After 20 CVs	Post 85h-OER
$R_{ct}$ ( $\Omega$ )	6.17	5.34	5.23
$R_{ads}$ ( $\Omega$ )	14.9	6.87	0.11

EIS was later performed on activated silicides and IrO<sub>2</sub>. As shown in the Nyquist plot (**Figure II-10e**), the diameter of the semicircle in the high frequency region independent of the applied potential (**Figure II-10f**) represents  $R_{ct}$ . NiFeSi-50 exhibits the smallest  $R_{ct}$  (**Figure II-10e**).  $R_{ct}$  increases with the Fe content of NiFe silicide. This observation is consistent with the higher electrical conductivity of nickel silicides than of iron silicides.<sup>23,60</sup> The second semicircle in the low frequency region decreasing with the applied potential corresponds to  $R_{ads}$  (**Figure**

**II-10f).** From **Figure II-10e**, the  $R_{ads}$  values are very close for the three NiFe silicides, which indicates similar surface states for these materials during electrocatalysis. The low values  $R_{ct}+R_{ads}$  (**Figure II-10e**) highlight the low overall resistances of NiFe silicide catalysts.

**Table II-5** OER electrocatalytic activity and stability of previously reported NiFe-based catalysts in 0.1 M KOH on GC substrate.

Catalyst	Loading amount (mg cm <sup>-2</sup> )	Overpotential (mV) @10mA cm <sup>-2</sup>	Stability (h)	Tafel slope (mV dec <sup>-1</sup> )	Ref
NiFeSi-50	0.17	337	85	63.8	This work
NiFeSi-12	0.17	345	85	85.4	This work
NiFeSi-3	0.17	393	85	75.3	This work
nNiFe-LDH/NGF <sup>a)</sup>	0.25	337	3.3	45	61
Amorphous Ni <sub>70</sub> Fe <sub>30</sub> (OH) <sub>x</sub>	0.14	292	2	30.4	62
NiFe <sub>2</sub> O <sub>4</sub> /α-Ni(OH) <sub>2</sub> <sup>b)</sup>	~0.2	340	2.7	41	21
Ni <sub>3</sub> FeN	~0.13	355	3.3	70	12
Fe <sup>3+</sup> -doped β-Ni(OH) <sub>2</sub>	0.25	260	10	32	63
NiFe-N/C <sup>c)</sup>	0.4	320	2000 cycles	44.2	64
NiFe-NC <sup>d)</sup>	0.2	380	2.8	115	65
graphene/NiFe (oxy)hydroxides	0.25	372	2.2	76	66
Ni <sup>III</sup> Fe <sup>III</sup> @NC	0.29	397	12	81	67
NiFe-LDH NS <sup>e)</sup>	0.14	290	8	33.4	68
Porous NiFe Oxide	0.14	328	12	42	18
Ni <sub>2</sub> Co <sup>III</sup> Fe-LDH/N-GO <sup>f)</sup>	0.18	317	8.3	74.1	7
Ni <sub>3</sub> Fe/N-C	0.13	370	3.3	77	69
NiFe/C	0.5	330	21	57	70
m-NiFe/CN <sub>x</sub>	0.51	360	5.6	59.1	71
NiFe LDH/oGSH <sup>g)</sup>	0.25	350	2.8	54	17
NiFe LDH	0.1	360	2	51	72
NiFe@NC <sub>x</sub>	0.4	320	10	60.6	73

<sup>a)</sup> NGF: N-doped graphene framework, <sup>b)</sup> measured in 0.1M NaOH, <sup>c)</sup> MM'-N/C: bimetal-decorated, pyridinic N-dominated large-size carbon tubes, <sup>d)</sup> MM'-NC: MM' alloy and nitrogen-codoped porous carbon, <sup>e)</sup> NS: layered double hydroxide (LDH) nanosheets (NSs, ~ 1.3 nm), <sup>f)</sup> N-GO: nitrogen-doped graphene oxide, <sup>g)</sup> oGSHs: oxidized graphene/single-walled CNT hybrids.

### II.3.3 *Post mortem* studies

To elucidate the mechanisms at the origin of the high durability of the electrocatalytic performances of the NiFeSi-12 sample, the corresponding electrodes were analyzed after operation at 10 mA cm<sup>-2</sup> for different durations. SEM images (**Figure II-11a-c**) show a roughening of the electrode surface. The XRD diagram of the post-OER electrode subjected 10 h to OER at 10 mA cm<sup>-2</sup> (**Figure II-11d**) suggests that the main crystalline phase remains Ni<sub>2-x</sub>Fe<sub>x</sub>Si, although the low signal-to-background ratio due to low amounts of material does not enable identifying minor phases. Then, the elemental distribution was analyzed by STEM-EDX. The chemical maps (**Figure II-11e** and **Figure II-12a-c**) show that the outer oxidic layer of the particles is poor in Si and rich in Ni and Fe, which could be explained by the formation of a NiFe (oxy)hydroxide/oxide at the surface of the particles during OER. This is consistent with the self-activation step observed **Figure II-9**, *i.e.*, the catalyst activation corresponds to the building of a NiFe (oxy)hydroxide/oxide layer. This observation is also in agreement with the previously reported formation of an electrocatalytically active amorphous or crystalline NiFe (oxy)hydroxide/oxide layer at the surface of NiFe borides, phosphides, nitrides and sulfides.<sup>9,14</sup>

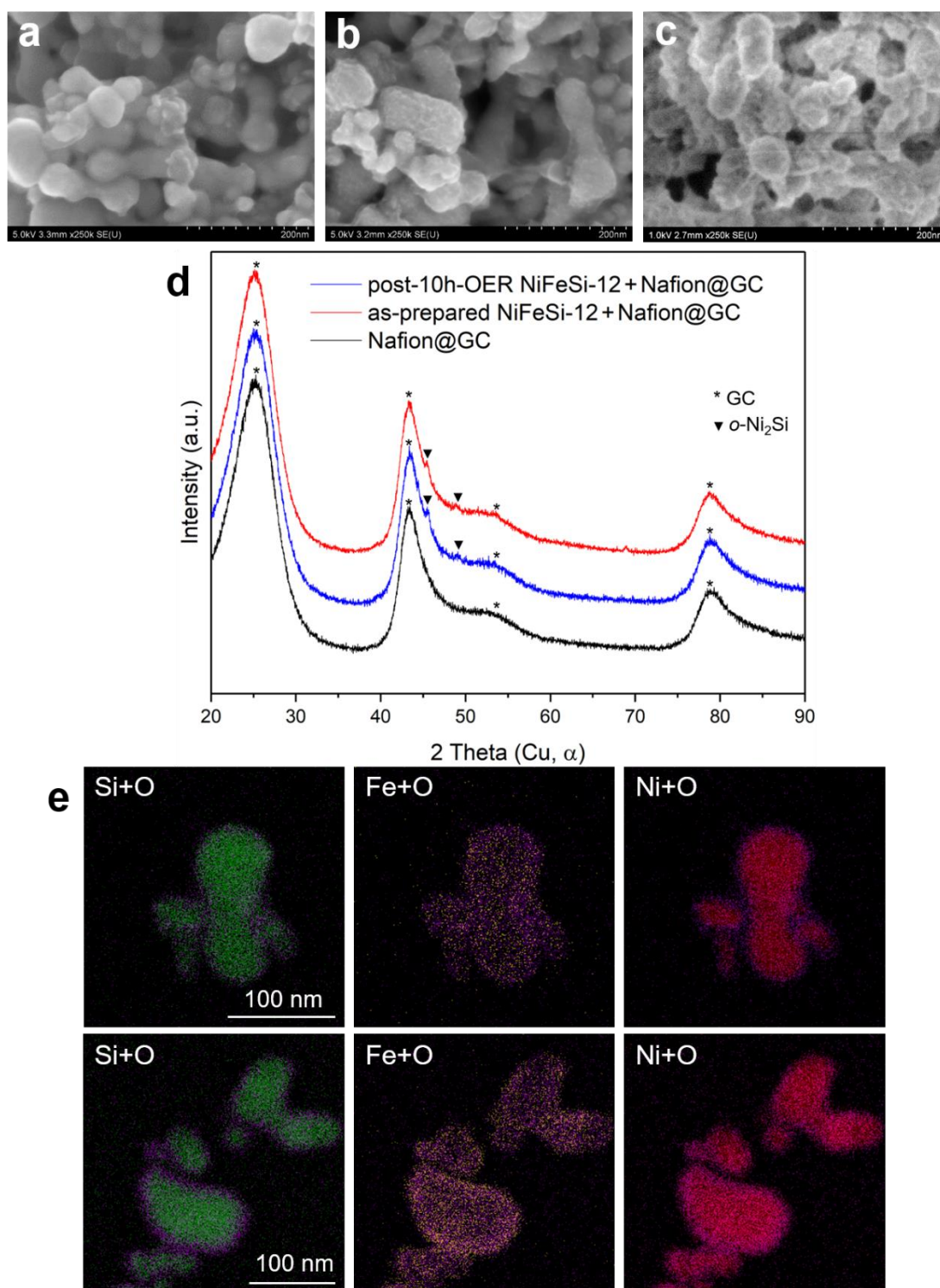


**Figure II-11** SEM images of a working electrode made of NiFeSi-12 nanoparticles deposited on a GC substrate (a) before electrochemical study, (b) post 10 h OER, and (c) post 85 h OER. (d) XRD patterns of a NiFeSi-12/glassy carbon electrode as-prepared and *post mortem* after 10 h of OER at 10 mA cm<sup>-2</sup>. The pattern of a blank electrode without catalyst is shown as reference. (e) comparison of oxide layer content of pristine sample (top) and post 85 h OER sample (bottom).

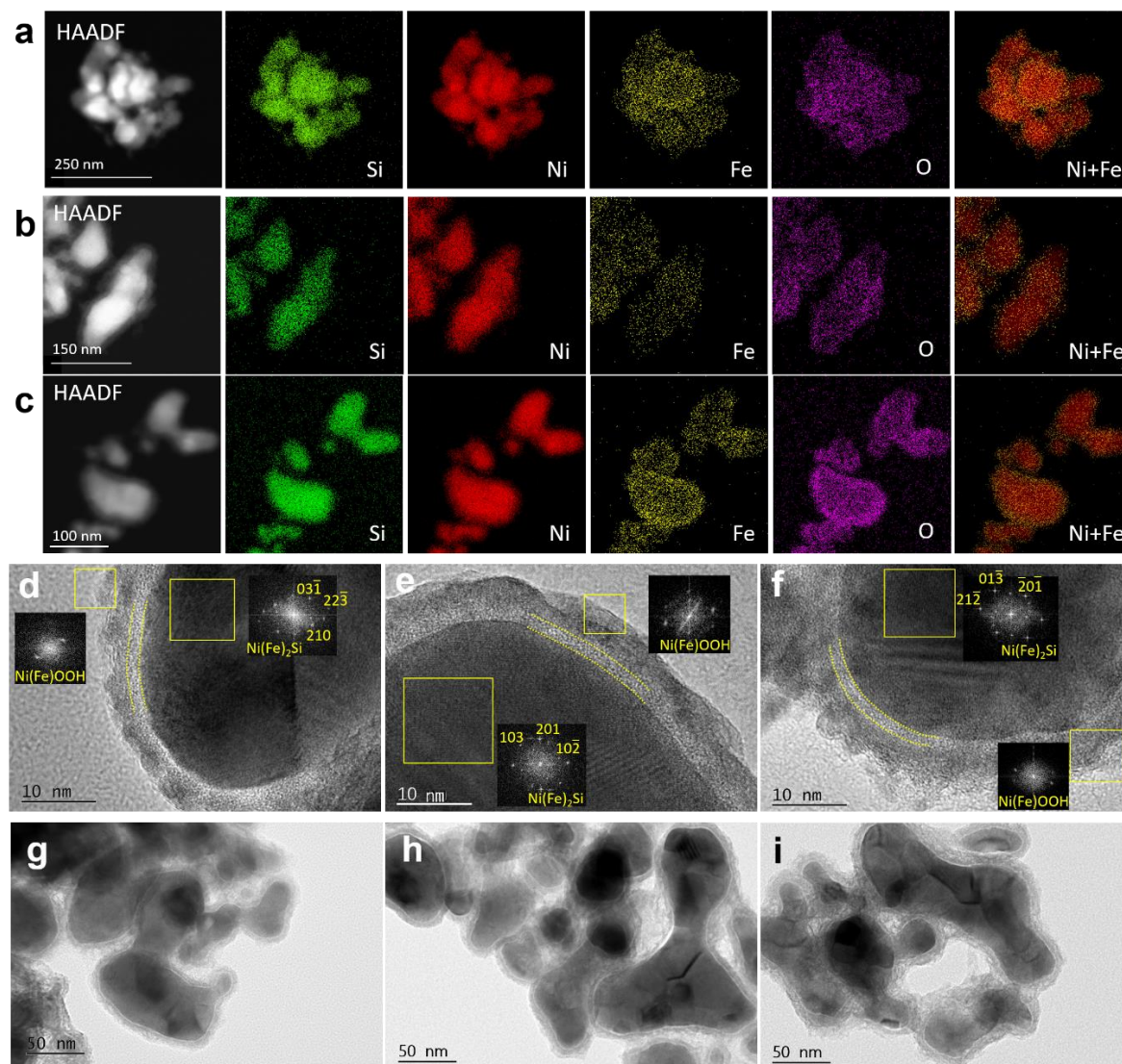


**Figure II-12** STEM-HAADF and STEM-EDX chemical mapping of NiFeSi-12 catalyst: (a) post 10 h OER, (b) post 65 h OER, (c) post 85 h OER. HRTEM images and corresponding FFTs (insets) of NiFeSi-12 catalyst (d) post 10 h OER, (e) post 65 h OER, (f) post 85 h OER. TEM images of NiFeSi-12 catalyst (g) post 10 h OER, (h) post 65 h OER, (i) post 85 h OER at 10 mA cm<sup>-2</sup>.

Further information on the nanostructure of the catalysts was then sought by HRTEM (**Figure II-12d-f**). Surprisingly, the post-OER material exhibits a triple component, core-shell-shell structure. HRTEM images and the corresponding Fast Fourier Transforms (FFT) of core areas are fully indexed along the o-Ni<sub>2</sub>Si structure, confirming that the silicide is maintained as the main component of the material. An intermediate layer does not show any crystalline feature and is then ascribed to an amorphous phase. The outer layer exhibits many ~5 nm areas with a 2.1 Å lattice distance that could be attributed to the (105) reflection of NiOOH.<sup>14</sup> The outer shell

then consists of Fe-doped NiOOH nanodomains. The interface between the non-oxidic core and the oxidized shell remains clear after 85 h of OER. This confirms the stability of the nanostructure once the activation has occurred, although TEM images (**Figure II-12d-i**) indicate that the outer oxyhydroxide shell grew thicker and rougher during OER, while the intermediate layer barely changed in thickness. The apparent thickening of the outer hydroxide layer while the core and the intermediate layer dimensions remain steady requires a dedicated discussion. First, the increased roughness of the outer shell is consistent with the growth of nanocrystalline domains of layered NiFe oxyhydroxide. This increase in roughness yields a decrease in overall density of this shell. Second, NiFe oxyhydroxides exhibit a lower crystallographic density ( $\sim 4.6 \text{ g cm}^{-3}$ ) than nickel silicide Ni<sub>2</sub>Si ( $7.3 \text{ g cm}^{-3}$ ). Both features indicate that the density of the outer nanocrystalline NiFe oxyhydroxide shell is much lower than the nickel silicide core. Therefore, constructing the outer shell requires only small amounts of Ni and Fe from the core and then hardly impacts the size of the core. Once the outer shell is formed and crystallized, we discuss below the ability of the material to reach a steady state where further corrosion of the core is impeded by the intermediate component acting as a passivating layer.

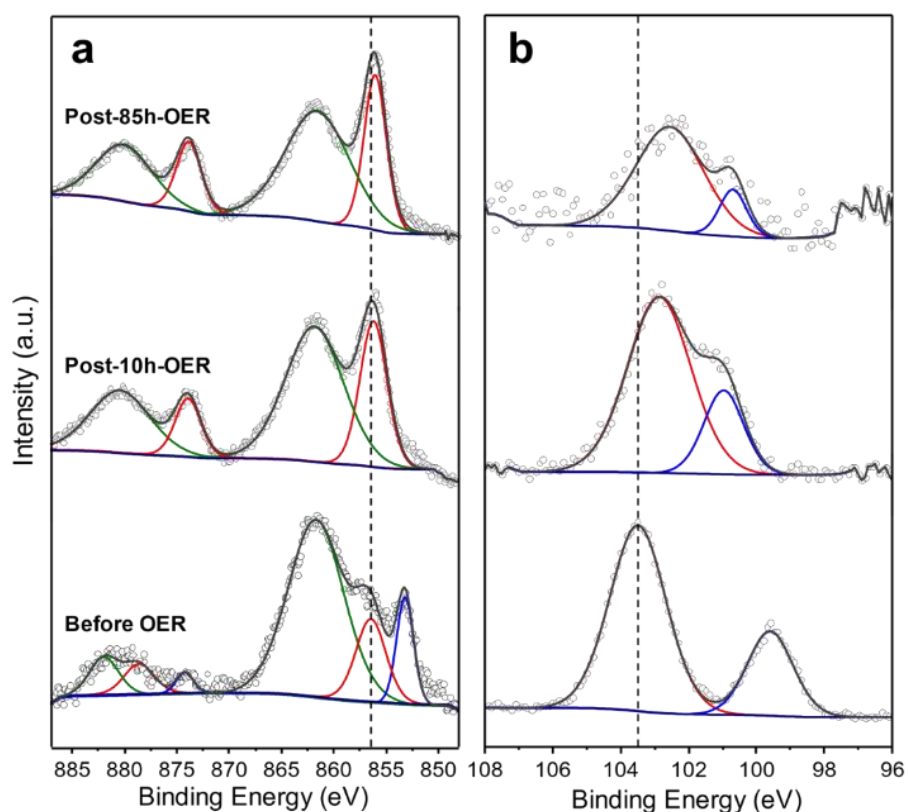


**Figure II-13** XPS of a NiFeSi-12 working electrode before OER, post 10h OER and post 85h OER in (a) Ni 2p and (b) Si 2p regions.

To further understand the nature of the outer shell and of the intermediate layer, the surface chemical bonding was analyzed by XPS for a NiFeSi-12 working electrode as-prepared and *post mortem*, after 10 h and 85 h of OER operation. The Ni 2p spectrum of the as-prepared electrode (**Figure II-13a**) exhibits two peaks at 853.1 eV and 856.4 eV ascribed to Ni silicide and nickel silicate, respectively.<sup>47-49</sup> Accordingly, the Si 2p region (**Figure II-13b**) shows two peaks located at 99.6 eV and 103.5 eV attributed to silicides and oxidized silicon, respectively.<sup>47-49</sup> Thus, the surface chemical states of the as-synthesized powder is maintained after processing of the electrode. Beyond 10h of OER operation, no low oxidation state Ni and Si species could be detected contrary to the detection of silicides by TEM (**Figure II-12**). This discrepancy shows that the silicide core is out of the detection depth of XPS due to the growth of a Si-free NiFe (oxy)hydroxide shell. After 85h of OER operation, the oxidic Ni peak slightly shifted to 856.0 eV. This could be explained by the chemical evolution from silicate to NiFe (oxy)hydroxide in the outer layer.<sup>74</sup> This is further confirmed by the decrease of the Si signal in the Si 2p region, highlighted by a decrease in the signal-to-noise ratio. STEM-EDX maps (**Figure II-12**) and line profiles across the outer and intermediate layers (**Figure II-14**) indicate that the outer layer is mostly made of Ni and O, in agreement with XPS. From the outside of the particles to the inside, the line profiles also show an intermediate area containing Si and O besides Ni and Fe, and where the Si signal is maintained at low, but not negligible values. This observation is consistent with the attribution of the oxidic Si species detected by XPS to the amorphous intermediate layer, which then consists of metal oxide and silicates.

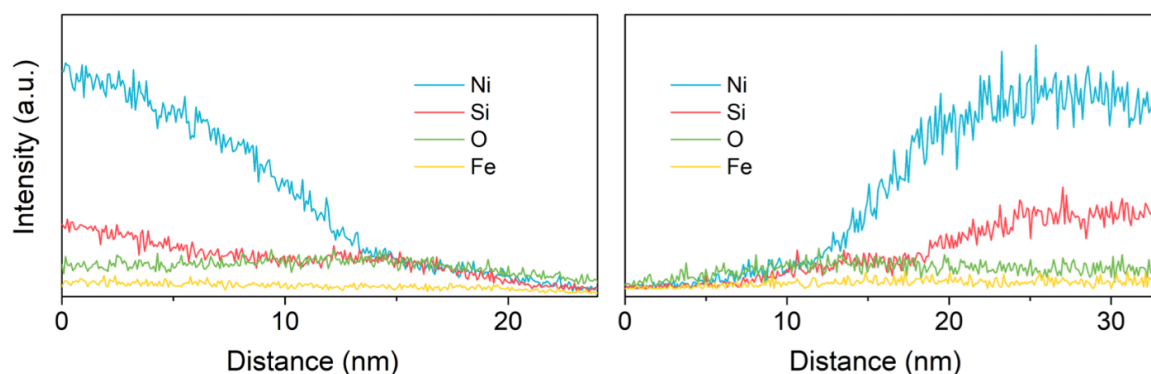


**Figure II-14** STEM-EDX line profile mapping of two NiFeSi-12 particles post 85 h OER at 10 mA cm<sup>-2</sup>.

The overall composition of post-OER catalyst samples was also determined by SEM-EDX (**Table II-6**). The Ni:Fe ratio does not change, while a loss of Si can be detected in the first 65 h. Nonetheless, the overall composition stabilizes after 65 h, with a (Ni+Fe)/Si ratio of 2.6, in agreement with a maintained (Ni<sub>1-x</sub>Fe<sub>x</sub>)<sub>2</sub>Si core and an outer Si-free shell of nickel iron

(oxy)hydroxide. This is consistent with partial dissolution of SiO<sub>2</sub> or silicates<sup>75</sup> in 0.1 M KOH in the first 65 h. Because the composition of the electrode material does not evolve after 65h and the conductive silicide core is maintained, the amorphous ~1.5 nm-thick intermediate layer observed by TEM (**Figure II-12b-d**) should play a role in passivating the silicide core and protecting it from oxidation and silicon leaching. XPS (**Figure II-13**) shows that this intermediate shell contains metal oxide, silicate and/or silicon oxide. This passivation layer generated in anodic and basic conditions can protect the silicide core from further dissolution.<sup>76</sup> TEM (**Figure II-12b-d**) also indicates that this shell is denser than the outer Fe-doped NiOOH shell, which implies further reactivity with water to form the outer oxyhydroxide shell. The intermediate layer is buried below this outer shell and is then not in contact with water. Overall, these reactivity considerations support the interpretation that this intermediate layer is a mixture of amorphous nickel oxide and silicates that may be doped with iron.

**Table II-6** Elemental composition determined by SEM-EDX of a pristine NiFeSi-12 sample and of corresponding post mortem electrode materials after 65 and 85 h of OER operation.

	<b>Pristine</b>	<b>Post 65h-OER</b>	<b>Post 85h-OER</b>
Ni	1.85	1.85	1.85
Fe	0.15	0.12	0.11
Si	1.74	0.77	0.76

## II.4 Conclusion

We synthesized FeSi, Ni<sub>2</sub>Si and NiFe silicide nanocrystals through a redox reaction between silicon nanoparticles and metal chlorides by designing a strategy to fasten and bring this reaction to completion hundreds of degrees below the usual temperature of the solid-state reaction between bulk reagents: the high reactivity of silicon nanoparticles was combined with two specific features of molten salts, namely their ability to operate as liquid media at 300-400 °C and their low vapor pressure that enables running reactions under dynamic vacuum to shift equilibria. This synthesis strategy delivers a pathway to a wide range of nanomaterials.

The resulting NiFe silicide nanoparticles delivered high activity for OER electrocatalysis, with an activity stable for at least 85h of continuous electrolysis at 10 mA cm<sup>-2</sup>. These high performances arise from the NiFe silicide nanocrystals acting as pre-catalysts, forming upon silicon leaching an electrocatalytically active crystalline Fe-doped NiOOH shell. The resulting nanostructures are however highly stable because of a dense oxidic intermediate layer containing metal and silicon that avoids contact of the silicide core with the electrolyte. Therefore, the

metallic core can play its role of enhancing charge transfer within the electrode. This *in situ* evolution of nickel iron silicides towards core-shell-shell nanostructures with a passivating intermediate layer has not been observed yet for other metal-p block element compounds, including nickel silicides formed in molten salts. Therefore, this original behavior shows the ability to design hierarchically structured electrocatalysts built from Earth abundant elements.

## References

- (1) Zhao, J.; Zhang, J. J.; Li, Z. Y.; Bu, X. H. Recent Progress on NiFe-Based Electrocatalysts for the Oxygen Evolution Reaction. *Small* **2020**, *16* (51), 1–23.
- (2) Mohammed-Ibrahim, J. A Review on NiFe-Based Electrocatalysts for Efficient Alkaline Oxygen Evolution Reaction. *J. Power Sources* **2020**, *448*, 227375.
- (3) Wang, Y.; Yan, D.; El Hankari, S.; Zou, Y.; Wang, S. Recent Progress on Layered Double Hydroxides and Their Derivatives for Electrocatalytic Water Splitting. *Adv. Sci.* **2018**, *5* (8), 1800064.
- (4) Xu, M.; Wei, M. Layered Double Hydroxide-Based Catalysts: Recent Advances in Preparation, Structure, and Applications. *Adv. Funct. Mater.* **2018**, *28* (47), 1–20.
- (5) Feng, C.; Faheem, M. B.; Fu, J.; Xiao, Y.; Li, C.; Li, Y. Fe-Based Electrocatalysts for Oxygen Evolution Reaction: Progress and Perspectives. *ACS Catal.* **2020**, *10* (7), 4019–4047.
- (6) Ma, W.; Ma, R.; Wang, C.; Liang, J.; Liu, X.; Zhou, K.; Sasaki, T. A Superlattice of Alternately Stacked Ni-Fe Hydroxide Nanosheets and Graphene for Efficient Splitting of Water. *ACS Nano* **2015**, *9* (2), 1977–1984.
- (7) Zhou, D.; Cai, Z.; Lei, X.; Tian, W.; Bi, Y.; Jia, Y.; Han, N.; Gao, T.; Zhang, Q.; Kuang, Y.; Pan, J.; Sun, X.; Duan, X. NiCoFe-Layered Double Hydroxides/N-Doped Graphene Oxide Array Colloid Composite as an Efficient Bifunctional Catalyst for Oxygen Electrocatalytic Reactions. *Adv. Energy Mater.* **2018**, *8* (9), 1701905.
- (8) Joo, T.; Hu, L.; Hong, B. K.; Oh, J. G.; Litster, S. On the Origin of Deactivation of Reversal-Tolerant Fuel Cell Anodes under Voltage Reversal Conditions. *J. Power Sources* **2020**, *472*, 228439.
- (9) Hong, W.; Sun, S.; Kong, Y.; Hu, Y.; Chen, G. Ni<sub>x</sub>Fe<sub>1-x</sub>B Nanoparticle Self-Modified Nanosheets as Efficient Bifunctional Electrocatalysts for Water Splitting: Experiments and Theories. *J. Mater. Chem. A* **2020**, *8* (15), 7360–7367.
- (10) An, L.; Sun, Y.; Zong, Y.; Liu, Q.; Guo, J.; Zhang, X. Nickel Iron Boride Nanosheets on rGO for Active Electrochemical Water Oxidation. *J. Solid State Chem.* **2018**, *265* (May), 135–139.
- (11) Li, P.; Zeng, H. C. Bimetallic Ni-Fe Phosphide Nanocomposites with a Controlled Architecture and Composition Enabling Highly Efficient Electrochemical Water Oxidation. *J. Mater. Chem. A* **2018**, *6* (5), 2231–2238.

- (12) Fu, G.; Cui, Z.; Chen, Y.; Xu, L.; Tang, Y.; Goodenough, J. B. Hierarchically Mesoporous Nickel-Iron Nitride as a Cost-Efficient and Highly Durable Electrocatalyst for Zn-Air Battery. *Nano Energy* **2017**, *39*, 77–85.
- (13) Chen, W.; Wang, H.; Li, Y.; Liu, Y.; Sun, J.; Lee, S.; Lee, J. S.; Cui, Y. *In situ* Electrochemical Oxidation Tuning of Transition Metal Disulfides to Oxides for Enhanced Water Oxidation. *ACS Cent. Sci.* **2015**, *1* (5), 244–251.
- (14) Zhou, M.; Weng, Q.; Zhang, X.; Wang, X.; Xue, Y.; Zeng, X.; Bando, Y.; Golberg, D. *In situ* Electrochemical Formation of Core-Shell Nickel-Iron Disulfide and Oxyhydroxide Heterostructured Catalysts for a Stable Oxygen Evolution Reaction and the Associated Mechanisms. *J. Mater. Chem. A* **2017**, *5* (9), 4335–4342.
- (15) Xu, X.; Song, F.; Hu, X. A Nickel Iron Diselenide-Derived Efficient Oxygen-Evolution Catalyst. *Nat. Commun.* **2016**, *7*, 1–7.
- (16) Li, Y.; Zhang, H.; Jiang, M.; Zhang, Q.; He, P.; Sun, X. 3D Self-Supported Fe-Doped Ni<sub>2</sub>P Nanosheet Arrays as Bifunctional Catalysts for Overall Water Splitting. *Adv. Funct. Mater.* **2017**, *27* (37), 1–8.
- (17) Zhu, X.; Tang, C.; Wang, H. F.; Zhang, Q.; Yang, C.; Wei, F. Dual-Sized NiFe Layered Double Hydroxides *in situ* Grown on Oxygen-Decorated Self-Dispersal Nanocarbon as Enhanced Water Oxidation Catalysts. *J. Mater. Chem. A* **2015**, *3* (48), 24540–24546.
- (18) Qi, J.; Zhang, W.; Xiang, R.; Liu, K.; Wang, H. Y.; Chen, M.; Han, Y.; Cao, R. Porous Nickel–Iron Oxide as a Highly Efficient Electrocatalyst for Oxygen Evolution Reaction. *Adv. Sci.* **2015**, *2* (10), 1–8.
- (19) Qian, Y.; An, T.; Sarnello, E.; Liu, Z.; Li, T.; Zhao, D. Janus Electrocatalysts Containing MOF-Derived Carbon Networks and NiFe-LDH Nanoplates for Rechargeable Zinc-Air Batteries. *ACS Appl. Energy Mater.* **2019**, *2* (3), 1784–1792.
- (20) Wang, W.; Liu, Y.; Li, J.; Luo, J.; Fu, L.; Chen, S. NiFe LDH Nanodots Anchored on 3D Macro/Mesoporous Carbon as a High-Performance ORR/OER Bifunctional Electrocatalyst. *J. Mater. Chem. A* **2018**, *6* (29), 14299–14306.
- (21) Chen, H.; Yan, J.; Wu, H.; Zhang, Y.; Liu, S. One-Pot Fabrication of NiFe<sub>2</sub>O<sub>4</sub> Nanoparticles on  $\alpha$ -Ni(OH)<sub>2</sub> Nanosheet for Enhanced Water Oxidation. *J. Power Sources* **2016**, *324*, 499–508.
- (22) Meyer, B.; Gottlieb, U.; Laborde, O.; Yang, H.; Lasjaunias, J. C.; Sulpice, A.; Madar, R.

Intrinsic Properties of NiSi. *J. Alloys Compd.* **1997**, 262–263, 235–237.

(23) E. G. Colgan, M. Maenp, M. Finetti, M.-A. N. Electrical Characteristics of Thin Ni<sub>2</sub>Si, NiSi, and NiSi<sub>2</sub> Layers Grown on Silicon. *J. Chem. Inf. Model.* **1982**, 53 (9), 1689–1699.

(24) Chiu, W. L.; Chiu, C. H.; Chen, J. Y.; Huang, C. W.; Huang, Y. T.; Lu, K. C.; Hsin, C. L.; Yeh, P. H.; Wu, W. W. Single-Crystalline  $\delta$ -Ni<sub>2</sub>Si Nanowires with Excellent Physical Properties. *Nanoscale Res. Lett.* **2013**, 8 (1), 1–5.

(25) Schmitt, A. L.; Higgins, J. M.; Szczech, J. R.; Jin, S. Synthesis and Applications of Metal Silicide Nanowires. *J. Mater. Chem.* **2010**, 20 (2), 223–235.

(26) Agarwal, S.; Ganesan, V.; Tyagi, A. K.; Jain, I. P. Effect of Annealing on Magnetic Properties and Silicide Formation at Co/Si Interface. *Bull. Mater. Sci.* **2006**, 29 (6), 647–651.

(27) Lin, J. Y.; Hsu, H. M.; Lu, K. C. Growth of Single-Crystalline Nickel Silicide Nanowires with Excellent Physical Properties. *CrystEngComm* **2015**, 17 (9), 1911–1916.

(28) Mccanney, J. M.; Schaak, R. E. Solution Synthesis of Metal Silicide Nanoparticles. *Inorg. Chem.* **2015**, 54 (3), 707–709.

(29) Kumar, R.; Bahri, M.; Song, Y.; Gonell, F.; Thomas, C.; Ersen, O.; Sanchez, C.; Laberty-Robert, C.; Portehault, D. Phase Selective Synthesis of Nickel Silicide Nanocrystals in Molten Salts for Electrocatalysis of the Oxygen Evolution Reaction. *Nanoscale* **2020**, 12 (28), 15209–15213.

(30) Chen, X.; Wang, J.; Yang, K.; Meng, C.; Williams, C. T.; Liang, C. Structure Investigation and Dibenzothiophene Hydrodesulfurization Properties of Fe-Substituted Ni-Si Intermetallics. *J. Phys. Chem. C* **2015**, 119 (52), 29052–29061.

(31) Buonsanti, R.; Loiudice, A.; Mantella, V. Colloidal Nanocrystals as Precursors and Intermediates in Solid State Reactions for Multinary Oxide Nanomaterials. *Acc. Chem. Res.* **2021**, 54 (4), 754–764.

(32) Manna, L.; Cheon, J.; Schaak, R. E. Why Do We Care about Studying Transformations in Inorganic Nanocrystals? *Acc. Chem. Res.* **2021**, 54 (7), 1543–1544.

(33) Saruyama, M.; Sato, R.; Teranishi, T. Transformations of Ionic Nanocrystals via Full and Partial Ion Exchange Reactions. *Acc. Chem. Res.* **2021**, 54 (4), 765–775.

(34) Schaak, R. E.; Steimle, B. C.; Fenton, J. L. Made-to-Order Heterostructured Nanoparticle Libraries. *Acc. Chem. Res.* **2020**.

- (35) Toso, S.; Baranov, D.; Manna, L. Metamorphoses of Cesium Lead Halide Nanocrystals. *Acc. Chem. Res.* **2021**, *54* (3), 498–508.
- (36) Portehault, D.; Delacroix, S.; Gouget, G.; Grosjean, R.; Chan-Chang, T. H. C. Beyond the Compositional Threshold of Nanoparticle-Based Materials. *Acc. Chem. Res.* **2018**, *51* (4), 930–939.
- (37) Gupta, S. K.; Mao, Y. Recent Developments on Molten Salt Synthesis of Inorganic Nanomaterials: A Review. *J. Phys. Chem. C* **2021**.
- (38) Trotochaud, L.; Young, S. L.; Ranney, J. K.; Boettcher, S. W. Nickel-Iron Oxyhydroxide Oxygen-Evolution Electrocatalysts: The Role of Intentional and Incidental Iron Incorporation. *J. Am. Chem. Soc.* **2014**, *136* (18), 6744–6753.
- (39) Seo, K.; Varadwaj, K. S. K.; Mohanty, P.; Lee, S.; Jo, Y.; Jung, M. H.; Kim, J.; Kim, B. Magnetic Properties of Single-Crystalline CoSi Nanowires. *Nano Lett.* **2007**, *7* (5), 1240–1245.
- (40) Dahal, N.; Chikan, V. Phase-Controlled Synthesis of Iron Silicide (Fe<sub>3</sub>Si and FeSi<sub>2</sub>) Nanoparticles in Solution. *Chem. Mater.* **2010**, *22* (9), 2892–2897.
- (41) Ouyang, L.; Thrall, E. S.; Deshmukh, M. M.; Park, H. Vapor-Phase Synthesis and Characterization of ε-FeSi Nanowires. *Adv. Mater.* **2006**, *18* (11), 1437–1440.
- (42) Chen, X.; Liang, C. Transition Metal Silicides: Fundamentals, Preparation and Catalytic Applications. *Catal. Sci. Technol.* **2019**, *9* (18), 4785–4820.
- (43) Godfroy, M.; Russel, A.; Mercier, F.; Granier, M.; Jarrosson, T.; Niebel, C.; Serein Spirau, F.; Viennois, R.; Beaudhuin, M. Nanocrystalline Chromium Disilicide Synthesized by a Fast Chlorine-Transfer-Reaction. *Mater. Lett.* **2019**, *247*, 7–10.
- (44) Hsu, H. F.; Tsai, P. C.; Lu, K. C. Single-Crystalline Chromium Silicide Nanowires and Their Physical Properties. *Nanoscale Res. Lett.* **2015**, *10* (1), 4–11.
- (45) Collins, W. Silicon Compounds, Silicon Halides. *Kirk - Othmer Encycl. Chem. Technol.* **2000**.
- (46) TDnucl - Thermodata Nuclear Phase Diagrams. Ni-Si  
[https://www.crct.polymtl.ca/fact/phase\\_diagram.php?file=Ni-Si.jpg&dir=TDnucl](https://www.crct.polymtl.ca/fact/phase_diagram.php?file=Ni-Si.jpg&dir=TDnucl).
- (47) Shalvoy, R. B.; Reucroft, P. J.; Davis, B. H. Characterization of Coprecipitated Nickel on Silica Methanation Catalysts by X-Ray Photoelectron Spectroscopy. *J. Catal.* **1979**, *56* (3), 336–348.
- (48) Cao, Y.; Nyborg, L.; Jelvestam, U. XPS Calibration Study of Thin-Film Nickel Silicides.

*Surf. Interface Anal.* **2009**, *41* (6), 471–483.

(49) Lorenz, P.; Finster, J.; Wendt, G.; Salyn, J. V.; Žumadilov, E. K.; Nefedov, V. I. Esca Investigations of Some NiO/SiO<sub>2</sub> and NiO-Al<sub>2</sub>O<sub>3</sub>/SiO<sub>2</sub> Catalysts. *J. Electron Spectros. Relat. Phenomena* **1979**, *16* (3), 267–276.

(50) Dayah, M. Ptable <https://ptable.com>.

(51) Graat, P. C. J.; Somers, M. A. J. Simultaneous Determination of Composition and Thickness of Thin Iron-Oxide Films from XPS Fe 2p Spectra. *Appl. Surf. Sci.* **1996**, *100–101*, 36–40.

(52) Tam, P. L.; Cao, Y.; Nyborg, L. XRD and XPS Characterisation of Transition Metal Silicide Thin Films. *Surf. Sci.* **2012**, *606* (3–4), 329–336.

(53) Zhang, K.; Brötzmann, M.; Hofsäss, H. Sharp Transition from Ripple Patterns to a Flat Surface for Ion Beam Erosion of Si with Simultaneous Co-Deposition of Iron. *AIP Adv.* **2012**, *2* (3), 032123.

(54) Masa, J.; Piontek, S.; Wilde, P.; Antoni, H.; Eckhard, T.; Chen, Y. T.; Muhler, M.; Apfel, U. P.; Schuhmann, W. Ni-Metalloid (B, Si, P, As, and Te) Alloys as Water Oxidation Electrocatalysts. *Adv. Energy Mater.* **2019**, *9* (26), 1–8.

(55) Junge, H.; Beller, M.; Agapova, A.; Ryabchuk, P.; Lund, H.; Junge, K.; Agostini, G.; Pohl, M.-M. Intermetallic Nickel Silicide Nanocatalyst—A Non-Noble Metal-Based General Hydrogenation Catalyst. *Sci. Adv.* **2018**, *4* (6), eaat0761.

(56) Trotochaud, L.; Young, S. L.; Ranney, J. K.; Boettcher, S. W. Nickel-Iron Oxyhydroxide Oxygen-Evolution Electrocatalysts: The Role of Intentional and Incidental Iron Incorporation. *J. Am. Chem. Soc.* **2014**, *136* (18), 6744–6753.

(57) Farhat, R.; Dhainy, J.; Halaoui, L. I. Oer Catalysis at Activated and Codeposited Nife-Oxo/Hydroxide Thin Films Is Due to Postdeposition Surface-Fe and Is Not Sustainable without Fe in Solution. *ACS Catal.* **2020**, *10* (1), 20–35.

(58) Hausmann, J. N.; Beltrán - Suito, R.; Mebs, S.; Hlukhyy, V.; Fässler, T. F.; Dau, H.; Driess, M.; Menezes, P. W. Evolving Highly Active Oxidic Iron(III) Phase from Corrosion of Intermetallic Iron Silicide to Master Efficient Electrocatalytic Water Oxidation and Selective Oxygenation of 5-Hydroxymethylfurfural. *Adv. Mater.* **2021**, *33*, 2008823.

(59) Franco, D. V.; Da Silva, L. M.; Jardim, W. F.; Boodts, J. F. C. Influence of the Electrolyte Composition on the Kinetics of the Oxygen Evolution Reaction and Ozone Production

Processes. *J. Braz. Chem. Soc.* **2006**, *17* (4), 746–757.

(60) Paschen, S.; Felder, E.; Chernikov, M.; Degiorgi, L.; Schwer, H.; Ott, H.; Young, D.; Sarrao, J.; Fisk, Z. Low-Temperature Transport, Thermodynamic, and Optical Properties of FeSi. *Phys. Rev. B - Condens. Matter Mater. Phys.* **1997**, *56* (20), 12916–12930.

(61) Tang, C.; Wang, H. Sen; Wang, H. F.; Zhang, Q.; Tian, G. L.; Nie, J. Q.; Wei, F. Spatially Confined Hybridization of Nanometer-Sized NiFe Hydroxides into Nitrogen-Doped Graphene Frameworks Leading to Superior Oxygen Evolution Reactivity. *Adv. Mater.* **2015**, *27* (30), 4516–4522.

(62) Lee, E.; Park, A. H.; Park, H. U.; Kwon, Y. U. Facile Sonochemical Synthesis of Amorphous NiFe-(oxy)Hydroxide Nanoparticles as Superior Electrocatalysts for Oxygen Evolution Reaction. *Ultrason. Sonochem.* **2018**, *40*, 552–557.

(63) Zhu, K.; Liu, H.; Li, M.; Li, X.; Wang, J.; Zhu, X.; Yang, W. Atomic-Scale Topochemical Preparation of Crystalline Fe<sup>3+</sup>-Doped β-Ni(OH)<sub>2</sub> for an Ultrahigh-Rate Oxygen Evolution Reaction. *J. Mater. Chem. A* **2017**, *5* (17), 7753–7758.

(64) Wang, J.; Ciucci, F. Boosting Bifunctional Oxygen Electrolysis for N-Doped Carbon via Bimetal Addition. *Small* **2017**, *13* (16), 1–15.

(65) Yang, L.; Zeng, X.; Wang, D.; Cao, D. Biomass-Derived FeNi Alloy and Nitrogen-Codoped Porous Carbons as Highly Efficient Oxygen Reduction and Evolution Bifunctional Electrocatalysts for Rechargeable Zn-Air Battery. *Energy Storage Mater.* **2018**, *12* (December 2017), 277–283.

(66) Tang, C.; Wang, H. F.; Wang, H. Sen; Wei, F.; Zhang, Q. Guest-Host Modulation of Multi-Metallic (oxy)Hydroxides for Superb Water Oxidation. *J. Mater. Chem. A* **2016**, *4* (9), 3210–3216.

(67) Du, L.; Luo, L.; Feng, Z.; Engelhard, M.; Xie, X.; Han, B.; Sun, J.; Zhang, J.; Yin, G.; Wang, C.; Wang, Y.; Shao, Y. Nitrogen-Doped Graphitized Carbon Shell Encapsulated NiFe Nanoparticles: A Highly Durable Oxygen Evolution Catalyst. *Nano Energy* **2017**, *39*, 245–252.

(68) Gao, R.; Yan, D. Fast Formation of Single-Unit-Cell-Thick and Defect-Rich Layered Double Hydroxide Nanosheets with Highly Enhanced Oxygen Evolution Reaction for Water Splitting. *Nano Res.* **2018**, *11* (4), 1883–1894.

(69) Fu, G.; Cui, Z.; Chen, Y.; Li, Y.; Tang, Y.; Goodenough, J. B. Ni<sub>3</sub>Fe-N Doped Carbon Sheets as a Bifunctional Electrocatalyst for Air Cathodes. *Adv. Energy Mater.* **2017**, *7* (1), 1–8.

- (70) Andronesco, C.; Barwe, S.; Ventosa, E.; Masa, J.; Vasile, E.; Konkana, B.; Möller, S.; Schuhmann, W. Powder Catalyst Fixation for Post-Electrolysis Structural Characterization of NiFe Layered Double Hydroxide Based Oxygen Evolution Reaction Electrocatalysts. *Angew. Chemie - Int. Ed.* **2017**, *56* (37), 11258–11262.
- (71) Ci, S.; Mao, S.; Hou, Y.; Cui, S.; Kim, H.; Ren, R.; Wen, Z.; Chen, J. Rational Design of Mesoporous NiFe-Alloy-Based Hybrids for Oxygen Conversion Electrocatalysis. *J. Mater. Chem. A* **2015**, *3* (15), 7986–7993.
- (72) Dionigi, F.; Reier, T.; Pawolek, Z.; Glich, M.; Strasser, P. Design Criteria, Operating Conditions, and Nickel-Iron Hydroxide Catalyst Materials for Selective Seawater Electrolysis. *ChemSusChem* **2016**, *9* (9), 962–972.
- (73) Zhu, J.; Xiao, M.; Zhang, Y.; Jin, Z.; Peng, Z.; Liu, C.; Chen, S.; Ge, J.; Xing, W. Metal-Organic Framework-Induced Synthesis of Ultrasmall Encased NiFe Nanoparticles Coupling with Graphene as an Efficient Oxygen Electrode for a Rechargeable Zn-Air Battery. *ACS Catal.* **2016**, *6* (10), 6335–6342.
- (74) Lian, K. K.; Kirk, D. W.; Thorpe, S. J. Investigation of a ‘Two - State’ Tafel Phenomenon for the Oxygen Evolution Reaction on an Amorphous Ni - Co Alloy. *J. Electrochem. Soc.* **1995**, *142* (12), 4309–4309.
- (75) Brady, P. V.; Walther, J. V. Controls on Silicate Dissolution Rates in Neutral and Basic pH Solutions at 25°C. *Geochim. Cosmochim. Acta* **1989**, *53* (11), 2823–2830.
- (76) Rakityanskaya, I. L.; Shein, A. B. Anodic Behavior of Iron, Cobalt, and Nickel Silicides in Alkaline Electrolytes. *Russ. J. Electrochem.* **2006**, *42* (11), 1208–1212.

# Chapter III. Ferromagnetic and electrocatalytically active CoSi nanoparticles

## III.1 Introduction

The nanoscale largely impacts the magnetic and catalytic properties of transition metal silicides. These materials exhibit a large diversity of magnetic properties.<sup>1-6</sup> Generally, binary transition metal silicides only show magnetic ordering in the metal-rich phases (*e.g.* Co<sub>3</sub>Si, Fe<sub>3</sub>Si).<sup>2,7</sup> Their counterpart Si-rich silicides or monosilicides do not show magnetic order. For example, FeSi is paramagnetic. NiSi and CoSi are diamagnetic.<sup>3,8,9</sup> However, unusual magnetic order has been demonstrated in many nanowires of binary disilicides or monosilicides.<sup>10-12</sup> This ferromagnetism has been attributed to the unpaired spins produced by crystal defects, undercoordinated metal atoms and dangling bonds at the interface and/or grain boundaries. These features can be tuned by the size and morphology of the nano-objects.<sup>2</sup>

Nanoscaled metal silicides have also raised interest in hydrogenation catalysis<sup>13</sup> and electrocatalysis of water splitting<sup>14-16</sup>. Although cobalt silicide nanoparticles have not been investigated as catalysts for the hydrogen evolution and oxygen evolution reactions (HER and OER), other cobalt-p-block element compounds<sup>17-23</sup>, like carbides, nitrides, phosphides, sulfides and borides have demonstrated outstanding OER electrocatalytic activity. They undergo an electrode reconstruction by dissolution of p-block-element under the oxidizing conditions of OER, which results in a partial or complete conversion to electrocatalytically active cobalt (oxy)hydroxides. Because the nature of the p-block element could influence the local structure, geometry and thickness of the generated (oxy)hydroxides due to differences in radii, electronegativity and bonding nature with Co,<sup>23</sup> It is necessary to evaluate the OER electrocatalytic properties of nanoscaled cobalt silicides.

CoSi nanowires have previously been grown,<sup>11</sup> while CoSi nanoparticles supported on graphene or other solid matrices achieved by chemical vapor deposition have been investigated as efficient catalysts for hydrogenation,<sup>24–26</sup> oxidation of methanol/ethanol,<sup>27,28</sup> but their magnetic property have not been reported.<sup>24–28</sup> As the interaction between nanoparticles and the support could change the exposed facets and especially the electronic state of surface atom of nanoparticles,<sup>29</sup> one can foresee that designing freestanding cobalt silicide nanoparticles could deeply impact electrocatalytic activity and magnetism.

In this work, freestanding CoSi nanoparticles are achieved through the reactivity of cobalt chloride and Si nanoparticles in molten salts based on the synthesis approach developed in the previous chapter. The obtained CoSi nanoparticles show either homogeneous or core-shell morphologies under different reaction temperatures (300–400 °C). The obtained CoSi nanoparticles show ferromagnetism below 300 K. Then, the OER electrocatalytic activity and stability of core-shell CoSi nanoparticles have been studied. Core-shell CoSi nanoparticles are a pre-catalyst for OER, yielding electrocatalytic activity surpassing IrO<sub>2</sub> in the same conditions.

## III.2 Experimental methods

**Reagents.** Lithium iodide (99%, Alfa Aesar), potassium iodide (99%, Sigma-Aldrich), silicon nanoparticles (99%, Nanomakers<sup>®</sup>, France) and cobalt(II) chloride (99.7%, Alfa Aesar) were stored and manipulated as received in an Ar-filled glovebox (H<sub>2</sub>O < 0.5 ppm, O<sub>2</sub> < 0.5 ppm). Methanol (VWR Normapur grade) was used for washing.

**Synthesis of core-shell and homogeneous cobalt monosilicide nanoparticles.** 63.2 mg Si nanoparticles (2.3 mmol), 194.8 mg CoCl<sub>2</sub> (1.5 mmol), 2.9 g LiI (21.7 mmol) and 2.1 g KI (12.7 mmol) (molar ratio LiI:KI 0.63:0.37) were ball-milled during 2 min at 20 Hz (Retsch MM400 ball mill airtight vial of 50 mL, filled with one steel ball of 62.3 g with a diameter of 23 mm) to get a well-mixed fine powder. The mixture was loaded in a quartz tube (Ø28×H345 mm) which was then connected to a Schlenk line and was evacuated under vacuum. An intermediate liquid nitrogen trap between the quartz tube and the Schlenk line was set to condensate the byproduct SiI<sub>4</sub> to avoid the pollution of the Schlenk line. A vertical furnace from Eraly<sup>®</sup> was pre-heated to the reaction temperature 300 and 400 °C for core-shell and homogenous nanoparticles, respectively. Then, the quartz tube was put in the furnace, followed by 6 hours of thermal treatment under dynamic vacuum (10<sup>-3</sup> mbar). Later, the hot quartz tube was taken out and cooled down to room temperature under vacuum. The as-prepared mixture

was washed in methanol by seven cycles of centrifugation/redispersion and was later dried in a Schlenk tube under vacuum during the night. The dried powder was transferred and stored in an Ar-filled glovebox.

**Electrochemical measurements** A typical three-electrode configuration was used, which includes a working electrode, a Pt coil as counter electrode and a Ag/AgCl saturated KCl electrode as reference electrode. There are two types of substrates used for the working electrode in this work. A glassy carbon (GC) rotating disk electrode (RDE) with a diameter of 5 mm was used for cyclic voltammetry (CV). Glassy carbon sheets were used for chronopotentiometry (CP) measurements. The working electrode was prepared by drop casting. 3.4 mg of catalyst was sonicated in 480  $\mu\text{L}$  absolute ethanol for 15 min, followed by adding 20  $\mu\text{L}$  of Nafion solution (5% in alcohols and water, Sigma-Aldrich) for another 10 min of ultrasonication. The well-dispersed ink was then dropped onto the as-polished RDE or the GC sheet substrate to obtain a catalyst loading of  $170 \mu\text{g}_{\text{catalyst}} \cdot \text{cm}^{-2}_{\text{electrode}}$ , and then the substrate was dried for at least 30 min under air.

A custom-made PMMA electrochemical cell was used for all measurements. The electrolyte was bubbled with  $\text{O}_2$  for at least 20 min before measurement. The rotating rate of the RDE was set at 1600 rpm for all cyclic voltammetry (CV) measurements. Cyclic voltammograms were recorded from 0 to 1.05 V vs. saturated KCl Ag/AgCl reference electrode at scan rate of  $20 \text{ mV s}^{-1}$ , until overlapped cycles were obtained. For the chronopotentiometry (CP), the current density was set at  $10 \text{ mA cm}^{-2}$  to monitor the potential evolution.

The ohmic drop  $iR$  compensation was considered for the potentials reported, where the resistance is approximately equal to the total impedance measured at a frequency of 50 kHz. The potentials vs. RHE are obtained from conversion of measured potentials based on the equation:  $E_{\text{RHE}} = E_{\text{measured}} + 0.197 + 0.0591 \times \text{pH}$ .

**PDF Refinements** were performed for the core-shell CoSi nanoparticles using PDFGui<sup>30</sup> in the range 1.3-20  $\text{\AA}$ . CoSi with 9 nm coherence length was used as a starting point. Cell parameters, scale factor, thermal parameters, atomic positions and peak broadening effect (sratio and rcut) parameters were allowed to vary, and lead to an acceptable reliability factor of 20.9 %. Crystalline Si phase and amorphous  $\text{SiO}_2$  (coherence length 8  $\text{\AA}$ ) were added in the structural model. The reliability factor R for (CoSi/amorphous  $\text{SiO}_2$ /crystalline Si) mixture decreased down to 15.8 %, better than CoSi alone, CoSi/amorphous silica (R=20.1 %) or CoSi/crystalline Si (R=19.7 %). This is the decrease of the reliability factor that allows us to validate the addition of

a new phase in the mixture. Scale factor ratio were adapted between 0 and 1 (0.1 steps) to obtain the best R reliability factor.

Crystalline cobalt was also tested as additional phase (in addition to CoSi, amorphous SiO<sub>2</sub> and crystalline Si) with PDF analysis. The refinement got worse with this phase addition (R=15.9 %), meaning that the presence of crystalline Co is highly improbable.

Amorphous Co was also tested in addition to the CoSi / amorphous SiO<sub>2</sub> / crystalline Si mixture, and it did not improve the refinement (R=15.8 %). A CoSi and amorphous Co mixture was tested as well and compared with CoSi alone. This led to a slightly worse reliability factor (21.0 %) than CoSi alone. The degradation of CoSi-alone refinement resulting from adding amorphous Co and the lack of improvement of the refined CoSi / amorphous SiO<sub>2</sub> / crystalline Si mixture allow us to eliminate amorphous Co as a component of the material.

**Magnetic measurements** Vibrating sample magnetometry (VSM) on quantum design PPMS was used to determine the curves of magnetization versus applied field at 5 and 300 K for the samples. Zero-field-cooled and field-cooled magnetization versus temperature curves were acquired on a Quantum Design MPMS-XL superconducting quantum interference device (SQUID) magnetometer at magnetic field of 20 Oe from 5 to 300 K. All measurements were done on powder samples.

### III.3 Results and discussion

The reactivity between silicon and cobalt chloride has been previously employed in the chemical vapor deposition (CVD) of CoSi nanowires at 850 °C.<sup>11</sup> Herein, we employ the synthesis approach developed in the previous section for nickel iron silicides. Silicon nanoparticles are reacted with metal chlorides in LiI-KI molten salts under vacuum. The reaction temperature is largely decreased compared to the CVD process to be compatible with nanoparticle design.

#### III.3.1 Characterization of CoSi nanoparticles

The powder X-ray diffraction (XRD) reflections (**Figure III-1a**) of the sample synthesized at 300 °C indicate that the main crystalline phase is CoSi. A minor phase is attributed to crystalline d-Si. According to high angle annular dark-field (HAADF) imaging in a scanning transmission

electron microscope (STEM) and high-resolution transmission electron microscopy (HRTEM) (**Figure III-1b and c**), the nanoparticles obtained at 300 °C are *ca.* 50 nm, and show a core-shell structure with a highly contrasted shell, surrounded by an amorphous passivation layer (**Figure III-1b and Figure III-2**). Crystalline phases of the core-shell are identified by HRTEM. The polycrystalline contrasted shell can be fully indexed along the CoSi structure (**Figure III-1b and Figure III-2**). On contrary, the core exhibits a poor crystallinity and few areas can be attributed to d-Si (**Figure III-2**). This disordered state could be due to the lattice distortion induced by interstitial Co atoms in an Si matrix.

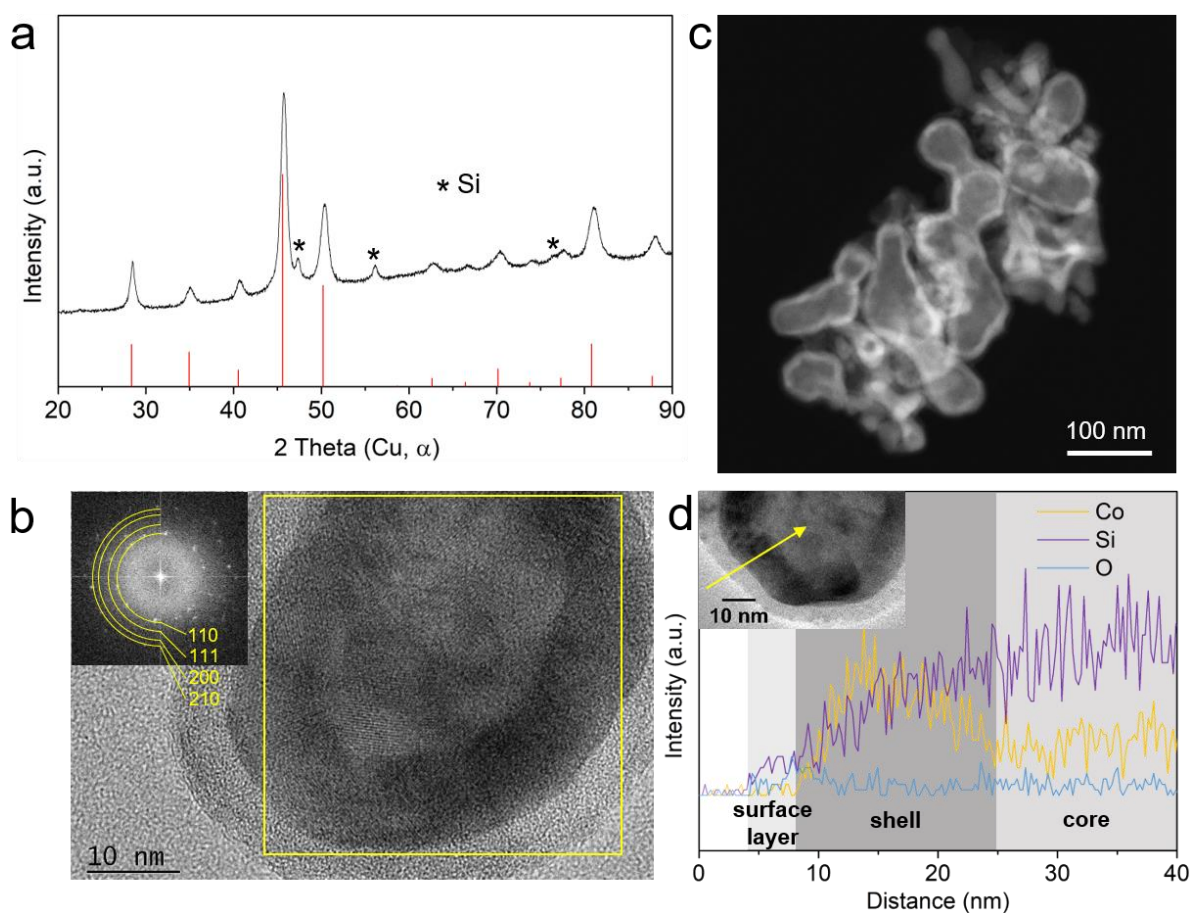


**Figure III-1** (a) Powder XRD pattern of the as-prepared core-shell CoSi. The red drop lines denote the CoSi reference. The asterisks mark indicative peaks of d-Si references. (b) HRTEM image with corresponding Fast Fourier Transform (FFT) in the inset. The FFT is indexed along the CoSi structure. (c) STEM-HAADF image and (d) STEM-EDX linear scan along the line indicated in the inset.

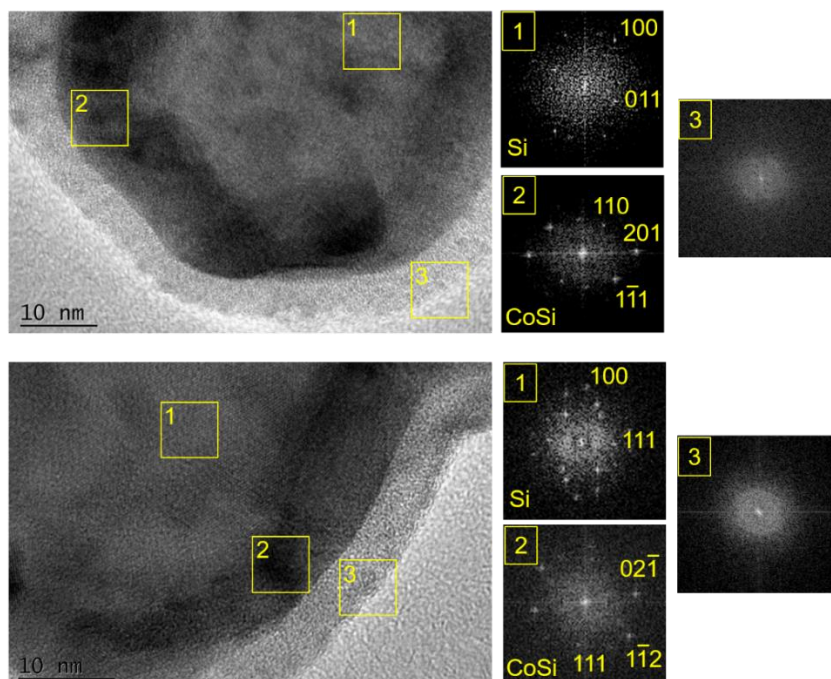


**Figure III-2** HRTEM images of core-shell CoSi nanoparticles and the FFTs of corresponding areas. The core and the shell are indexed along d-Si and CoSi structures, respectively. The lighter contrast outer layer shows no crystalline feature.

Compositional analysis was then conducted. The overall Co/Si ratio of the core-shell and homogeneous CoSi is respectively 0.5 and 0.6, determined by analysis energy-dispersive X-ray spectroscopy (EDX) in a scanning electron microscope (SEM). Both samples exhibit an excess of silicon compared to the composition expected from XRD phase identification. We then attribute this excess of silicon to disordered silicon in the core or to oxidized silicon observed at the surface of the particles.

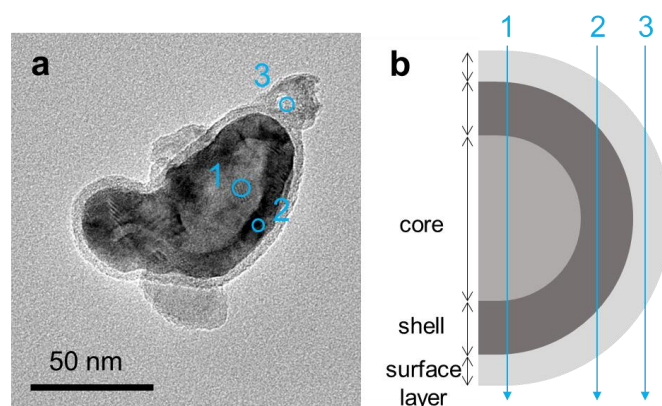


**Figure III-3** (a) TEM image and the three positions used for point STEM-EDX analysis 1, 2, and 3. (b) Schematic analyzed zones of each position.

The native amorphous surface layer is ascribed to silica according to the elemental STEM-EDX linear profile (**Figure III-1d**) showing a Co-poor composition. As for the core, it is rich in Si. Co appears with a weaker signal, which indicates the Co-doped silicon nature of the core, in agreement with the HRTEM indexation. In order to determine the composition of each component of core-shell CoSi, STEM-EDX analysis was performed on three representative positions (**Figure III-3a**). The obtained Co/Si atomic ratios are 0.3, 0.6 and 0.05 respectively for position 1, 2 and 3. According to the TEM image, the thicknesses of core, shell and surface layer are *ca.* 30, 10 and 5 nm. Based on these values and the EDX values at each position (**Figure III-3b**), approximative Co/Si atomic ratios are calculated as 0.9 for the shell and 0 for the core. These results are consistent with the HRTEM indexation. This core-shell morphology could originate from the limited diffusion rate of Co in cobalt silicides and Si below 350 °C (**Figure III-4**).<sup>31</sup>

Consistently, homogeneous CoSi nanoparticles were achieved at 400 °C (**Figure III-5a-b**), where diffusion of Co in Si or silicides is thermally activated. According to the XRD diagram, additional to Si,  $\text{Co}_2\text{Si}_3$  is present in the homogeneous CoSi nanoparticle sample as a side-product. HRTEM image and FFT (**Figure III-5d**) confirm the formation of CoSi, and show that the homogeneous nanoparticles exhibit larger crystal domains than the core-shell CoSi nanoparticles obtained at 300 °C. Elemental STEM-EDX profiles (**Figure III-5e**) further confirm the homogeneous intraparticle distribution of Co and Si. A Co-poor surface oxide layer is also observed.

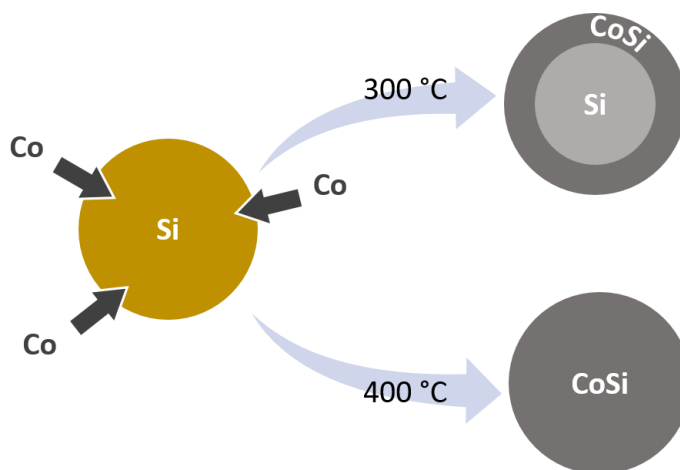


**Figure III-4** Schema of synthesis towards core-shell CoSi and homogeneous CoSi nanoparticles.

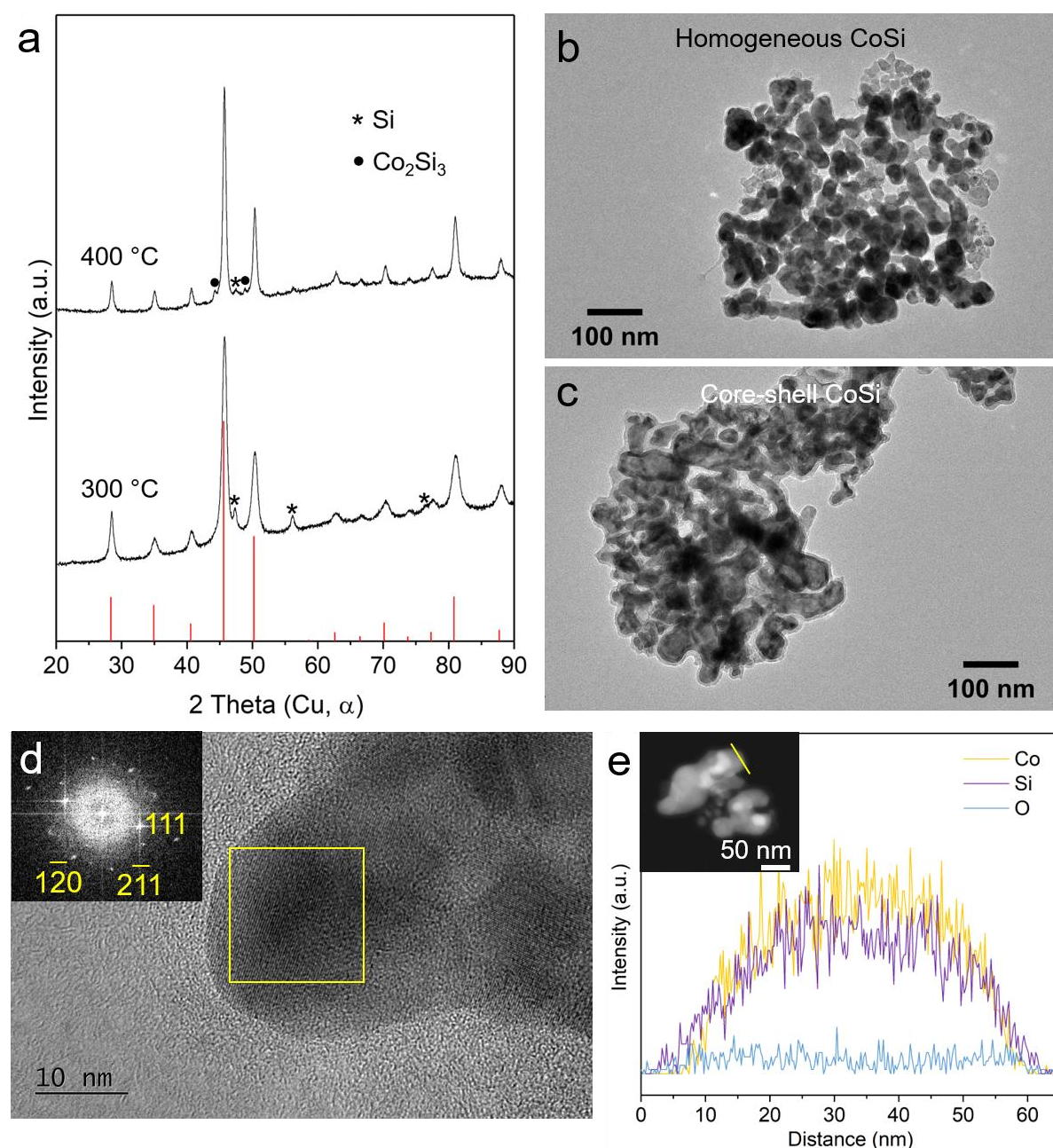


**Figure III-5** Comparison of (a) powder XRD diagrams of CoSi samples obtained at 400 and 300 °C and TEM images of corresponding (b) homogeneous CoSi and (c) core-shell CoSi nanoparticles. Homogeneous CoSi nanoparticles: (d) HRTEM image and FFT of corresponding area. The FFT can be fully indexed along the CoSi structure. (e) STEM-HAADF image (inset) and elemental STEM-EDX linear profile along the line indicated in the inset.

The surface states of core-shell CoSi were analyzed by X-ray photoelectron spectroscopy (XPS). In the region of Co  $2p_{3/2}$  (**Figure III-6a**), the peaks at 778.0 and 781.7 eV can be respectively ascribed to Co-Si and oxidized cobalt formed by air exposure.<sup>32-34</sup> As for the Si region, the peak at 103.4 eV corresponds to silicate and  $\text{SiO}_2$ . The component at 98.6 eV can be assigned

to metal silicides.<sup>34–36</sup> The peak at 100.2 eV is due to the photoelectron emission from the Co 3s state.<sup>37</sup>

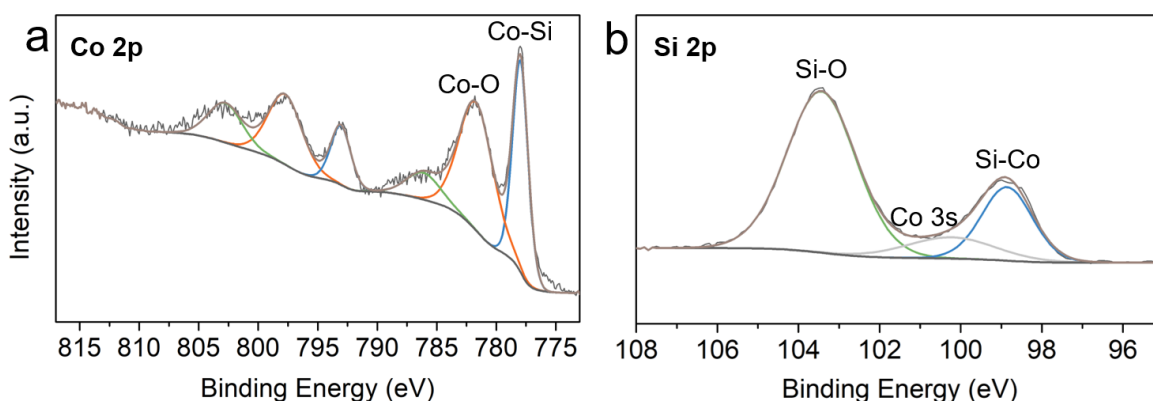


**Figure III-6** XPS of as-prepared core-shell CoSi nanoparticles: (a) Co 2p and (b) Si 2p regions.

Unlike bulk CoSi, CoSi nanoparticles obtained in this work react to a magnet. In order to eliminate the possible influence of amorphous elemental Co, the core-shell CoSi sample was analyzed by pair distribution functions (PDFs). PDF analysis based on characterisation of the  $G(r)$  curve describing the inter-atomic distances from X-ray total diffraction analysis is a powerful technique to assess the local structure when X-ray diffraction fails to probe amorphous materials, defects and small clusters. Indeed, it has been recently used to identify amorphous iron phosphide catalysts,<sup>38</sup> or to attest the presence of embedded molecular catalysts<sup>39</sup> or Ni clusters<sup>40</sup> as well as their post-catalytic structural integrity. It is used here to assess the presence or absence of additional phases that could be unseen from X-ray diffraction and yet responsible for the observed magnetic solid behaviour.

The best local structure description is obtained when the calculated  $G(r)_{\text{calc}}$  from the refined structure is the closest to the experimental  $G(r)_{\text{exp}}$ , where the reliability R factor is at its lowest. Refinement of the crystalline CoSi led to a fairly acceptable (reliability factor  $R=20.9\%$ ) but yet improvable solution. The addition of crystalline Si and amorphous silica has thus led to the best refinement ( $R=15.8\%$ , **Figure III-7a**). More importantly, amorphous Co undetected by X-ray diffraction and crystalline Co could be excluded since their addition did not improve the reliability factor (**Figure III-7b-c**). Therefore, the reaction of the core-shell sample to magnet is attributed to the CoSi phase (See experimental methods for details of refinement process).

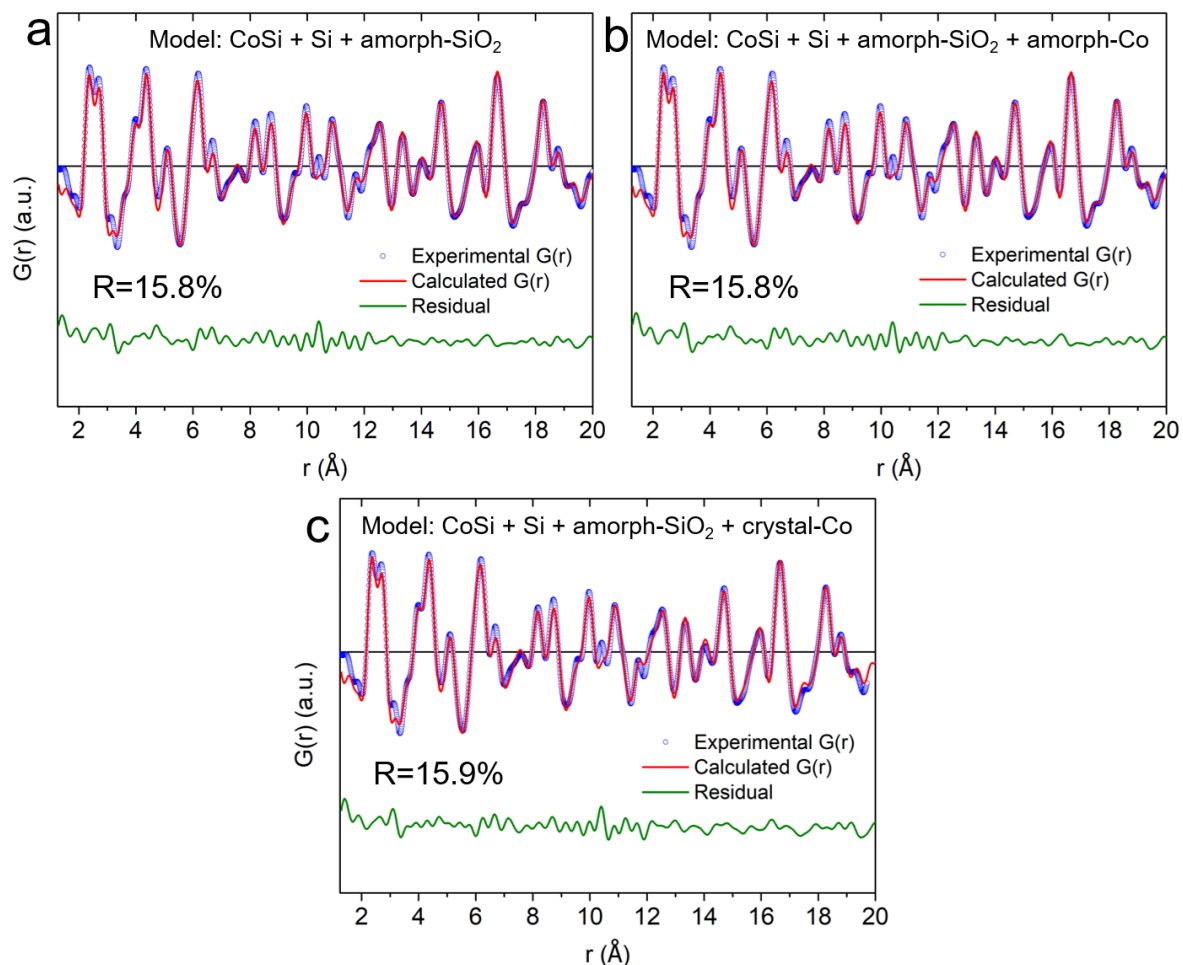


**Figure III-7** PDF experimental  $G(r)$  curve (blue dotted line) of core-shell CoSi nanoparticles superimposed with the calculated  $G(r)$  curve (red line) of different models, and residual profile (green).

### III.3.2 Magnetic properties

Both core-shell and homogeneous CoSi nanoparticles show ferromagnetic behaviors at low temperatures that persist to temperature close to room temperature (**Figure III-8a**). Core-shell CoSi nanoparticles show coercive fields of 15 Oe and 945 Oe at 300 and 5 K, respectively. Similar coercivities were observed for the homogenous sample (**Figure III-8b**), 5 Oe and 1000 Oe at 300 and 5 K. The saturated magnetizations ( $M_s$ ) of both samples were further calculated through the law of approach to saturation.<sup>41,42</sup> The linear fitting of  $M$  versus  $1/H$  gives  $M_s$  values of 7.9 and 10.6  $\text{emu}\cdot\text{g}^{-1}$  at 300 K and 5K, respectively, for core-shell CoSi particles, corresponding to 0.17 and 0.22  $\mu_B/\text{Co}$ . The saturated magnetizations for homogeneous CoSi particles are 2.6  $\text{emu}\cdot\text{g}^{-1}$  (0.048  $\mu_B/\text{Co}$ ) and 3.6  $\text{emu}\cdot\text{g}^{-1}$  (0.067  $\mu_B/\text{Co}$ ) at 300 and 5 K, respectively. These values are much

lower than that of metallic Co ( $1.72 \mu_B/\text{Co}$  at 4 K),<sup>11</sup> in agreement with the absence of Co clusters deduced by PDF analysis. Bulk CoSi is reported as intrinsically diamagnetic (**Table III-1**).<sup>9</sup> CoSi thin films are non-magnetic.<sup>7</sup> The ferromagnetism of single crystal CoSi nanowires has been ascribed to the Co atoms in some defective positions, *e.g.* interfaces, grain boundaries and crystal defects.<sup>2,11</sup> Herein, as the polycrystalline core-shell CoSi nanoparticles demonstrate rich boundaries and interfaces, this effect is therefore more pronounced than for the reported CoSi single crystal nanowires ( $0.03 \mu_B/\text{Co}$  at 300 K)<sup>11</sup> and the homogeneous CoSi nanoparticles prepared in this work ( $0.05 \mu_B/\text{Co}$  at 300 K).

**Table III-1** Comparison of the magnetic properties of different Co-based materials.

Phase	Morphology	Temperature (K)	Coercivity (Oe)	Saturation magnetization		Ref.
				$\mu_B/\text{Co}$	emu/g	
CoSi	Polycrystalline core-shell nanoparticles	300	15	0.17	7.7	This work
		5	945	0.22	10.6	This work
CoSi	Polycrystalline nanoparticles (50 nm)	300	5	0.05	2.6	This work
		5	1000	0.07	3.6	This work
CoSi	Single crystal nanowires (20-60 nm)	300	460	0.03	1	11
CoSi	Thin film	-	non-magnetic			7
CoSi	Bulk	<20	diamagnetic			9
Co <sub>3</sub> B	Nanoparticles (10-20 nm)	300	1300	-	-	33
		5	1400	1.02	91	33
Co	Nanoparticles (1.5 nm)	5	-	1.94	185	43
Co	Nanoparticles (1.5 nm) surface covered by CO	5	-	0.58	55	43
Co	Thin film	4.2	1000	1.72	166	44

The zero-field cooled (ZFC) and field cooled (FC) magnetization curves of core-shell CoSi nanoparticles at 20 Oe are shown in **Figure III-8b**. The ZFC curve shows a maximum at *ca.* 275 K. This result is in agreement with the recorded hysteresis loops at different temperatures. In a polycrystalline CoSi sample, the spins of each crystal domain are spontaneously oriented along their easy axis at room temperature. These macroscopic disordered spin orientations are frozen

at low temperature (5 K) before the ZFC measurement, so that a low magnetization is recorded at the beginning of ZFC measurement. As the temperature increases, the spins are defrosted to be aligned under the applied field, so the magnetization increases. The rise of temperature also leads to thermal disturbance and decrease of coercivity. As a result, after reaching the maximum magnetization, the FC and ZFC curves converge above 300 K, where the sample becomes paramagnetic.

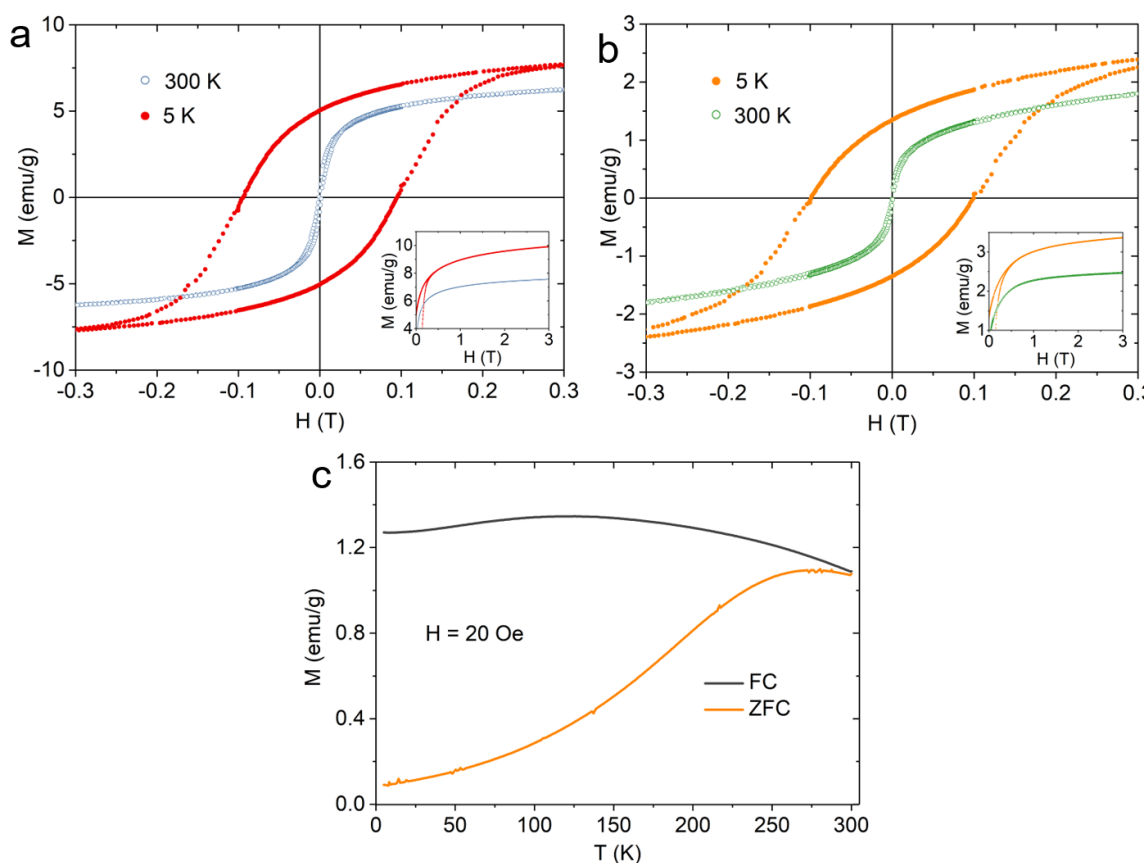


**Figure III-8** Magnetization curves of (a) core-shell CoSi nanoparticles and (b) homogeneous CoSi nanoparticles: as a function of magnetic field at 300 and 5 K. (b) Magnetization of core-shell CoSi nanoparticles as a function of temperature at applied field of 20 Oe, recorded after cooling in a 20 Oe field (FC) and after cooling in zero field (ZFC), respectively.

### III.3.3 Electrocatalytic properties and *post mortem* studies

The electrocatalytic properties of core-shell CoSi nanoparticles were then evaluated in 0.1 M KOH. An inert glassy carbon substrate covered with a drop-casted nanoparticles/Nafion film was used as working electrode. The cyclic voltammograms (CV) of core-shell CoSi nanoparticles

and reference commercial IrO<sub>2</sub> nanoparticles are shown in **Figure III-9a**. In the first CV of CoSi, an irreversible flat anodic wave is observed at *ca.* 1.35~1.55 V. This peak could thus correspond to the oxidation of cobalt and/or silicon.<sup>32</sup> The latter could be followed by dissolution of silicon.<sup>23</sup> Moreover, this process is not observed again in the second cycle, and is then irreversible. As the current density of oxygen evolution remained almost unchanged afterward, it can be deduced that the quantity of active sites for OER was retained after the evolution of the material during the first CV. The overpotential at current density of 10 mA cm<sup>-2</sup> in 0.1 M KOH of core-shell CoSi nanoparticles is *ca.* 410 mV, *versus* 440 mV for commercial IrO<sub>2</sub> nanoparticles, showing that core-shell CoSi nanoparticles exhibit a higher activity than IrO<sub>2</sub>. The activities normalized *versus* the amount of Co are further calculated and compared to Co-based catalysts previously reported (**Table III-2**). The normalized activity of core-shell CoSi nanoparticles is superior to the listed Co-based OER electrocatalysts.

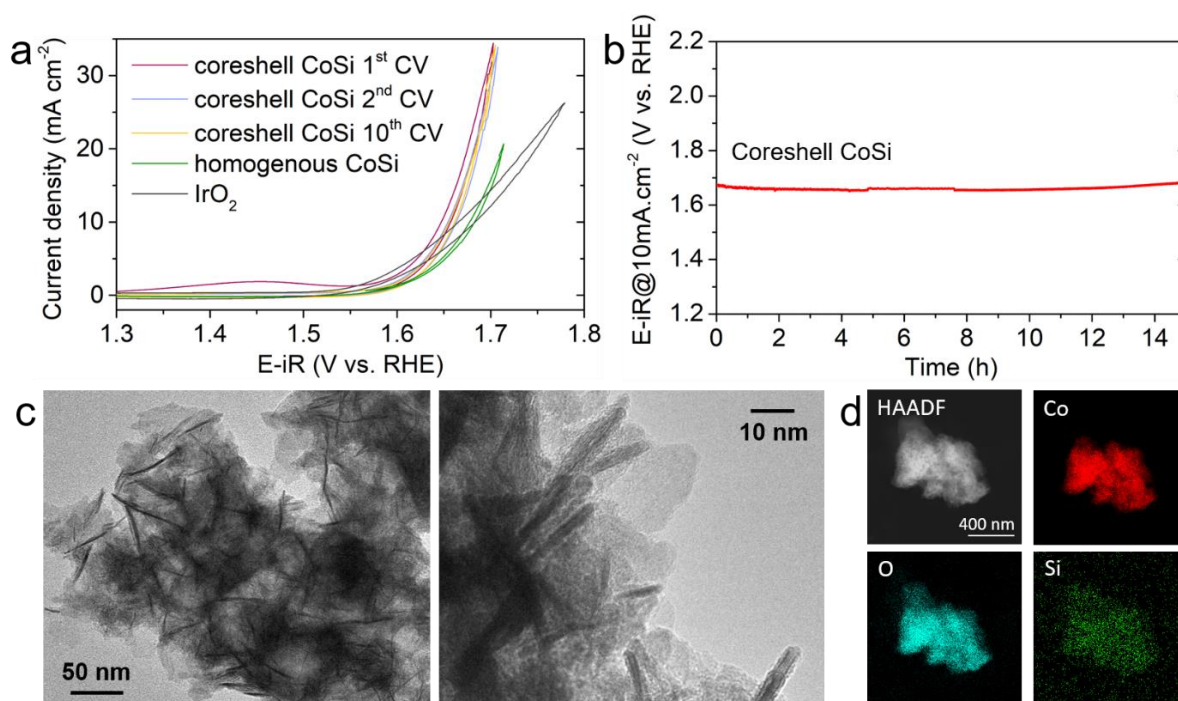


**Figure III-9** The OER electrocatalytic properties of CoSi nanoparticles. (a) CVs of core-shell and homogeneous CoSi nanoparticles and of reference commercial IrO<sub>2</sub> nanoparticles in an aqueous O<sub>2</sub>-saturated 0.1 M KOH electrolyte. (b) CP measurement at 10 mA cm<sup>-2</sup> for core-shell CoSi nanoparticles. (c) TEM images and (d) STEM-EDX chemical mapping of the core-shell CoSi nanoparticles after 15 h CP measurement.

To evaluate the durability of the electrocatalytic activity of the core-shell CoSi nanomaterials, the anodic potential was monitored for 15 h at 10 mA cm<sup>-2</sup> (**Figure III-9b**). The increment of potential after at least 15 h is negligible, testifying a durability for 15 h of the performances.

TEM images (**Figure III-9c**) of a post-OER sample show a complete conversion of CoSi nanoparticles to a layered phase. STEM-EDX chemical mapping (**Figure III-9d**) shows that the modified catalyst is mainly oxidized Co species, but a small amount of Si can also be detected in the nanostructure.

**Table III-2** OER electrocatalytic normalized activity and stability of previously reported Co-based catalysts in 0.1 M KOH on GC substrate.

Catalyst	Loading amount (mg cm <sup>-2</sup> )	Overpotential (mV) @10mA cm <sup>-2</sup>	Overpotential (mV) @40mA cm <sup>-2</sup> g <sub>Co</sub> <sup>-1</sup>	Stability (h)	Ref.
Core-shell CoSi	0.17	410	360	15 h	This work
Amorphous Co <sub>2</sub> B	0.21	380	370	60 h	<sup>22</sup>
CoSe <sub>2</sub>	0.20	484	420	/	<sup>45</sup>
CoB	0.21	370	390	51 h	<sup>46</sup>
Co <sub>2</sub> B	0.20	405	360	1000 cycles	<sup>47</sup>

To elucidate the evolution of the surface chemical states and of the material, the post OER sample was analyzed by XPS. As shown in **Figure III-10**, after 15h of OER operation, the peaks of the Co 2p<sub>3/2</sub> spectrum are shifted to higher binding energy (**Figure III-6**). The deconvoluted peaks at 780.1 eV and 781.2 eV and the satellite features indicate the presence of Co<sup>3+</sup>, which corresponds to CoOOH and/or Co<sub>3</sub>O<sub>4</sub>.<sup>48-51</sup> In the O 1s region, the peak at the lowest binding energy 529.5 eV is attributed to cobalt oxide. The component at 530.5 eV can be assigned to typical non-stoichiometric oxygen in spinel (Co<sub>3</sub>O<sub>4</sub>) or cobalt hydroxide.<sup>33,48</sup> These results are further confirmed by the decrease of the signal-to-noise ratio of the Si 2p signal, which is ascribed to Si-leaching. The residual Si shows a peak at 102.9 eV. It could be attributed to Si oxoanions<sup>52</sup> implanted in the interlayer regions of cobalt oxide/(oxyhydroxide), which may assist the formation of the layered structure.<sup>23</sup> Hence, according to STEM-EDX and XPS results, cobalt oxide/(oxy)hydroxide is identified as the active electrocatalytic species after OER, which is consistent with the full conversion of the initial catalyst observed from TEM (**Figure III-9b**).

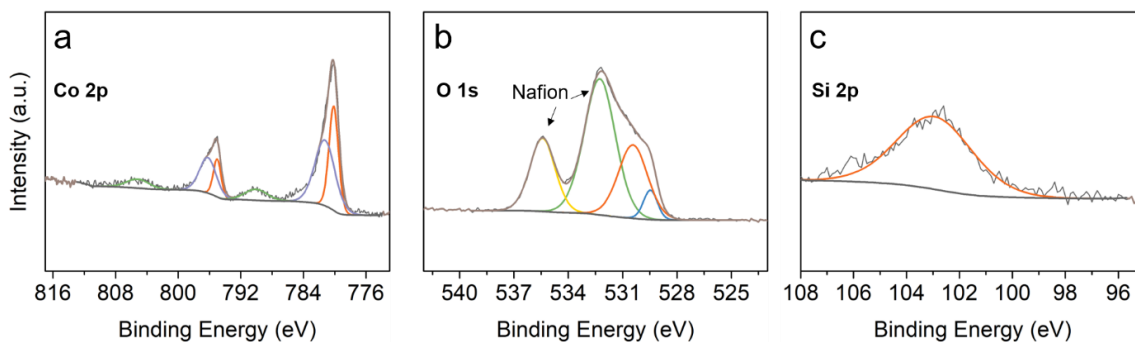


**Figure III-10** XPS of the core-shell CoSi sample after 15 h of OER at  $10 \text{ mA cm}^{-2}$ : (a) Co 2p region, (b) O 1s region, (c) Si 2p region. In (b), the Nafion peaks are identified according to the literature.<sup>33</sup>

Because of the low signal-to-noise ratio for the XPS Si 2p spectrum, the oxidation states of Si in core-shell CoSi before and after OER electrocatalysis were further studied by X-ray absorption near edge structure (XANES) (**Figure III-11**). The pristine sample and the as-prepared electrode show two Si components similar to Si wafer and  $\text{SiO}_2$  references, which can be attributed to non-oxidic Si in the silicide and Si in the  $\text{SiO}_2$  and/or silicate surface layer. However, the spectrum of an electrode subjected to OER for 15 h only shows oxidized Si feature. This observation confirms the above results indicating that after the complete conversion of CoSi phases during OER, some Si remains in the layered structure of the catalyst and that it is in the form of Si oxoanions.

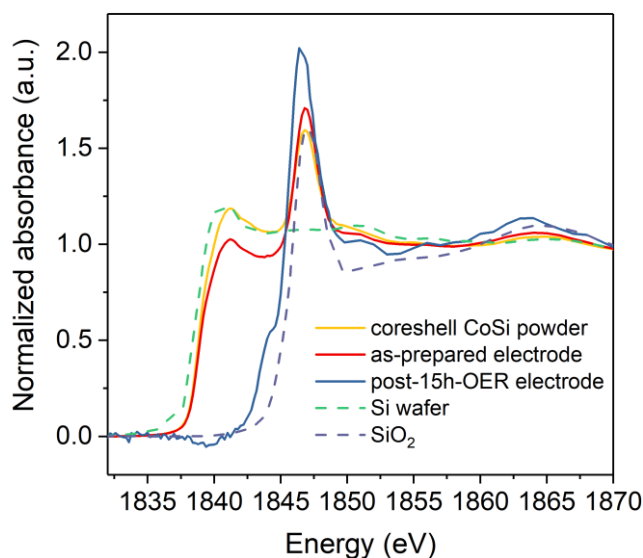


**Figure III-11** XANES spectra at the Si K-edge recorded on the core-shell CoSi sample, the corresponding as-prepared electrode, post-15h-OER electrode, and the Si wafer and fumed silica references.

### III.4 Conclusion

Based on the synthesis method developed in the previous chapter, freestanding CoSi nanoparticles are obtained as core-shell Si-CoSi nanoparticles and homogeneous nanoparticles by reacting Si nanoparticles with a cobalt salt at 300 or 400 °C respectively. Unlike diamagnetic bulk CoSi, the cobalt silicide nanoparticles are ferromagnetic below 300 K. This magnetic ordering arises from Co atoms at the interfaces, grain boundary or crystal defects. Hence, the polycrystalline core-shell CoSi nanoparticles obtained in this work exhibit higher magnetic moment ( $0.17 \mu_B/\text{Co}$  at 300 K) than the reported CoSi single crystal nanowires ( $0.03 \mu_B/\text{Co}$  at 300 K)<sup>11</sup> and the homogeneous CoSi nanoparticles prepared in this work ( $0.05 \mu_B/\text{Co}$  at 300 K). On the other hand, the core-shell CoSi nanoparticles deliver high OER electrocatalytic activity surpassing IrO<sub>2</sub> through *in situ* Si-assisted conversion to a layered Co oxide/(oxy)hydroxide. The modified electrode demonstrates stability for at least 15 h.

## References

- (1) Dahal, A.; Gunasekera, J.; Harringer, L.; Singh, D. K.; Singh, D. J. Metallic Nickel Silicides: Experiments and Theory for NiSi and First Principles Calculations for Other Phases. *J. Alloys Compd.* **2016**, *672*, 110–116.
- (2) Goldfarb, I.; Cesura, F.; Dascalu, M. Magnetic Binary Silicide Nanostructures. *Adv. Mater.* **2018**, *30* (41), 1–11.
- (3) Wernick, J. H.; Wertheim, G. K.; Sherwood, R. C. Magnetic Behavior of the Monosilicides of the 3d-Transition Elements. *Mater. Res. Bull.* **1972**, *7* (12), 1431–1441.
- (4) Robins, D. A. The Magnetic Susceptibility and Electrical Resistivity of Some Transition Metal Silicides. *Philos. Mag.* **1958**, *3* (28), 313–327.
- (5) Han, N.; Liu, H.; Zhao, J. Novel Magnetic Monolayers of Transition Metal Silicide. *J. Supercond. Nov. Magn.* **2015**, *28* (6), 1755–1758.
- (6) Williams, H. J.; Wernick, J. H.; Sherwood, R. C.; Wertheim, G. K. Magnetic Properties of the Monosilicides of Some 3d Transition Elements. *J. Appl. Phys.* **1966**, *37* (3), 1256.
- (7) Gomoyunova, M. V.; Grebenyuk, G. S.; Pronin, I. I.; Solov'ev, S. M.; Vilkov, O. Y.; Vyalykh, D. V. Formation and Magnetic Properties of the Silicon-Cobalt Interface. *Phys. Solid State* **2013**, *55* (2), 437–442.
- (8) Petrova, A. E.; Krasnorussky, V. N.; Shikov, A. A.; Yuhasz, W. M.; Lograsso, T. A.; Lashley, J. C.; Stishov, S. M. Elastic, Thermodynamic, and Electronic Properties of MnSi, FeSi, and CoSi. *Phys. Rev. B - Condens. Matter Mater. Phys.* **2010**, *82* (15), 1–6.
- (9) Stishov, S. M.; Petrova, A. E.; Sidorov, V. A.; Krasnorussky, V. N.; Menzel, D. Self-Doping Effects in Cobalt Silicide CoSi: Electrical, Magnetic, Elastic, and Thermodynamic Properties. *Phys. Rev. B - Condens. Matter Mater. Phys.* **2012**, *86* (6), 1–5.
- (10) Lin, J. Y.; Hsu, H. M.; Lu, K. C. Growth of Single-Crystalline Nickel Silicide Nanowires with Excellent Physical Properties. *CrystEngComm* **2015**, *17* (9), 1911–1916.
- (11) Seo, K.; Varadwaj, K. S. K.; Mohanty, P.; Lee, S.; Jo, Y.; Jung, M. H.; Kim, J.; Kim, B. Magnetic Properties of Single-Crystalline CoSi Nanowires. *Nano Lett.* **2007**, *7* (5), 1240–1245.
- (12) Liang, S.; Islam, R.; Smith, D. J.; Bennett, P. A.; O'Brien, J. R.; Taylor, B. Magnetic Iron Silicide Nanowires on Si(110). *Appl. Phys. Lett.* **2006**, *88* (11), 1–3.
- (13) Junge, H.; Beller, M.; Agapova, A.; Ryabchuk, P.; Lund, H.; Junge, K.; Agostini, G.; Pohl,

M.-M. Intermetallic Nickel Silicide Nanocatalyst—A Non-Noble Metal-Based General Hydrogenation Catalyst. *Sci. Adv.* **2018**, *4* (6), eaat0761.

(14) Kumar, R.; Bahri, M.; Song, Y.; Gonell, F.; Thomas, C.; Ersen, O.; Sanchez, C.; Laberty-Robert, C.; Portehault, D. Phase Selective Synthesis of Nickel Silicide Nanocrystals in Molten Salts for Electrocatalysis of the Oxygen Evolution Reaction. *Nanoscale* **2020**, *12* (28), 15209–15213.

(15) Hausmann, J. N.; Beltrán-Suito, R.; Mebs, S.; Hlukhyy, V.; Fässler, T. F.; Dau, H.; Driess, M.; Menezes, P. W. Evolving Highly Active Oxidic Iron(III) Phase from Corrosion of Intermetallic Iron Silicide to Master Efficient Electrocatalytic Water Oxidation and Selective Oxygenation of 5-Hydroxymethylfurfural. *Adv. Mater.* **2021**, *33*, 2008823.

(16) Mccanney, J. M.; Schaak, R. E. Solution Synthesis of Metal Silicide Nanoparticles. *Inorg. Chem.* **2015**, *54* (3), 707–709.

(17) Kim, J. H.; Kawashima, K.; Wygant, B. R.; Mabayoje, O.; Liu, Y.; Wang, J. H.; Mullins, C. B. Transformation of a Cobalt Carbide (Co<sub>3</sub>C) Oxygen Evolution Precatalyst. *ACS Appl. Energy Mater.* **2018**, *1* (10), 5145–5150.

(18) Chen, P.; Xu, K.; Tong, Y.; Li, X.; Tao, S.; Fang, Z.; Chu, W.; Wu, X.; Wu, C. Cobalt Nitrides as a Class of Metallic Electrocatalysts for the Oxygen Evolution Reaction. *Inorg. Chem. Front.* **2016**, *3* (2), 236–242.

(19) Masa, J.; Barwe, S.; Andronescu, C.; Sinev, I.; Ruff, A.; Jayaramulu, K.; Elumeeva, K.; Konkena, B.; Roldan Cuenya, B.; Schuhmann, W. Low Overpotential Water Splitting Using Cobalt-Cobalt Phosphide Nanoparticles Supported on Nickel Foam. *ACS Energy Lett.* **2016**, *1* (6), 1192–1198.

(20) Gao, Q.; Huang, C. Q.; Ju, Y. M.; Gao, M. R.; Liu, J. W.; An, D.; Cui, C. H.; Zheng, Y. R.; Li, W. X.; Yu, S. H. Phase-Selective Syntheses of Cobalt Telluride Nanofleeces for Efficient Oxygen Evolution Catalysts. *Angew. Chemie - Int. Ed.* **2017**, *56* (27), 7769–7773.

(21) Fan, K.; Zou, H.; Lu, Y.; Chen, H.; Li, F.; Liu, J.; Sun, L.; Tong, L.; Toney, M. F.; Sui, M.; Yu, J. Direct Observation of Structural Evolution of Metal Chalcogenide in Electrocatalytic Water Oxidation. *ACS Nano* **2018**, *12* (12), 12369–12379.

(22) Masa, J.; Weide, P.; Peeters, D.; Sinev, I.; Xia, W.; Sun, Z.; Somsen, C.; Muhler, M.; Schuhmann, W. Amorphous Cobalt Boride (Co<sub>2</sub>B) as a Highly Efficient Nonprecious Catalyst for Electrochemical Water Splitting: Oxygen and Hydrogen Evolution. *Adv. Energy Mater.* **2016**, *6* (6), 1–10.

- (23) Masa, J.; Schuhmann, W. The Role of Non-Metallic and Metalloid Elements on the Electrocatalytic Activity of Cobalt and Nickel Catalysts for the Oxygen Evolution Reaction. *ChemCatChem* **2019**, *11* (24), 5842–5854.
- (24) Zhao, A.; Zhang, X.; Chen, X.; Guan, J.; Liang, C. Cobalt Silicide Nanoparticles in Mesoporous Silica as Efficient Naphthalene Hydrogenation Catalysts by Chemical Vapor Deposition. *J. Phys. Chem. C* **2010**, *114* (9), 3962–3967.
- (25) Zhang, L.; Chen, X.; Li, C.; Armbrüster, M.; Peng, Z.; Liang, C. Cobalt Silicides Nanoparticles Embedded in N-Doped Carbon as Highly Efficient Catalyst in Selective Hydrogenation of Cinnamaldehyde. *ChemistrySelect* **2018**, *3* (6), 1658–1666.
- (26) Zhang, L.; Chen, X.; Chen, Y.; Peng, Z.; Liang, C. Acid-Tolerant Intermetallic Cobalt-Nickel Silicides as Noble Metal-like Catalysts for Selective Hydrogenation of Phthalic Anhydride to Phthalide. *Catal. Sci. Technol.* **2019**, *9* (5), 1108–1116.
- (27) Zhang, M.; Pan, D.; Li, Y.; Yan, Z.; Meng, S.; Xie, J. Formation of Cobalt Silicide Nanoparticles on Graphene with a Synergistic Effect and High Stability for Ethanol Oxidation. *RSC Adv.* **2016**, *6* (36), 30293–30300.
- (28) Zhang, M.; Yan, Z.; Li, Y.; Jing, J.; Xie, J. Preparation of Cobalt Silicide on Graphene as Pt Electrocatalyst Supports for Highly Efficient and Stable Methanol Oxidation in Acidic Media. *Electrochim. Acta* **2015**, *161*, 48–54.
- (29) Ndolomingo, M. J.; Bingwa, N.; Meijboom, R. Review of Supported Metal Nanoparticles: Synthesis Methodologies, Advantages and Application as Catalysts. *J. Mater. Sci.* **2020**, *55* (15), 6195–6241.
- (30) Farrow, C. L.; Juhas, P.; Liu, J. W.; Bryndin, D.; Boin, E. S.; Bloch, J.; Proffen, T.; Billinge, S. J. L. PDFfit2 and PDFgui: Computer Programs for Studying Nanostructure in Crystals. *J. Phys. Condens. Matter* **2007**, *19* (33).
- (31) Madar, R.; D'Anterrosches, C.; Arnaud D'Avitaya, F.; Boursier, D.; Thomas, O.; Senateur, J. P. Magnetic and Transmission Electron Microscopy Studies of the Formation of Cobalt Silicide Thin Films. *J. Appl. Phys.* **1988**, *64* (6), 3014–3017.
- (32) Rakityanskaya, I. L.; Shein, A. B. Anodic Behavior of Iron, Cobalt, and Nickel Silicides in Alkaline Electrolytes. *Russ. J. Electrochem.* **2006**, *42* (11), 1208–1212.
- (33) Zieschang, A. M.; Bocarsly, J. D.; Schuch, J.; Reichel, C. V.; Kaiser, B.; Jaegermann, W.; Seshadri, R.; Albert, B. Magnetic and Electrocatalytic Properties of Nanoscale Cobalt Boride,

Co<sub>3</sub>B. *Inorg. Chem.* **2019**, *58* (24), 16609–16617.

(34) Hao, S. M.; Yu, M. Y.; Zhang, Y. J.; Abdelkrim, Y.; Qu, J. Hierarchical Mesoporous Cobalt Silicate Architectures as High-Performance Sulfate-Radical-Based Advanced Oxidization Catalysts. *J. Colloid Interface Sci.* **2019**, *545*, 128–137.

(35) García-Méndez, M.; Castellón, F. F.; Hirata, G. A.; Fariás, M. H.; Beamson, G. XPS and HRTEM Characterization of Cobalt-Nickel Silicide Thin Films. *Appl. Surf. Sci.* **2000**, *161* (1), 61–73.

(36) Kichigin, V. I.; Shein, A. B. Anodic Behavior of Cobalt Silicides in Potassium Hydroxide Solutions. *Prot. Met. Phys. Chem. Surfaces* **2013**, *49* (3), 336–343.

(37) Van Campen, D. G.; Klebanoff, L. E. Spin-Resolved and High-Energy-Resolution XPS Studies of the 3s and 2s Levels of Metallic Cobalt. *Phys. Rev. B* **1994**, *49* (3), 2040–2046.

(38) D'Accriscio, F.; Schrader, E.; Sassoye, C.; Selmane, M.; André, R. F.; Lamaison, S.; Wakerley, D.; Fontecave, M.; Mougel, V.; Le Corre, G.; Grützmacher, H.; Sanchez, C.; Carenco, S. A Single Molecular Stoichiometric P-Source for Phase-Selective Synthesis of Crystalline and Amorphous Iron Phosphide Nanocatalysts. *ChemNanoMat* **2020**, *6* (8), 1208–1219.

(39) Benseghir, Y.; Lemarchand, A.; Duguet, M.; Mialane, P.; Gomez-Mingot, M.; Roch-Marchal, C.; Pino, T.; Ha-Thi, M. H.; Haouas, M.; Fontecave, M.; Dolbecq, A.; Sassoye, C.; Mellot-Draznieks, C. Co-Immobilization of a Rh Catalyst and a Keggin Polyoxometalate in the UiO-67 Zr-Based Metal-Organic Framework: In Depth Structural Characterization and Photocatalytic Properties for CO<sub>2</sub> Reduction. *J. Am. Chem. Soc.* **2020**, *142* (20), 9428–9438.

(40) Daoura, O.; Fornasieri, G.; Boutros, M.; El Hassan, N.; Beaunier, P.; Thomas, C.; Selmane, M.; Miche, A.; Sassoye, C.; Ersen, O.; Baaziz, W.; Massiani, P.; Bleuzen, A.; Launay, F. One-Pot Prepared Mesoporous Silica SBA-15-like Monoliths with Embedded Ni Particles as Selective and Stable Catalysts for Methane Dry Reforming. *Appl. Catal. B Environ.* **2021**, *280*, 119417.

(41) Cullity, B. D.; Graham, C. D. *Introduction to Magnetic Materials*; Wiley, 2011.

(42) Zhang, H.; Zeng, D.; Liu, Z. The Law of Approach to Saturation in Ferromagnets Originating from the Magnetocrystalline Anisotropy. *J. Magn. Magn. Mater.* **2010**, *322* (16), 2375–2380.

(43) Osuna, J.; De Caro, D.; Amiens, C.; Chaudret, B.; Snoeck, E.; Respaud, M.; Broto, J. M.; Fert, A. Synthesis, Characterization, and Magnetic Properties of Cobalt Nanoparticles from an

Organometallic Precursor. *J. Phys. Chem.* **1996**, *100* (35), 14571–14574.

(44) Nishikawa, M.; Kita, E.; Erata, T.; Tasaki, A. Enhanced Magnetization in Co/MgO Multilayer Thin Films. *J. Magn. Magn. Mater.* **1993**, *126* (1–3), 303–306.

(45) Gao, M.; Cao, X.; Gao, Q.; Xu, Y.; Zheng, Y.; Jiang, J.; Yu, S. Nitrogen-Doped Graphene Supported CoSe<sub>2</sub> Nanobelt Composite Catalyst for Efficient Water Oxidation. *ACS Nano* **2014**, No. 4, 3970–3978.

(46) Elumeeva, K.; Masa, J.; Medina, D.; Ventosa, E.; Seisel, S.; Kayran, Y. U.; Genç, A.; Bobrowski, T.; Weide, P.; Arbiol, J.; Muhler, M.; Schuhmann, W. Cobalt Boride Modified with N-Doped Carbon Nanotubes as a High-Performance Bifunctional Oxygen Electrocatalyst. *J. Mater. Chem. A* **2017**, *5* (40), 21122–21129.

(47) Ma, X.; Wen, J.; Zhang, S.; Yuan, H.; Li, K.; Yan, F.; Zhang, X.; Chen, Y. Crystal Co<sub>x</sub>B (x = 1-3) Synthesized by a Ball-Milling Method as High-Performance Electrocatalysts for the Oxygen Evolution Reaction. *ACS Sustain. Chem. Eng.* **2017**, *5* (11), 10266–10274.

(48) Yang, J.; Liu, H.; Martens, W. N.; Frost, R. L. Synthesis and Characterization of Cobalt Hydroxide, Cobalt Oxyhydroxide, and Cobalt Oxide Nanodiscs. *J. Phys. Chem. C* **2010**, *114* (1), 111–119.

(49) Biesinger, M. C.; Payne, B. P.; Grosvenor, A. P.; Lau, L. W. M.; Gerson, A. R.; Smart, R. S. C. Resolving Surface Chemical States in XPS Analysis of First Row Transition Metals, Oxides and Hydroxides: Cr, Mn, Fe, Co and Ni. *Appl. Surf. Sci.* **2011**, *257* (7), 2717–2730.

(50) Weidler, N.; Paulus, S.; Schuch, J.; Klett, J.; Hoch, S.; Stenner, P.; Maljusch, A.; Brötz, J.; Wittich, C.; Kaiser, B.; Jaegermann, W. CoO<sub>x</sub> Thin Film Deposited by CVD as Efficient Water Oxidation Catalyst: Change of Oxidation State in XPS and Its Correlation to Electrochemical Activity. *Phys. Chem. Chem. Phys.* **2016**, *18* (16), 10708–10718.

(51) Qiao, L.; Xiao, H. Y.; Meyer, H. M.; Sun, J. N.; Rouleau, C. M.; Paretzky, A. A.; Geohegan, D. B.; Ivanov, I. N.; Yoon, M.; Weber, W. J.; Biegalski, M. D. Nature of the Band Gap and Origin of the Electro-/Photo-Activity of Co<sub>3</sub>O<sub>4</sub>. *J. Mater. Chem. C* **2013**, *1* (31), 4628–4633.

(52) Shen, Y.; Cao, Z.; Wu, Y.; Cheng, Y.; Xue, H.; Zou, Y.; Liu, G.; Yin, D.; Cavallo, L.; Wang, L.; Ming, J. Catalysis of Silica-Based Anode (de-)Lithiation: Compositional Design within a Hollow Structure for Accelerated Conversion Reaction Kinetics. *J. Mater. Chem. A* **2020**, *8* (25), 12306–12313.



# Chapter IV. Synthesis of Na<sub>4</sub>Si<sub>4</sub>

## IV.1 Zintl phase Na<sub>4</sub>Si<sub>4</sub>

This chapter is dedicated to the synthesis of an important precursor for our synthesis approaches. Na<sub>4</sub>Si<sub>4</sub> is a Zintl phase that contains tetrahedral polyanions [Si<sub>4</sub>]<sup>4-</sup>, which are isoelectronic and then isostructural to the P<sub>4</sub> molecule (**Figure IV-1**). They are compensated by Na<sup>+</sup> cations as a result of charge transfer from electropositive sodium to silicon. The [Si<sub>4</sub>]<sup>4-</sup> clusters are highly reactive, which has been discussed to provide a potential portable hydrogen source upon reaction with water.<sup>1</sup> Additionally, the low oxidation state of silicon and the fact that Si is only involved in intra-cluster bonds, which provides high flexibility for designing silicon-based materials under mild conditions. For instance, depending on the conditions of decomposition, Na<sub>4</sub>Si<sub>4</sub> yields readily silicon clathrates<sup>2,3</sup> or silicon nanoparticles.<sup>4</sup>

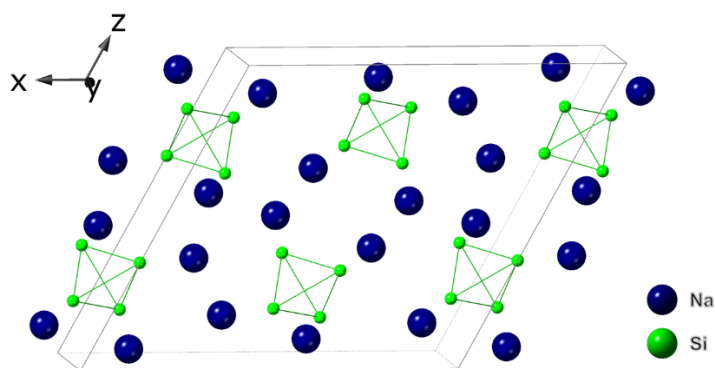


**Figure IV-1** Schematic crystal structure of Na<sub>4</sub>Si<sub>4</sub>.

Unfortunately, Na<sub>4</sub>Si<sub>4</sub> is usually accompanied by elemental silicon and sodium impurities,<sup>2,3,5-10</sup> which are detrimental to the precise control of the reactions where sodium silicide is used afterward. For instance, Si impurities are relatively inert and remain in the final product. Na impurities can also act as additional reducing agent,<sup>11</sup> although they might be separated from Na<sub>4</sub>Si<sub>4</sub> by vacuum heating at 230~300 °C.<sup>5,6,8</sup> Hence, a synthesis procedure for high purity Na<sub>4</sub>Si<sub>4</sub> (*ca.* 90 mol. %) is yet to be developed.

The reaction between elemental sodium and silicon is the most known approach to obtain Na<sub>4</sub>Si<sub>4</sub> (**Table IV-1**).<sup>5,8</sup> To avoid sodium evaporation, the reagents must be sealed by arc-welding in tantalum or niobium tubes, further introduced into silica ampules or steel pressure vessels and heated at 650~750 °C for several days to one week. The procedure requires specific equipment and metal containers not readily available in most laboratories. It also requires special care to avoid the presence of sodium at the welded closure, which is detrimental to sealing and reproducibility.<sup>7</sup> Overall, the resulting material encompasses Na<sub>4</sub>Si<sub>4</sub> and excess elemental silicon and/or sodium. For instance, a stoichiometric mixture of silicon and sodium yields a mixture of Si and Na<sub>4</sub>Si<sub>4</sub> with a purity of *ca.* 44 mol. % (**Table IV-1**).<sup>3</sup> Another approach involves the reaction of sodium with silica gel to yield *ca.* 15 mol. % Na<sub>4</sub>Si<sub>4</sub> mixed with Na<sub>2</sub>SiO<sub>3</sub> (**Table IV-1**).<sup>12,13</sup> A third method of Na<sub>4</sub>Si<sub>4</sub> synthesis was reported first by Ma *et al.*,<sup>7</sup> who triggered the reaction between previously ball-milled sodium hydride and silicon powders at 420 °C under argon flow over several days. The procedure did not require any specific container nor sealing and then appeared simple, but a long ball-milling pretreatment of 0.5-1 h was required.<sup>6,14</sup> More important, the outcome strongly depended on experimental parameters, including the preliminary ball-milling time and especially the argon flow rate, since reaction intermediates (sodium) and by-products (dihydrogen) are volatile or gaseous at the reaction temperature. Therefore, despite the attractiveness of this procedure, reaching high purity (*ca.* 90 mol. %) sodium silicide remains an arduous task: a large excess of sodium hydride is required, while elemental silicon and sodium are commonly encountered as impurities.

**Table IV-1** Comparison of reported syntheses towards Na<sub>4</sub>Si<sub>4</sub>

Reactants	Setup	Ball-milling time	Reaction time	Reaction temperature	Purity	Purification procedure	Ref.
NaH+Si nanoparticles Na in 10 mol.% excess	Covered h-BN crucible in a quartz tube	2min	24h	395 °C	98%	/	This work
NaH+Si Na in 90 mol.% excess	Covered alumina crucible in a silica glass tube	30min	48h	420 °C	Na detected by XRD	/	14
NaH+Si Na in 60 mol.% excess	Covered alumina crucible	1h	48h	395 °C	/	Excess Na removed by vacuum at 250°C for 3h	6

Reactants	Setup	Ball-milling time	Reaction time	Reaction temperature	Purity	Purification procedure	Ref.
Na+Si Na in slight excess	Ta crucible sealed in stainless steel tube	/	72h	650 °C	/	Excess Na removed by evacuation at 300°C for 6h	2
Na+Si Na in 10 mol.% excess	Nb tube welded sealed in fused silica jacket	/	83h	650 °C	/	Excess Na removed by vacuum sublimation at 300°C	15
Na+Si Na in excess	Closed Ta container sealed in evacuated quartz glass ampoule	/	100h	750 °C	/	Excess Na removed by vacuum distillation at 230 °C and 5.10 <sup>-6</sup> mbar	5
Na+Si Na in 6 mol.% excess	Ni crucible sealed in steel autoclave	/	30-40h	650 °C	/	Excess Na removed at 240°C for 15-20h	9
Na+Si Na in 10 mol.% excess	W crucible sealed in stainless steel canister	/	36h	650 °C	Na in excess	/	10
Na+Si Stoichiometric mixture	Sealed Ta tube	/	1h10min	800-1200 °C	44% (Si in excess)	/	3
Na+silica gel	Sealed Erlenmeyer flask	/	/	400 °C	15%	/	13

Herein we report a procedure to enhance the reactivity of silicon with sodium hydride by using silicon nanoparticles as reagents and by carefully controlling experimental parameters (**Figure IV-2**). Thanks to this approach, we demonstrate the ability with regular lab equipment to reproducibly produce sodium silicide with a purity of *ca.* 98 mol.% and at the scale of several hundreds of milligrams, both features strongly exceeding those previously reported.<sup>7</sup> We then deliver a simple scalable protocol that will enable wide-spread use of this material. To exemplify the use of this material, we show that it is efficient in the selective synthesis of silicon clathrates.

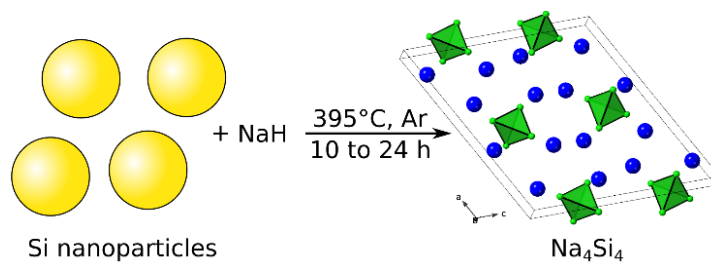


**Figure IV-2** Scheme of the synthesis route towards high purity  $\text{Na}_4\text{Si}_4$ .

## IV.2 Experimental methods

**Reagents:** Commercial NaH (95 %, Sigma-Aldrich) and bulk Si powder (99 %, Sigma-Aldrich) were used as received. Commercially available silicon nanoparticles (99 %) were obtained from Nanomakers<sup>®</sup> (**Figure IV-3**), France. All the reagents and products were stored and manipulated in an argon-filled glovebox free of  $\text{H}_2\text{O}$  (< 0.5 ppm) and  $\text{O}_2$  (< 0.5 ppm) and with standard Schlenk procedures. **Caution:** the  $\text{Na}_4\text{Si}_4$  powders produced by the procedure described herein are air sensitive and burn spontaneously when exposed to water. All manipulations described were performed by handling these powders under inert atmosphere, except when stated otherwise.

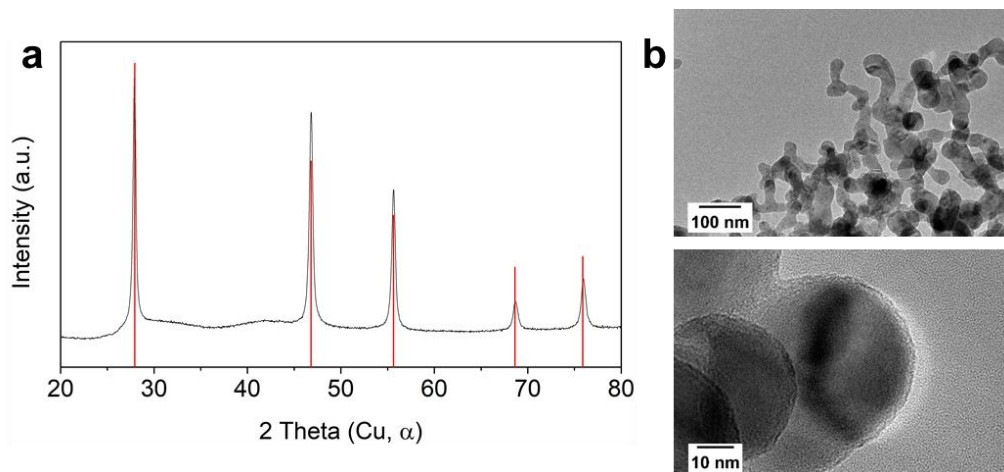


**Figure IV-3** (a) Powder XRD pattern (bottom) of Si nanoparticles used as reagents. The XRD pattern is indexed along the silicon diamond structure (red bars). (b) TEM images of as-received Si nanoparticles used as reagents.

**$\text{Na}_4\text{Si}_4$  synthesis from Si nanoparticles:** 470 mg of NaH (20 mmol) and 500 mg of Si nanoparticles (20 mmol) were firstly ball-milled for 2 minutes at 20 Hz (Retsch MM400 ball mill airtight stainless-steel vial of 50 mL, one steel ball of 62.3 g with a diameter of 23 mm). Then, the

fine powder was loaded in a pyrolytic h-BN crucible (cylinder Ø25×H60 mm) covered with a cap of pyrolytic h-BN, then placed in a bottom closed quartz tube. The tube was heated in a vertical furnace at 395 °C with different reaction times from 2 to 24 hours, under argon flow. The as-synthesized sample was made of a dark pellet with another white pellet on the top. The latter corresponds to Na<sub>2</sub>O and NaOH coming from the reaction between NaH and the native silicon oxide layer on the surface of Si nanoparticles (**Figure IV-3**). The upper white pellet was scratched away. The synthesis of Na<sub>4</sub>Si<sub>4</sub> under the optimal conditions described here was repeated 20 times to ensure reproducibility.

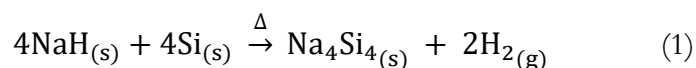
**Na<sub>4</sub>Si<sub>4</sub> synthesis from bulk Si powder:** The same procedure and reagents proportion described above were followed, but bulk Si powder was used instead of Si nanoparticles. The thermal treatment was performed at 395 °C for 10 hours.

**Si clathrates synthesis:** The Na<sub>4</sub>Si<sub>4</sub> powder (4 mmol) synthesized as described above was loaded in a pyrolytic h-BN crucible (Ø25×H60 mm) previously dried at 400 °C under vacuum (10<sup>-3</sup> mbar) for 10 hours to remove adsorbed moisture. The crucible was placed in a bottom-closed quartz tube. The tube was heated in a vertical furnace. Na<sub>8</sub>Si<sub>46</sub> (type I) and Na<sub>x</sub>Si<sub>136</sub> (type II) were obtained by heat treatment at 470 °C and 440 °C, respectively, under dynamic vacuum (10<sup>-3</sup> mbar) for 90 min. These temperatures were chosen according to the literature.<sup>2</sup> For Na<sub>8</sub>Si<sub>46</sub> (type I), the h-BN crucible was covered with an h-BN cap prior heating, to maintain a higher Na vapor pressure. For Na<sub>x</sub>Si<sub>136</sub> (type II), the crucible was maintained opened. During the reaction, a thin deposit of Na appeared on the upside cold part of the quartz tube. After dwelling and cooling down, the quartz tube with the h-BN crucible and its containment was transferred into an argon-filled glovebox without exposure to air.

## IV.3 Results and discussion

### IV.3.1 Optimal synthesis of Na<sub>4</sub>Si<sub>4</sub>

Reaction (1) between NaH and Si nanoparticles (1.1:1 mol. ratio) was performed for 24 hours at 395 °C with an argon flow of 55 mL min<sup>-1</sup>:



Under these optimal conditions, Na<sub>4</sub>Si<sub>4</sub> with optimized purity was obtained. The atomic ratio between Na and Si was evaluated to Na:Si = 1:1.02 by EDX analysis. The formation of Na<sub>4</sub>Si<sub>4</sub> (S.G. *C2/c*) was supported by Le Bail analysis of the powder XRD pattern (**Figure IV-4**). NaOH was also detected (**Figure IV-4**) and ascribed to leakage of air into the XRD sample holder during the long acquisition of the XRD diagram. This is confirmed by the fact that no crystalline NaOH was observed in a prior fast acquisition on a fresh sample (**Figure IV-4**).

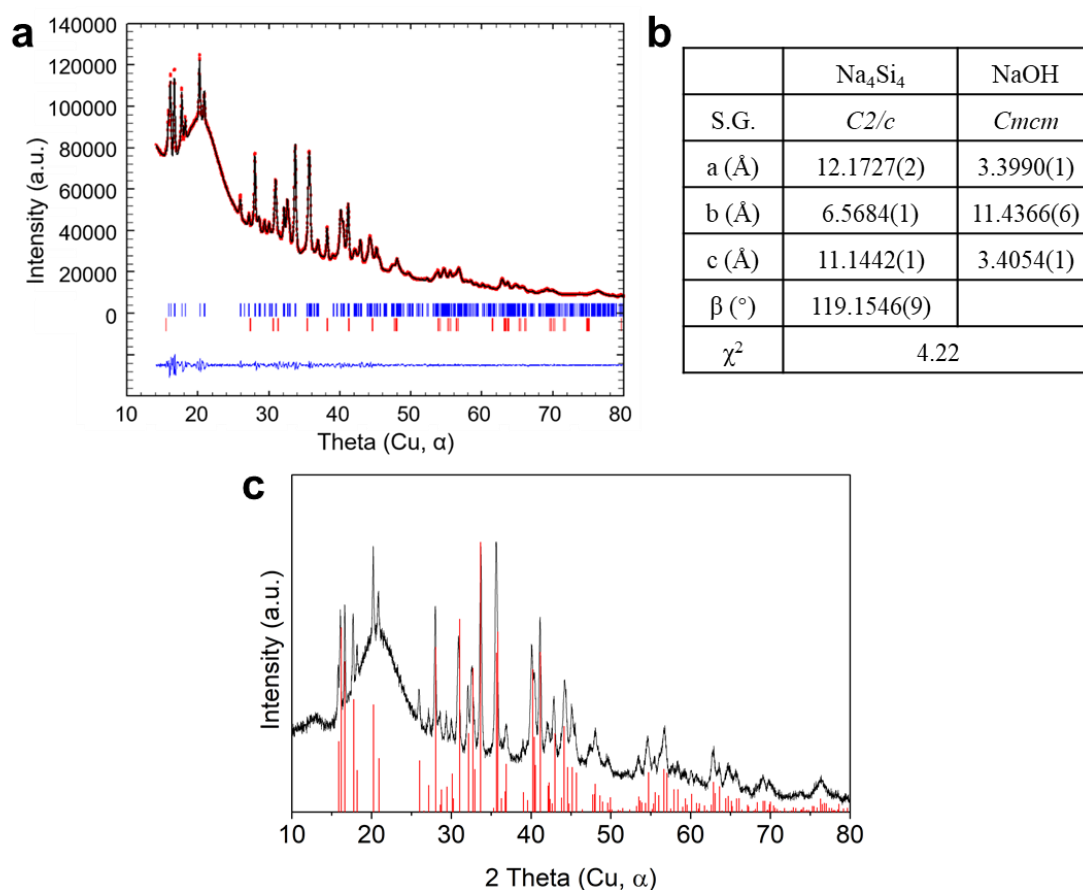


**Figure IV-4** (a) Le Bail analysis of the XRD pattern of the powder obtained after 24 h at 395 °C under 55 mL min<sup>-1</sup> Ar flow. The observed pattern, calculated pattern and difference curve are shown in red dots, black curve and blue curve, respectively. Upper blue and lower red tick marks correspond to Na<sub>4</sub>Si<sub>4</sub> and NaOH, respectively. (b) Na<sub>4</sub>Si<sub>4</sub> lattice parameters obtained by Le Bail analysis. (c) Quickly acquired (5 min) powder XRD pattern of the same Na<sub>4</sub>Si<sub>4</sub> sample. Red drop lines indicate Na<sub>4</sub>Si<sub>4</sub> reference.

The <sup>29</sup>Si MAS solid-state NMR spectrum of Na<sub>4</sub>Si<sub>4</sub> (**Figure IV-5**) shows two resonances centered at -362 and -366 ppm corresponding respectively to the two crystallographic non-equivalent Si sites in the crystal structure.<sup>5</sup> This upfield shift compared to silicon is due to electron transfer from Na to Si.<sup>8</sup> Besides, neither broad signal of amorphous SiO<sub>2</sub> and Si centered at

*ca.* - 110 and - 40 ppm<sup>16,17</sup> nor any contribution of *d*-Si expected at *ca.* - 80 ppm<sup>18</sup> is observed. It thus confirms the high purity of Na<sub>4</sub>Si<sub>4</sub>. The <sup>23</sup>Na spectrum (**Figure IV-5**) shows two quadrupolar resonance patterns at 56.3 ppm ( $C_Q = 1.32$  MHz,  $\eta_Q = 0.47$ ) and 49.8 ppm ( $C_Q = 2.34$  MHz,  $\eta_Q = 0.27$ ) corresponding to two Na crystallographic sites in Na<sub>4</sub>Si<sub>4</sub>. In addition, no peak at *ca.* 50 ppm corresponding to Na<sub>2</sub>O could be detected,<sup>19</sup> suggesting no contamination from the upper white pellet made mainly of Na<sub>2</sub>O and of a minor portion of NaOH (**Figure IV-6**). The thin peak at 18.5 ppm is assigned to crystalline NaOH accounting for less than 5 % of the total amount of sodium.<sup>20</sup> Because crystalline NaOH could not be detected by XRD, its observation by NMR is ascribed to the degradation of Na<sub>4</sub>Si<sub>4</sub> during preparation of NMR analyses.

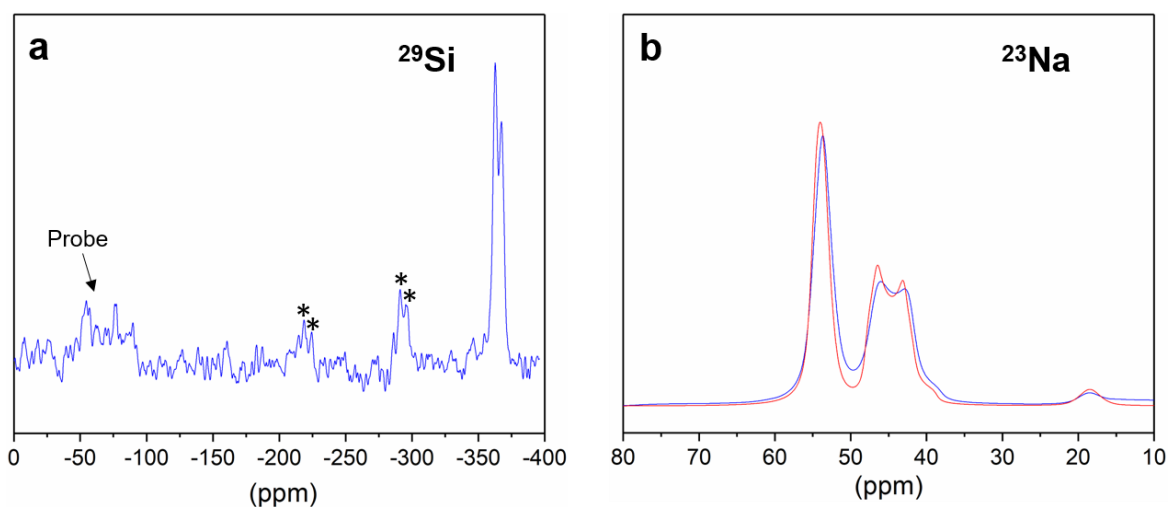


**Figure IV-5** <sup>29</sup>Si and (b) <sup>23</sup>Na solid-state NMR spectra of the Na<sub>4</sub>Si<sub>4</sub> powder obtained after 24 h at 395 °C under 55 mL min<sup>-1</sup> Ar flow. Asterisks indicate spinning sidebands. The measured spectra are shown by the blue curves, and the fitting curve is shown in red.

Overall, EDX, XRD and NMR support the formation of crystalline Na<sub>4</sub>Si<sub>4</sub>. EDX yields a purity of *ca.* 98 mol. %, and amorphous Si is the main impurity. The synthesis yield is about 80 %, which corresponds to *ca.* 700 mg of powders, *i.e.*, 10 times increase compared to previous approaches using the reaction between sodium hydride and silicon (**Table IV-1**). This result is achieved with only a slight excess of sodium hydride reagent (10 mol. %) compared to previous reports (60-90 mol. % excess) (**Table IV-1**),<sup>6,14</sup> which enables bypassing purification steps (**Table IV-1**). The preliminary ball-milling time is also shortened from over 30 min to only 2 min and the reaction time is further reduced to 24 h. A comparison with the most commonly used reaction between elemental sodium and silicon (**Table IV-1**) shows that the reaction time and the temperature are strongly reduced with the approach we describe herein, while purification steps and complex set-ups encompassing metal containers are avoided.

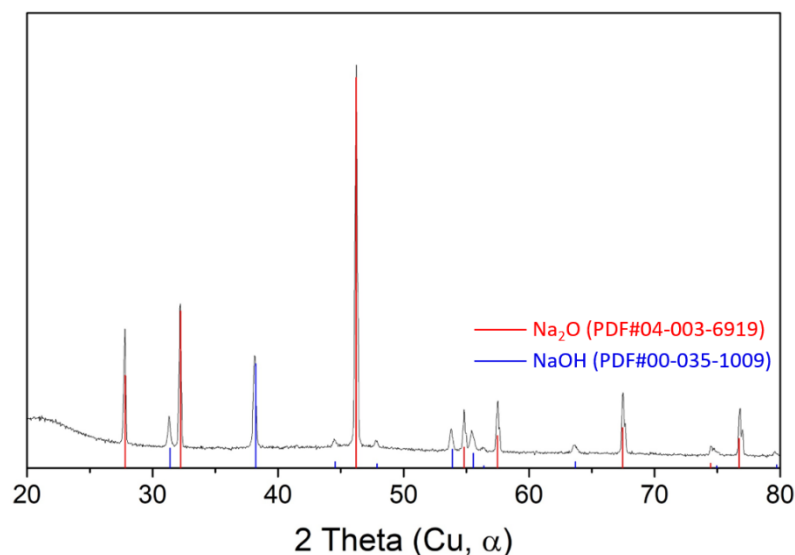


**Figure IV-6** Powder XRD pattern of the white pellet on the top of the as-prepared product of  $\text{Na}_4\text{Si}_4$  synthesis.

#### IV.3.2 Impact of the Si source

To assess the role of the silicon source in the synthesis, we have followed the same protocol as above but by using bulk Si powder as precursor. The reaction was performed over 10 h under  $15 \text{ mL min}^{-1}$  Ar flow rate. The initial NaH:Si ratio was kept at 1.1:1 mol. The resulting product was pale grey aggregates. According to XRD (**Figure IV-7**), the main crystalline phases are unreacted Na and Si. Therefore, silicon nanoparticles play a primary role in the completion of the reaction at low temperature and short time. Their higher reactivity ensures a reaction in close-to-stoichiometry reagents ratio compared to bulk Si that required a large excess of NaH (NaH:Si = 1.9:1 mol.) to yield  $\text{Na}_4\text{Si}_4$  as major product.<sup>7,21</sup> Note also that while bulk Si required ball-milling over 1 hour,<sup>6,7</sup> using Si nanoparticles enables shortening the milling step down to 2 min. Likewise, the reaction was performed over 10 to 24 h compared to more than two days as reported for bulk silicon.<sup>7</sup>

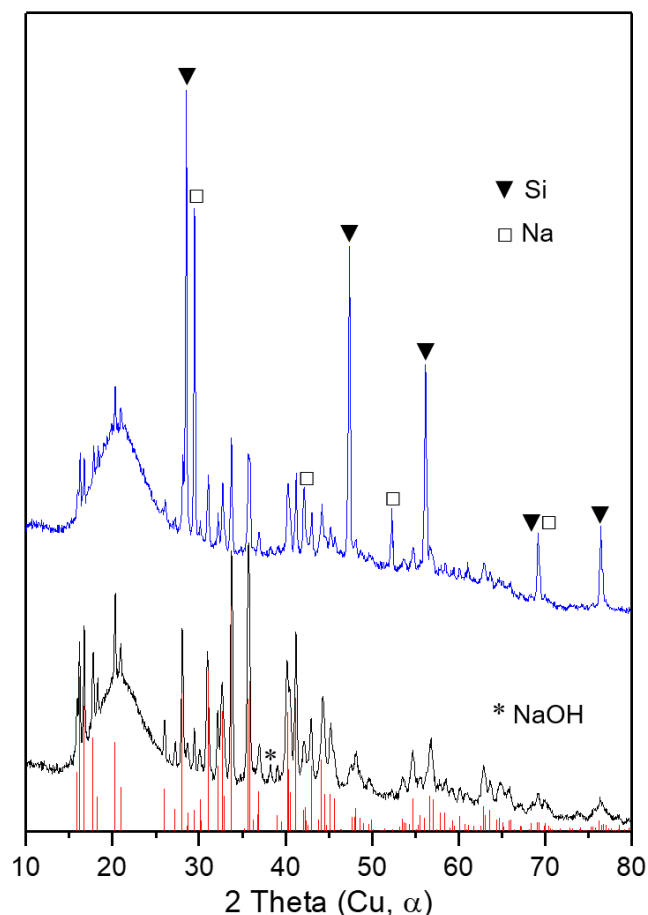


**Figure IV-7** Powder XRD patterns of the  $\text{Na}_4\text{Si}_4$  samples synthesized respectively with Si nanoparticles (black bottom curve) and bulk Si powder (blue top curve) at 395 °C for 10 hours with an Ar flow rate 15 mL min<sup>-1</sup>. Red lines indicate  $\text{Na}_4\text{Si}_4$  reference. Si, Na, and NaOH impurities are marked on the most informative peaks.

### IV.3.3 Impact of the reaction time

By using Si nanoparticles, we varied the reaction time from 2 to 24 hours to investigate the course of the reaction. XRD (**Figure IV-8**) shows that a 2 h reaction produces crystalline  $\text{Na}_4\text{Si}_4$  together with Na and Si, as minor phases. The absence of peaks assigned to  $\text{Na}_2\text{O}$  confirmed the thorough separation of  $\text{Na}_4\text{Si}_4$  from oxidic side-products. The NaOH observed is again attributed to air leaks of the XRD sample holder over XRD pattern acquisition. Increasing the reaction time to 10 h decreases the relative intensity of Na and Si peaks. Further decrease of the XRD peak occurs from 10 to 24 h. It confirms that Si nanoparticles allow shortening the reaction time to

24 h. Note that the XRD pattern obtained at 10 hours is similar to the one previously reported for Na<sub>4</sub>Si<sub>4</sub> produced from bulk silicon over 2 days.<sup>7</sup>

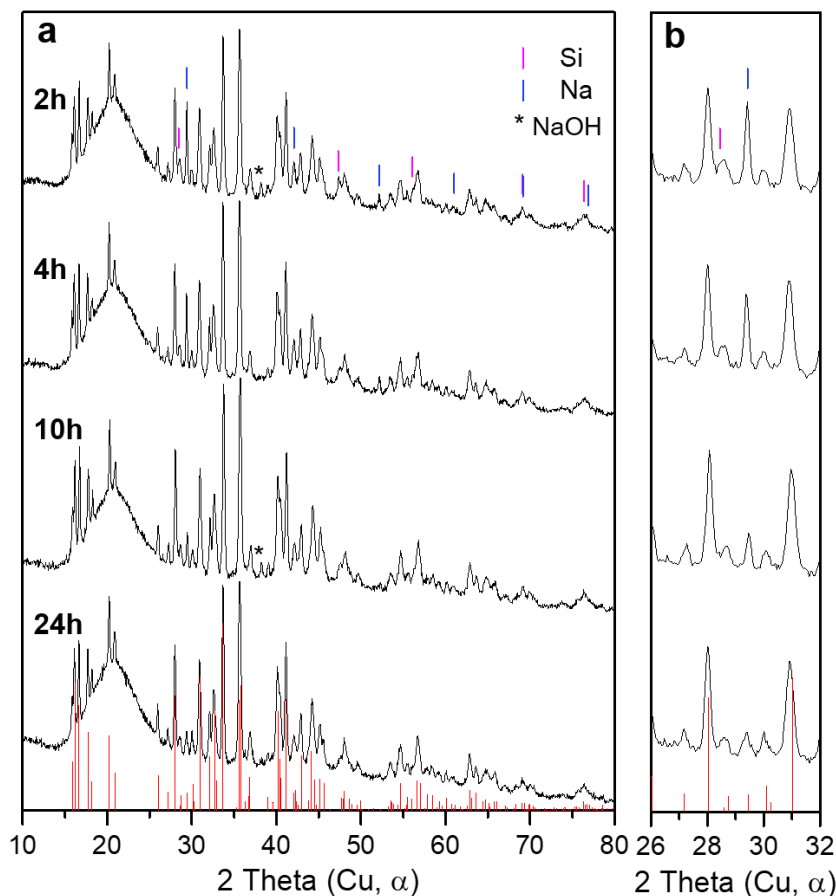


**Figure IV-8** (a) Powder XRD patterns of Na<sub>4</sub>Si<sub>4</sub> samples synthesized during various reaction times at 395 °C with a 15 mL min<sup>-1</sup> Ar flow. Red lines account for Na<sub>4</sub>Si<sub>4</sub> reference. Si, Na, and NaOH impurities are marked on the most informative peaks. (b) An enlarged view of the XRD pattern in the range of 26–32 °.

Comparison of the results from bulk Si and Si nanoparticles shows a dramatic reduction of reaction time that we ascribe to the reactivity of Si nanoparticles, in relation to their larger interface between NaH and Si, and shorter atomic diffusion paths.

#### IV.3.4 Impact of the argon flow rate

Ma *et al.* described that a large argon flow rate (50 mL min<sup>-1</sup>) resulted in excess Si, while residual Na was observed when using moderate argon flow rate (10 mL min<sup>-1</sup>).<sup>7</sup> This reaction sensitivity *versus* gas-flow-rate comes from two sides. Firstly, H<sub>2</sub> gas forms during the reaction (1). Secondly, reaction (1) proceeds by decomposition of NaH at *ca.* 317 °C<sup>22</sup> into Na, which then

reacts with silicon. Nonetheless, Na is also volatile at the temperature of synthesis and can leave the reaction medium depending on the argon flow rate. Herein, the reaction was performed at 395 °C in 10 hours under different Ar flow rates (NaH:Si = 1.1:1) to study the impact of Ar flow on the completion of the reaction. XRD (**Figure IV-9**) shows that the relative peak intensities for the Na impurity barely changed with the Ar flow rates and that the product Na<sub>4</sub>Si<sub>4</sub> is always the major crystalline product. Therefore, the influence of Ar flow on the reaction appears negligible in the range 15-100 mL min<sup>-1</sup> when using silicon nanoparticles, contrary to the bulk silicon source.<sup>7</sup> Hence, the higher reactivity of Si nanoparticles ensures reaction of sodium and silicon before sodium leaves the reaction medium by evaporation. The ability to perform the reaction with low dependency *versus* the Ar flow rate improves strongly the repeatability of the synthesis.

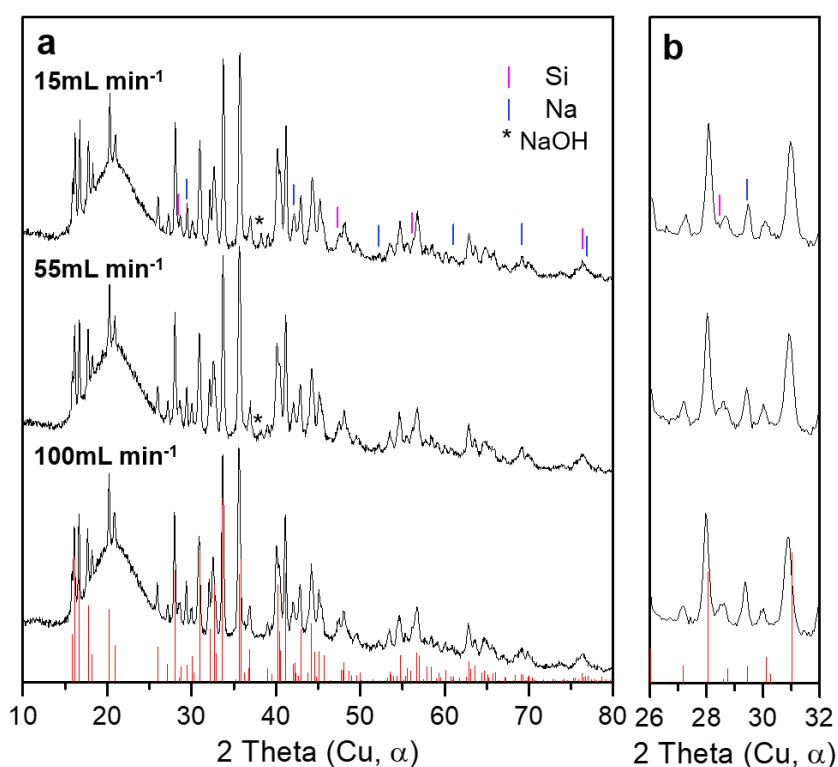


**Figure IV-9** Powder XRD patterns of Na<sub>4</sub>Si<sub>4</sub> samples synthesized with different Ar flow rates at 395 °C with a reaction time of 10 hours. Red lines account for Na<sub>4</sub>Si<sub>4</sub> reference. Si, Na, and NaOH impurities are marked on the most informative peaks, where NaOH is ascribed to incidental oxidation of sample. (b) An enlarged view of the XRD pattern in the range of 26–32 °.

#### IV.4 Simple approach to silicon clathrates

Silicon clathrates hold cage structures based on 4-coordinated silicon atoms (**Figure IV-10**). These tetrahedral frameworks can adopt a wide range of elemental substitutions to tune thermal, electrical and thermoelectric properties among others.<sup>23,24</sup> To assess the usefulness of the as-synthesized sodium silicide as precursor for inorganic synthesis, we have studied its thermal decomposition as a well-known pathway to type I  $\text{Na}_8\text{Si}_{46}$  and type II  $\text{Na}_x\text{Si}_{136}$  ( $0 \leq x \leq 24$ ) silicon clathrates.

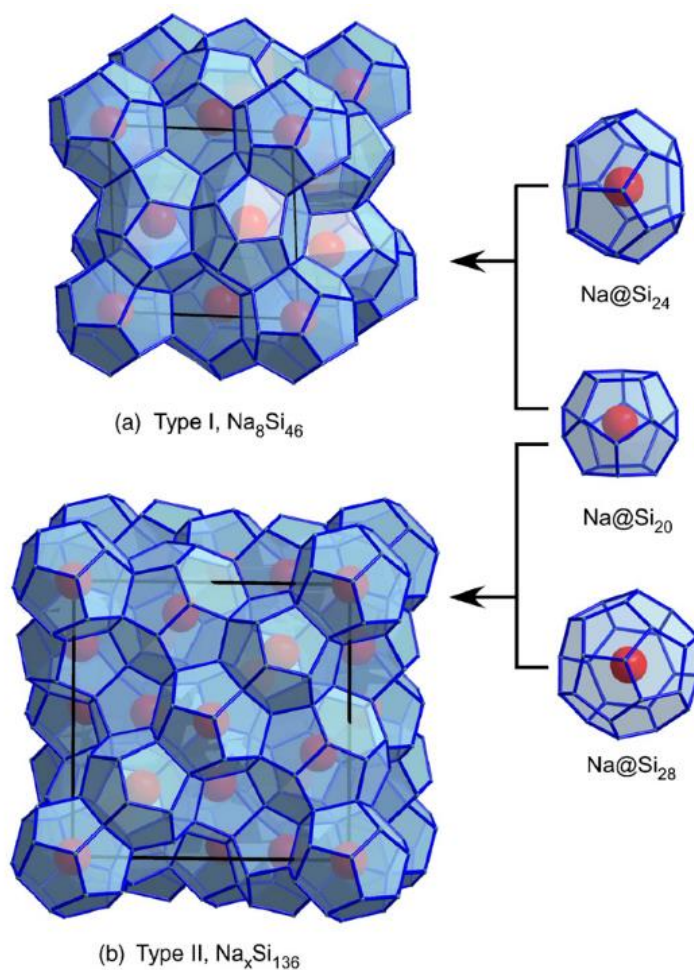


**Figure IV-10** Schematic structural model of clathrate compounds: (a) type I  $\text{Na}_8\text{Si}_{46}$  and (b) type II  $\text{Na}_x\text{Si}_{136}$ .<sup>2</sup>

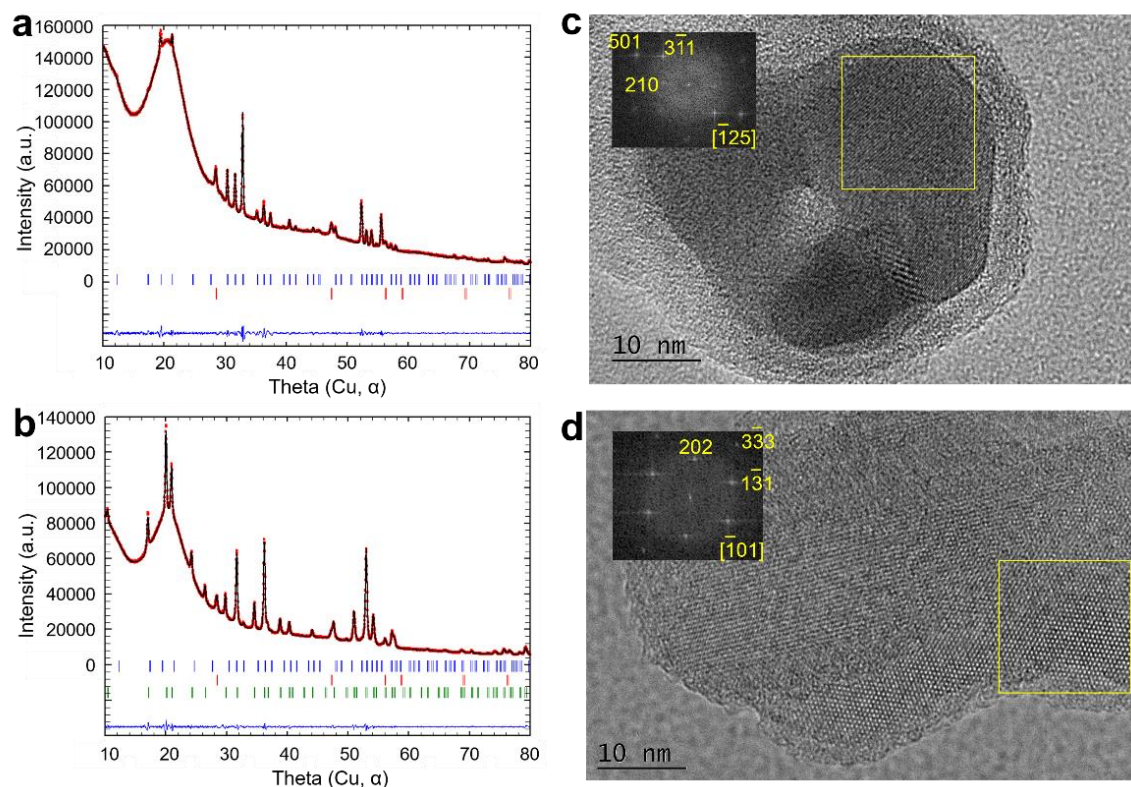


**Figure IV-11** (a, b) Le Bail analysis of the powder XRD patterns of products obtained by Na<sub>4</sub>Si<sub>4</sub> thermal decomposition at (a) 470 and (b) 440 °C. The observed pattern, calculated pattern and difference curve are shown in red, black line and blue, respectively. Blue, green and red tick marks correspond to Na<sub>8</sub>Si<sub>46</sub> (type I), Na<sub>x</sub>Si<sub>136</sub> (type II) and Si, respectively. HRTEM images and corresponding Fast Fourier Transforms (FFTs) of powders obtained at (c) 470 °C and (d) 440 °C. FFTs are indexed along the (c) type I and (d) type II silicon clathrate structures.

Type I and type II silicon clathrates are generally obtained by thermal decomposition<sup>2,6</sup> or oxidation<sup>3</sup> of Na<sub>4</sub>Si<sub>4</sub>. Thermal decomposition of Na<sub>4</sub>Si<sub>4</sub> under vacuum at 400-500 °C yields type I and type II clathrates,<sup>2,6</sup> with phase selectivity depending on various factors that are related to the vapor pressure of sodium. The impurities were the other type I/type II clathrate and *d*-Si. By using a setup to control the Na relative pressure, Krishna *et al.* reported a phase selective approach to type II clathrates.<sup>6</sup> By aiming for a simple and straightforward procedure, we have thermally decomposed the as-synthesized Na<sub>4</sub>Si<sub>4</sub> in a very simple setup. It consists in an h-BN crucible introduced in a bottom-closed quartz tube heated in a vertical oven under dynamic vacuum (10<sup>-3</sup> mbar).

Le Bail analysis of powder XRD patterns (**Figure IV-11** and **Table IV-2**) shows that the samples obtained by decomposition of Na<sub>4</sub>Si<sub>4</sub> at 470 °C with a closed crucible and 440 °C with an opened crucible contain Na<sub>8</sub>Si<sub>46</sub> and Na<sub>x</sub>Si<sub>136</sub> as major phases, respectively. HRTEM images of

the corresponding powders are also indexed against the Na<sub>8</sub>Si<sub>46</sub> (**Figure IV-11c**) and Na<sub>x</sub>Si<sub>136</sub> (**Figure IV-11d**) structures, respectively, thus confirming the identity of the phases. In **Figure IV-11c**, the amorphous oxide layer on the surface is ascribed to SiO<sub>x</sub> or sodium silicate generated during sample manipulation.

**Table IV-2** Lattice parameters obtained by Le Bail analysis of the XRD pattern of the clathrate powders obtained by Na<sub>4</sub>Si<sub>4</sub> thermal decomposition at 470 and 440 °C.

	Space group	a <sub>470°C</sub> (Å)	a <sub>440°C</sub> (Å)
Na <sub>8</sub> Si <sub>46</sub>	Pm-3n	10.1943(1)	10.2050(3)
Na <sub>x</sub> Si <sub>136</sub>	Fd-3m		14.6581(1)
Si	Fd3-m	5.4248(1)	5.4418(2)
χ <sup>2</sup>		4.78	4.17

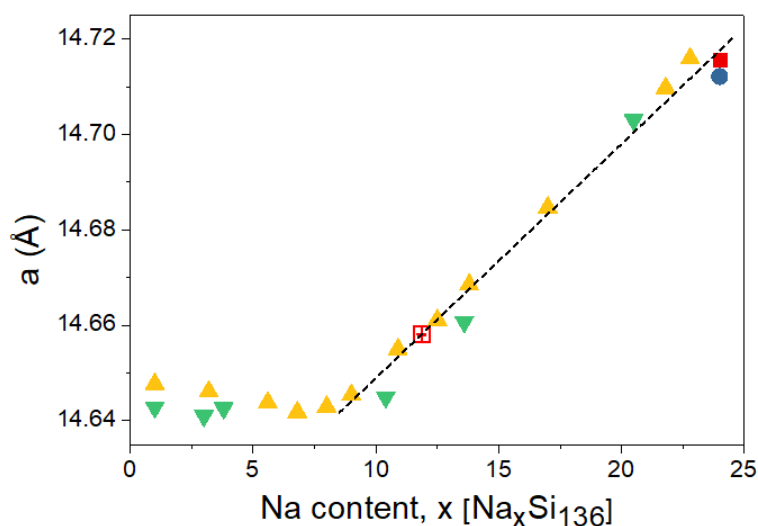


**Figure IV-12** a lattice parameter evolution with the Na content of Na<sub>x</sub>Si<sub>136</sub> (0 ≤ x ≤ 24) clathrate. Solid red square, blue circle, yellow and green triangles represent data reported by Beekman *et al.*,<sup>25</sup> Stefanoski *et al.*,<sup>26</sup> Beekman *et al.*,<sup>27</sup> and Renny *et al.*,<sup>24</sup> respectively, while the empty red square corresponds to this work. The broken line corresponds to data linear fit.

The electronic and thermal properties of Na<sub>x</sub>Si<sub>136</sub> (0 ≤ x ≤ 24) type II clathrates depend strongly on the occupancy of structural cages by Na.<sup>24</sup> Therefore, we have estimated the *x* value according to the dependency of the *a* cell parameter as a function of *x* (**Figure IV-12**). We retrieve an overall composition of Na<sub>11.86(2)</sub>Si<sub>136</sub> corresponding to a partial occupancy of Na sites.<sup>2,28</sup>

## IV.5 Conclusion

Herein we have shown that using silicon nanoparticles as chemical reagents provides a convenient way to solve usual limitations of the synthesis of silicon compounds with poor thermal stability and from poorly reactive elemental silicon: the high reactivity of silicon nanoparticles enables synthesis at high yield, close to the theoretical reagent stoichiometry, and at lowered temperature below the decomposition threshold of the product, thus significantly enhancing its purity. It also enhances the robustness of the synthesis *versus* experimental conditions, especially by eliminating the dependence of the reaction *versus* gas flow. We demonstrated that the as-obtained  $\text{Na}_4\text{Si}_4$  powder is a convenient precursor towards the selective synthesis of type I and type II silicon clathrates, thus supporting the relevance of the material for further use towards silicon-based materials. In the next chapter, the use of  $\text{Na}_4\text{Si}_4$  as reagent for synthesis of intermetallic binary nickel silicides and ternary nickel silicophosphides will be discussed.

## References

- (1) Agrawal, T.; Ajitkumar, R.; Prakash, R.; Nandan, G. Sodium Silicide As A Hydrogen Source for Portable Energy Devices: A Review. *Mater. Today Proc.* **2018**, *5* (2), 3563–3570.
- (2) Horie, H. omi; Kikudome, T.; Teramura, K.; Yamanaka, S. Controlled Thermal Decomposition of NaSi to Derive Silicon Clathrate Compounds. *J. Solid State Chem.* **2009**, *182* (1), 129–135.
- (3) Simon, P.; Tang, Z.; Carrillo-Cabrera, W.; Chiong, K.; Böhme, B.; Baitinger, M.; Lichte, H.; Grin, Y.; Guloy, A. M. Synthesis and Electron Holography Studies of Single Crystalline Nanostructures of Clathrate-II Phases K<sub>x</sub>Ge<sub>136</sub> and Na<sub>x</sub>Si<sub>136</sub>. *J. Am. Chem. Soc.* **2011**, *133* (19), 7596–7601.
- (4) Nolan, B. M.; Henneberger, T.; Waibel, M.; Fässler, T. F.; Kauzlarich, S. M. Silicon Nanoparticles by the Oxidation of [Si<sub>4</sub>]<sup>4-</sup> and [Si<sub>9</sub>]<sup>4-</sup>-Containing Zintl Phases and Their Corresponding Yield. *Inorg. Chem.* **2015**, *54* (1), 396–401.
- (5) Goebel, T.; Prots, Y.; Haarmann, F. Refinement of the Crystal Structure of Tetrasodium Tetrasilicide, Na<sub>4</sub>Si<sub>4</sub>. *Zeitschrift für Krist. - New Cryst. Struct.* **2008**, *223* (3), 187–188.
- (6) Krishna, L.; Baranowski, L. L.; Martinez, A. D.; Koh, C. A.; Taylor, P. C.; Tamboli, A. C.; Toberer, E. S. Efficient Route to Phase Selective Synthesis of Type II Silicon Clathrates with Low Sodium Occupancy. *CrystEngComm* **2014**, *16* (19), 3940–3949.
- (7) Ma, X.; Xu, F.; Atkins, T. M.; Goforth, A. M.; Neiner, D.; Navrotsky, A.; Kauzlarich, S. M. A Versatile Low Temperature Synthetic Route to Zintl Phase Precursors: Na<sub>4</sub>Si<sub>4</sub>, Na<sub>4</sub>Ge<sub>4</sub> and K<sub>4</sub>Ge<sub>4</sub> as Examples. *J. Chem. Soc. Dalton Trans.* **2009**, No. 46, 10250–10255.
- (8) Mayeri, D.; Phillips, B. L.; Augustine, M. P.; Kauzlarich, S. M. NMR Study of the Synthesis of Alkyl-Terminated Silicon Nanoparticles from the Reaction of SiCl<sub>4</sub> with the Zintl Salt, NaSi. **2001**, *727* (14), 765–770.
- (9) Cabrera, R. Q.; Salamat, A.; Barkalov, O. I.; Leynaud, O.; Hutchins, P.; Daisenberger, D.; Machon, D.; Sella, A.; Lewis, D. W.; McMillan, P. F. Pressure-Induced Structural Transformations of the Zintl Phase Sodium Silicide. *J. Solid State Chem.* **2009**, *182* (9), 2535–2542.
- (10) Blosser, M. C.; Nolas, G. S. Synthesis of Na<sub>8</sub>Si<sub>46</sub> and Na<sub>24</sub>Si<sub>136</sub> by Oxidation of Na<sub>4</sub>Si<sub>4</sub> from Ionic Liquid Decomposition. *Mater. Lett.* **2013**, *99*, 161–163.
- (11) Kumar, R.; Bahri, M.; Song, Y.; Gonell, F.; Thomas, C.; Ersen, O.; Sanchez, C.; Laberty-Robert, C.; Portehault, D. Phase Selective Synthesis of Nickel Silicide Nanocrystals in Molten

Salts for Electrocatalysis of the Oxygen Evolution Reaction. *Nanoscale* **2020**, *12* (28), 15209–15213.

(12) Shatnawi, M.; Paglia, G.; Dye, J. L.; Cram, K. C.; Lefenfeld, M.; Billinge, S. J. L. Structures of Alkali Metals in Silica Gel Nanopores: New Materials for Chemical Reductions and Hydrogen Production. *J. Am. Chem. Soc.* **2007**, *129* (5), 1386–1392.

(13) Dye, J. L.; Cram, K. D.; Urbin, S. A.; Redko, M. Y.; Jackson, J. E.; Lefenfeld, M. Alkali Metals plus Silica Gel: Powerful Reducing Agents and Convenient Hydrogen Sources. *J. Am. Chem. Soc.* **2005**, *127* (26), 9338–9339.

(14) Ma, X.; Xu, F.; Atkins, T. M.; Goforth, A. M.; Neiner, D.; Navrotsky, A.; Kauzlarich, S. M. A Versatile Low Temperature Synthetic Route to Zintl Phase Precursors: Na<sub>4</sub>Si<sub>4</sub>, Na<sub>4</sub>Ge<sub>4</sub> and K<sub>4</sub>Ge<sub>4</sub> as Examples. *Dalt. Trans.* **2009**, No. 46, 10250–10255.

(15) Mayeri, D.; Phillips, B. L.; Augustine, M. P.; Kauzlarich, S. M. NMR Study of the Synthesis of Alkyl-Terminated Silicon Nanoparticles from the Reaction of SiCl<sub>4</sub> with the Zintl Salt, NaSi. *Chem. Mater.* **2001**, *13* (3), 765–770.

(16) Khouchaf, L.; Hamoudi, A.; Cordier, P. Evidence of Depolymerisation of Amorphous Silica at Medium- and Short-Range Order: XANES, NMR and CP-SEM Contributions. *J. Hazard. Mater.* **2009**, *168* (2–3), 1188–1191.

(17) Shao, W. L.; Shinar, J.; Gerstein, B. C.; Li, F.; Lannin, J. S. Magic-Angle Spinning <sup>29</sup>Si NMR Study of Short-Range Order in a-Si. *Phys. Rev. B* **1990**, *41* (13), 9491–9494.

(18) Pandolfi, S.; Renero-Lecuna, C.; Le Godec, Y.; Baptiste, B.; Menguy, N.; Lazzeri, M.; Gervais, C.; Spektor, K.; Crichton, W. A.; Kurakevych, O. O. Nature of Hexagonal Silicon Forming via High-Pressure Synthesis: Nanostructured Hexagonal 4H Polytype. *Nano Lett.* **2018**, *18* (9), 5989–5995.

(19) Krawietz, T. R.; Murray, D. K.; Haw, J. F. Alkali Metal Oxides, Peroxides, and Superoxides: A Multinuclear MAS NMR Study. *J. Phys. Chem. A* **1998**, *102* (45), 8779–8785.

(20) Wang, J.; Sen, S.; Yu, P.; Browning, N. D.; Kauzlarich, S. M. Synthesis and Spectroscopic Characterization of P-Doped Na<sub>4</sub>Si<sub>4</sub>. *J. Solid State Chem.* **2010**, *183* (11), 2522–2527.

(21) Courac, A.; Le Godec, Y.; Renero-Lecuna, C.; Moutaabbid, H.; Kumar, R.; Coelho-Diogo, C.; Gervais, C.; Portehault, D. High-Pressure Melting Curve of Zintl Sodium Silicide Na<sub>4</sub>Si<sub>4</sub> by *In situ* Electrical Measurements. *Inorg. Chem.* **2019**, *58* (16), 10822–10828.

- (22) Kawaguchi, M. Measurement of Thermal Decomposition Temperature and Rate of Sodium Hydride. In *International Conference on Nuclear Engineering*; 2020; pp ICONE2020-16423.
- (23) Beekman, M.; Nolas, G. S. Inorganic Clathrate-II Materials of Group 14: Synthetic Routes and Physical Properties. *J. Mater. Chem.* **2008**, *18* (8), 842–851.
- (24) Reny, E.; Gravereau, P.; Cros, C.; Pouchard, M. Structural Characterisations of the NaSi<sub>136</sub> and Na<sub>8</sub>Si<sub>46</sub> Silicon Clathrates Using the Rietveld Method. *J. Mater. Chem.* **1998**, *8* (12), 2839–2844.
- (25) Beekman, M.; Baitinger, M.; Borrmann, H.; Schnelle, W.; Meier, K.; Nolas, G. S.; Grin, Y. Preparation and Crystal Growth of Na<sub>24</sub>Si<sub>136</sub>. *J. Am. Chem. Soc.* **2009**, *131* (28), 9642–9643.
- (26) Stefanoski, S.; Beekman, M.; Wong-Ng, W.; Zavalij, P.; Nolas, G. S. Simple Approach for Selective Crystal Growth of Intermetallic Clathrates. *Chem. Mater.* **2011**, *23* (6), 1491–1495.
- (27) Beekman, M.; Nenghabi, E. N.; Biswas, K.; Myles, C. W.; Baitinger, M.; Grin, Y.; Nolas, G. S. Framework Contraction in Na-Stuffed Si(*cF*136). *Inorg. Chem.* **2010**, *49* (12), 5338–5340.
- (28) Bobev, S.; Sevov, S. C. Clathrates of Group 14 with Alkali Metals : An Exploration. **2000**, *105*, 92–105.

# Chapter V. Synthesis and electrocatalytic properties of a ternary nickel silicophosphide

## V.1 Introduction

Intermetallic compounds combining transition metals and p-block elements are receiving tremendous attention because of their diverse properties on semiconductivity, magnetism, thermoelectricity and catalysis.<sup>1,2</sup> The catalytic properties of binary borides, phosphides and silicides can be strongly improved by synergetic effects in ternary bimetallic systems.<sup>3</sup> On the opposite, the combination of two nonmetals with a metal and its impact on catalysis is understudied. In the case of Si and P, despite many compositions and crystal structures of ternary metal silicophosphides (M-Si-P), the properties of most them remain unreported.<sup>4,5</sup>

Very recently, some attractive properties of Si- and P-rich silicophosphides have been revealed (**Table V-1**). For example, silicophosphides of Cu, Co, Zn and Fe have been investigated as Li-ion battery anode materials. The silicophosphide anodes exhibit highly improved cycling stability and rate capability compared to Si- and P-based anodes.<sup>6-12</sup> Furthermore, ternary M-Si-P are considered more likely to form noncentrosymmetric phases than binary metal silicides M-Si or phosphides M-P. This statement has led to outstanding nonlinear optical properties.<sup>13,14</sup>

On the other hand, research on metal-rich silicophosphides has been seldom conducted to date. Amorphous ternary Ni-rich borophosphides have demonstrated catalytic activities in hydrogenation superior to their binary counterpart borides and phosphides.<sup>15-17</sup> The enhanced activities were attributed to the variation of the metal electron density induced by metalloid elements.<sup>17</sup> Similar effects may arise in silicophosphides, as well as other behaviors due to special crystal structures. Therefore, studying catalytic properties of silicophosphides is highly relevant. This also implies developing nanoscaled silicophosphides to benefit from their high surface area.

However, transition metal silicophosphide nanoparticles have not been reported, while many properties (*e.g.*, thermoelectrics, magnetism and catalysis) could be impacted, if not improved through nanostructuring of crystalline phases.<sup>2,18,19</sup> Accessing nanoscaled ternary transition metal silicophosphide materials requires design of new synthesis methods. Inorganic molten salts have been demonstrated as appropriate reaction media for achieving nanomaterials with high crystallization temperature.<sup>20–24</sup> Therefore, they could be adapted for the synthesis of nanoparticles of ternary silicophosphides enabling the combination of two p-block elements into crystal structures bearing a covalent character.

**Table V-1** Reported Si- and P-rich transition metal silicophosphides and their properties.

Properties	Phase	Precursors	Synthesis method	Morphology	Ref.
Li-ion or Na-ion battery anode materials	Cu <sub>4</sub> SiP <sub>8</sub>	Cu, red P, Si	Mechanochemistry	Micrograin	6
	CuSi <sub>2</sub> P <sub>3</sub>	Cu, red P, Si	Mechanochemistry	Micro to nano grain	25
	CoSi <sub>3</sub> P <sub>3</sub>	Co, red P, Si	Mechanochemistry	Micrograin	8
	ZnSiP <sub>2</sub>	Zn, red P, Si	Mechanochemistry	Micrograin	9
	ZnSi <sub>2</sub> P <sub>3</sub>	Zn, red P, Si	Mechanochemistry	Micrograin	10
	FeSi <sub>4</sub> P <sub>4</sub>	Fe, red P, Si	Mechanochemistry	Micrograin	11
	FeSi <sub>4</sub> P <sub>4</sub>	Fe, red P, Si	Mechanochemistry	Micrograin	26
Nonlinear optical materials	MnSiP <sub>2</sub>	Mn, red P, Si	Solid-state reaction	Bulk	14
	RuSi <sub>4</sub> P <sub>4</sub>	RuSi <sub>4</sub> , red P	Solid-state reaction	Bulk	13
	IrSi <sub>3</sub> P <sub>3</sub>	IrSi <sub>3</sub> , red P	Solid-state reaction	Bulk	13
Thermoelectric materials	CuSi <sub>2</sub> P <sub>3</sub>	Cu, red P, Si	Solid-state reaction	-	27
	CuSi <sub>4</sub> P <sub>3</sub>	Cu, red P, Si	Solid-state reaction	-	27

The Ni-Si-P ternary system presents a variety of thermodynamic phases.<sup>5</sup> By reacting elemental powders, bulk Ni<sub>2</sub>Si<sub>0.75</sub>P<sub>0.25</sub> has been obtained at 800 °C.<sup>28</sup> In this work, we demonstrate the synthesis of ternary Ni<sub>2</sub>Si<sub>0.75</sub>P<sub>0.25</sub> nanoparticles by reacting P-doped Ni nanoparticles and Zintl phase Na<sub>4</sub>Si<sub>4</sub> in a molten LiI-KI eutectic mixture at 500 °C. Herein, nanoparticles act as reactive reagents and nanotemplate for the ternary phase.<sup>29,30</sup> Ni<sub>2</sub>Si nanoparticles are also obtained by tuning down the P content in the Ni nanoparticle precursor. A preliminary investigation of their electrocatalytic properties on water splitting is conducted. The obtained ternary Ni<sub>2</sub>Si<sub>0.75</sub>P<sub>0.25</sub> nanoparticles show higher electrocatalytic activities in alkaline oxygen evolution reaction (OER) and hydrogen evolution reaction (HER) than binary Ni<sub>2</sub>Si nanoparticles synthesized in this work.

*Post mortem* studies unveil the evolution of morphology, composition and chemical states of  $\text{Ni}_2\text{Si}_{10.75}\text{P}_{0.25}$  nanoparticles under cathodic and anodic conditions of water electrolysis.

## V.2 Experimental methods

**Reagents.** Lithium iodide (99%, Alfa Aesar), potassium iodide (99%, Sigma-Aldrich), silicon nanoparticles (99%, Nanomakers<sup>®</sup>, France), sodium hydride (95 %, Sigma-Aldrich), Nickel (II) acetylacetonate (95%,  $\text{Ni}(\text{acac})_2$ , Strem Chemicals) and trioctylphosphine (TOP, 97%,  $\text{P}(\text{C}_8\text{H}_{16})_3$ , Strem Chemicals) are stored and manipulated as received in an Ar-filled glovebox ( $\text{H}_2\text{O} < 0.5$  ppm,  $\text{O}_2 < 0.5$  ppm). Oleylamine (technical grade 70%, Sigma-Aldrich) is stored and used in the air. Acetone (VWR Normapur grade), tetrahydrofuran (THF, VWR Normapur grade), methanol (VWR Normapur grade) was used for washing.

**Synthesis of Ni nanoparticles.** The synthesis is based on a reported protocol.<sup>31</sup> 20.8 g (25.6 mL, 78 mmol) oleylamine and a Teflon-coated stir bar were put in a 50 mL three-necked round-bottomed flask connected to a reflux condenser and Schlenk line. Then, oleylamine was stirred and degassed at room temperature under vacuum during 30 min to remove dissolved air. Afterward, 2 g (7.8 mmol)  $\text{Ni}(\text{acac})_2$  and 2.1 mL (4.7 mmol) TOP were added. With a heating mantle, the mixture was degassed at 100 °C for 3 min to remove the side product water. Then, the contents were rapidly heated to 220 °C and maintained for 2 h under flowed nitrogen. The suspension was cooled to room temperature and transferred to a centrifuge tube for wash. The nanoparticles were isolated by centrifugation at 21000 rpm for 3 min. After removing the supernatant, 30 mL acetone and 10 mL THF were added. Then, this process was repeated nine times. The washed nanoparticles were dried in a Schlenk tube under vacuum and then stored in an Ar-filled glovebox for further manipulation.

**Synthesis of  $\text{Na}_4\text{Si}_4$ .** This synthesis is an improvement of a reported protocol.<sup>32</sup> 470 mg (20 mmol) of NaH and 500 mg (20 mmol) of Si nanoparticles were ball-milled for 2 min at 20 Hz. Then, the fine mixture was loaded in a pyrolytic *b*-BN crucible (cylinder  $\text{Ø}25 \times \text{H}60$  mm) covered with a cap of the same material, then placed in a bottom closed quartz tube. The tube was heated in a vertical furnace at 395 °C for 48 h under Ar flow. After cooling, the system was transferred to an Ar-filled glovebox. The as-synthesized sample was a dark pellet with another white pellet on the top. The latter corresponding to  $\text{Na}_2\text{O}$  and NaOH was scratched away. The obtained  $\text{Na}_4\text{Si}_4$  powder was stored in the Ar-filled glovebox until reacting with Ni nanoparticles.

**Caution:** The  $\text{Na}_4\text{Si}_4$  powder is air sensitive and burn spontaneously when exposed to water. All manipulations described were performed by handling these powders under inert atmosphere, except when stated otherwise.

**Synthesis of ternary nickel silicophosphide nanoparticles.** 88 mg (1.5 mmol) Ni nanoparticles, 45 mg (0.21 mmol)  $\text{Na}_4\text{Si}_4$ , 2.9 g LiI (21.7 mmol) and 2.1 g KI (12.7 mmol) were ball-milled during 2 min at 20 Hz to get a homogeneous mixture, which was later transferred in a glassy carbon crucible ( $\text{Ø}10 \times \text{H}200$  mm). The crucible was placed in a bottom closed quartz tube and then connected to Schlenk line under Ar flow. A vertical furnace from Eraly® was pre-heated to the reaction temperature of 500 °C. Then, the quartz tube was put in the furnace. After holding the temperature for 4 h under Ar flow, the hot quartz tube was taken out and cooled down. The as-prepared mixture was washed in methanol by seven cycles of centrifugation/redispersion and was later dried in a Schlenk tube under vacuum overnight. The dried powder was transferred and stored in an Ar-filled glovebox.

**Working electrode preparation.** Two types of working electrode substrates were used for different measurements. A glassy carbon (GC) rotating disk electrode (RDE) with a diameter of 5 mm was used for cyclic voltammetry (CV) and linear sweep voltammetry (LSV). A GC sheet was used for chronopotentiometry (CP) measurements. The catalyst film was prepared by drop casting. 3.5 mg of catalyst was sonicated in 480  $\mu\text{L}$  absolute ethanol for 60 min, followed by adding 20  $\mu\text{L}$  of Nafion solution (5% in alcohols and water, Sigma-Aldrich) for another 15 min of ultrasonication. The well-dispersed ink was then dropped onto the as-polished RDE or the GC sheet substrate to obtain a catalyst loading of 350  $\mu\text{g}_{\text{catalyst}} \cdot \text{cm}^{-2}_{\text{electrode}}$ , and then the coating was dried under air for 30 min.

**Measurements of OER properties.** Electrochemical measurements were performed with a typical three-electrode configuration which includes the working electrode, a Pt coil as counter electrode and an Ag/AgCl in saturated KCl electrode as reference electrode. 0.1 M KOH was used as electrolyte ( $\text{pH} = 13$ ). In order to remove the Fe impurity in the electrolyte, *ca.* 1 g of as-prepared  $\text{Ni}(\text{OH})_2$  solid was put into 200 mL as-prepared 0.1M KOH. The suspension was sonicated for 3 min and then rested for at least 6 h. The purified 0.1M KOH supernatant was separated by centrifugation, stored under nitrogen and later used as electrolyte. Before measurements, the electrolyte was bubbled by  $\text{O}_2$  for 20 min. The rotating disk electrode rotated at 1600 rpm. Cyclic voltammograms were recorded in the potential range of 0 to 1.05 V vs. Ag/AgCl reference electrode at a scan rate of 20  $\text{mV s}^{-1}$ . For the chronopotentiometry measurement, a carbon sheet was used for working electrode substrate, a Teflon-coated stir bar

was put in the electrolyte and stirred at 400 rpm to enhance the ions diffusion. For the potentials reported in this work, the ohmic drop  $iR$  was corrected by considering the total impedance measured at a frequency of 50 kHz as the solution resistance. The measured potentials were converted by the equation:  $E_{\text{RHE}} = E_{\text{measured}} + 0.197 + 0.0591 \times \text{pH}$ , where  $\text{pH}=13$ .

**Measurements of HER properties.** The same configuration as for OER studies was used except that a carbon rod was used as counter electrode. 0.1 M KOH was used as electrolyte ( $\text{pH} = 13$ ). Before measurements, the electrolyte was bubbled by Ar for 20 min. The rotating disk electrode rotated at 1600 rpm. The potential was cycled in the range of -0.5 to -2.0 V vs. Ag/AgCl reference electrode at a scan rate of  $20 \text{ mV s}^{-1}$ . The parameters for OER CP measurement were followed for HER CP measurement.

### V.3 Results and discussion

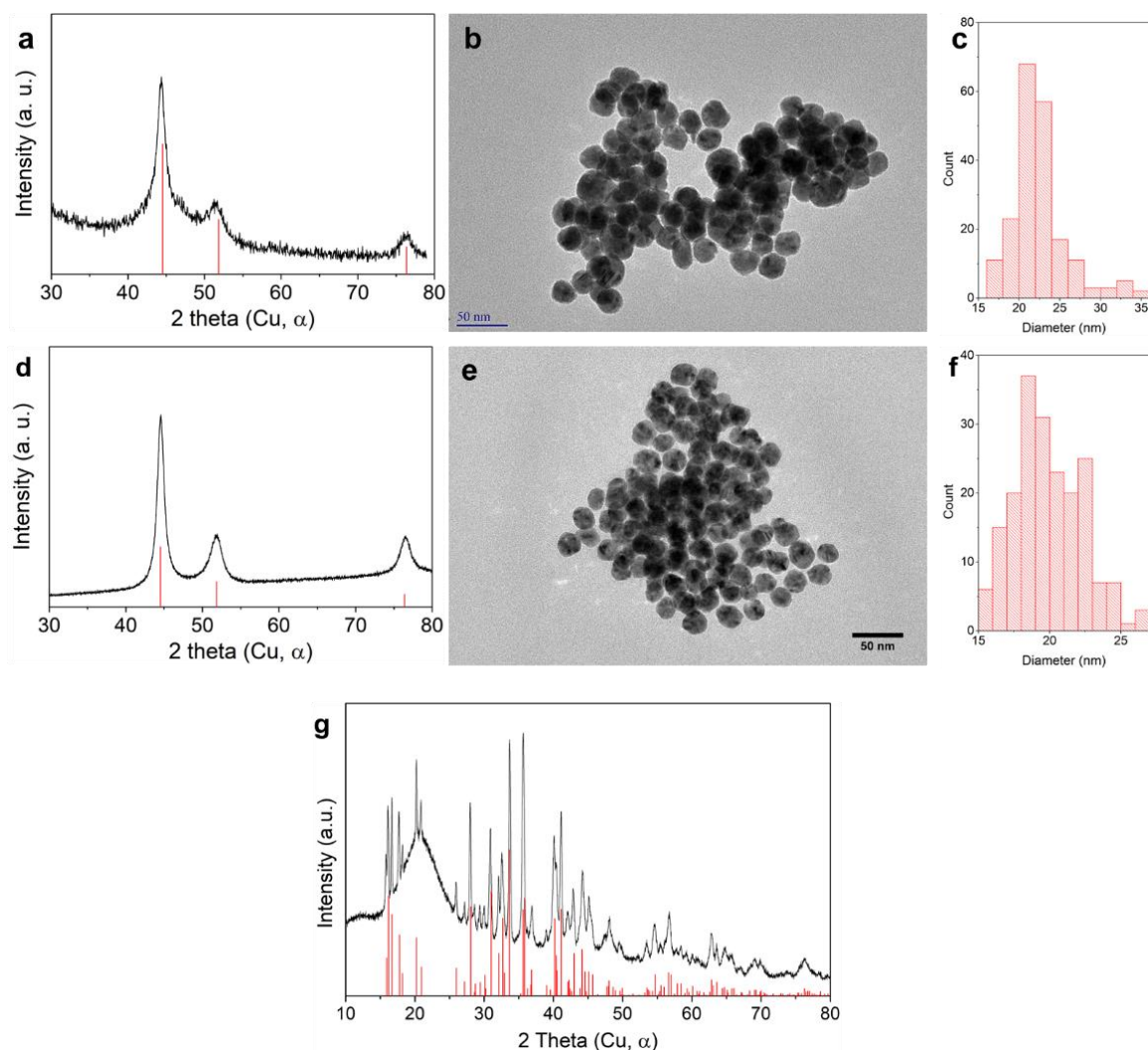
#### V.3.1 Synthesis and characterization

The P-doped Ni nanoparticle precursors of *ca.* 20 nm (**Figure V-1a-f**) has been obtained by a reported colloidal synthesis involving the reaction between  $\text{Ni}(\text{acac})_2$ , oleylamine (OA) and trioctylphosphine (TOP)<sup>31</sup>. Here, TOP is used as surface stabilizing agent and phosphorus source (equivalent TOP per Ni = 0.6). The P/Ni atomic ratio of P-doped Ni nanoparticles determined by scanning electron microscope - analysis energy-dispersive X-ray spectroscopy (SEM-EDX) is 0.17 (**Table V-2**). The Si source  $\text{Na}_4\text{Si}_4$  containing  $[\text{Si}_4]^+$  species was synthesized through the reaction of commercial Si nanoparticles and NaH (**Figure V-1g**).<sup>24</sup>

For the synthesis of nickel silicophosphide nanoparticles, the LiI-KI eutectic mixture (melting point =  $286 \text{ }^\circ\text{C}$ ) was chosen as the inorganic solvent, because of its large stability temperature range, low vapor pressure, inertness to  $\text{Na}_4\text{Si}_4$ .<sup>24</sup> P-doped Ni nanoparticles and  $\text{Na}_4\text{Si}_4$  were reacted in molten LiI-KI at  $500 \text{ }^\circ\text{C}$  for 4 h under Ar flow. After reaction, the salts were removed from the resulting mixture by washing in methanol (see experimental section for more details of the synthesis). Following the same synthesis protocol by changing the TOP amount used in Ni the precursor synthesis (equivalent TOP per Ni = 0.2) results in orthorhombic  $\text{Ni}_2\text{Si}$  as main phase (**Figure V-2**).

**Table V-2** Ni, Si and P ratio determined by EDX of Ni nanoparticle precursors and of their corresponding products.

	Ni	Si	P
Ni nanoparticles (high P content)	2	/	0.3
$\text{Ni}_2\text{Si}_{0.75}\text{P}_{0.25}$	2	1.1	0.3
Ni nanoparticles (low P content)	2	/	0.1
$\text{Ni}_2\text{Si}$	2	1.3	0.1

**Figure V-1** Ni nanoparticles used as reagents for  $\text{Ni}_2\text{Si}_{0.75}\text{P}_{0.25}$  synthesis: (a) powder XRD pattern, red drop lines indicating Ni reference, (b) TEM image and (c) size distribution. Ni nanoparticles used as reagents for  $\text{Ni}_2\text{Si}$  synthesis: (d) powder XRD pattern, red drop lines indicating Ni reference, (e) TEM image and (f) size distribution. (g) Powder XRD pattern of as-prepared  $\text{Na}_4\text{Si}_4$  used as reagent. Red drop lines indicate  $\text{Na}_4\text{Si}_4$  reference.

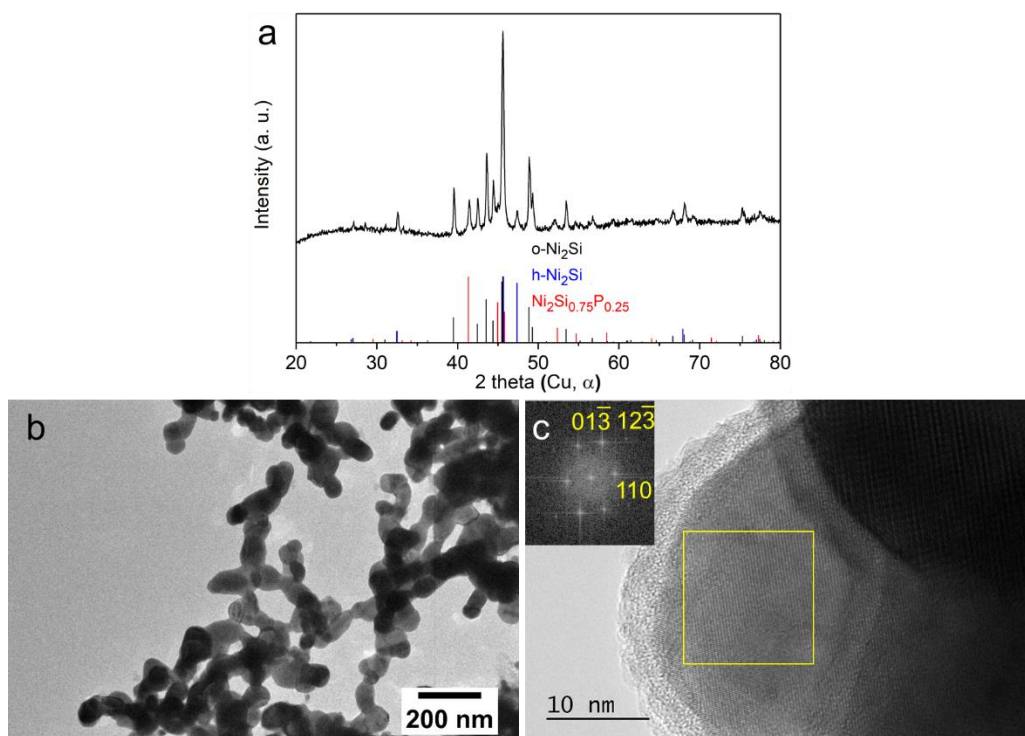


**Figure V-2** Ni<sub>2</sub>Si nanoparticles: (a) powder XRD pattern of as-prepared Ni<sub>2</sub>Si. Black, blue, and red lines indicate o-Ni<sub>2</sub>Si, h-Ni<sub>2</sub>Si and Ni<sub>2</sub>Si<sub>0.75</sub>P<sub>0.25</sub> references. (b) TEM image and (c) HRTEM and FFT of the corresponding area. The FFT can be fully indexed along the o-Ni<sub>2</sub>Si structure.

The powder X-ray diffraction (XRD) pattern of nickel silicophosphide is shown in **Figure V-3a**, Ni<sub>2</sub>Si<sub>0.75</sub>P<sub>0.25</sub> crystallizes in the hexagonal space group *P*-62m. Orthorhombic Ni<sub>2</sub>Si (*Pnma*) and Si are detected as minor impurities. Ni<sub>2</sub>Si<sub>0.75</sub>P<sub>0.25</sub> exhibits the same crystal structure as Ni<sub>2</sub>P. One can then expect a solid solution range of Ni<sub>2</sub>Si<sub>x</sub>P<sub>1-x</sub> compounds with Ni<sub>2</sub>P structure (**Figure V-4**).<sup>28</sup>

According to EDX analysis (**Table V-2**), the atomic ratios Ni/Si/P of nickel silicophosphide are 2/1.1/0.3. Excess Si is present as crystalline Si and Ni<sub>2</sub>Si (**Figure V-3a**) or amorphous silicon oxide at the surface of nanoparticles. The excess P suggests the composition of ternary silicophosphide is not in stoichiometry of Ni<sub>2</sub>Si<sub>0.75</sub>P<sub>0.25</sub>, which is consistent with the literature that the crystal structure of Ni<sub>2</sub>Si<sub>0.75</sub>P<sub>0.25</sub> can adapt a range of Si/P ratio.<sup>5</sup> The Ni/Si/P ratios are 2/1.3/0.1 for the Ni<sub>2</sub>Si product. The excess Si could be amorphous impurities of silicon or silicon oxide layer on the particle surface. On the other hand, the P/Ni ratio in P-doped Ni precursors is maintained in the ternary phase, as well as in Ni<sub>2</sub>Si (**Table V-2**).

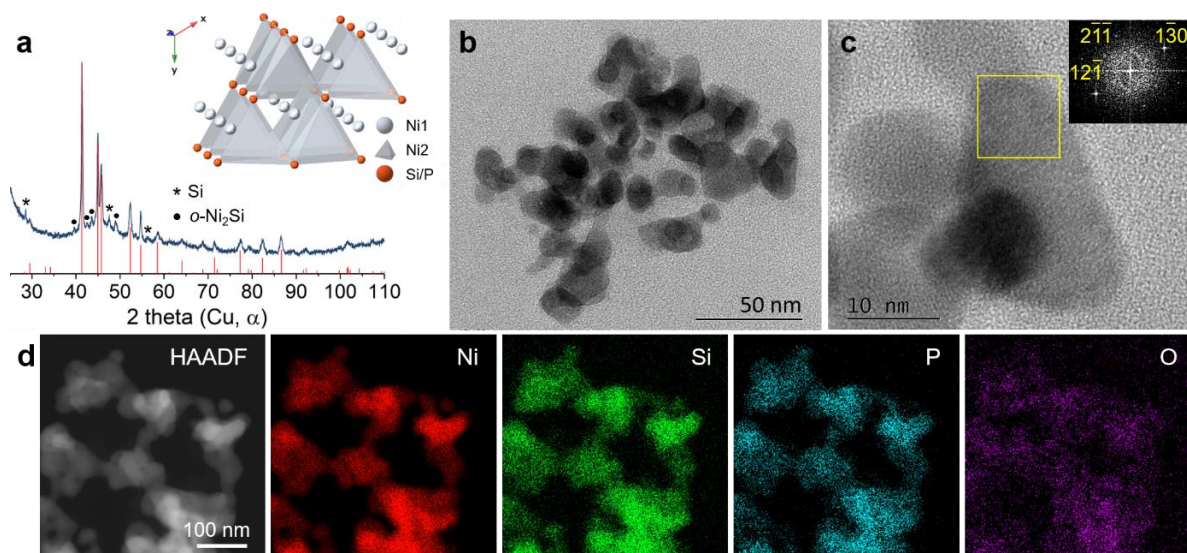


**Figure V-3** (a) XRD patterns of the as-prepared  $\text{Ni}_2\text{Si}_{0.75}\text{P}_{0.25}$  nanoparticles. The red drop lines denote the references of  $\text{Ni}_2\text{Si}_{0.75}\text{P}_{0.25}$ . The asterisks and circles mark respectively the indicative peaks of Si and o- $\text{Ni}_2\text{Si}$  references. The inset shows the crystal structure of  $\text{Ni}_2\text{Si}_{0.75}\text{P}_{0.25}$ . (b) TEM image of the as-prepared  $\text{Ni}_2\text{Si}_{0.75}\text{P}_{0.25}$  nanoparticles. (c) HRTEM image and Fast Fourier Transform (FFT, inset) of the corresponding area. (d) STEM-HAADF image and EDX chemical mapping of  $\text{Ni}_2\text{Si}_{0.75}\text{P}_{0.25}$  nanoparticles.

Transmission electron microscopy (TEM) (**Figure V-3b**) show that the silicophosphide is obtained as nanoparticles. High resolution TEM images and the Fast Fourier Transforms (FFTs) fully indexed along the  $\text{Ni}_2\text{Si}_{0.75}\text{P}_{0.25}$  structure (**Figure V-3c**) confirm the formation of a  $\text{Ni}_2\text{P}$ -type structure. According to the overlapping Ni, Si and P STEM-EDX maps (**Figure V-3d**), homogeneous ternary nanoparticles are formed.

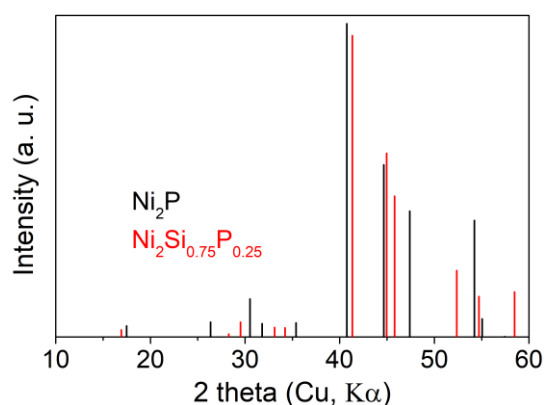


**Figure V-4** Comparison of XRD patterns of  $\text{Ni}_2\text{P}$  and  $\text{Ni}_2\text{Si}_{0.75}\text{P}_{0.25}$ .

X-ray photoelectron spectroscopy (XPS) analysis was conducted to study the surface chemical state of nickel silicophosphide (**Figure V-5**). In the Ni  $2p_{2/3}$  region, the peaks at

853.3 eV and 856.1 eV can be respectively assigned to low valence Ni of the silicophosphide and Ni oxide of the oxide layer evolved during handling.<sup>24,33–35</sup> The binding energy of Ni silicophosphide (853.3 eV) is close to the reported values for Ni<sub>2</sub>P and Ni<sub>2</sub>Si (*ca.* 853.0 – 853.5 eV),<sup>24,34,36,37</sup> showing a positive shift (*ca.* 0.5 eV) compared to elemental Ni (*ca.* 852.6 eV).<sup>36,38</sup> It indicates that Ni in the silicophosphide is also positively charged. The Si 2p spectrum shows two components. The low binding energy one at 99.6 eV corresponds to low oxidation state Si of silicide, while the one at 102.8 eV can be ascribed to silicate or SiO<sub>2</sub>.<sup>38,39</sup> As shown in P 2p spectrum, the initial P-doped Ni nanoparticles show a peak at 129.4 eV (2p<sub>3/2</sub>), which can be a Ni-rich phosphide formed at the Ni surface, in agreement with previous results.<sup>40</sup> The peak at 130.9 eV corresponds to trioctylphosphine adsorbed on the Ni surface.<sup>40</sup> The peak at high binding energy 133.0 eV could be partly oxidized P species on the surface.<sup>41</sup> As for Ni<sub>2</sub>Si<sub>0.75</sub>P<sub>0.25</sub>, the phosphide contribution is observed at 129.9 eV. The adsorbed phosphine peak is not observed anymore for Ni<sub>2</sub>Si<sub>0.75</sub>P<sub>0.25</sub>. The peak at 133.5 eV is assigned to nickel phosphate.<sup>42</sup>

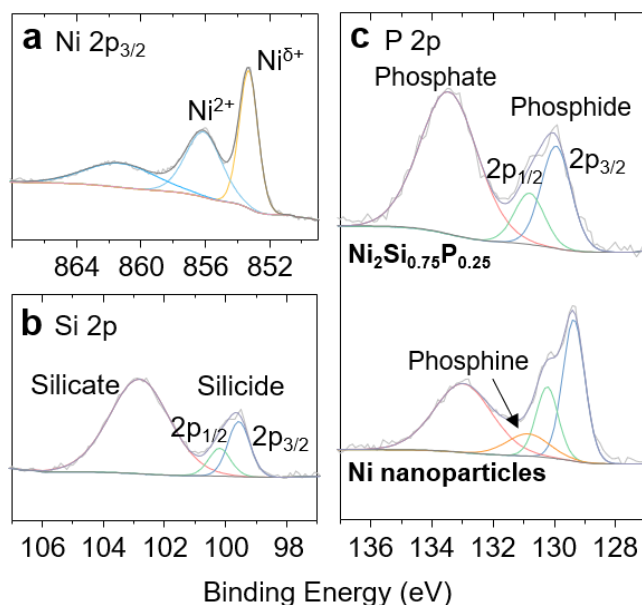


**Figure V-5** XPS of Ni<sub>2</sub>Si<sub>0.75</sub>P<sub>0.25</sub> nanoparticles: (a) Ni 2p<sub>3/2</sub> and (b) Si 2p region. (c) The comparison of P 2p regions for Ni<sub>2</sub>Si<sub>0.75</sub>P<sub>0.25</sub> nanoparticles and P-doped Ni nanoparticles used as precursor.

According to XPS, Ni<sub>2</sub>Si nanoparticles synthesized in this work exhibit similar chemical states with Ni<sub>2</sub>Si<sub>0.75</sub>P<sub>0.25</sub> nanoparticles (**Figure V-6**), the low valence Ni peak at 853.1 eV is close to that of silicophosphide and binary phosphide.<sup>36,37</sup> And the silicide component in Si 2p region at 99.7 eV also shows no obvious shift compared to silicophosphide. However, the oxidized

species of o-Ni<sub>2</sub>Si are in higher proportion than for Ni<sub>2</sub>Si<sub>0.75</sub>P<sub>0.25</sub>, signifying a thicker native oxide layer (**Figure V-2**) for the binary phase.

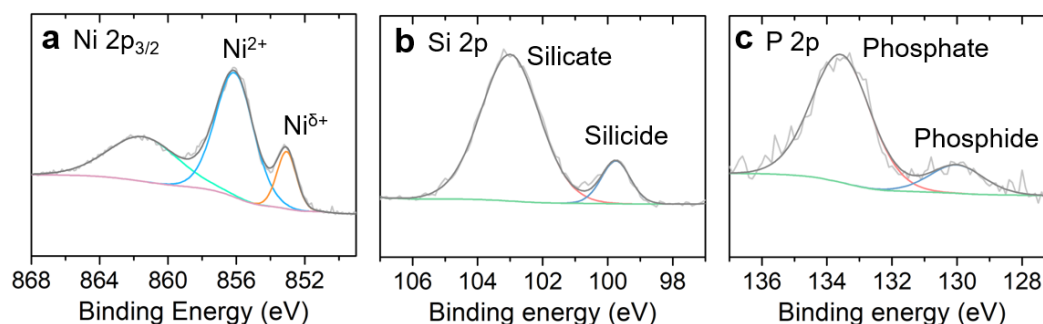


**Figure V-6** XPS of o-Ni<sub>2</sub>Si nanoparticles in (a) Ni2p<sub>3/2</sub>, (b) Si 2p, (c) P 2p region.

The overall chemical states of Ni<sub>2</sub>Si<sub>0.75</sub>P<sub>0.25</sub> nanoparticles and P-doped Ni nanoparticles were also investigated through their X-ray absorption near edge structure (XANES). The Si K-edge (**Figure V-7a**) exhibits two Si peaks at 1840 and 1846 eV. The former is similar to Si wafer (1840 eV), which can be assigned to non-oxidic silicide. This value is close to the reported binary silicide.<sup>43</sup> And the peak at higher energy is similar to SiO<sub>2</sub> (1847 eV) references, corresponding to silicon oxide on the surface of nanoparticles. The shoulder at *ca.* 1844 eV can be assigned to the Si<sup>3+</sup> oxidation state of the central Si atom in Si-SiO<sub>3</sub> tetrahedron.<sup>44</sup> Similarly, through the comparison with red phosphorus and Na<sub>3</sub>PO<sub>4</sub>, two main peaks observed on the P K-edge of Ni<sub>2</sub>Si<sub>0.75</sub>P<sub>0.25</sub> and P-doped Ni (**Figure V-7b**) at 2142 and 2150 eV are attributed to elemental P (2142 eV) and phosphates (2150 eV). The shoulder peaks at *ca.* 2147 eV and 2156 eV could be assigned to oxidized phosphorus with different coordination or neighbors compared to PO<sub>4</sub><sup>3-</sup>.<sup>45</sup> The feature at 2147 eV shows a more important contribution in P-doped Ni, because this energy could also be attributed to phosphine,<sup>46</sup> which was previously detected by XPS.

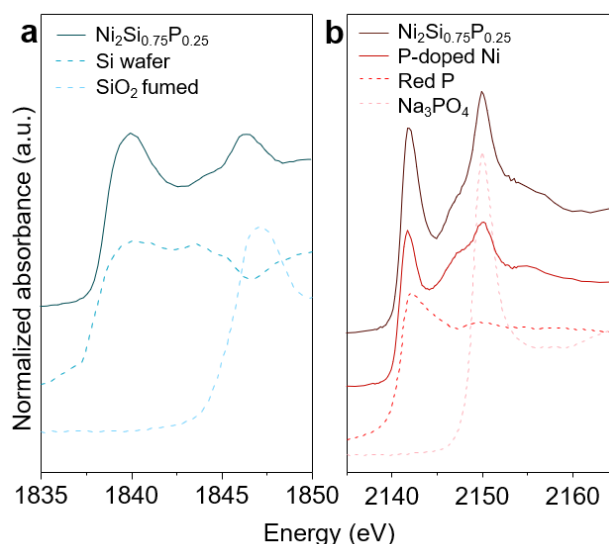


**Figure V-7** XANES on (a) Si K-edge (b) P K-edge of  $\text{Ni}_2\text{Si}_{0.75}\text{P}_{0.25}$  and P-doped Ni nanoparticles.

### V.3.2 Electrocatalysis of water splitting

The electrocatalytic properties on HER and OER of ternary  $\text{Ni}_2\text{Si}_{0.75}\text{P}_{0.25}$  and binary  $\text{Ni}_2\text{Si}$  obtained from the same synthesis method were investigated in 0.1 M KOH. Because the electrocatalytic properties of Ni-based catalyst can be strongly influenced by Fe impurity in electrolyte,<sup>47,48</sup> a reported Fe-elimination protocol by co-precipitation of Ni and Fe in the KOH electrolyte was adopted to assess the intrinsic properties of the ternary phase.<sup>47</sup> The electrochemical measurements were performed with electrodes made of hybrid nanocrystals/Nafion films deposited on glassy carbon sheet (see experimental section for more details).

**Figure V-8a-c** show electrocatalytic properties in OER of  $\text{Ni}_2\text{Si}_{0.75}\text{P}_{0.25}$  and  $\text{Ni}_2\text{Si}$  with a comparison of their 1<sup>st</sup> and 25<sup>th</sup> cyclic voltammograms (CVs). The reversible anodic wave at ca. 1.5 V of CV curves (**Figure V-8a**) correspond to oxidation of nickel species.<sup>47</sup> For  $\text{Ni}_2\text{Si}$ , an activation process can be observed, *i.e.*, the water oxidation current increases along with the Ni oxidation/reduction wave area upon cycling. This correlated increase indicates that the high-valence Ni involved in the reversible oxidation is the active surface site of the catalyst. Its increase upon cycling indicates a progressive surface evolution of the material which results in an enhanced electrocatalytic activity.

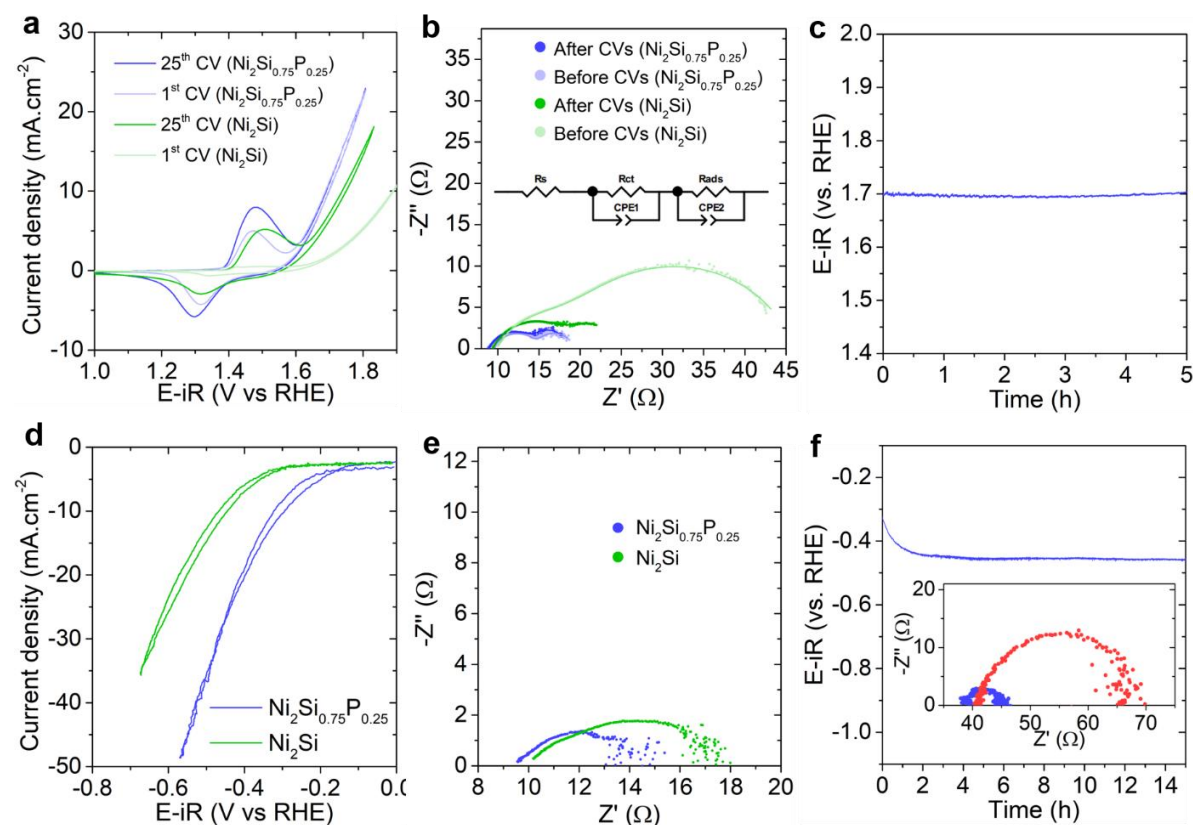


**Figure V-8** Electrochemical measurements of  $\text{Ni}_2\text{Si}_{0.75}\text{P}_{0.25}$  and  $\text{Ni}_2\text{Si}$  nanoparticles in an aqueous Fe-free  $\text{O}_2$ -saturated 0.1 M KOH electrolyte. OER electrocatalytic properties: (a) CV curves (b) Nyquist plot recorded at 1.80 V vs. RHE. (c) CP measurements at 10 mA  $\text{cm}^{-2}$  for  $\text{Ni}_2\text{Si}_{0.75}\text{P}_{0.25}$  nanoparticles. HER electrocatalytic properties: (d) CV curves (e) Nyquist plot recorded under -0.60 V vs. RHE. (f) CP measurements at -10 mA  $\text{cm}^{-2}$  for  $\text{Ni}_2\text{Si}_{0.75}\text{P}_{0.25}$  nanoparticles. Inset shows the EIS of the electrode before (blue dots) and after (red dots) CP measurement.

However, in the case of  $\text{Ni}_2\text{Si}_{0.75}\text{P}_{0.25}$ , such an activation step is not observed. The Ni oxidation/reduction wave area of the 1<sup>st</sup> CV of  $\text{Ni}_2\text{Si}_{0.75}\text{P}_{0.25}$  is already as large as for the activated  $\text{Ni}_2\text{Si}$ . With the fair assumptions that oxidized Ni species form at the surface of the catalyst,<sup>49</sup> these results indicate an enriched Ni content on the native surface of  $\text{Ni}_2\text{Si}_{0.75}\text{P}_{0.25}$ , while  $\text{Ni}_2\text{Si}$  requires a preliminary dissolution of its relatively thick silicon oxide layer for exposing surface Ni (**Figure V-6**). Moreover, even if the Ni oxidation/reduction wave area increases upon cycling, the water oxidation current remains the same for the silicophosphide. It suggests that part of the *in situ* oxidized Ni of  $\text{Ni}_2\text{Si}_{0.75}\text{P}_{0.25}$  is not involved in the catalysis and most probably buried under the active layer.  $\text{Ni}_2\text{Si}$  and  $\text{Ni}_2\text{Si}_{0.75}\text{P}_{0.25}$  nanoparticles show at the 25<sup>th</sup> CV overpotentials at 510 mV and 460 mV for 10 mA  $\text{cm}^{-2}$ , respectively. The ternary silicophosphide is more active than the binary silicide. As for OER electrocatalytic activity of binary phosphide, reported  $\text{Ni}_2\text{P}$  nanoparticles in Fe-free 1 M KOH demonstrates an overpotential at 410 mV for 10 mA  $\text{cm}^{-2}$ ,

which is 120 mV higher than in KOH with presence of Fe.<sup>50</sup> Note that the high overpotentials of the ternary silicophosphide and binary silicide compared to the reported OER catalysts might be related to the lack of Fe in the catalytic layer as for Ni<sub>2</sub>P.<sup>50–52</sup> We then questioned the role of the incorporation of both nonmetal elements on electrocatalysis.

Electrochemical impedance spectroscopy (EIS) was performed before the 1<sup>st</sup> CV and after the 25<sup>th</sup> CV to assess charge transport in the electrodes and at the electrode-electrolyte interfaces for the ternary silicophosphide and binary silicide catalysts at different stages. As shown in the Nyquist plot (**Figure V-8b**), the diameter of the first semicircle in the high frequency region represents the charge transfer resistance ( $R_{ct}$ ), and the second semicircle in the low frequency region corresponds to mass transfer related to reaction intermediates adsorbed at the electrode surface ( $R_{ads}$ ). The low values  $R_{ct}+R_{ads}$  highlight the lower overall resistances of ternary Ni<sub>2</sub>Si<sub>0.75</sub>P<sub>0.25</sub> nanoparticles. To simulate this system, an equivalent circuit with three main components of solution resistance ( $R_s$ ),  $R_{ct}$  and  $R_{ads}$  is used.<sup>53,54</sup> As shown in **Table V-3**, the slight increase of  $R_{ct}$  of both catalysts after cycling could relate to the formation of the insulating metal (oxyhydro)oxide layer. On the other hand, both catalysts, especially Ni<sub>2</sub>Si, show a decrease of  $R_{ads}$ , which indicates that the *in situ* generated oxide layer is more efficient for adsorption/desorption processes on the catalyst surface. The large change of  $R_{ads}$  of Ni<sub>2</sub>Si during the activation process suggests a strong reorganization of the Ni<sub>2</sub>Si nanoparticle surface. This observation is consistent with the CV curves, *i.e.* the activation process of Ni<sub>2</sub>Si could be related to the dissolution of a native Si-rich oxide layer. As for Ni<sub>2</sub>Si<sub>0.75</sub>P<sub>0.25</sub>, its  $R_{ct}$  barely changed during cycling, meaning that the thickness of the surface oxide layer is still under the thickness that allows tunneling electron transport after 25 cycles. This result is in agreement with the CV curves for Ni<sub>2</sub>Si<sub>0.75</sub>P<sub>0.25</sub>.

**Table V-3** Comparison of  $R_{ct}$  and  $R_{ads}$  for Ni<sub>2</sub>Si<sub>0.75</sub>P<sub>0.25</sub> and Ni<sub>2</sub>Si electrodes in different stages of electrolysis.

Electrode	Ni <sub>2</sub> Si <sub>0.75</sub> P <sub>0.25</sub>		Ni <sub>2</sub> Si	
	Before CVs	After CVs	Before CVs	After CVs
R <sub>ct</sub> (Ω)	5.2	5.8	9.3	9.6
R <sub>ads</sub> (Ω)	4.5	3.8	27.0	5.5

To study the evolution of the ternary Ni<sub>2</sub>Si<sub>0.75</sub>P<sub>0.25</sub> nanoparticles under anodic condition, chronopotentiometry (CP) was performed at 10 mA cm<sup>-2</sup> (**Figure V-8c**) after a pre-cycling of the electrode for 25 times between 1.0 and 2.0 V vs. RHE. According to the CP curve, Ni<sub>2</sub>Si<sub>0.75</sub>P<sub>0.25</sub> nanoparticles maintain their OER electrocatalytic activity for at least 5 h.

The HER electrocatalytic properties of Ni<sub>2</sub>Si<sub>0.75</sub>P<sub>0.25</sub> and Ni<sub>2</sub>Si nanoparticles were also studied in Fe-free 0.1 M KOH. According to the CV curves (**Figure V-8d**), ternary Ni<sub>2</sub>Si<sub>0.75</sub>P<sub>0.25</sub>

nanoparticles exhibit an overpotential at  $10 \text{ mA cm}^{-2}$  (294 mV). Even if it is much lower than that of binary  $\text{Ni}_2\text{Si}$  nanoparticles (445 mV), ternary silicophosphide in alkaline HER electrocatalysis is not as efficient as binary  $\text{Ni}_2\text{P}$ , which can usually attain an overpotential below 200 mV at  $10 \text{ mA cm}^{-2}$ .<sup>55,56</sup> Indeed, phosphorus has been considered playing important roles as proton-acceptor to initiate HER and weakening the bond strength of metal and adsorbed hydrogen,<sup>56</sup> which is highly favorable for alkaline HER.<sup>57</sup> The EIS measurement (**Figure V-8e**) confirms that the electrical conductivity of  $\text{Ni}_2\text{Si}_{0.75}\text{P}_{0.25}$  nanoparticles are higher than that of  $\text{Ni}_2\text{Si}$  nanoparticles. However, CP measurements (**Figure V-8f**) reveal that the electrocatalytic activity of  $\text{Ni}_2\text{Si}_{0.75}\text{P}_{0.25}$  nanoparticles degraded in the first 2 h until the stabilized potential was reached. This potential was then maintained during at least 13 h. The drop of activity in the first stage could be related to the increase of  $R_{\text{ct}}$  during electrocatalysis (**Figure V-8f**).

### V.3.3 *Post mortem* study

In order to further understand the evolution of morphology, composition and chemical state of  $\text{Ni}_2\text{Si}_{0.75}\text{P}_{0.25}$  nanoparticles during electrocatalysis under anodic and cathodic conditions of water splitting, *post mortem* studies on post 5 h OER and post 15 h HER samples were achieved by HRTEM, STEM-EDX chemical mapping, SEM-EDX, XPS and XANES.

The TEM images of  $\text{Ni}_2\text{Si}_{0.75}\text{P}_{0.25}$  nanoparticles after 5 h OER and after 15 h HER show a thicker oxide layer grown on the surface compared to pristine nanoparticles (**Figure V-3b-c** and **Figure V-9a-b**). The HRTEM images (**Figure V-9c-d**) show the amorphous nature of these oxide layers, while the crystalline core can be fully indexed to  $\text{Ni}_2\text{Si}_{0.75}\text{P}_{0.25}$ . This partial oxidation reveals the good corrosion resistance of  $\text{Ni}_2\text{Si}_{0.75}\text{P}_{0.25}$  nanoparticles under anodic and cathodic conditions of water electrolysis. It is further confirmed by elemental mapping on post OER/HER samples (**Figure V-9e-f**), which demonstrates the homogeneous distribution of Ni, Si and P in  $\text{Ni}_2\text{Si}_{0.75}\text{P}_{0.25}$  nanoparticles after electrocatalysis. Compositional analysis carried out by SEM-EDX (**Table V-4**) shows that Si was partially leached from the nanoparticles during electrocatalysis. On the opposite, P was maintained in the material. Note that after initial leaching of Si, the  $\text{Ni}/(\text{Si}+\text{P})$  ratio approaches the expected value for the sole silicophosphide.

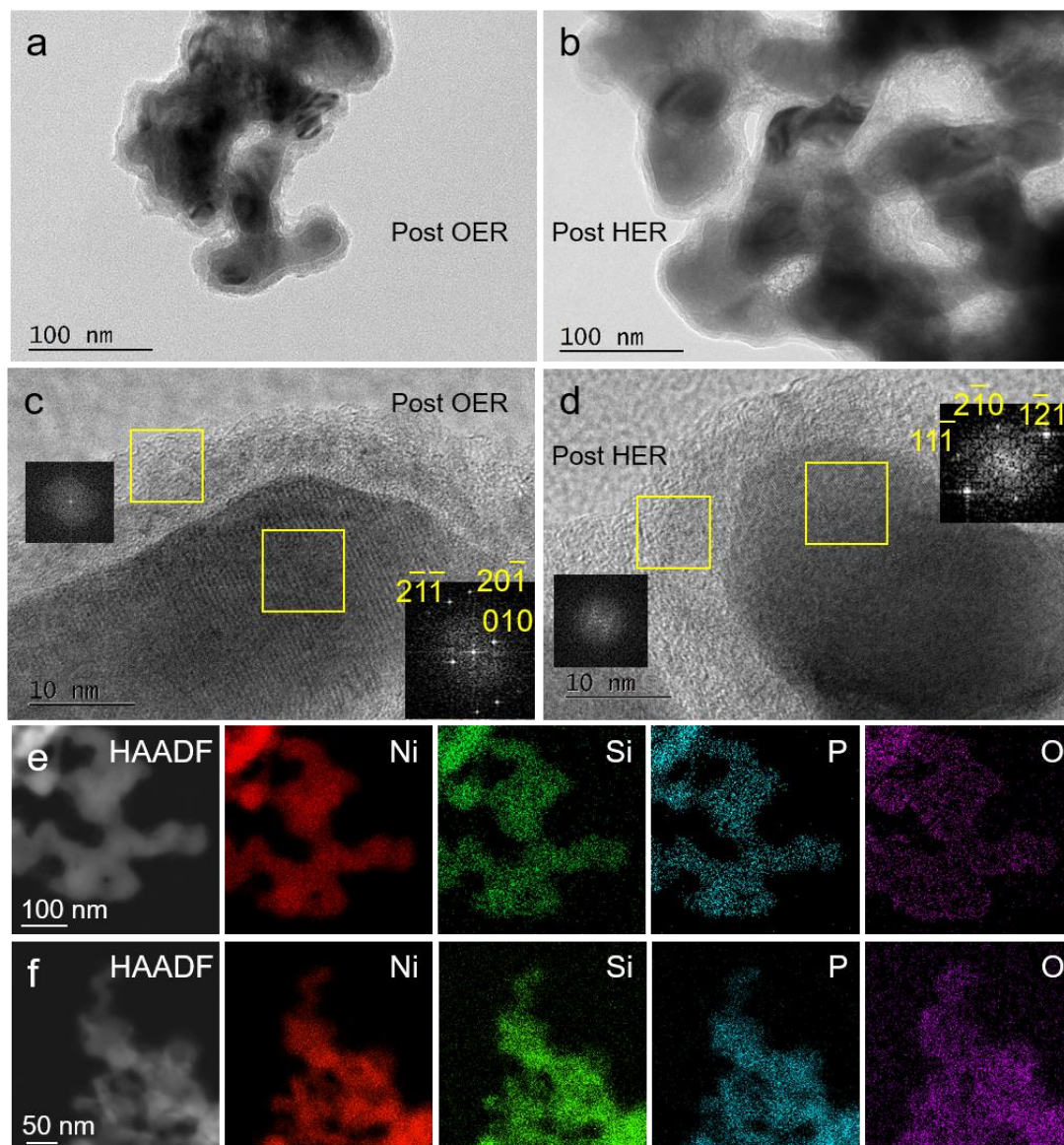


**Figure V-9**  $\text{Ni}_2\text{Si}_{0.75}\text{P}_{0.25}$  nanoparticles: TEM images (a) after 5 h OER and (b) after 15 h HER, HRTEM images and FFTs of the corresponding areas (c) after 5 h OER and (d) after 15 h HER, STEM-HAADF image and STEM-EDX chemical mapping after 15 h HER (e) after 5 h OER and (f) after 15 h HER.

**Table V-4** Ni, Si and P ratio of post electrochemical measurement  $\text{Ni}_2\text{Si}_{0.75}\text{P}_{0.25}$  sample determined by EDX.

	Ni	Si	P
t=0	2	1.1	0.3
Post-5h-OER	2	0.8	0.3
Post-15h-HER	2	0.6	0.2

To elucidate the chemical state of the reorganized surface of post electrocatalysis sample, *post mortem* XPS was conducted (**Figure V-10**). Compared to the as-prepared electrode, only oxidized Ni at *ca.* 856 eV can be detected in the electrodes after OER and HER. Consistently, the Si 2p spectra of post electrocatalysis electrodes show no Si(0) peak, while oxidized Si species are observed. However, no P can be detected in electrodes after OER or HER, which indicates that the oxide layer in **Figure V-9c-d** contains mainly oxidized Ni and Si.

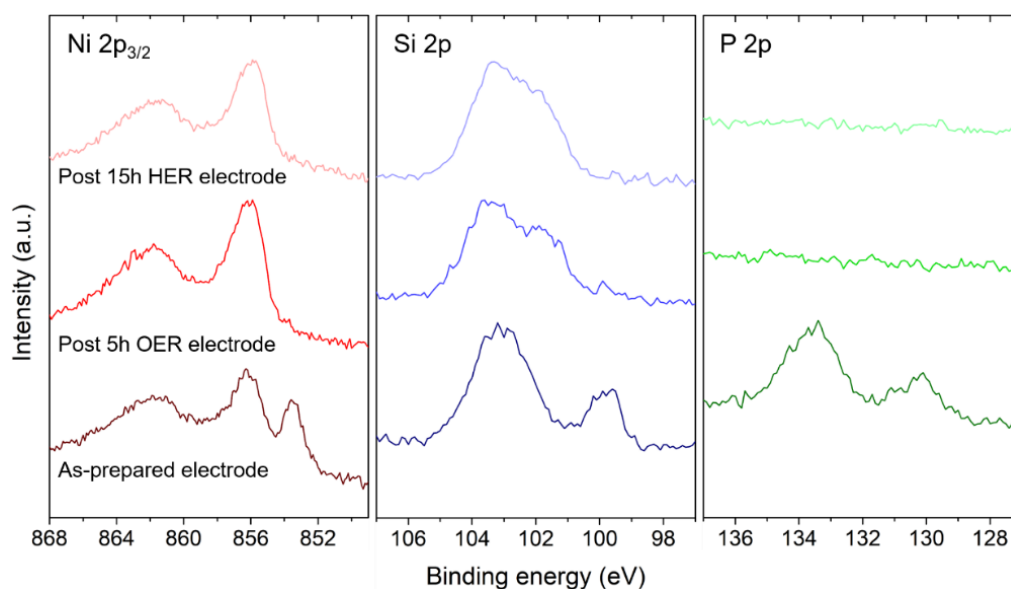


**Figure V-10** XPS of as-prepared electrode, post 5h OER electrode and post 15h HER electrode in Ni 2p<sub>3/2</sub>, Si 2p and P 2p regions.

In order to investigate the overall chemical state of post OER/HER Ni<sub>2</sub>Si<sub>0.75</sub>P<sub>0.25</sub> nanoparticles, the electrodes were analyzed by XANES at the Si K-edge and P K-edge before and after electrochemical measurements. As shown in **Figure V-11**, the non-oxidic species of Si and P can still be detected after electrocatalysis (1840 eV for Si K-edge, 2142 eV for P K-edge), together with the other components at high energy (1844-1846 eV for Si K-edge, 2147-2156 eV for P K-edge) corresponding to Si/P oxoanions. The evolution of the proportion between non-oxidized and oxidized species shows opposite trends for Si and P. In the case of Si, the post-electrocatalysis electrodes contain more oxidized Si than the as-prepared electrode. However, the proportions of non-oxidic P in post-electrocatalysis electrodes increase after catalysis. This observation is consistent with the above results that P cannot be detected in *post mortem* XPS analysis (**Figure V-10**). It suggests a depletion of phosphorus in the *in situ* generated oxide layer or a favorable oxidation of Si over P under the applied electrocatalytic conditions. Despite this evolution in the overall chemical states of Si and P, the majority of the sample keeps its intermetallic nature, which confirms that the modification only occurs on the surface.

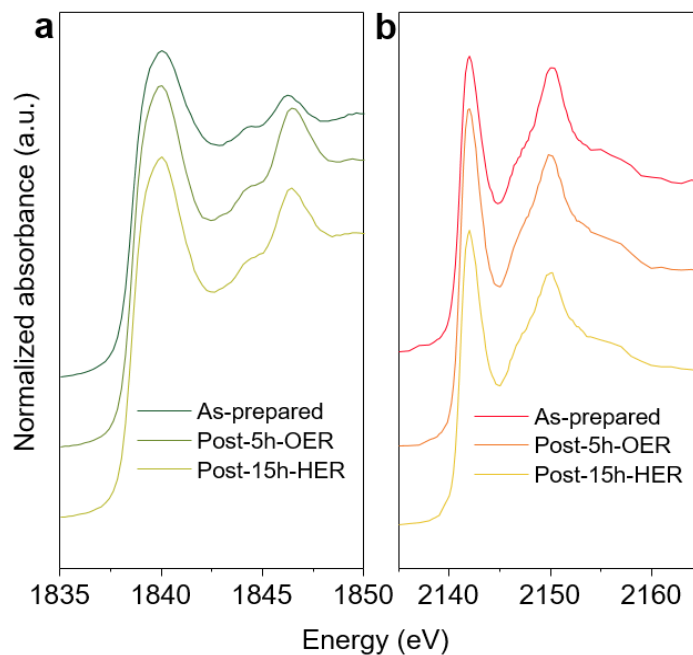


**Figure V-11** XANES at (a) Si K-edge and (b) P K-edge of post electrocatalysis on as-prepared electrode ( $t = 0$ ), electrode after 5 h OER and electrode after 15 h HER.

#### V.4 Conclusion

In summary, ternary  $\text{Ni}_2\text{Si}_{0.75}\text{P}_{0.25}$  nanoparticles are obtained through a liquid-mediated synthesis method in high temperature inorganic solvents of LiI-KI molten salts. P-doped Ni nanoparticles and  $\text{Na}_4\text{Si}_4$  are used as precursors. By tuning the P content of Ni nanoparticles, either  $\text{Ni}_2\text{Si}_{0.75}\text{P}_{0.25}$  or  $\text{Ni}_2\text{Si}$  can be achieved. Electrocatalytic properties in OER and HER of ternary  $\text{Ni}_2\text{Si}_{0.75}\text{P}_{0.25}$  nanoparticles and binary  $\text{Ni}_2\text{Si}$  nanoparticles are compared. The ternary nanoparticles exhibit higher electrical conductivity and show a higher electrocatalytic activity in OER and HER than binary nanoparticles. The activation process obtained for binary  $\text{Ni}_2\text{Si}$  in OER catalysis is not observed for the ternary phase, which indicates a different reorganization of the catalyst surface. The *post mortem* studies reveal that  $\text{Ni}_2\text{Si}_{0.75}\text{P}_{0.25}$  nanoparticles maintain their intermetallic nature under an oxide layer. The oxide layers show an amorphous feature and are rich in Si. In the application view, the electrocatalytic properties of  $\text{Ni}_2\text{Si}_{0.75}\text{P}_{0.25}$  nanoparticles could be further improved by doping additional metals, such as Fe, which is well-known as efficient dopant for improving the OER electrocatalytic properties of Ni-based materials.

## References

- (1) Carencu, S.; Portehault, D.; Boissière, C.; Mézailles, N.; Sanchez, C. Nanoscaled Metal Borides and Phosphides: Recent Developments and Perspectives. *Chem. Rev.* **2013**, *113*, 7981–8065.
- (2) Chen, X.; Liang, C. Transition Metal Silicides: Fundamentals, Preparation and Catalytic Applications. *Catal. Sci. Technol.* **2019**, *9* (18), 4785–4820.
- (3) Mohammed-Ibrahim, J. A Review on NiFe-Based Electrocatalysts for Efficient Alkaline Oxygen Evolution Reaction. *J. Power Sources* **2020**, *448*, 227375.
- (4) O. N. Il'nitskaya. Phase Equilibrium in the Co-Si-P System at 800°C. *Sov. Powder Metall. Met. Ceram.* **1988**, *27*, 741–743.
- (5) Liu, Y.; Cao, D.; Tu, H.; Su, X.; Wang, J.; Wu, C.; Peng, H. Phase Equilibria of the Ni-Si-P System at 800°C. *J. Alloys Compd.* **2013**, *577*, 643–649.
- (6) Nazarian-Samani, M.; Nazarian-Samani, M.; Haghghat-Shishavan, S.; Kim, K. B. Efficient Stress Alleviation and Interface Regulation in Cu<sub>4</sub>SiP<sub>8</sub>-CNT Hybrid for Ultra-Durable Li and Na Storage. *Nano Energy* **2021**, *86*, 106134.
- (7) Li, W.; Ma, Q.; Shen, P.; Zhou, Y.; Soule, L.; Li, Y.; Wu, Y.; Zhang, H.; Liu, M. Yolk-Shell Structured CuSi<sub>2</sub>P<sub>3</sub>@Graphene Nanocomposite Anode for Long-Life and High-Rate Lithium-Ion Batteries. *Nano Energy* **2021**, *80*, 105506.
- (8) Nazarian-Samani, M.; Nazarian-Samani, M.; Haghghat-Shishavan, S.; Kim, K. B. Si,P Vacancy-Enriched CoSi<sub>3</sub>P<sub>3</sub> Anode with Exceptional Li Storage Performance. *Energy Storage Mater.* **2021**, *36*, 229–241.
- (9) Li, W.; Li, X.; Liao, J.; Zhao, B.; Zhang, L.; Huang, L.; Liu, G.; Guo, Z.; Liu, M. A New Family of Cation-Disordered Zn(Cu)-Si-P Compounds as High-Performance Anodes for next-Generation Li-Ion Batteries. *Energy Environ. Sci.* **2019**, *12* (7), 2286–2297.
- (10) Li, W.; Liao, J.; Li, X.; Zhang, L.; Zhao, B.; Chen, Y.; Zhou, Y.; Guo, Z.; Liu, M. Zn(Cu)Si<sub>2+x</sub>P<sub>3</sub> Solid Solution Anodes for High-Performance Li-Ion Batteries with Tunable Working Potentials. *Adv. Funct. Mater.* **2019**, *29* (34), 1–10.
- (11) Liu, Q.; Wang, J.; Luo, Y.; Miao, L.; Yan, Y.; Xue, L.; Zhang, W. Facile Synthesis of FeSi<sub>4</sub>P<sub>4</sub> and Its Sodium Ion Storage Performance. *Electrochim. Acta* **2017**, *247*, 820–825.
- (12) Coquil, G.; Fullenwarth, J.; Grinbom, G.; Sougrati, M. T.; Stievano, L.; Zitoun, D.;

Monconduit, L. FeSi<sub>4</sub>P<sub>4</sub>: A Novel Negative Electrode with Atypical Electrochemical Mechanism for Li and Na-Ion Batteries. *J. Power Sources* **2017**, *372*, 196–203.

(13) Lee, S.; Carnahan, S. L.; Akopov, G.; Yox, P.; Wang, L. L.; Rossini, A. J.; Wu, K.; Kovnir, K. Noncentrosymmetric Tetrel Pnictides RuSi<sub>4</sub>P<sub>4</sub> and IrSi<sub>3</sub>P<sub>3</sub>: Nonlinear Optical Materials with Outstanding Laser Damage Threshold. *Adv. Funct. Mater.* **2021**, *31* (16), 1–8.

(14) Yu, T.; Wang, S.; Zhang, X.; Li, C.; Qiao, J.; Jia, N.; Han, B.; Xia, S. Q.; Tao, X. MnSiP<sub>2</sub>: A New Mid-IR Ternary Phosphide with Strong SHG Effect and Ultrabroad Transparency Range. *Chem. Mater.* **2019**, *31* (6), 2010–2018.

(15) Mo, M.; Han, L.; Lv, J.; Zhu, Y.; Peng, L.; Guo, X.; Ding, W. Noncrystalline NiPB Nanotubes for Hydrogenation of P-Chloronitrobenzene. *Chem. Commun.* **2010**, *46* (13), 2268–2270.

(16) Lee, S.; Chen, Y. Selective Hydrogenation of Furfural on Ni-P, Ni-B, and Ni-P-B Ultrafine Materials. *Society* **1999**, 2548–2556.

(17) Lee, S. P.; Chen, Y. W. Nitrobenzene Hydrogenation on Ni-P, Ni-B and Ni-P-B Ultrafine Materials. *J. Mol. Catal. A Chem.* **2000**, *152* (1–2), 213–223.

(18) Nozariasbmarz, A.; Agarwal, A.; Coutant, Z. A.; Hall, M. J.; Liu, J.; Liu, R.; Malhotra, A.; Norouzzadeh, P.; Öztürk, M. C.; Ramesh, V. P.; Sargolzaeiaval, Y.; Suarez, F.; Vashae, D. Thermoelectric Silicides: A Review. *Jpn. J. Appl. Phys.* **2017**, *56*, 0–27.

(19) Seo, K.; Varadwaj, K. S. K.; Mohanty, P.; Lee, S.; Jo, Y.; Jung, M. H.; Kim, J.; Kim, B. Magnetic Properties of Single-Crystalline CoSi Nanowires. *Nano Lett.* **2007**, *7* (5), 1240–1245.

(20) Delacroix, S.; Igoa, F.; Song, Y.; Le Godec, Y.; Coelho-Diogo, C.; Gervais, C.; Rousse, G.; Portehault, D. Electron Precise Sodium Carbaboride Nanocrystals from Molten Salts: Single Sources to Boron Carbides. *Inorg. Chem.* **2021**.

(21) Portehault, D.; Delacroix, S.; Gouget, G.; Grosjean, R.; Chan-Chang, T. H. C. Beyond the Compositional Threshold of Nanoparticle-Based Materials. *Acc. Chem. Res.* **2018**, *51* (4), 930–939.

(22) Nersisyan, H. H.; Lee, T. H.; Ri, V.; Lee, J. H.; Suh, H.; Kim, J. G.; Son, H. T.; Kim, Y. H. NaF-Assisted Combustion Synthesis of MoSi<sub>2</sub> Nanoparticles and Their Densification Behavior. *J. Phys. Chem. Solids* **2017**, *102* (October 2016), 34–41.

(23) Estruga, M.; Girard, S. N.; Ding, Q.; Chen, L.; Li, X.; Jin, S. Facile and Scalable Synthesis of Ti<sub>5</sub>Si<sub>3</sub> Nanoparticles in Molten Salts for Metal-Matrix Nanocomposites. *Chem. Commun.* **2014**,

50 (12), 1454–1457.

(24) Kumar, R.; Bahri, M.; Song, Y.; Gonell, F.; Thomas, C.; Ersen, O.; Sanchez, C.; Laberty-Robert, C.; Portehault, D. Phase Selective Synthesis of Nickel Silicide Nanocrystals in Molten Salts for Electrocatalysis of the Oxygen Evolution Reaction. *Nanoscale* **2020**, *12* (28), 15209–15213.

(25) Li, W.; Ma, Q.; Shen, P.; Zhou, Y.; Soule, L.; Li, Y.; Wu, Y.; Zhang, H.; Liu, M. Yolk-Shell Structured  $\text{CuSi}_2\text{P}_3$ @Graphene Nanocomposite Anode for Long-Life and High-Rate Lithium-Ion Batteries. *Nano Energy* **2021**, *80*, 105506.

(26) Coquil, G.; Fullenwarth, J.; Grinbom, G.; Sougrati, M. T.; Stievano, L.; Zitoun, D.; Monconduit, L.  $\text{FeSi}_4\text{P}_4$ : A Novel Negative Electrode with Atypical Electrochemical Mechanism for Li and Na-Ion Batteries. *J. Power Sources* **2017**, *372*, 196–203.

(27) Wang, P.; Ahmadpoura, F.; Kolodiaznyib, T.; Kracherc, A.; Cranswickd, L. M. D.; Mozharivskyj, Y. Composition, Structure, Bonding and Thermoelectric Properties of “ $\text{CuT}_2\text{P}_3$ ” and “ $\text{CuT}_4\text{P}_3$ ”, Members of the  $\text{T}_{1-x}(\text{CuP}_3)_x$  Series with T Being Si and Ge. *Dalt. Trans.* **2010**, *39* (4), 978–992.

(28) IL'NITSKAYA, O. N.; KUZ'MA, Y. B. The reaction of nickel with silicon and phosphorus. *Russ. J. Inorg. Chem.* **1992**, *37* (4), 364–366.

(29) Buonsanti, R.; Loiudice, A.; Mantella, V. Colloidal Nanocrystals as Precursors and Intermediates in Solid State Reactions for Multinary Oxide Nanomaterials. *Acc. Chem. Res.* **2021**, *54* (4), 754–764.

(30) Gupta, S. K.; Mao, Y. Recent Developments on Molten Salt Synthesis of Inorganic Nanomaterials: A Review. *J. Phys. Chem. C* **2021**.

(31) Carenco, S.; Boissière, C.; Nicole, L.; Sanchez, C.; Le Floch, P.; Mézailles, N. Controlled Design of Size-Tunable Monodisperse Nickel Nanoparticles. *Chem. Mater.* **2010**, *22* (4), 1340–1349.

(32) Ma, X.; Xu, F.; Atkins, T. M.; Goforth, A. M.; Neiner, D.; Navrotsky, A.; Kauzlarich, S. M. A Versatile Low Temperature Synthetic Route to Zintl Phase Precursors:  $\text{Na}_4\text{Si}_4$ ,  $\text{Na}_4\text{Ge}_4$  and  $\text{K}_4\text{Ge}_4$  as Examples. *J. Chem. Soc. Dalt. Trans.* **2009**, No. 46, 10250–10255.

(33) Shalvoy, R. B.; Reucroft, P. J.; Davis, B. H. Characterization of Coprecipitated Nickel on Silica Methanation Catalysts by X-Ray Photoelectron Spectroscopy. *J. Catal.* **1979**, *56* (3), 336–348.

- (34) Cao, Y.; Nyborg, L.; Jelvestam, U. XPS Calibration Study of Thin-Film Nickel Silicides. *Surf. Interface Anal.* **2009**, *41* (6), 471–483.
- (35) Lorenz, P.; Finster, J.; Wendt, G.; Salyn, J. V.; Žumadilov, E. K.; Nefedov, V. I. Esca Investigations of Some NiO/SiO<sub>2</sub> and NiO-Al<sub>2</sub>O<sub>3</sub>/SiO<sub>2</sub> Catalysts. *J. Electron Spectros. Relat. Phenomena* **1979**, *16* (3), 267–276.
- (36) Blanchard, P. E. R.; Grosvenor, A. P.; Cavell, R. G.; Mar, A. X-Ray Photoelectron and Absorption Spectroscopy of Metal-Rich Phosphides M<sub>2</sub>P and M<sub>3</sub>P (M=Cr-Ni). **2008**, No. 13, 369–371.
- (37) Zhang, Y.; Liu, Y.; Ma, M.; Ren, X.; Liu, Z.; Du, G.; Asiri, A. M.; Sun, X. A Mn-Doped Ni<sub>2</sub>P Nanosheet Array: An Efficient and Durable Hydrogen Evolution Reaction Electrocatalyst in Alkaline Media. *Chem. Commun.* **2017**, *53* (80), 11048–11051.
- (38) Masa, J.; Piontek, S.; Wilde, P.; Antoni, H.; Eckhard, T.; Chen, Y. T.; Muhler, M.; Apfel, U. P.; Schuhmann, W. Ni-Metalloid (B, Si, P, As, and Te) Alloys as Water Oxidation Electrocatalysts. *Adv. Energy Mater.* **2019**, *9* (26), 1–8.
- (39) Junge, H.; Beller, M.; Agapova, A.; Ryabchuk, P.; Lund, H.; Junge, K.; Agostini, G.; Pohl, M.-M. Intermetallic Nickel Silicide Nanocatalyst—A Non-Noble Metal-Based General Hydrogenation Catalyst. *Sci. Adv.* **2018**, *4* (6), eaat0761.
- (40) Carenco, S.; Liu, Z.; Salmeron, M. The Birth of Nickel Phosphide Catalysts: Monitoring Phosphorus Insertion into Nickel. *ChemCatChem* **2017**, *9* (12), 2318–2323.
- (41) Shimizu, M.; Tsushima, Y.; Arai, S. Electrochemical Na-Insertion/Extraction Property of Ni-Coated Black Phosphorus Prepared by an Electroless Deposition Method. *ACS Omega* **2017**, *2* (8), 4306–4315.
- (42) Watson, I. M.; Connor, J. A.; Whyman, R. Non-Crystalline Chromium, Molybdenum and Tungsten Phosphate Films Prepared by Metal Organic Chemical Vapour Deposition. *Thin Solid Films* **1991**, *201* (2), 337–349.
- (43) Naftel, S.; Coulthard, I.; Sham, T.; Das, S.; Xu, D. Structural and Electronic Property Evolution of Nickel and Nickel Silicide Thin Films on Si(100) from Multicore X-Ray-Absorption Fine-Structure Studies. *Phys. Rev. B - Condens. Matter Mater. Phys.* **1998**, *57* (15), 9179–9185.
- (44) Flank, A. M.; Karnatak, R. C.; Blancard, C.; Esteva, J. M.; Lagarde, P.; Connerade, J. P. Probing Matrix Isolated SiO Molecular Clusters by X-Ray Absorption Spectroscopy. *Zeitschrift für Phys. D Atoms, Mol. Clust.* **1991**, *21* (4), 357–366.

- (45) Schmidt, S.; Sallard, S.; Borca, C.; Huthwelker, T.; Novák, P.; Villevieille, C. Phosphorus Anionic Redox Activity Revealed by Operando P K-Edge X-Ray Absorption Spectroscopy on Diphosphonate-Based Conversion Materials in Li-Ion Batteries. *Chem. Commun.* **2018**, *54* (39), 4939–4942.
- (46) Morel, F. L.; Pin, S.; Huthwelker, T.; Ranocchiari, M.; Van Bokhoven, J. A. Phosphine and Phosphine Oxide Groups in Metal-Organic Frameworks Detected by P K-Edge XAS. *Phys. Chem. Chem. Phys.* **2015**, *17* (5), 3326–3331.
- (47) Trotochaud, L.; Young, S. L.; Ranney, J. K.; Boettcher, S. W. Nickel-Iron Oxyhydroxide Oxygen-Evolution Electrocatalysts: The Role of Intentional and Incidental Iron Incorporation. *J. Am. Chem. Soc.* **2014**, *136* (18), 6744–6753.
- (48) Farhat, R.; Dhainy, J.; Halaoui, L. I. Oer Catalysis at Activated and Codeposited Nife-Oxo/Hydroxide Thin Films Is Due to Postdeposition Surface-Fe and Is Not Sustainable without Fe in Solution. *ACS Catal.* **2020**, *10* (1), 20–35.
- (49) Masa, J.; Schuhmann, W. The Role of Non-Metallic and Metalloid Elements on the Electrocatalytic Activity of Cobalt and Nickel Catalysts for the Oxygen Evolution Reaction. *ChemCatChem* **2019**, *11* (24), 5842–5854.
- (50) Lucas-Alexandre Stern, Ligang Feng, Fang Song, and X. H. Ni<sub>2</sub>P as a Janus Catalyst for Water Splitting: The Oxygen Evolution Activity of Ni<sub>2</sub>P Nanoparticles. *Energy Environ. Sci.* **2015**, *8*, 2347–2351.
- (51) Trotochaud, L.; Young, S. L.; Ranney, J. K.; Boettcher, S. W. Nickel-Iron Oxyhydroxide Oxygen-Evolution Electrocatalysts: The Role of Intentional and Incidental Iron Incorporation. *J. Am. Chem. Soc.* **2014**, *136* (18), 6744–6753.
- (52) Valizadeh, A.; Najafpour, M. M. Is Nickel Phosphide an Efficient Catalyst for the Oxygen-Evolution Reaction at Low Overpotentials? *New J. Chem.* **2020**, *44* (45), 19630–19641.
- (53) Franco, D. V.; Da Silva, L. M.; Jardim, W. F.; Boodts, J. F. C. Influence of the Electrolyte Composition on the Kinetics of the Oxygen Evolution Reaction and Ozone Production Processes. *J. Braz. Chem. Soc.* **2006**, *17* (4), 746–757.
- (54) Qi, J.; Zhang, W.; Xiang, R.; Liu, K.; Wang, H. Y.; Chen, M.; Han, Y.; Cao, R. Porous Nickel–Iron Oxide as a Highly Efficient Electrocatalyst for Oxygen Evolution Reaction. *Adv. Sci.* **2015**, *2* (10), 1–8.
- (55) Hu, C.; Lv, C.; Liu, S.; Shi, Y.; Song, J.; Zhang, Z.; Cai, J.; Watanabe, A. Nickel Phosphide

Electrocatalysts for Hydrogen Evolution Reaction. *Catalysts* **2020**, *10* (2).

(56) Xiao, P.; Chen, W.; Wang, X. A Review of Phosphide-Based Materials for Electrocatalytic Hydrogen Evolution. *Adv. Energy Mater.* **2015**, *5* (24), 1–13.

(57) Sahoo, P. K.; Bisoi, S. R.; Huang, Y.; Tsai, D. Evolution Reaction : Fundamentals to Applications. **2021**, 1–24.



# General conclusion

The rare occurrence of transition metal silicide nanomaterials limits the investigation of their properties. This thesis is dedicated to the exploration of synthesis pathways towards transition metal silicide nanomaterials, and then to the study of their electrocatalytic for water splitting and magnetic properties.

In this thesis, two synthesis approaches in molten salts using nanoparticles as precursors have been developed towards nanoparticles of transition metal silicides (M-Si, M = Ni, Fe, NiFe, Co) and ternary nickel silicophosphides (M-Si-P). The electrocatalytic properties in alkaline OER were measured for all materials. Ternary nickel silicophosphide nanoparticles were also assessed as HER electrocatalysts in alkaline media. *Post mortem* studies were conducted to investigate the evolution of catalysts on phase, composition and morphology. Apart from electrocatalysis, the magnetism of cobalt monosilicide nanoparticles was evaluated.

The first synthesis method used the redox reaction between Si nanoparticles and metal chlorides at 300-400 °C in a low vapor pressure molten salts LiI-KI, which allows to run reaction under dynamic vacuum to remove volatile byproducts. Ni<sub>2</sub>Si, FeSi and NiFe silicide nanoparticles of *ca.* 40 nm were achieved. The reaction temperature in our synthesis method is hundreds of degrees below the reaction temperature of traditional solid-state synthesis towards these phases. The enhanced reactivity is achieved through three features of this synthesis method: (1) high temperature liquid media provided by inorganic solvents, (2) dynamic vacuum shift of reaction equilibria and (3) a reactive Si nanoparticle precursor. The latter also enables a better control over particle morphology by acting as a nanotemplate.

Among the obtained Ni<sub>2</sub>Si, FeSi and NiFe silicide nanoparticles, NiFe silicides delivered the best electrocatalytic activity in OER electrocatalysis surpassing benchmarking IrO<sub>2</sub>, combined to a stability for at least 85 h at 10 mA cm<sup>-2</sup>. *Post mortem* studies of NiFe silicide nanoparticles subjected to different durations of electrocatalysis reveal that a core-shell-shell nanostructure formed during electrocatalysis. The outer shell is the actual catalytically active species, which is identified as crystalline Fe-doped NiOOH formed by reorganization of the catalyst surface upon Si leaching under electrocatalytic conditions. The intermediate amorphous layer contains oxidic

metal and silicon. This dense oxide layer originates from the passivation of the core and avoids the contact of silicide core with the corrosive electrolyte. The silicide core can thus keep its intermetallic nature and enable charge transfer in the electrode. This *in situ* evolution of NiFe silicide nanoparticles towards core-shell-shell nanostructure is reported for the first time. The passivating intermediate layer has not been observed for other metal-p block element OER catalysts. The outstanding electrocatalytic properties of NiFe silicide are attributed to this original nanostructure, and NiFe silicide itself is considered as a precatalyst made by Earth abundant elements.

Based on this synthesis method, freestanding polycrystalline CoSi nanoparticles core also achieved as core-shell Si-CoSi nanoparticles at 300 °C and as homogeneous nanoparticles at 400 °C. Different than bulk CoSi, the obtained CoSi nanoparticles in this work are ferromagnetic below 300 K. This magnetic order is attributed to the unpaired spins produced by undercoordinated Co atoms at interfaces, grain boundaries or crystal defects.<sup>1</sup> The core-shell CoSi nanoparticles exhibit small crystal domains, thus demonstrating higher magnetic moment ( $0.17 \mu_B/\text{Co}$  at 300 K) than reported single crystal CoSi nanowires ( $0.03 \mu_B/\text{Co}$  at 300 K)<sup>2</sup> and the homogeneous CoSi nanoparticles ( $0.05 \mu_B/\text{Co}$  at 300 K) obtained in this work. The electrocatalytic properties of core-shell CoSi nanoparticles in OER were also investigated. Upon a complete conversion towards layered Si-doped Co oxide/(oxy)hydroxide, core-shell CoSi nanoparticles delivered high OER catalytic activity surpassing IrO<sub>2</sub>. This activity of modified electrodes was stable for at least 15 h.

Aside from the above synthesis method, a second molten salt synthesis method using Ni nanoparticles and Na<sub>4</sub>Si<sub>4</sub> as precursors was developed. Sodium silicide Na<sub>4</sub>Si<sub>4</sub> is a reductive and reactive source of silicon highly relevant to design non-oxidic silicon materials, including clathrates, various silicon allotropes, and metal silicides. Despite the importance of this compound, its production in high amounts and high purity is yet a bottleneck with reported methods.

In this work, we demonstrated that readily available Si nanoparticles react with sodium hydride with a stoichiometry close to the theoretical one and at a temperature of 395 °C for shorter duration than previously reported. This enhanced reactivity of Si nanoparticles makes the procedure robust and less dependent on experimental parameters, such as gas flow. As a result, we delivered a procedure to achieve Na<sub>4</sub>Si<sub>4</sub> with purity of *ca.* 98 mol.% at the gram scale. We showed that this compound is an efficient precursor to deliver selectively type I and type II

sodium silicon clathrates depending on the conditions of thermal decomposition. It suggests the efficiency of the material for further use towards silicon-based materials.

Through the second synthesis approach, binary nickel silicide nanoparticles and ternary nickel silico-phosphide nanoparticles were achieved in LiI-KI molten salts under 1 atm. Ar flow. P-doped Ni nanoparticles obtained through a reported colloidal synthesis and  $\text{Na}_4\text{Si}_4$  synthesized in this work were used as precursors. With different P contents of Ni nanoparticles, the synthesis yielded nickel silicophosphide or  $\text{Ni}_2\text{Si}$  nanoparticles at 500 °C. The intrinsic electrocatalytic properties in OER and HER of ternary nickel silicophosphide nanoparticles and binary  $\text{Ni}_2\text{Si}$  nanoparticles were investigated. Experimental results showed that ternary silico-phosphide nanoparticles exhibit higher electrical conductivity and demonstrate higher electrocatalytic activities in alkaline OER and HER than binary silicide nanoparticles. Moreover, the binary silicide required an activation process by cycling the electrode for reaching its maximum catalytic activity, while this stage was not observed for ternary silicophosphide. It indicates different chemical surface states of the native oxide layers and reorganization process of the catalyst surface. *Post mortem* studies revealed that the core of silicophosphide nanoparticles maintain its intermetallic nature after OER and HER electrocatalysis, while a thicker amorphous P-poor oxide layer was observed. Further mechanistic study on the role of Si and P in electrocatalysis will be conducted in the future.

Overall, the two synthesis pathways developed in this work provide a new insight of the design of transition metal silicide nanomaterials in molten salts. Preliminary results on ternary silicophosphide show the potential of these methods towards ternary or multinary compounds, which deliver improved properties in (electro)catalysis. Furthermore, the *post mortem* studies conducted in this thesis provide a basis of electrocatalytic mechanism of transition metal-p block element compounds for future research on multinary catalysts.

## References

- (1) Goldfarb, I.; Cesura, F.; Dascalu, M. Magnetic Binary Silicide Nanostructures. *Adv. Mater.* **2018**, *30* (41), 1–11.
- (2) Seo, K.; Varadwaj, K. S. K.; Mohanty, P.; Lee, S.; Jo, Y.; Jung, M. H.; Kim, J.; Kim, B. Magnetic Properties of Single-Crystalline CoSi Nanowires. *Nano Lett.* **2007**, *7* (5), 1240–1245.



# Appendix

## Instruments

**Powder X-ray diffraction (XRD)** was performed on a Bruker D8 Advance diffractometer equipped with an X-ray source working with Cu K $\alpha$  radiation. Due to the air-sensitivity of Na<sub>4</sub>Si<sub>4</sub>, the powder was loaded in an airtight sample holder into an argon-filled glovebox and capped with a protective plastic dome. Beam scattering by the dome gives rise to a broad bump between 15-25° (2 $\theta$  Cu K $\alpha$ ). Powder XRD patterns used for Le Bail analysis were acquired with a step size of 0.029° and an acquisition time of 10 s per step, which correspond to 13 h of measurement. Over this long duration, the sample holder shows evidences of air leaks (see results and discussion chapter IV.). Otherwise, 5 min fast acquisitions with a step size of 0.05° and an acquisition time of 0.19 s per step were performed as standard program to avoid sample degradation during XRD measurement.

XRD references: o-Ni<sub>2</sub>Si (ICDD 04-010-3516), h-Ni<sub>2</sub>Si (ICDD 01-072-2547), FeSi (ICDD 04-007-2551), NiOOH (ICDD 00-06-0075), CoSi (ICDD 04-012-6522), Co<sub>2</sub>Si<sub>3</sub> (ICDD 04-002-9806), Na<sub>4</sub>Si<sub>4</sub> (ICDD 04-015-9208), Na (ICDD 00-022-0948), Si (ICDD 00-027-1402), NaOH (ICDD 00-035-1009), Ni<sub>2</sub>Si<sub>0.75</sub>P<sub>0.25</sub> (ICDD 04-005-5697), Ni<sub>2</sub>P (ICDD 01-072-2514).

**<sup>29</sup>Si and <sup>23</sup>Na magic angle spinning solid-state nuclear magnetic resonance (MAS solid-state NMR) spectra** were acquired on a 700 MHz AVANCE III Bruker spectrometer operating at 139.05 MHz and at 185.20 MHz respectively and using a 3.2 mm Bruker triple resonance probe. Samples were transferred to ZrO<sub>2</sub> rotors spun at a MAS rate of 10kHz for <sup>29</sup>Si and 20kHz for <sup>23</sup>Na. A single-pulse excitation was used with a recycle delay of 500s and 400 scans for <sup>29</sup>Si and 1s and 1960 scans for <sup>23</sup>Na. <sup>29</sup>Si and <sup>23</sup>Na chemical shifts were referenced to TMS and 0.1 M NaCl (aq) respectively. The spectra were treated with the DMFIT program.<sup>31</sup>

**Scanning electron microscopy (SEM)** was carried out on a Hitachi SU-70 FESEM. Postmortem electrodes were observed without any surface coating, accelerating voltage settings as indicated in images.

**Energy-dispersive X-ray spectroscopy (EDX)** (Oxford Instruments – X-max) on the Scanning electron microscope (SEM) was performed on a SEM HITACHI S3400N at 20 kV to determine the sample composition. Cobalt was used for calibration of quantitative analyses. Powder samples were flatly smeared on a carbon adhesive tape on sample holder. Carbon deposition was required for the  $\text{Na}_4\text{Si}_4$  sample to enable the EDX analysis on insulating sample. In order to avoid equipment damage and for safety concern, air-sensitive  $\text{Na}_4\text{Si}_4$  samples were pre-neutralized by exposure to air during 4 days.

**Transmission electron microscopy (TEM)** images were acquired on a Technai Spirit 2 microscope operating at 120 kV. The samples were prepared by depositing a drop of ethanolic suspension on carbon coated Cu grids.

**High resolution TEM (HRTEM)** was performed with JEOL JEM 2100 FEG microscope operating at 200 kV. The samples were prepared by depositing a drop of ethanolic suspension on carbon coated Cu grids.

**Pair Distribution Function (PDF)** X-ray scattering data were acquired on a Bruker D8 ADVANCE diffractometer equipped with a Gobel mirror and a LYNXEYE detector, with  $\text{Mo K}\alpha$  radiation (mean  $\lambda(\text{K}\alpha 1\alpha 2) = 0.71073 \text{ \AA}$ ) at room temperature. Powder sample was loaded in a  $\varnothing 0.5 \text{ mm}$  borosilicate capillary. Measurements were performed from  $Q_{\min} = 0.12 \text{ \AA}^{-1}$  to  $Q_{\max} = 17.0 \text{ \AA}^{-1}$  ( $Q = 4\pi\sin\left(\frac{\theta}{\lambda}\right)$ ) on rotating capillaries with evolving counting parameters as a function of  $Q$ -range in order to optimize the counting rate at high  $Q$ . The final XRD diagram was thus obtained from the combination of 7 patterns ( $2\theta_i$  (°)-  $2\theta_f$  (°)- step size (°)- step time (°): 0.8-31-0.02-2, 29-61-0.04-6, 59-91-0.06-15, 89-121-0.1-40 twice, 119-150-0.1-100 twice) for a total measuring time of 34 h. Additional scattering measurements from empty capillary were performed in the same conditions for background subtraction. Raw data were treated using the PDFgetX3 program<sup>62</sup> to obtain the total PDF  $G(r)$  function, using the following parameters:  $Q_{\min} = 0.15 \text{ \AA}^{-1}$ ,  $Q_{\max} = 16.6 \text{ \AA}^{-1}$ ,  $r_{\text{poly}} = 1.75$ . These data were also used for Rietveld refinement.

**X-ray photoelectron spectroscopy (XPS)** analyses were performed on an Omicron Argus X-ray photoelectron spectrometer, equipped with a monochromated  $\text{AlK}\alpha$  radiation source (1486.6 eV) and a 280 W electron beam power. Binding energies were calibrated against the C 1s (C-C) binding energy at 284.8 eV. Raw data were treated on Thermo Scientific™ Avantage.

**X-ray absorption near edge structure (XANES)** data were collected on the LUCIA in SOLEIL. The incident beam energy was monochromatized using a Si (111) double crystal monochromator. Data were collected in a primary vacuum chamber as fluorescence spectra with

an outgoing angle of  $5^\circ$  using a Bruker silicon drift detector. The data were normalized by the intensity of incident energy and processed with the Athena software. Powder samples were measured as an ingot prepared by pressing mixtures of nanoparticles and boron nitride powders. Electrode samples were measured as prepared and as recovered for electrochemical measurement.





**Abstract:**

Transition metal silicides are a family of intermetallic compounds, which have been widely studied as functional materials in integrated circuits, thermoelectricity, superconductivity, magnetism and heterogeneous catalysis. Nanostructuring offers the opportunity to extend the frontier of silicon-based materials science with novel phases and diverse properties. However, building transition metal silicides encompassing relatively high energy bonds usually requires high temperatures, which are not conducive for nanomaterial design and not compatible with the traditional colloidal synthesis methods. In this thesis, molten salts syntheses based on element insertion into nanoparticles are developed. Transition metal silicide nanoparticles (M-Si, M=Ni, Fe, NiFe, Co) and a ternary nickel silicophosphide are crystallized in high temperature inorganic solvents, where a diluted and carbon-free environment is provided. The obtained silicide nanoparticles are investigated in electrocatalysis of alkaline water oxidation and magnetism. NiFe silicides demonstrate outstanding activity and stability arising from an original *in situ* generated core-shell-shell structure, while defect-rich CoSi nanoparticles show an unusual surface related ferromagnetism. Moreover, the study of silicophosphide nanoparticles provides an insight in multinary material design in molten salts and the role of nonmetal elements in overall alkaline water splitting electrocatalysis.

Keywords: [transition metal silicides, nanoparticles, synthesis in molten salts, overall alkaline water splitting, magnetism]

**[Conception de nanoparticules de siliciure de métal en sels fondus : propriétés électrocatalytiques et magnétiques]**

**Résumé :**

Les siliciures de métaux de transition sont une famille de composés intermétalliques, qui ont été largement étudiés en tant que matériaux fonctionnels dans les circuits intégrés, la thermoélectricité, la supraconductivité, le magnétisme et la catalyse hétérogène. La nanostructuration offre la possibilité repousser les frontières de la science de ces matériaux avec de nouvelles phases et des propriétés diverses. Cependant, l'énergie de liaison relativement élevée des siliciures de métaux de transition nécessite généralement une température élevée pour leur formation, ce qui n'est pas propice à la conception de nanomatériaux et n'est pas compatible avec les méthodes de synthèse colloïdales traditionnelles. Dans cette thèse, des synthèses en sels fondus basées sur l'insertion d'éléments dans des nanoparticules sont développées. Des nanoparticules de siliciure de métal de transition (M-Si, M=Ni, Fe, NiFe, Co) et un silicophosphure de nickel ternaire sont cristallisés dans des solvants inorganiques à haute température, où un environnement dilué et sans carbone est fourni. Les nanoparticules de siliciures obtenues sont étudiées en électrocatalyse de l'oxydation de l'eau alcaline et du magnétisme. Les siliciures de NiFe démontrent une activité et une stabilité exceptionnelles résultant d'une structure originale cœur-coquille-coquille générée *in situ*, tandis que les nanoparticules de CoSi riches en défauts présentent un ferromagnétisme inhabituel. De plus, l'étude des nanoparticules de silicophosphure donne un aperçu de la conception de matériaux multinaires dans les sels fondus et du rôle des éléments non métalliques dans l'électrocatalyse de l'électrolyse de l'eau.

Mots clés : [siliciures de métal de transition, nanoparticules, synthèse en sels fondus, global électrolyse de l'eau alcaline, magnétisme]